FOSSIL ENERGY

DOE/PC/91008-19
(DE98000498)

CHARACTERIZATION OF FRACTURED RESERVOIRS USING STATIC AND DYNAMIC DATA: FROM SONIC AND 3D SEISMIC TO PERMEABILITY DISTRIBUTION

Final Report
September 30, 1998

By
Jorge O. Parra, Ph.D.
Christopher Hackert, Ph.D.
Raymon Brown, Ph.D.
Hughbert A. Collier, Ph.D.
Akhil Datta-Gupta, Ph.D.
Alejandro Idrobo

December 1998

Performed Under Subcontract No. G4S51731 Contract No. DE-AC22-94PC91008

Southwest Research Institute
San Antonio, Texas

National Petroleum Technology Office
U. S. DEPARTMENT OF ENERGY
Tulsa, Oklahoma

DOE/PC/91008-19
Distribution Category UC-122

Characterization of Fractured Reservoirs Using Static and Dynamic Data: From Sonic and 3D Seismic to Permeability Distribution

By
Jorge O. Parra, Ph.D.
Christopher Hackert, Ph.D.
Raymon Brown, Ph.D.
Hughbert A. Collier, Ph.D.
Akhil Datta-Gupta, Ph.D.
Alejandro Idrobo

December 1998

Work Performed Under Subcontract No. G4S51731 Contract DE-AC22-94PC91008

Prepared for
U.S. Department of Energy
Assistant Secretary for Fossil Energy

Robert E. Lemmon, Technology Manager
National Petroleum Technology Office
P.O. Box 3628
Tulsa, OK 74101

Prepared by:
Southwest Research Institute
Instrumentation and Space Research Division
6220 Culebra Road
San Antonio, TX 78238

TABLE OF CONTENTS

LIST OF FIGURES

FOREWORD AND ACKNOWLEDGMENTS

The accompanying report represents work on the characterization of fracture reservoirs using static and dynamic data from sonic and 3D seismic to permeability distribution. Project coordination and supervision, as well as geophysical studies, were performed by Dr. Jorge Parra from the Department of Electronics and Applied Physics, Instrumentation and Space Research Division, Southwest Research Institute. Software development, algorithm processing, and computer assistance throughout the project were provided by Dr. Christopher Hackert from Southwest Research Institute, and Dr. Raymon Brown from Oklahoma Geological Survey provided assistance on the implementation of the algorithms. The petrophysical studies were conducted by Dr. Hughbert Collier, consultant to SwRI. Petroleum engineering work was performed by Dr. Akhil Datta-Gupta and Mr. Alejandro Idrobo under a subcontract agreement between Southwest Research Institute and Texas A&M University.

The assistance of Dr. Min Tham, project manager from BDM-Oklahoma, is gratefully acknowledged. We also thank Chevron Production USA, in particular, Dr. Mike Morea, for his contribution of Buena Vista Hills field data.

The report is organized in 12 sections, beginning with an introduction and summary of project efforts. Section II contains the petrophysics and tomography used to estimate the contribution of elastic scattering and intrinsic attenuation at the Buena Vista Hills oil field. The third section details data sets collected from the field, and the fourth section describes resolution matching of sonic and density logs using Formation MicroImager (FMI) high resolution resistivity data. Section V includes an estimate of the contribution of elastic scattering and intrinsic attenuation to velocity dispersion using well control, and Section VI, drawing on the results of the Kankakee oil field study, shows how attenuation and dispersion are related to permeability in a poroelastic environment with azimuthal anisotropy. Section VII introduces data from the Lodgepole oil field used to characterize fractures with the aid of petrophysics and 2D seismic data. The eighth and ninth sections present theory and application, respectively, regarding the dispersion and attenuation of acoustic waves in randomly heterogeneous media at the Kankakee oil field. Section X describes methods developed to account for scattering and anisotropy at the Buena Vista Hills field, and Section XI reports how data integration techniques were incorporated into a 3D geostatistical reservoir model of Buena Vista Hills. The final section contains conclusions regarding the overall project.

CHARACTERIZATION OF FRACTURED RESERVOIRS USING STATIC AND DYNAMIC DATA: FROM SONIC AND 3D SEISMIC TO PERMEABILITY DISTRIBUTION

I. INTRODUCTION AND PROJECT SUMMARY

A. Background

In low porosity, low permeability zones, natural fractures are the primary source of permeability affecting both production and injection of fluids. The open fractures do not contribute much to porosity, but they provide an increased drainage network to existing porosity. They also may connect the borehole to remote zones of better reservoir characteristics. An important approach to characterizing the fracture orientation and permeability of reservoir formations is one based on the effects of such conditions on the propagation of acoustic and seismic waves in the rock.

The project objective is to evaluate acoustic logging and surface seismic measurement techniques as well as fluid flow and transport methods for mapping permeability anisotropy and other petrophysical parameters in a fractured reservoir. We will also determine fracture connectivity using multiphase production data. The work includes theoretical and numerical model studies linked with a balanced petrophysical and engineering program for the development of advanced concepts of borehole and surface seismic methods.

The project is organized in three phases. **Phase I** includes the development of theoretical models using deterministic interwell seismic solutions, petrophysical analysis, and rapid simulation of multiphase flow in reservoirs using a semianalytic streamline approach. **Phase II** includes the development of theoretical models using stochastic solutions, fractured connectivity using inversion of production data, and interwell seismic and sonic logs signal analysis. **Phase III** includes numerical modeling, analysis, and integration of geophysical and petrophysical data, and application of the inversion method to production data and reconciliation with geophysical data to characterize fracture reservoirs.

In the second year of the project, the research topics were modified from those originally proposed. The second year of the project thus involved petrophysical analysis and basic theoretical analysis in geophysics and petroleum engineering. Geophysical techniques included the analysis of plane-harmonic seismic waves in a random geological media, development of scattering correction techniques for extracting the intrinsic properties of the media, and several processing techniques that were required to interpret well logs and interwell seismic data at the Buena Vista Hills Field in California. Petroleum engineering techniques included the development of an inversion method for production data and reconciliation with geophysical data. The petrophysical analysis consisted of evaluating the Buena Vista Hills Field (partially owned by Chevron) and completing an evaluation of the Twin Creek fractured reservoir (owned by Union Pacific Resources) in the overthrust area of Utah and Wyoming to characterize fractures and rock physical properties for the validation of advanced theoretical concepts developed during this project.

B. Summary of Project Efforts

1. Summary of First-Year Effort and Accomplishments

The first year of the project involved petrophysical and basic theoretical analyses in geophysics and petroleum engineering. Geophysical techniques included the analysis of plane-harmonic seismic waves in poroelastic and anisotropic layered media, as well as the theoretical development of an acoustic logging system in a fluid-filled borehole surrounded by an isotropic poroelastic formation and an anisotropic viscoelastic formation. Petroleum engineering techniques included the development of a semianalytic approach to multiphase flow calculations and applications. The petrophysical analysis consisted of an evaluation of the Twin Creek reservoir to characterize fractures and rock physical properties. The feasibility of using seismic measurement techniques to map fracture zones (between wells spaced 2,400 feet apart at a depth of 11,000 feet) was completed.

2. Summary of Second-Year Effort and Accomplishments

Second-year research topics included geophysical techniques such as analysis of plane-harmonic seismic waves in a random geological media, as well as development of scattering correction techniques for extracting the intrinsic properties of the media, and several processing techniques that are required to interpret well logs and interwell seismic data at the Buena Vista Hills field. Petroleum engineering techniques include the development of an inversion method for production data and reconciliation with geophysical data. The petrophysical analysis consisted of a continuing evaluation of the Twin Creek reservoir to characterize fractures.

The analysis of elastic wave propagation in random geological media was completed, and several algorithms for processing well log data were developed and used to predict scattering and intrinsic attenuation at the Buena Vista Hills field. The solution of the transversely poroelastic wave equation was applied to predict dispersion of seismic waves in poroelastic media with azimuthal anisotropy. Additionally, software was developed for the characterization of hydrocarbon reservoirs using static and dynamic data.

3. Summary of Third-Year Effort

A geological and petrophysical analysis of part of the Twin Creek Reservoir was completed for the seismic modeling and in preparation for a crosswell survey. This analysis established the factors controlling fracturing in the reservoir. Integration of the results with a velocity inversion analysis of the 2D surface seismic data established a correlation between a high-velocity anomaly and the main fractured interval in a horizontal well that parallels the seismic line. Initial seismic modeling of the field provided the constraints for a crosswell survey and verified that the technique could be used in the field. The results of our study were very promising. However, after working on the data for one year, several obstacles arose:

- UPRC decided that the vertical wells we were going to use for the crosswell survey would not be available.

- UPRC reduced activity in the area because hydrocarbon production was too low to justify further development.

- Additional 2D surface seismic lines in the study area, owned by parties other than UPRC, were not released to us.

Our study was then switched to Buena Vista Hills Field because a plethora of geological, petrophysical, production, and seismic data was available, including crosswell surveys. Chevron is studying the field for a DOE project, and data are available for a wide range of scales: from centimeter (FMI and minipermeameter) to hundreds of meters (crosswell surveys).

To characterize the Buena Vista Hills field, we implemented modeling, processing, and interpretation methods. The modeling methods are based on deterministic and stochastic solutions. Deterministic solutions developed during Phase I were applied in Phase II to simulate acoustic responses of laminated reservoirs. Specifically, the simulations were aimed at implementing processing techniques to correct P-wave and S-wave velocity logs for scattering effects caused by thin layering. We also took steps to predict effective anisotropy and dispersion based on well control. We developed methods of estimating dispersion from crosswell data and well logs, and applied the methods to the Buena Vista Hills field. The complex lithology of the field made it difficult to interpret the results, so forward modeling was used to demonstrate the fundamental validity of the approach. In addition, preliminary findings from the Lodgepole Field Study and data gathered on vertical fractures during an earlier project at the Kankakee oil reservoir at the Buckhorn test site, Illinois, were used during algorithm development and testing.

The results suggested that, with some refinement, our methods will lead to improved imaging of reservoir properties. In the long term, we hope to use intrinsic velocity dispersion to map reservoir properties. The forward modeling method has shown the feasibility of this technique. To be successful, we must be able to obtain precise and accurate well log and anisotropy information from field measurements. We also expect this method to be better suited to reservoirs where the scale of the structure is more comparable to the seismic wavelength.

The theoretical solution for calculating full waveform dipole sonic developed in Phase I was applied to simulate dipole responses at different azimuthal source orientations, and the results used to interpret the effects of anisotropy associated with the vertical fractures at Buena Vista Hills. Stochastic solutions were developed to simulate seismic waves propagating in a heterogeneous random medium. Random wavefield simulations are being used to understand dispersion effects associated with heterogeneities at different scales, and new analytical solutions to calculate dispersion and attenuation effects in terms of the standard deviation of rock physical properties are being developed for 1D and 2D random geological media.

Using a variety of data from three different reservoirs- Kankakee, Twin Creek, and primarily Buena Vista Hills, we tested and applied the modeling techniques and processing algorithms developed in Phases I and II. These reservoir characterization techniques can be applied to similar oil fields to better understand the factors controlling production.

II. PETROPHYSICS AND TOMOGRAPHY USED TO ESTIMATE THE CONTRIBUTION OF ELASTIC SCATTERING AND INTRINSIC ATTENUATION AT BUENA VISTA HILLS FIELD

A. Introduction

The principal application of this study is to predict the dispersion characteristics of acoustic and seismic waves in the Buena Vista Hills oil field 25 miles southwest of Bakersfield in the southern San Joaquin Valley of California. Chevron is conducting a reservoir characterization program at the field, which lies in the Antelope shale a siliceous shale in the Monterrey formation — to establish the viability of CO_2 enhanced oil recovery (EOR). Chevron's study focuses on a new infill well (653Z-26B) and the four 1950s-vintage wells that surround it (see Figure II-1). The five wells will be used for the CO_2 pilot flood, with the new well serving as the injector.

At the Buena Vista Hills field, the shale-sand sequence is characterized by layering that is finer than that typically resolved by sonic logging. In some sections the vertical resolution ranges from a fraction of a centimeter to tens of centimeters, while in others zone bed thickness can vary from centimeters to meters. These heterogeneities, many of which are below the resolution of sonic logs, contribute to the apparent anisotropy in the sonic-to-seismic frequency range.

In general, attenuation of seismic energy and velocity anisotropy consists of an intrinsic component and an apparent component caused by scattering from velocity and density heterogeneity. The intrinsic component of attenuation is very important in determining fluid properties through a reservoir (Jones, 1986). However, it may be difficult to distinguish between the apparent (layer-induced) effects caused by elastic scattering and intrinsic components when thin layers are present, unless detailed information is available on the velocity structure. Several approaches exist to predict the effects of unresolved layering (Ozbech, 1993; and Sams, 1995). We use the resolution matching technique (Nelson and Mitchell, 1991) that employs Formation MicroImager to enhance the resolution of sonic and density logs. This idea was implemented by Sams (1995) to produce an estimate of vertical velocity heterogeneity with a resolution that matches that of the FMI data.

We present a high-resolution velocity model of a section at Buena Vista Hills, which includes P- and S-waves and the density determined from FMI-matched sonic and dipole sonic logs as well as an estimate of the density. The high-resolution velocity model was constructed at the FMI log scale to produce velocities at lower frequencies in the siliceous shale, with no sand or carbonate laminations. Since shales have intrinsic anisotropy which cannot be estimated directly from well logs, we developed empirical equations to predict anisotropy of the shales from Vp, Vs, and density measurements in the well. We estimated elastic constants at the FMI scale (C_{11}, C_{13}, C_{33}, and C_{44}) to predict seismic responses of formations at lower frequencies (i.e., crosswell frequency). With this information we produced the velocity accounting only for the effects of elastic scattering at the selected crosswell frequency using Backus averaging. Finally, intrinsic velocity dispersion was determined to estimate quality factors of the formation. These results were validated using computer models.

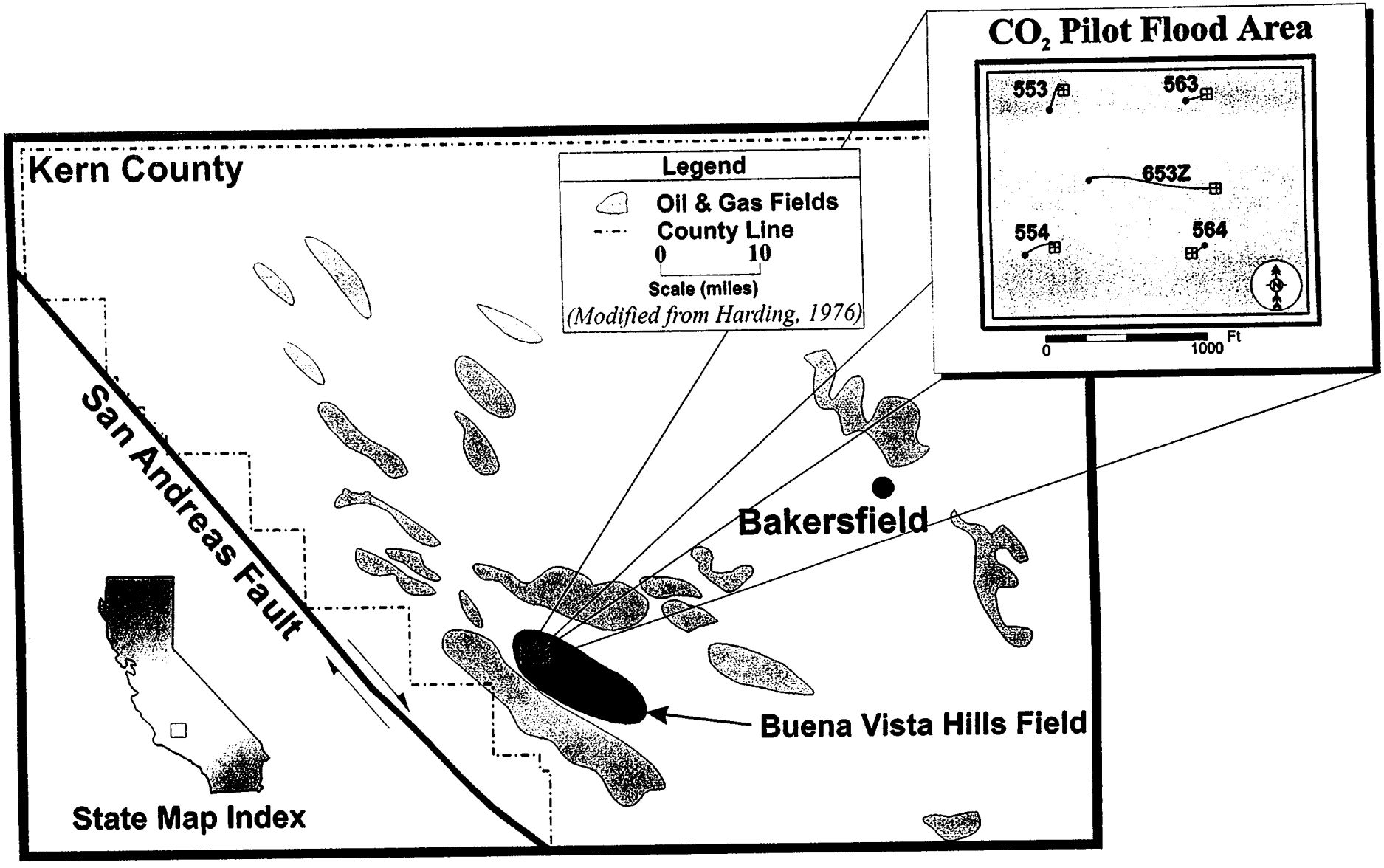

Figure II-1. Map of the Buena Vista Hills Field and the CO_2 pilot flood area.

This Section is devoted to geology, petrophysics and travel time tomography at the study area. The petrophysics includes well logs and core information from well 653Z-26B (the injector well). Also, geological cross sections between the injector and producer wells are presented to aid in a tomographic interpretation as well as an analysis of elastic scattering and intrinsic attenuation (presented in section V).

B. Geological Overview of the Buena Vista Hills Site

1. Field History

Primary production in the Buena Vista Hills field dates back to 1952. Initial oil production in the pilot study area ranged from 50 to 220 BOPD (barrel oil per day). Current oil production in this part of the field averages 20 BOPD. Oil gravity averages approximately 30 (degree) API in the pilot area (Toronyi, 1997), and the reservoir is predominately water-wet (Morea, 1997b).

An extensive petrophysical database is being amassed for the 653Z infill well. The entire producing interval (952.8 feet) was cored and 99.5 percent of the core was recovered. A number of tests were run on the core and a comprehensive suite of state-of-the-art wireline logs was run in the well. Crosswell seismic surveys were made of the pilot study wells.

2. Geology

Buena Vista Hills is a northwest-southeast trending, elongated, doubly-plunging anticline with two structural highs on the crest (Toronyi, 1997). The CO_2 pilot area is located on the west high, which is called West Dome.

The producing interval is a 1,300-foot thick section of the Upper Miocene Monterey Formation. Locally, the interval is referred to as the Antelope Shale and is subdivided into three units: the Brown Shale (upper quarter), the Upper Antelope Shale (middle half), and the Lower Antelope Shale (lower quarter). Only the Brown and Upper Antelope Shales were cored in the 653Z well. Geochemical analysis of the oil suggests that most of the present production comes from the Brown and upper Upper Antelope Shales (Morea, 1998).

The Antelope Shale is an unusual and unlikely reservoir rock (Morea, 1997a, 1997b; Toronyi, 1997):

1. Approximately 95 percent of the rock is thin (1 to 5 cm), graded, clay-free, siliceous shale beds.

2. Very thin (1 mm to 25 cm) clayey sand laminae are intercalated with the siliceous shale. The 653Z core contains 748 sand laminae; all but one are in the Upper Antelope Shale.

3. Porosity averages 28 percent, while permeability averages only 0.07 microdarcies. Permeability of the siliceous shale is in the microdarcy range.

4. The rock was deposited in a restricted basin as distal turbidite and hemipelagic siliceous beds. Diagenetically altered diatom tests were the source of the silica.

5. There is extensive lateral stratigraphic continuity across the field, except where sands are present.

Petrographically, the siliceous shale is silty, dolomitic, opaline mudstone. Very finely crystalline dolomite is dispersed in a matrix of isotropic opal-ct. Detrital grains are feldspar, clay, quartz, pyrite, and dolomite (Morea, 1997b).

Thin section analysis reveals that most of the porosity is matrix microporosity. Moldic and fracture pore types are also present. Interconnectedness of all pore types is poor. Pore throat radii of the siliceous shale are less than 0.5 micron and up to 2.5 - 10 microns for the sands (Morea, 1997b).

Mercury porosimetry tests indicate that at reservoir conditions only the sands are capable of producing oil (Morea, 1997b). The sands, however, constitute only 5 percent of the rock, so it appears that fractures may be contributing significantly to hydrocarbon production.

The extent to which the Antelope Shale is fractured and the significance of those fractures for fluid migration is open to debate. Pressure build-up analyses suggest that the fracture system is not pervasive (Toronyi, 1997). However, cores, crosswell seismic images, and satellite data all point to significant fracturing in the Buena Vista Hills field. Fracturing occurs on a variety of scales in the core and in the FMI images. Regardless of their relationship to fluid production, fractures are prevalent enough to affect borehole and interwell seismic measurements in most of the reservoir (see Figure II-2).

3. Example of an Interval

The petrophysical parameters of the interval from 4,130 to 4,160 feet were used for the preliminary seismic modeling. This interval was chosen because it is homogeneous and has few fractures (see the FMI image in Figure II-3). In fact, it is one of the least fractured intervals in the core. Core recovery was 100 percent. The interval is within the lower portion of the Brown Shale. Stratigraphic marker NA occurs at 4,147 feet.

The entire interval is siliceous shale, with no sand or carbonate beds. Laminations are distinct from 4,133 to 4,144 feet. They are mm?s to cm?s thick and most are parallel. From 4,144 to 4,160 feet the rock has a slightly mottled appearance in UV light. In plain light it looks very homogeneous, with only a few laminations. Most of the petrophysical properties are very consistent in the homogeneous zone, while the laminated interval has more variation (Figure II-3).

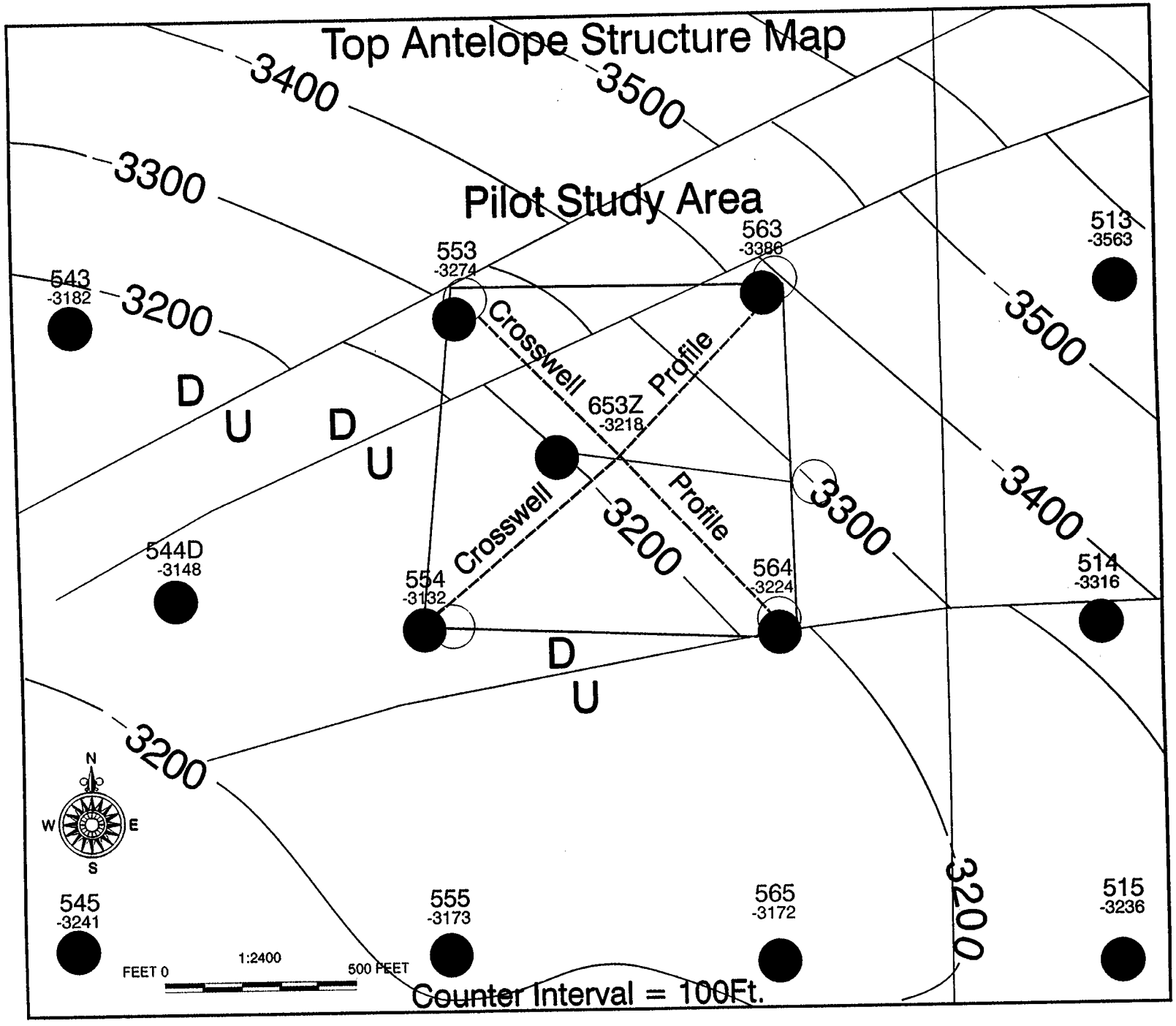

Figure II-2. Structural map and well locations.

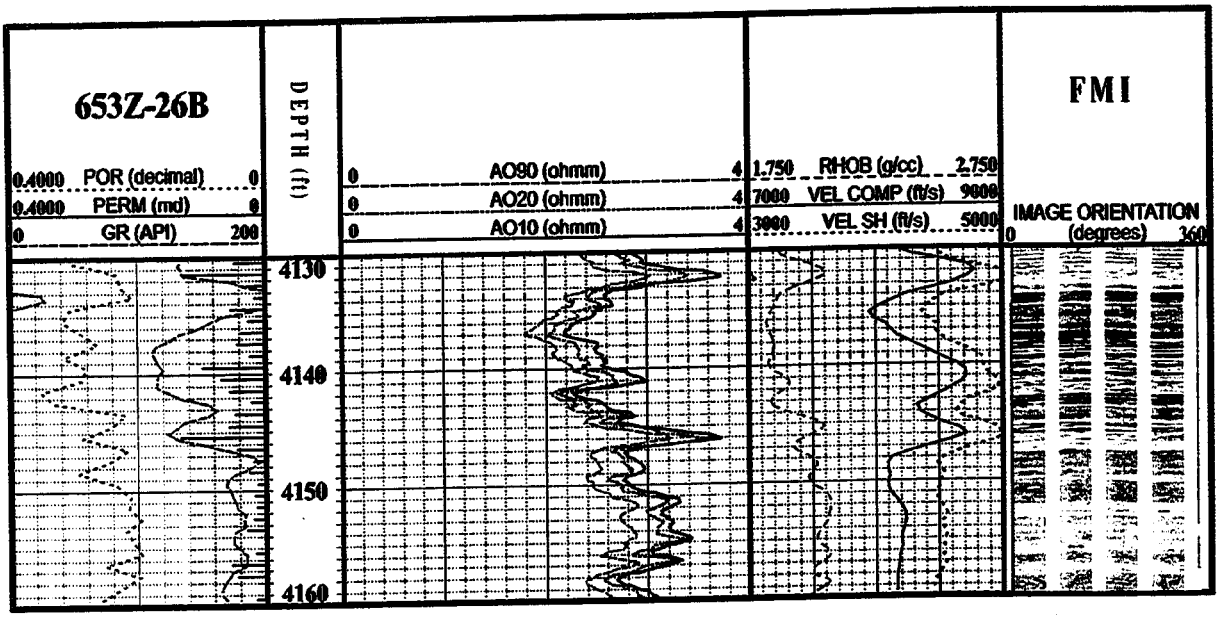

Figure II-3. Logs and FMI image of the study interval: 4130 to 4160 ft. Porosity (POR) and Permeability (PERM) are core values; all others are log curves. All curves have been depth corrected to the AO10 array induction curve.

The laminated portion has some fractures. Most of them are parallel and vertical to near vertical. The fractures are only a few inches long and terminate at bed boundaries. A fine grained, clay-rich material fills most of the fractures (Morea, 1997a).

Table II-1 summarizes the petrophysical properties plotted in Figure II-3 and used for the seismic modeling. The abbreviation for each property is the one used in Figure II-3.

Table II-1. Petrophysical Properties of the Interval (4,130 - 4,160 feet)

Property	Unit	Mean	Range
Grain Density*	g/cc	2.3	2.18 - 2.42
Permeability (Perm)	md	0.042	001 - 0.13
Porosity (POR)	%	0.26	0.19 - 0.33
Bulk Density (RHOB)	g/cc	1.94	1.82 - 2.06
Compressional Velocity (VEL COMP)	feet/second	8,313	7,930 - 8,770
Shear Velocity (VEL SH)	feet/second	4,638	4,360 - 5,040

***A grain density curve was not included in Figure II-2.**

In summary, the study interval is low density (2.3 g/cc), high porosity (26 percent), very low permeability (0.04 md), slightly fractured, laminated, siliceous shale. The mean compressional velocity is approximately 8,300 ft/sec and the shear velocity is 4,600 ft/sec.

4. Well 653Z Petrophysical and Lithologic Log of a Selected Interval in the Antelope Shale

In this section we examine the lithology of a large interval between 3950 to 4580 feet measured depth (MD) in the injector well 653Z-26B. In this well, the Platform Express logging suite (array induction, density, neutron, and SP) is the depth reference. Core analyses and core lithology descriptions have been depth corrected to Platform Express depths. All of the core and log depths are in excellent agreement (see Figure II-4).

The core is described as shale, sandstone, sandstone (cemented), sandstone rubble, sandstone/shale laminae <0.02 ft., carbonate, carbonate rubble, and gap/missing core. Sandstone, sandstone (cemented), and sandstone rubble are grouped together and labeled as sandstone for the log. Carbonate and carbonate rubble are both labeled carbonate. The carbonate is predominately dolomite.

All beds, no matter how thin, are displayed on the log. Unfortunately, at the scale of the display (5 in. = 100 ft.) thin sandstone laminae are not visible. All the dolomite beds (there are only four in this interval) are visible. The rest of the lithology is shale.

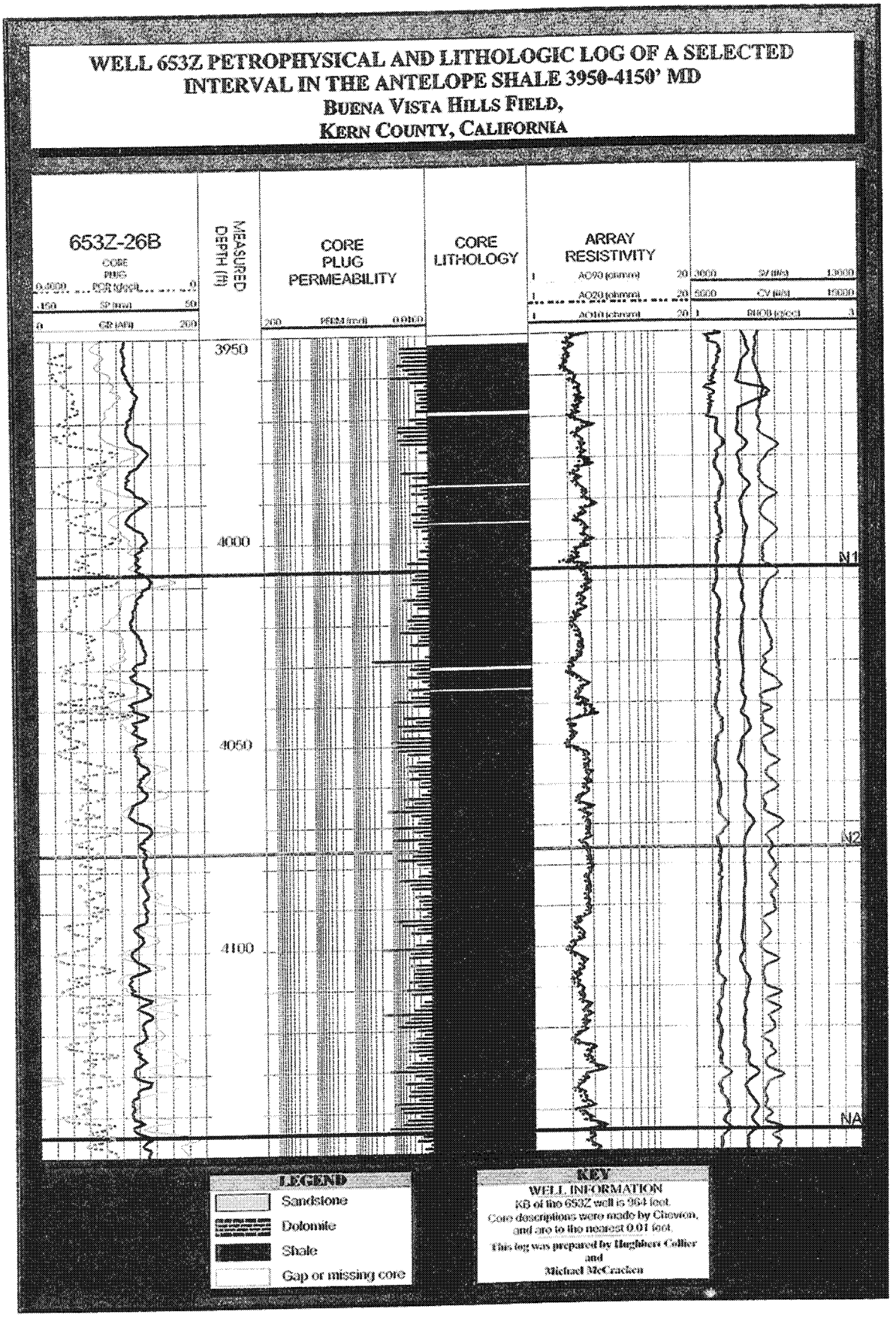

Figure II-4(a). Lithology from 3950-4150 ft.

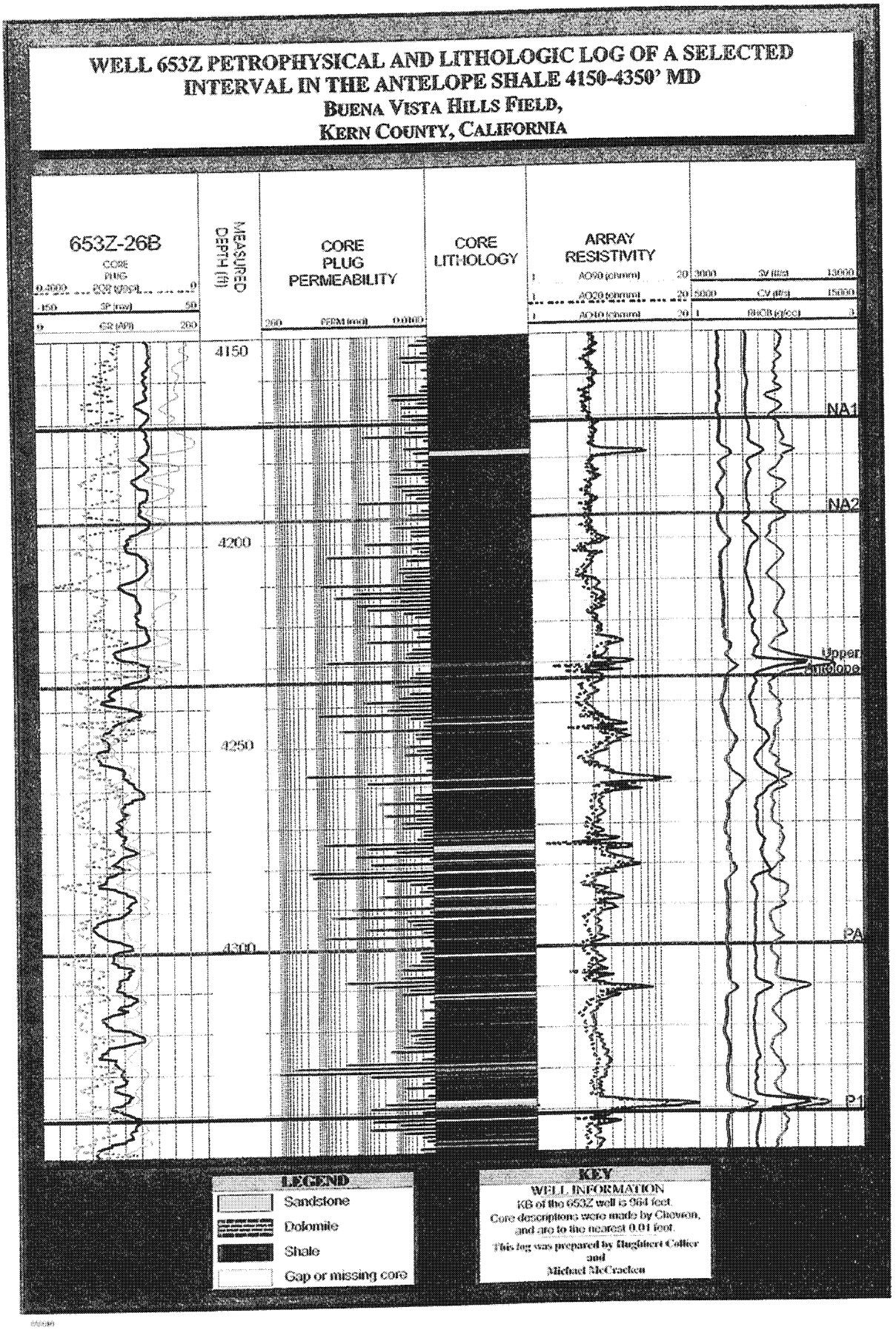

Figure II-4(b). Lithology from 4150-4350 ft.

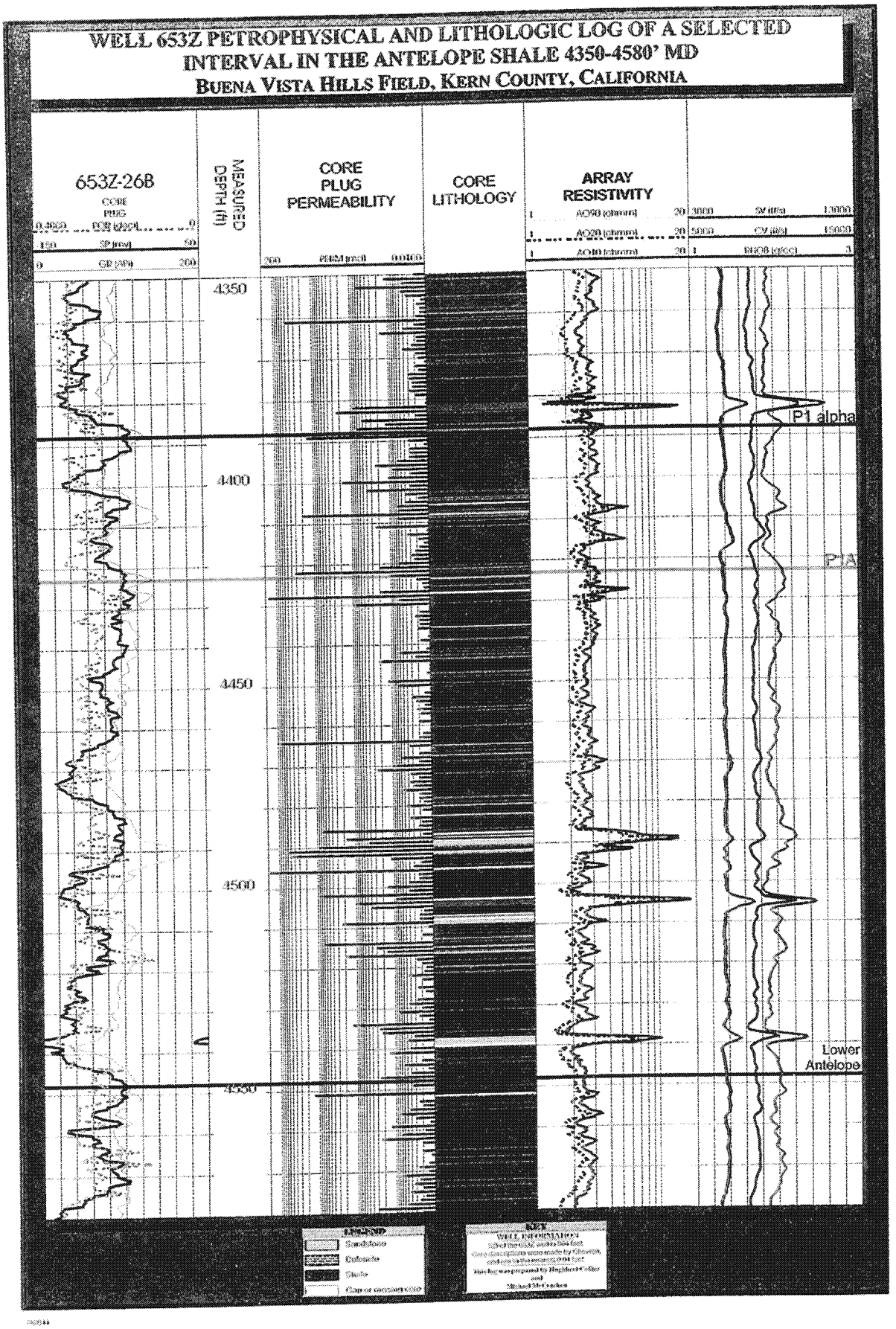

Figure II-4(c). Lithology from 4350-4580 ft.

5. Analysis of the Log

The log shown in Figure II-5 encompasses approximately two-thirds of the producing interval in the Antelope Shale, which is the local name for the Upper Miocene Monterey Formation. The Antelope Shale is subdivided into three units. This log includes all of the middle unit, the Upper Antelope Shale (4,233 to 4,548 feet MD), and most of the upper unit, the Brown Shale (3,950 to 4,233 feet MD). Geochemical analysis of the oil suggests that most of the present production comes from the Brown Shale and the Upper Antelope Shale.

Eleven marker bed tops (N1 thru Lower Antelope) are correlated on the cross section in Figure II-5. Notice that the SP, gamma ray, and core plug porosities correlate very well, especially within the Upper Antelope section. The resistivity, compression, shear, and bulk density curves also have a high degree of correlation with the Upper Antelope. Vertical and horizontal scales are not the same; the vertical scale is greatly exaggerated in the figure, making the dips of the beds appear steeper than they are.

There are 461 sandstone laminae within this 630-foot interval, which totals 35.31 feet of sandstone. There are four dolomite beds within the interval, with a total thickness of 4.88 feet. The rest of the interval is thin (1 to 5 cm) shale beds. The shale is a siliceous, silty, dolomitic, opaline mudstone. Very finely crystalline dolomite is dispersed in a matrix of isotropic opal-ct. Detrital grains are feldspar, clay, quartz, and pyrite (Moorea, 1997).

The interval from 3,950 to 4,580 ft. naturally subdivides into three or four intervals based on the petrophysical properties:

3,950 to 4,144 feet (NA Unit). The petrophysical properties of the Brown Shale are very consistent from 3,950 to 4,144 ft. The laminated nature of the shale is evident on the shallow resistivity curve (AO10). Below 4,144 ft., which is the NA marker unit, all of the petrophysical properties start increasing in value (except for the gamma ray curve, which starts decreasing). This is the same interval that changes thickness and dip direction on the cross section. It also corresponds to the beginning of sandstones and dolomites in the shale.

4,144 to 4,233 feet (Top of Upper Antelope Unit). The lithology from 4,144 to 4,233 ft. is predominately shale. The petrophysical properties, however, are more akin to the underlying Upper Antelope unit, which contains sandstones of varying thicknesses.

4,233 to 4,548 feet (Upper Antelope Unit). This unit consists of alternating shale and thin sandstone beds. Bulk density, compressional velocity, and shear velocity are fairly consistent throughout the unit. However, based on resistivity, gamma ray, SP, permeability, and porosity, the unit can be divided into two intervals at approximately 4,440 feet. Resistivity values increase below 4,200 ft., stay fairly consistent down to 4,440 ft., and then decrease to 2 to 3 ohms, which is the same range as in the Brown Shale unit. Gamma ray

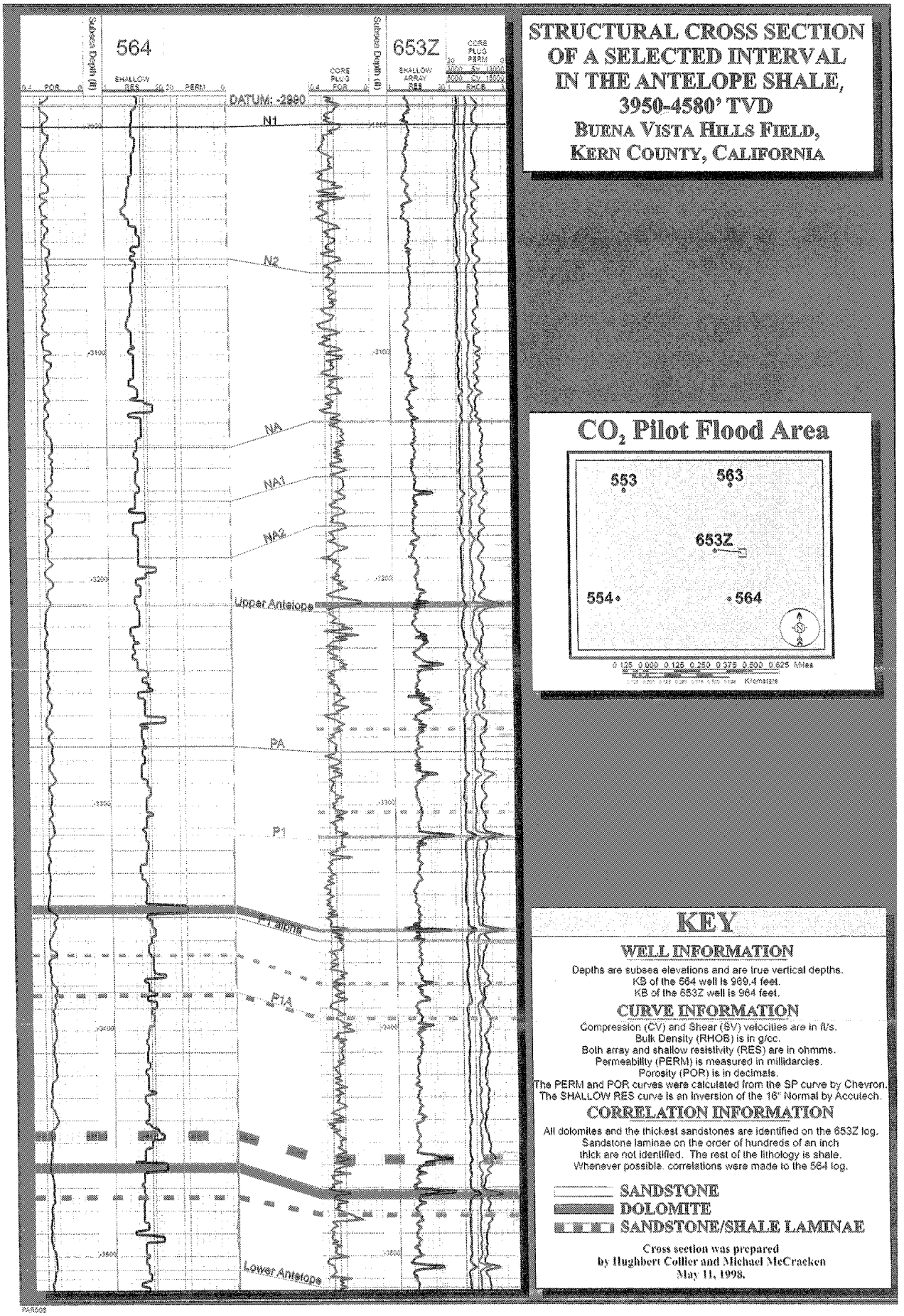

Figure II-5. Structural cross section of a selected interval in the Antelope Shale (3959-4580 ft.).

and permeability values are lower and core plug porosity values are higher below 4,400 ft.

Table II-2 gives average petrophysical properties for the three lithologies. The shale properties are from the 3,950 to 4,144-foot interval. The sandstones and dolomites have some variability in properties, which probably reflects the difficulty of measuring thin beds with logging tools . Further work needs to be done to refine the properties of the sandstones and dolomites; the values are rough estimates only.

Table II-2. Petrophysical Properties of Three Lithologies: Mean Values

Property	Unit	Shale	Sandstone	Dolomite
Compression Velocity (CV)	feet/sec	8,000	9,000	13,000
Shear Velocity (SV)	feet/sec	4,400	5,200	6,500
Bulk Density (RHOB)	g/cc	1.9	2.2	2.6
Permeability (PERM)	Md	0.05	10	1
Porosity (POR)	Decimal	27	27	15
Resistivity	Ohm	2.5	7	18

Examination of the log reveals that the three lithologies are distinctly different, and that petrophysical properties vary in a consistent manner throughout the interval and make for natural subdivisions.

C. Descriptions of Structural Cross Sections

The 653Z well is a deviated hole. The logs were converted to true vertical depth (TVD) for construction of the cross section, and the deviation data and plots are included in this report. Depths are subsea values because this is the only way that the Terrasciences software plots cross sections with deviated wells (see Figure II-5).

The shallow resistivity curve with the best vertical resolution was used for each well: reprocessed 16-inch normal for the 564 and 10-inch array induction for the 653Z. Correlations between wells were made using the shallow resistivity curves. The only other curve common to both logs is the SP. It was not included on this cross section due to space limitations. However, cross sections were produced between wells 553, 653Z and 564 (see Figure II-6), as well as between wells 554, 653Z, and 563 (see Figure II-7) using resistivity and SP logs. The SP log provided a good correlation curve for these wells. It should be included on future cross sections instead of the SP-derived porosity curve, which does not have as much character as the SP.

Two of the four dolomite beds were correlatable between the wells. These two beds appear to be thicker in the 564 well, however, this may be an artifact of the tool response. Six of the eleven thickest sandstone beds correlate between the two wells. Five additional thicker sandstones are present in the 653Z well, but could not be correlated. The sandstones vary from 0.5 to 1.5 ft.

Structure Section A-A'

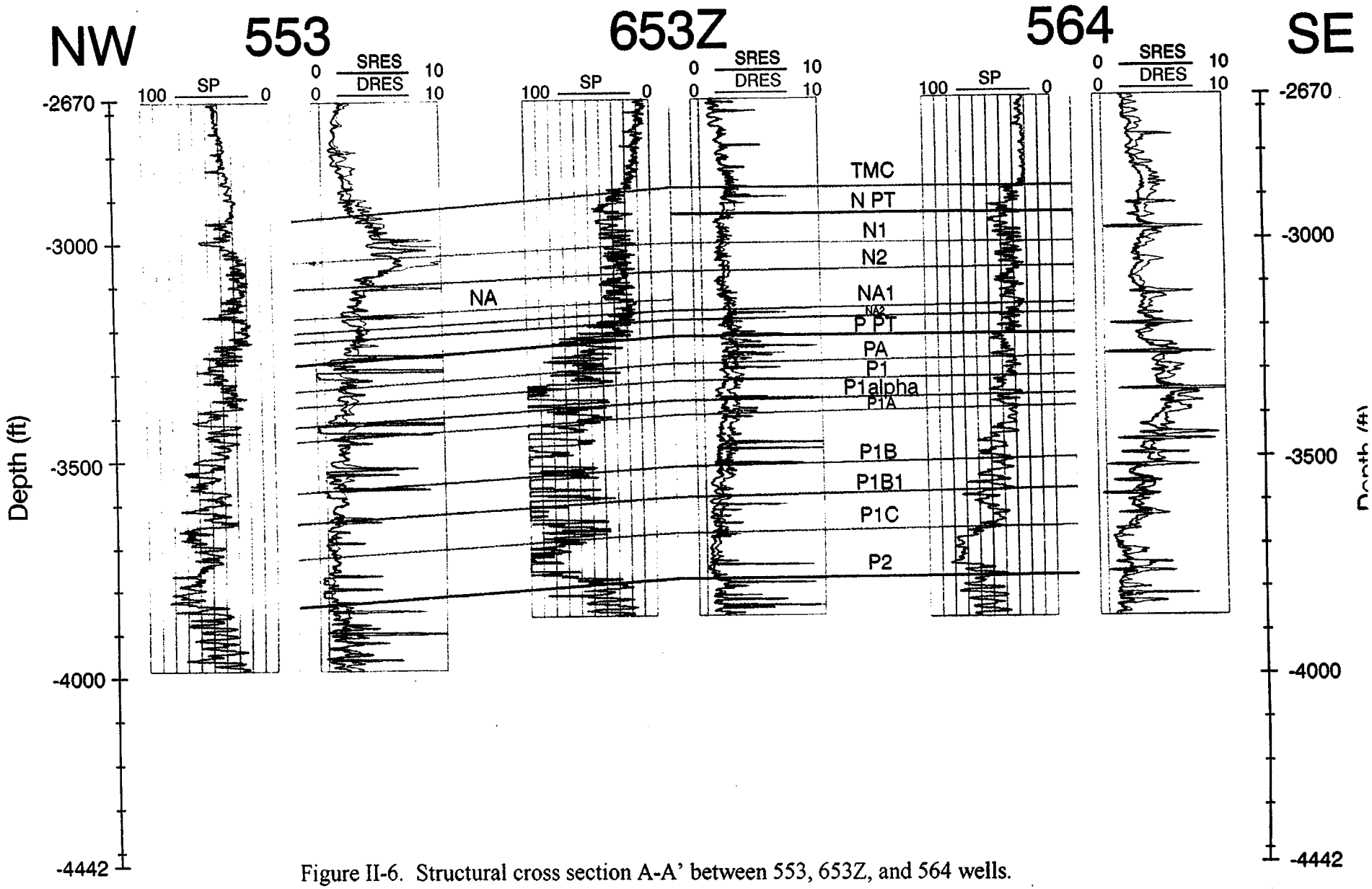

Figure II-6. Structural cross section A-A' between 553, 653Z, and 564 wells.

Structure Section B-B'

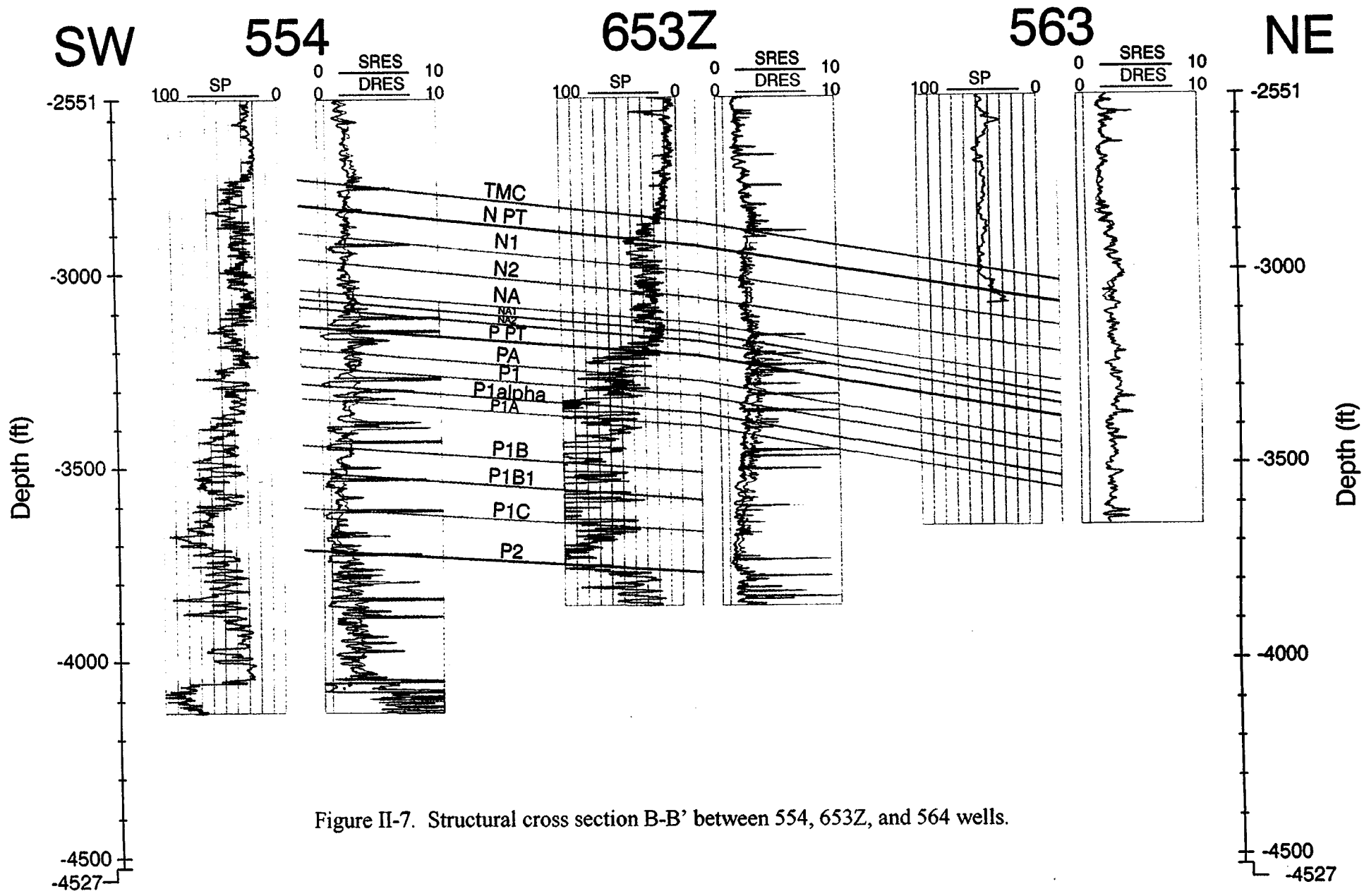

Figure II-7. Structural cross section B-B' between 554, 653Z, and 564 wells.

thick. In addition, four intervals of alternating sandstone/shale laminations are correlatable between the two. These intervals are 1 to 5 ft. thick.

In the 564 well, beds with a resistivity of 6 to 10 ohms are probably sandstone or sandstone/shale laminations. Resistivities greater than 10 ohms may be sandstone or dolomite and are probably dolomite. Slight variations in the resistivity values within the shale sections hint at the laminated nature of the shale. Laminations are slightly more obvious on the 653Z resistivity curve and are very obvious in the core photographs. None of these curves give evidence of fracturing, but then these curves do not normally distinguish fractures.

The dip of the beds between the two wells is fairly consistent within the Upper Antelope. Within the lower half of the Brown Shale, however, the dip changes and the N2 and the NA2 units change thicknesses. This is probably the product of depositional processes, but could possibly be due to faulting.

The cross sections confirm that numerous beds (sandstones and dolomites) are correlatable over the distances of the CO_2 pilot flood area (hundreds of feet). For a more detailed discussion of the selected interval, see the petrophysical and lithologic log, with its accompanying discussion.

D. Travel Time Tomography

Extensive crosswell data was recorded between the injector and the four producer wells. In each case, the source was placed in the producer well and the receiver in the injector. Sources and receivers were placed at 5-foot intervals in the wells over a range of about 1500 ft., although measurements were not taken for the extreme offsets. Waveforms were recorded for more than 30,000 source-receiver combinations for each well pair.

Tomography was done by TomoSeis for each well pair individually. The resulting tomograms yield velocity information with 2-foot vertical resolution and roughly 5-foot horizontal resolution, depending on the specific profile. The four tomographic profiles shown in Figure II-8(a) and in three dimensions in Figure II-8(b) unfortunately do not agree at the common injector well. This is due to several reasons, including:

- Deviation of the injector well: this well is sharply deviated (approximately 16 degrees from vertical). At the present time, tomographic accounting for the well deviation is not available, resulting in distortion of velocities near the injector well.

- Anisotropy in the medium: based on the difference between the sonic logs and the crosswell arrival times, anisotropy on the order of 20 percent is present in the Antelope shale. Ray curvature in the head-wave tomography suggests that errors introduced by anisotropy will be more prevalent near the wells.

- Sampling density: because of the reduced density of ray crossings, accuracy is not as great near the wells as in the bulk medium.

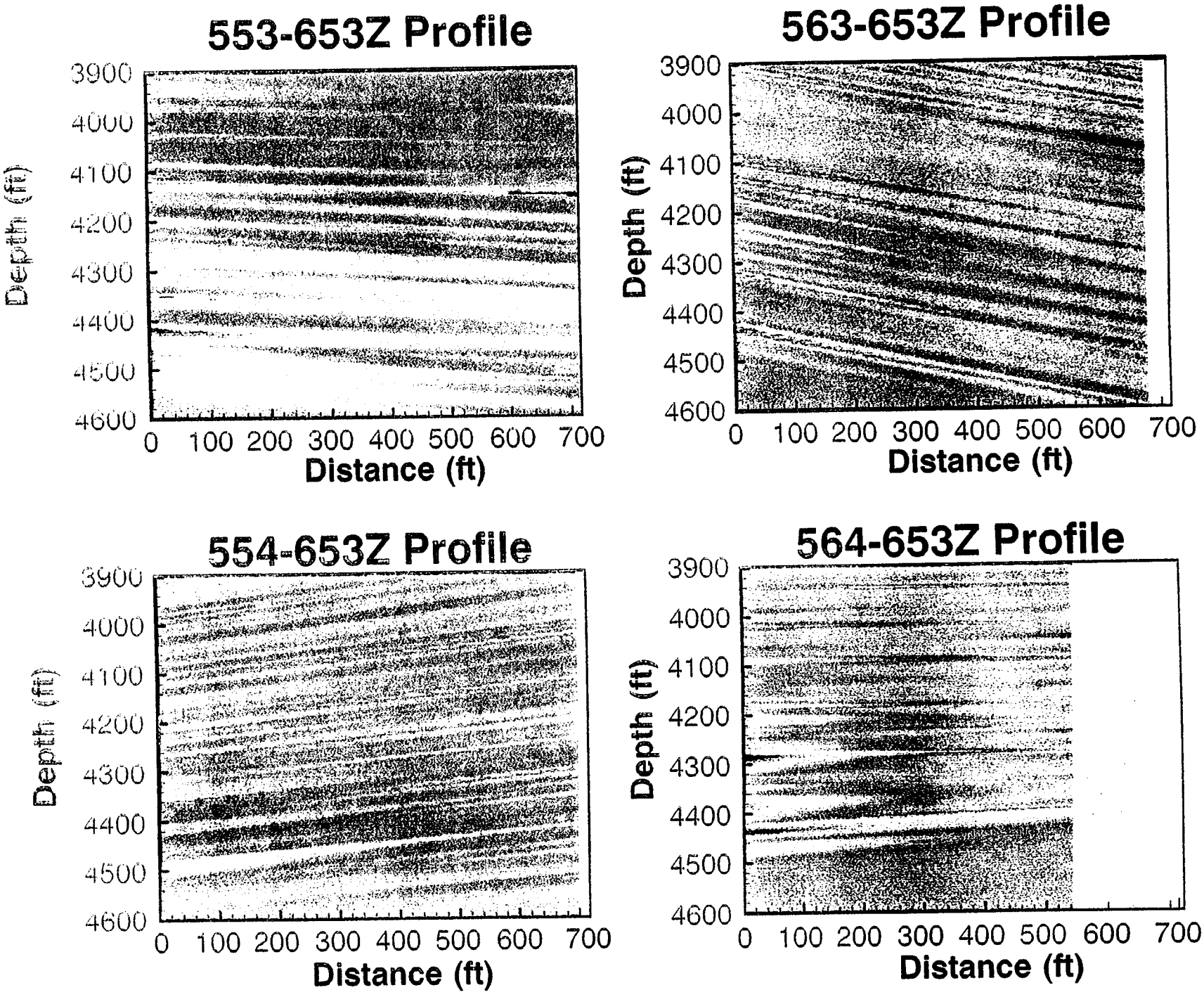

Figure II-8(a). Imaging at Buena Vista Hills. Four velocity profiles.

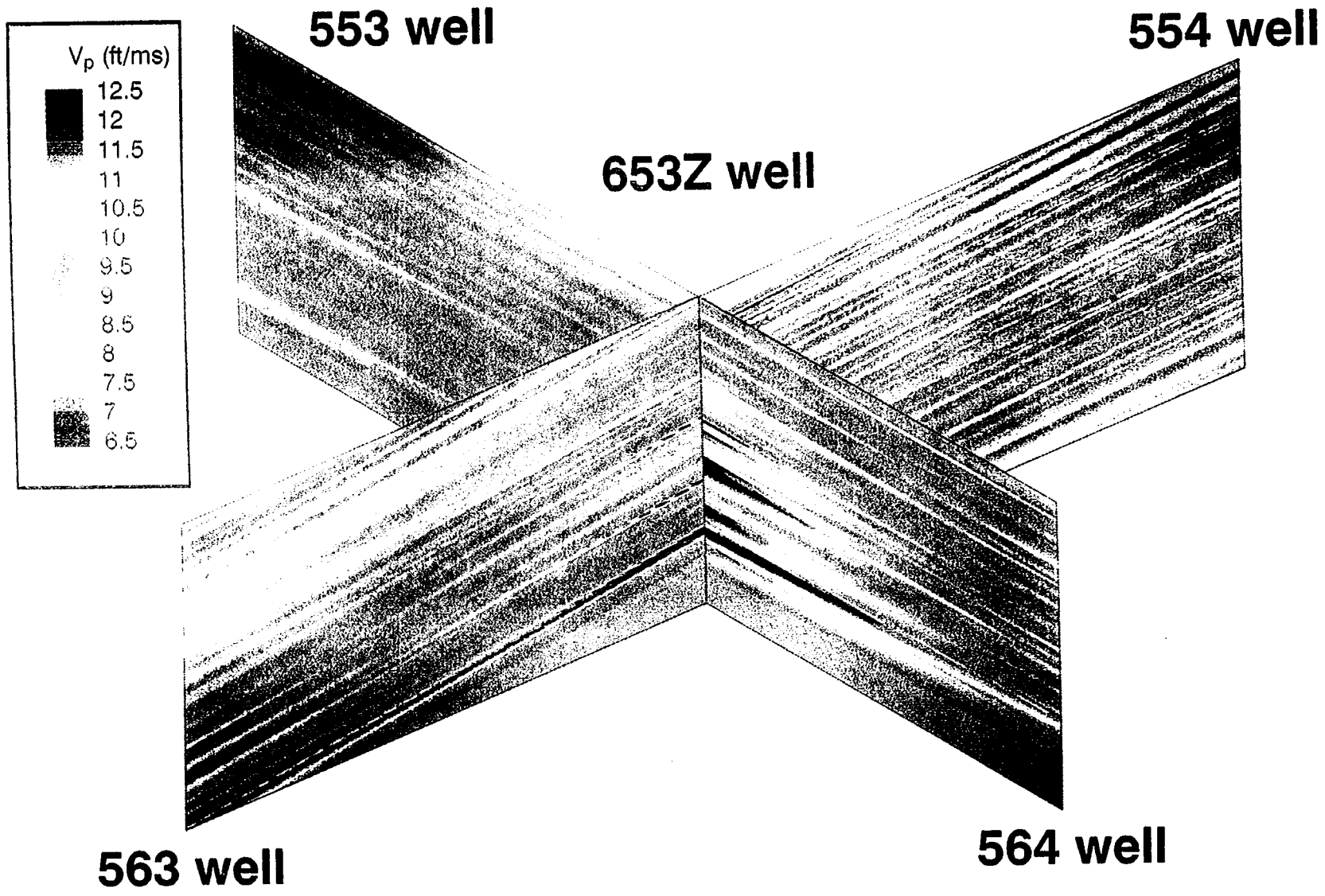

Figure II-8(b). Imaging at Buena Vista Hills. 3D view of velocity profiles.

Nevertheless, the tomographic image between the injector and 564 wells shows good correspondence with the known features of the sonic log recorded in the injector well. Images from all the tomographic profiles show the correct amount of dip based on the known formation depths in each well.

E. Summary

The cross sections confirm that numerous beds (sandstones and dolomites) are correlatable over the distances of the CO_2 pilot flood area (hundreds of feet). A good correlation is observed between the injector and the producers when the SP and the resistivity logs are used to produce the cross sections. The tomography images capture the stratigraphic sequences of the formations at Buena Vista Hills. In particular, the tomograms capture the sandstone and dolomites as high velocity anomalies. Integrating the lithology and the images can reveal the separation between these two geological units.

III. DATA SETS FROM THE BUENA VISTA HILLS FIELD

A. Introduction

SwRI researchers compiled a great deal of data from the Buena Vista Hills reservoir. This information includes:

- Standard well logs (Vp, Vs, density, resistivity)
- Core data (SP, porosity, permeability, oil saturation, water saturation)
- Detailed lithological data
- Tomographic velocity data

Additional data was acquired which so far has played only a minor role in the research covered in this report. This information which is expected to contribute to future research efforts, includes:

- Full FMI data (vertical and azimuthal coverage)
- Full waveform crosswell data
- Full waveform cross dipole sonic log data

A brief discussion of the supplemental data is presented in this section. We also expect to receive an improved, three-dimensional tomographic data set from TomoSeis after testing and processing is complete.

B. Formation MicroImager (FMI) Data

The FMI data consists of 96 azimuthal resistivity measurements taken at 2.5-mm vertical spacings in well 653Z. An additional 96 azimuthal measurements provided redundant information for tool placement and error checking. We used and show the FMI data as a scalar log (one value per depth), but this does not show the full range of the data. A false color image of a section of the FMI measurements is shown in Figure III-1. The presence and scale of many thin sands can be seen in this image. A close up of part of this image is shown in Figure III-2. At this scale, the slight dip of the formation is apparent. To obtain a single-valued log, we extracted the reading from a single resistivity button rather than average all buttons at a particular depth. This resulted in the unfortunate inclusion of local defects and exceptions in the data. Averaging around the borehole circumference, however, would result in loss of precision. As seen from Figure III-2, the formation dip results in a single thin layer occupying a range of depths. Thus, the influence of a one-inch thick layer may be spread over 5 inches. Since we sought an accuracy of 0.1 inch, this blurring was not acceptable.

C. Full Waveform Crosswell Data

The full waveform crosswell data set was inverted to provide the tomographic velocity information. Seismograms were recorded between injector well 653Z and the four producer wells with 5-foot source and receiver vertical spacings. True vertical depths for sources and receivers generally ranged from 3,000 ft. to 4,350 ft., covering only the top of the Antelope formation. Vertical offsets between wells ranged through about ±300 ft., giving only limited vertical propagation

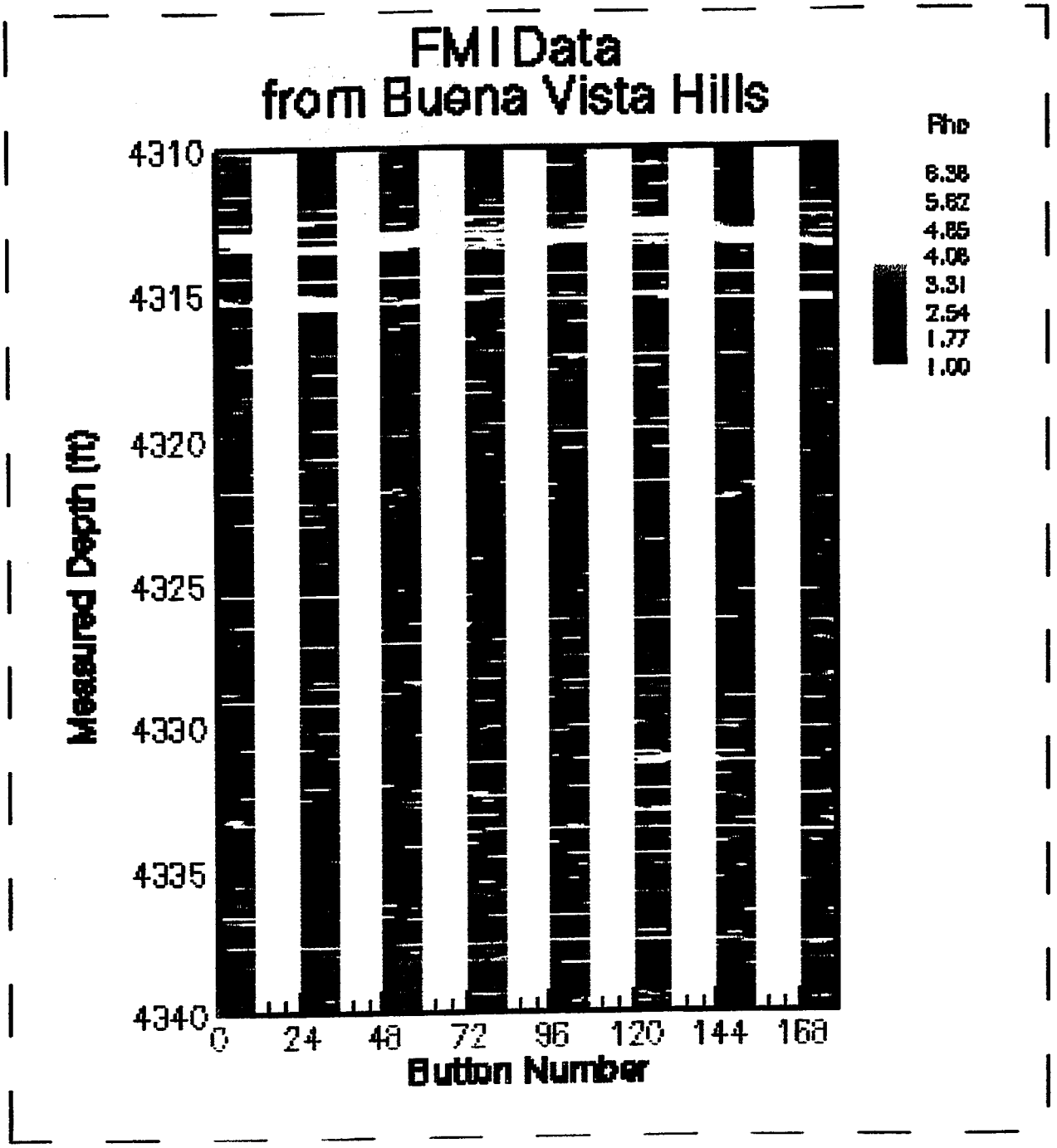

Figure III-1 Two-dimensional FMI data at the borehole of well 653Z.

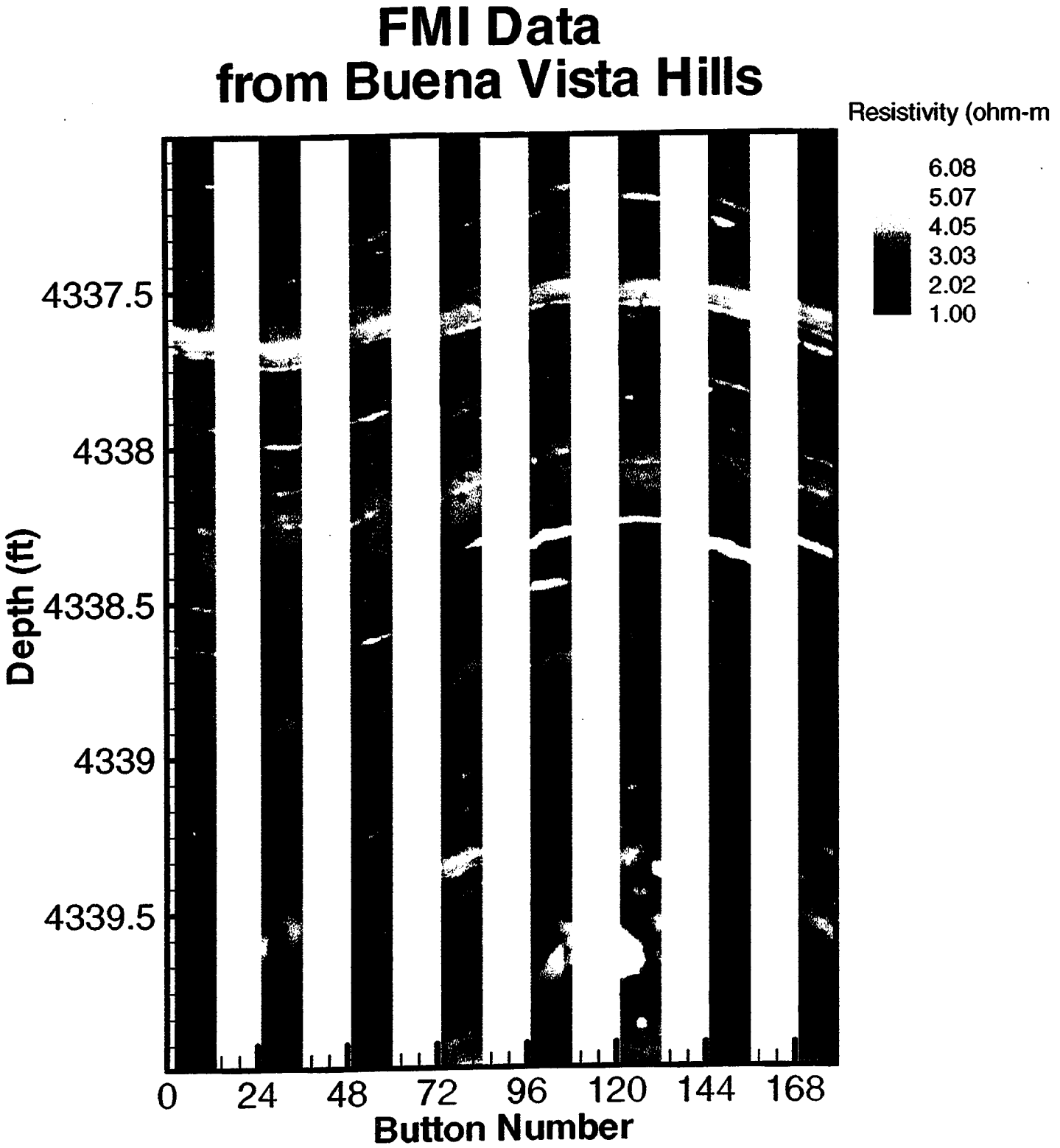

Figure III-2. Closeup of a section of Figure III-1. Note the visible effect of the formation dip and the small vertical scale of the features.

(compared to horizontal well separations of 500-700 feet). A sample of some of the zero vertical offset seismograms between wells 653Z and 564 is shown in Figure III-3. The increasing moveout with depth is a result of the deviation of the 653Z well, not a change in formation velocity with depth. Figure III-3 also shows the depths of some of the more prominent lithological features. (The formation has almost no dip in the plane of this well pair.) Interestingly, the seismograms seem to show longer wave trains in the near neighborhood of many of the noted high velocity layers. Time-frequency analysis (Figure III-4) shows how this energy is distributed as well as the contrast between waveforms in thick shales and waveforms near high velocity layers. The observed reverberation may be due to multiple arrivals or to some kind of interface or guided wave. As yet, no further analysis has been performed.

D. Full Waveform Sonic Data (Cross Dipole)

Full waveform sonic data is available for depths greater than 4,350 ft. (4,290 feet true vertical depth) in well 653Z. Thus, there is almost no overlap between the crosswell full waveform data and the sonic full waveform data. The cross dipole tool consisted of two perpendicular dipole sources and a set of eight pairs of perpendicular dipole receivers at 6-inch vertical spacings, providing four different combinations of source-receiver orientations. Figure III-5 shows waveforms from two of these orientations. Again, there seems to be curious behavior in the vicinity of thick fast layers. Much of this entire section is sprinkled with thin sandstones less than one inch thick, although the region from 4,397 to 4,408 ft. is pure shale. A comparatively thick interval from 4,386.9 ft. to 4,388.6 ft., however, is occupied by carbonate. Some distortion in the waveform is observed when the source is at these depths. This suggests that the waveform distortion observed in the crosswell data is due to some variation in the way the borehole fluid is coupled to the formation at the fast layers.

Time-frequency analysis for some of these traces is shown in Figure III-6. For comparative purposes, it should be noted that the expected time of arrival should be about 1 ms for a P wave, about 2 ms for a S wave, and about 6 ms for direct arrival through the borehole water. From the time-frequency representation, it may be seen that there is an interesting separation of frequencies, with distinct bands located near 1,500 Hz, 2,500 Hz, and in one case near 5,000 Hz. Some dispersive behavior may be seen in each of these bands, although the short distances and small propagation times leave little room for dispersive spreading.

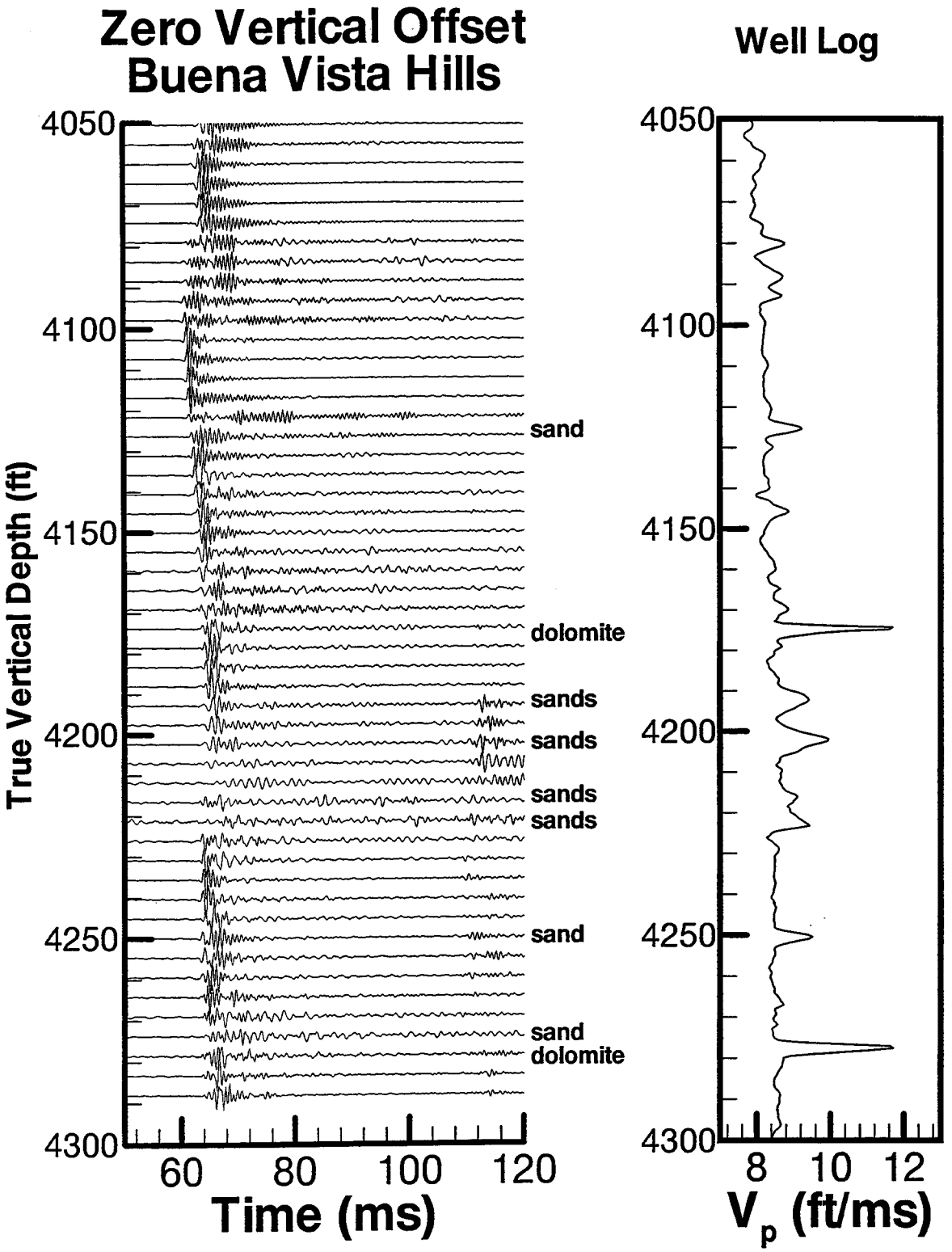

Figure III-3. Zero vertical offset seismograms and major lithological features between wells 653Z and 564. There is almost no formation dip in the plane formed by this well pair. The observed moveout is due to deviation in the 653Z well.

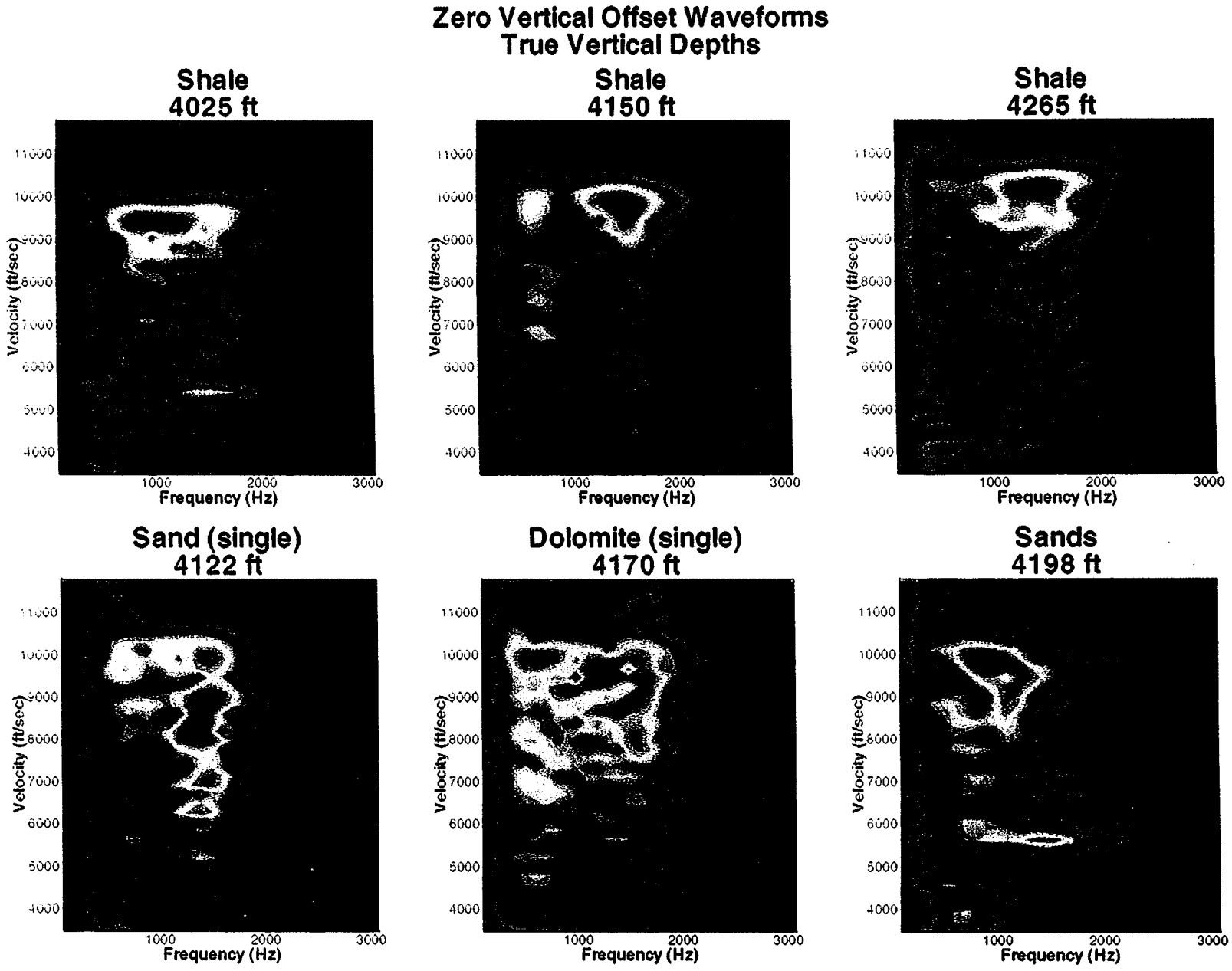

Figure III-4. Time-frequency analysis of some of the seismograms in Figure III-3. Ray paths near major lithological features seem to show some kind of reverberation effect.

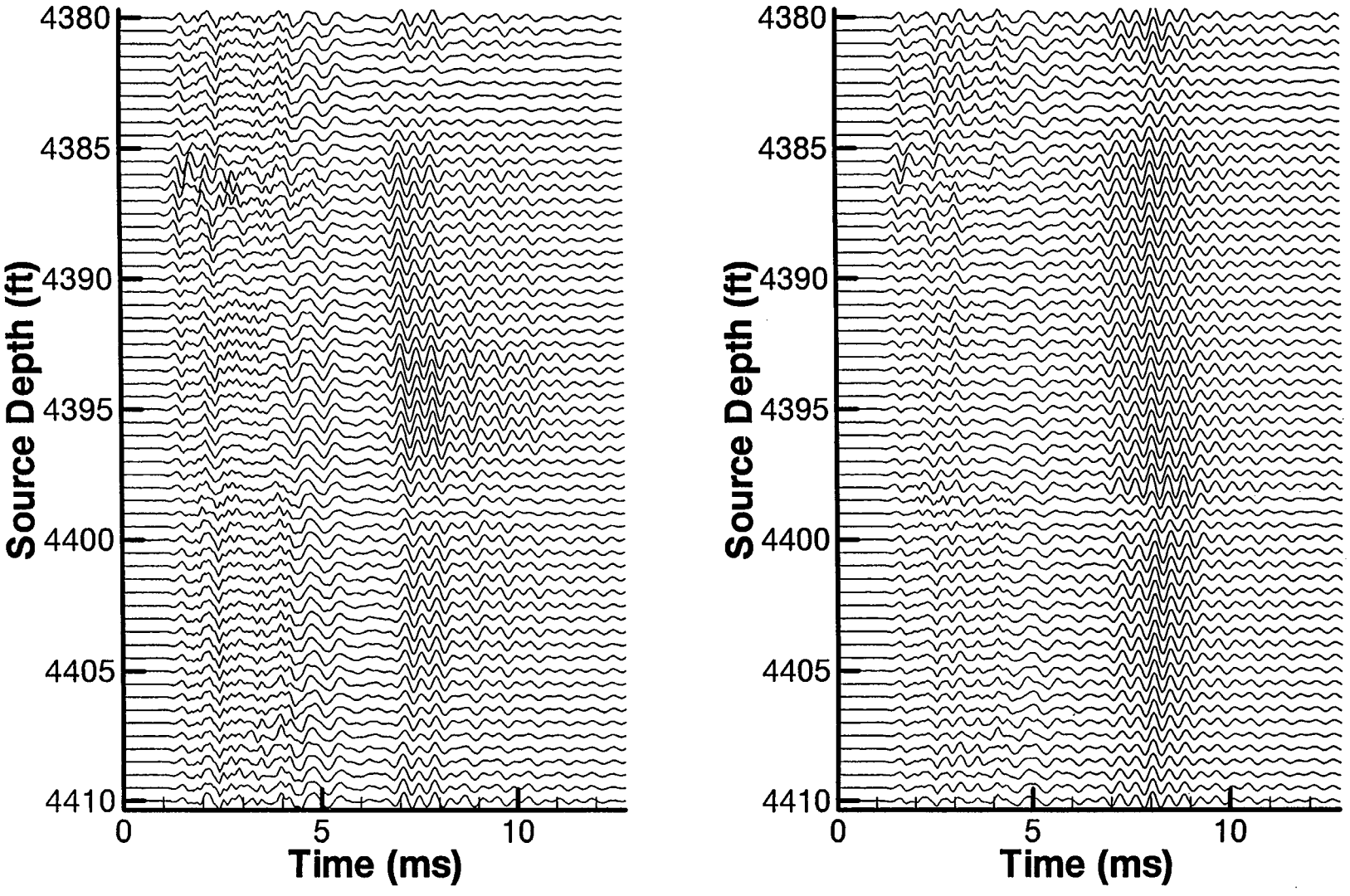

Figure III-5. Full waveforms from two orientations of the cross dipole sonic log. Source to receiver separation is 9 feet.

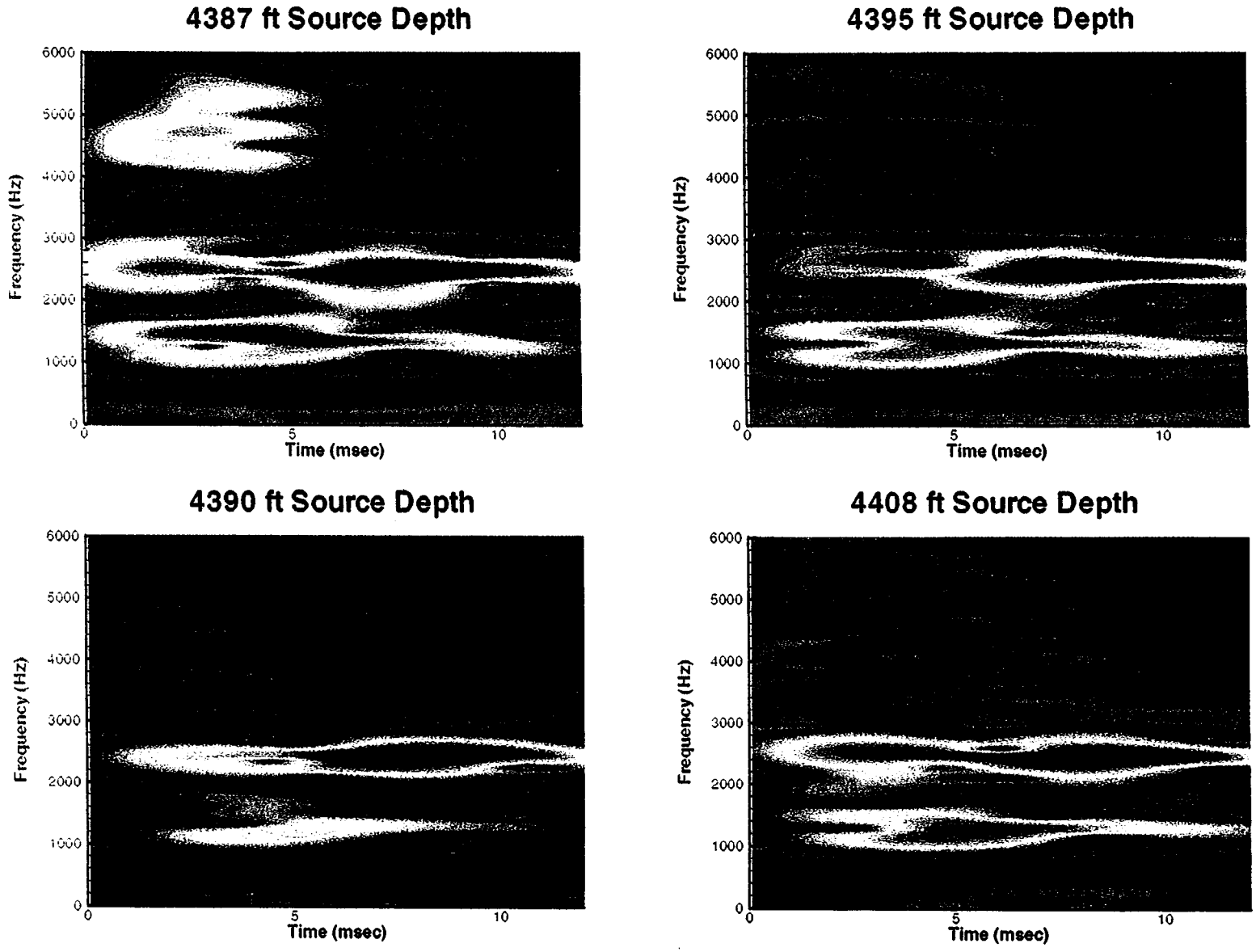

Figure III-6. Time-frequency analysis of some of the traces in Figure III-5 showing dispersive behavior.

IV. RESOLUTION MATCHING USING FMI

A. Introduction

Resolution enhancement of sonic and density logs using high resolution resistivity data is becoming more common. The accuracy of this method is difficult to determine, however. Spurious correlations may result in incorrect or inaccurate property predictions. Recent FMI measurements in a newly drilled well at Buena Vista Hills provide a unique opportunity for testing this method against known lithology from almost complete core recovery. In the following pages, we discuss the enhancement of a P wave velocity log using microresistivity measurements and describe some of the drawbacks and benefits of the method.

B. Background

As previously noted, the upper Antelope region of the Buena Vista Hills reservoir is predominantly shale, but it contains many very thin sandstone and carbonate laminations. Most of these laminations are less than 6 inches thick, and many are smaller than one inch thick. A few of the sandstones and carbonates are as thick as one to 3 feet. The presence of hundreds of these thin beds makes it difficult to obtain accurate log information, since most logs are based on a 6-inch sample interval and may actually measure the response of 6 to 20 inches of rock. To properly account for the small scale features that introduce scattering, anisotropy, and other items which affect wave propagation, a resolution matching technique is used to enhance the resolution of the sonic and density logs. The mathematics underlying the resolution matching technique is based on the assumption that the sonic and density logging tools measure properties averaged over the tool response length. If another log is available with a better resolution (smaller response length), then statistical correlations between the two logs can be used to increase the resolution of the less precise log. In the following method (based on Nelson and Mitchell, 1991, and also applied in Sams, 1995) the low resolution log will be referred to as the velocity log and the high resolution log will be referred to as the resistivity log.

Step 1:
Interpolate the velocity log (V_{old}) to the depth spacing of the resistivity log. This is necessary to provide a one-to-one correspondence at a given depth. For example, the velocity log may be at a 6-inch spacing while the resistivity log is at a 1/10-inch spacing. It is important to note that the interpolation does not provide information about the lithology.

Step 2:
Reduce the resolution (spatial precision) of the resistivity log by smoothing. The smoothing function chosen is the least squares optimum filter for matching the two response lengths.

Step 3:
Find a local correlation between the smoothed resistivity log and the original velocity log (V_{old}) using a moving window. For example, it might be determined that the best local fit in a particular section is velocity = 3(resistivity) + 1. Because the interpolated

points do not carry information about the lithology, only velocity points with the original spacing are used for the correlation. The best fit is chosen from candidates using several different windows and trial functions.

Step 4:
Use the local correlations with the original, high resolution resistivity to predict a new velocity value (V_{new}) for each depth. The new velocity log will have the same response length as the original resistivity log.

Step 5:
In regions of poor correlation, it is best to keep the original interpolated log. For this reason, the final high resolution velocity log (V_{HR}) is defined as
$V_{HR} = R^2 V_{new} + (1 - R^2) V_{old}$. Here, R^2 is the correlation coefficient for the local fit in step 3. In the case of a perfect fit, R^2 will be equal to one, and V_{HR} equal to V_{new}. In the case of a very poor fit, R^2 will be close to zero, and V_{HR} will be left equal to V_{old}.

Step 6:
Repeat steps 3 - 5 for every depth of interest. New correlations and new R^2 are found at each depth.

This process is used with the high resolution FMI resistivity data to produce enhanced resolution P velocity, S velocity, and density curves. These enhanced logs are used to produce high resolution isotropic elastic constants, C_{ij}. In an interesting occurrence, some of the most accurate and highest resolution information available is the lithology log. This is due to almost complete core recovery by Chevron in drilling this new test well. Since the rock type is known to 0.01-foot intervals, we can compute an exact V_{shale} with a 0.01-foot resolution, and use this new log as the high resolution data in the resolution matching algorithm.

Testing of the resolution matching technique on artificial data produced results which were quite good, even when synthetic "noise" was introduced to the data. In practice, however, several difficulties arose which had to be overcome to produce useful results. The first issue to arise was that of the depth matching between different logs. In many logs, depths of corresponding features were found to vary by up to 5 feet. In addition, there was often a drift, so that the depth offset between logs changed by several feet over several hundred feet of log data. Finally, with finely sampled logs such as the FMI resistivity, which side of the borehole is sampled becomes important in dipping formations. These offsets and drifts must be removed prior to applying the resolution matching technique.

The second problem had to do with sampling interval differences. As mentioned earlier, the FMI resistivity data is sampled every 0.1 inch, while the velocity log data is sampled every 6 inches. To make the necessary one-to-one correspondence, the FMI data must be decimated to the 6-inch spacing, or the velocity log must be interpolated to the 0.1-inch spacing. If decimation is applied, the user is essentially losing over 97 percent of the high resolution information. If interpolation is applied, the user must acknowledge that the interpolated data contains none of the small scale variability that would actually be measured in the field.

A third problem lies in the use of the resistivity as a correlating function. The Buena Vista Hills reservoir is heavily saturated with water, aside from occasional oil bearing sands. It is not uncommon for the thicker sands to contain both a predominantly water bearing section and a predominantly oil bearing section. In a case such as this, the measured resistivity may have one value in the host shale, a higher value in the oil saturated sand, and a lower value in the water saturated sand. At the same time, the velocity log will record a high value in all the sand, and a lower value for the shale. This dichotomy in resistivity values can result in the prediction of very low velocities in some of the sands.

The final problem is one of scale. To achieve a good correlation between the low resolution and high resolution logs, enough data must be used to make the correlation significant. Thus, data windows covering 5 to 20 feet must be used. In a geology such as that found at Buena Vista Hills, however, lithological features are generally smaller than 6 inches. Without adequate discrimination between shales and sands, we have a situation in which less resistive sands and more resistive shales can become confused. This leads to severe over- and underprediction of velocities.

E. Results

In examining the actual results of the resolution matching technique at the Buena Vista Hills reservoir, we concentrated on a 75-foot thick section from 4,335 to 4,410 ft. MD in well 653Z. This section is fairly typical and was chosen because it includes many of the very thin sands and also two of the infrequent thicker high velocity layers. Furthermore, 75 feet is large enough to show some variability, but small enough to still show some detail.

In any case, the first step of the resolution matching process was to obtain a high resolution log and a low resolution log, and filter the high resolution log down to the lower resolution. Figure IV-1 shows the result of this operation with the FMI data. The filtered FMI log now bears an obvious relation to the measured velocity log, both in the placement of the major peaks and in the general background structure. One difference between Figures IV-1(b) and IV-1(c) is that the resistivity peaks are several orders of magnitude over the resistivity background, while the velocity peaks are only 50 percent higher than the velocity background. In principle, the resolution matching technique should be able to deal with this nonlinear behavior.

The actual resolution enhanced velocity log and the R^2 value for the correlation between the curves of Figures IV-1(b) and IV-1(c) are shown in Figure IV-2. Much of the interval can now be seen to have many thin beds, most faster than the original velocity by 1,000 or 2,000 ft/sec, but some slower. The overall baseline structure of the original velocity log is still present. The R^2 value for the correlation is quite good, generally over 0.8. The enhanced velocity log looks more like what would be expected in a finely laminated region such as this part of Buena Vista Hills, but the actual velocity of the sandstone layers is probably closer to 12000 ft/sec than 9000 ft/sec. In addition, there are a few small areas where the lithology shows laminations but the enhanced log does not, and vice versa. Some of this may be due to local variability in the shale and sands; we cannot say that all sands have 50 percent higher velocities than all shales. This cannot be determined, however, without exhaustive testing of the core samples.

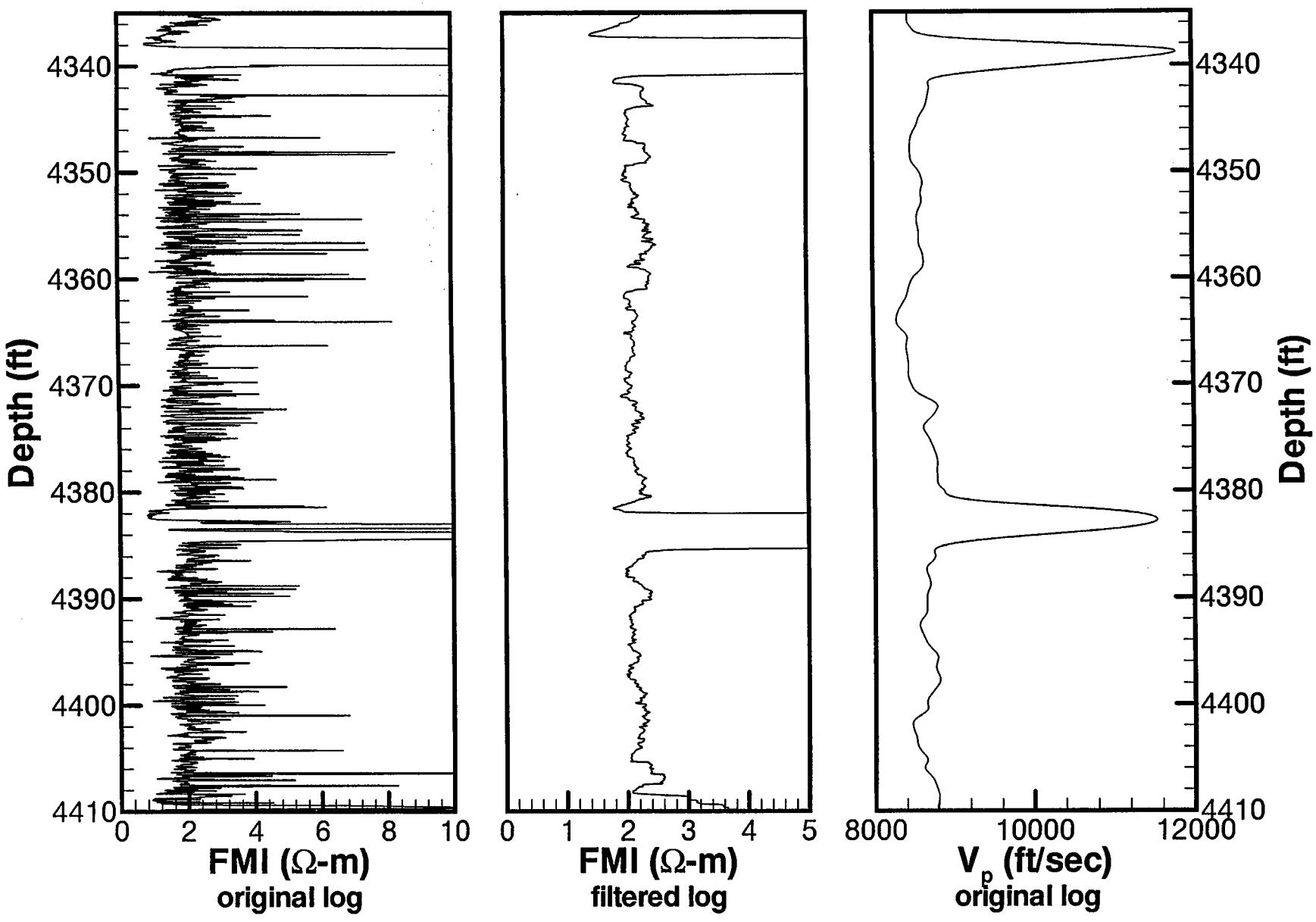

Figure IV-1. Relation of FMI resistivity data to original velocity log.

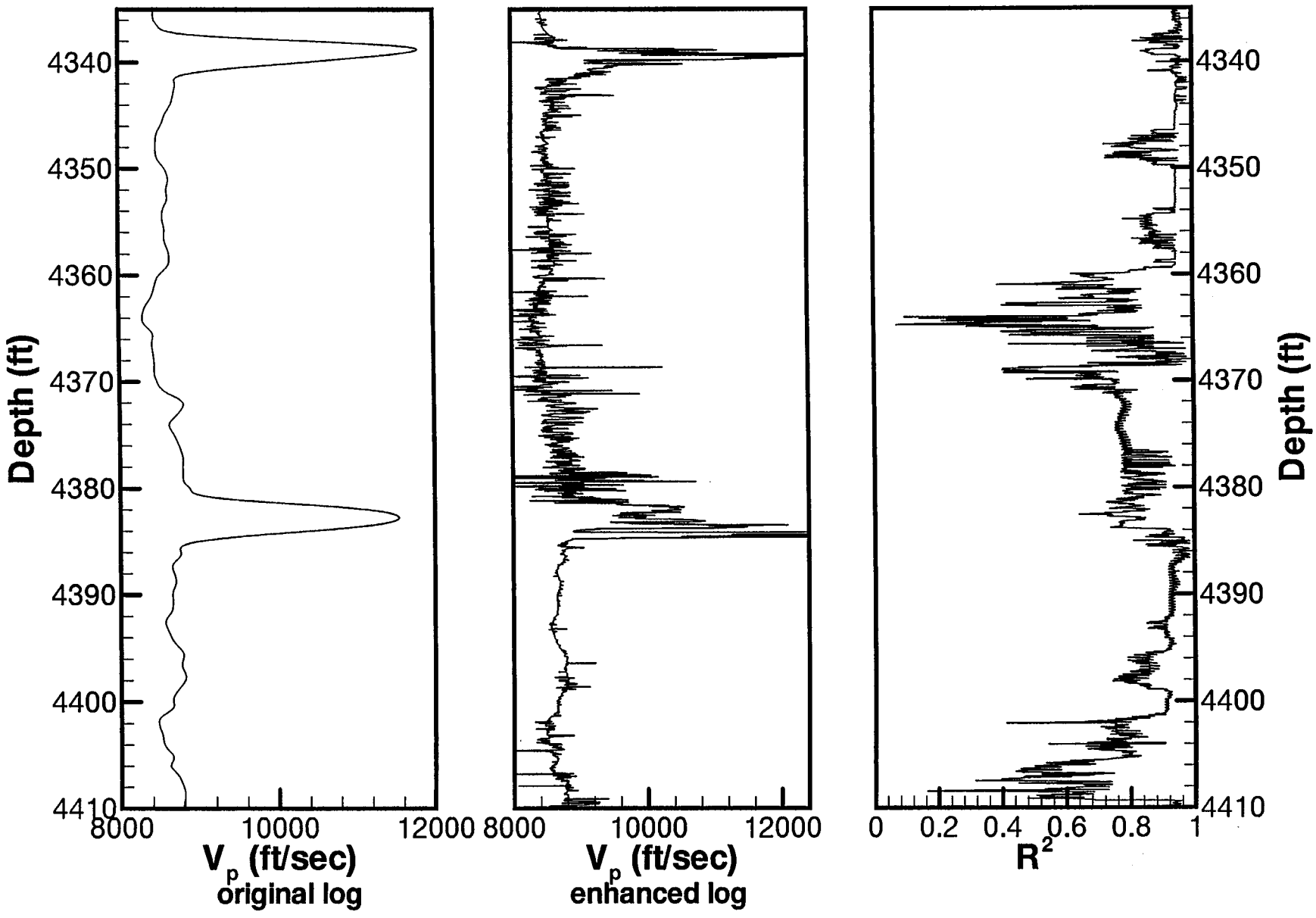

Figure IV-2. Velocity log enhanced with FMI resistivity data.

As mentioned earlier, we do have lithological information on a 0.01-foot scale from inspection of the core samples. This allows us to create a "% shale" or "V_{shale}" log with the value 1 in regions identified as shale and the value 0 in regions identified as sandstone or carbonate. This provides an alternate high resolution log for the resolution matching. In one respect, the lithological log is better than the FMI for resolution matching because its information content is known to be related to velocity in a more direct manner. On the other hand, the binary nature of this log (1 or 0) means that it carries less information about local variability of the sands and shales. Figure IV-3 shows the high resolution V_{shale} log, the filtered lower resolution V_{shale}, and the original velocity log. (Actually, the value $1-V_{shale}$ is shown to increase the visual agreement with the velocity log.) Not surprisingly, there is a good correspondence between the filtered lithological log and the observed velocity log.

The enhanced velocity log based on the lithological log is displayed in Figure IV-4 with the original velocity log and the R^2 value of the correlation. As might be expected, this version of the enhanced velocity log follows the lithology closely. The thicker high velocity layers show up in the enhanced log with squarer corners, making them look more like layers and less like part of a continuous, smoothly varying distribution. In addition, almost all of the thinner layers find an expression in the enhanced velocity log, this time with velocities of over 10000 ft/sec. The R^2 values in this case are generally slightly lower, however, when compared to the FMI data.

F. Summary

Resolution enhancement techniques were applied to the Buena Vista Hills reservoir near Bakersfield, California. Enhancement of the velocity log with an FMI microscale resistivity log produced high correlations (as measured by R^2), but while the enhanced velocity log contained a large amount of detail, it did not show as much of the known lithological structure as expected. This was probably due to the very fine structure of the lamination. It is difficult to determine a velocity over a distance much smaller than a wavelength. Detailed lithological data was also used in resolution enhancement, and provided logs with the expected fine layering but with lesser correlation. Resolution matching is a technique with great potential for providing high resolution verisimilitudinous data, but it should be used with caution in reservoirs with a high degree of small scale variability.

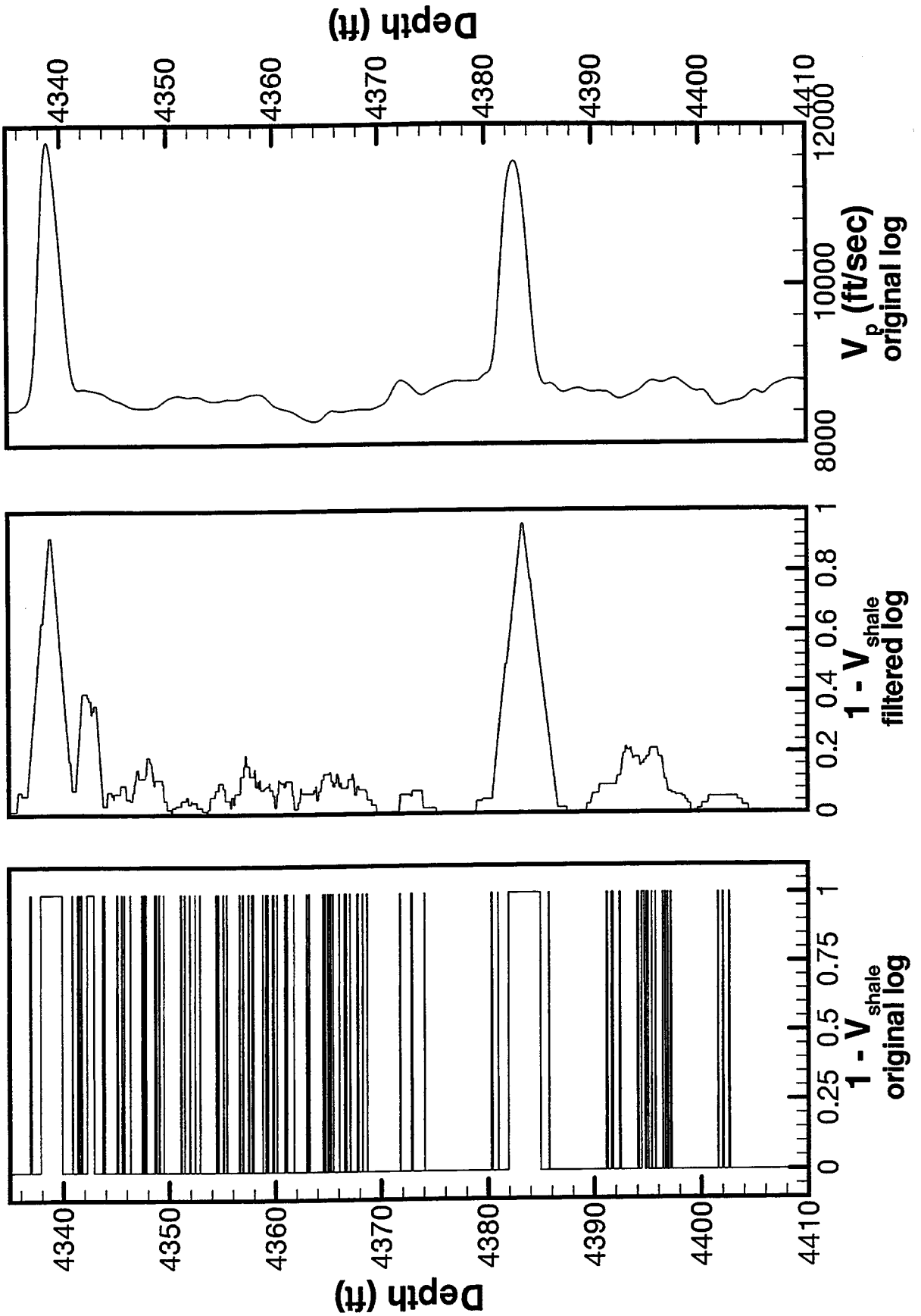

Figure IV-3. Relation of lithological data to original velocity log.

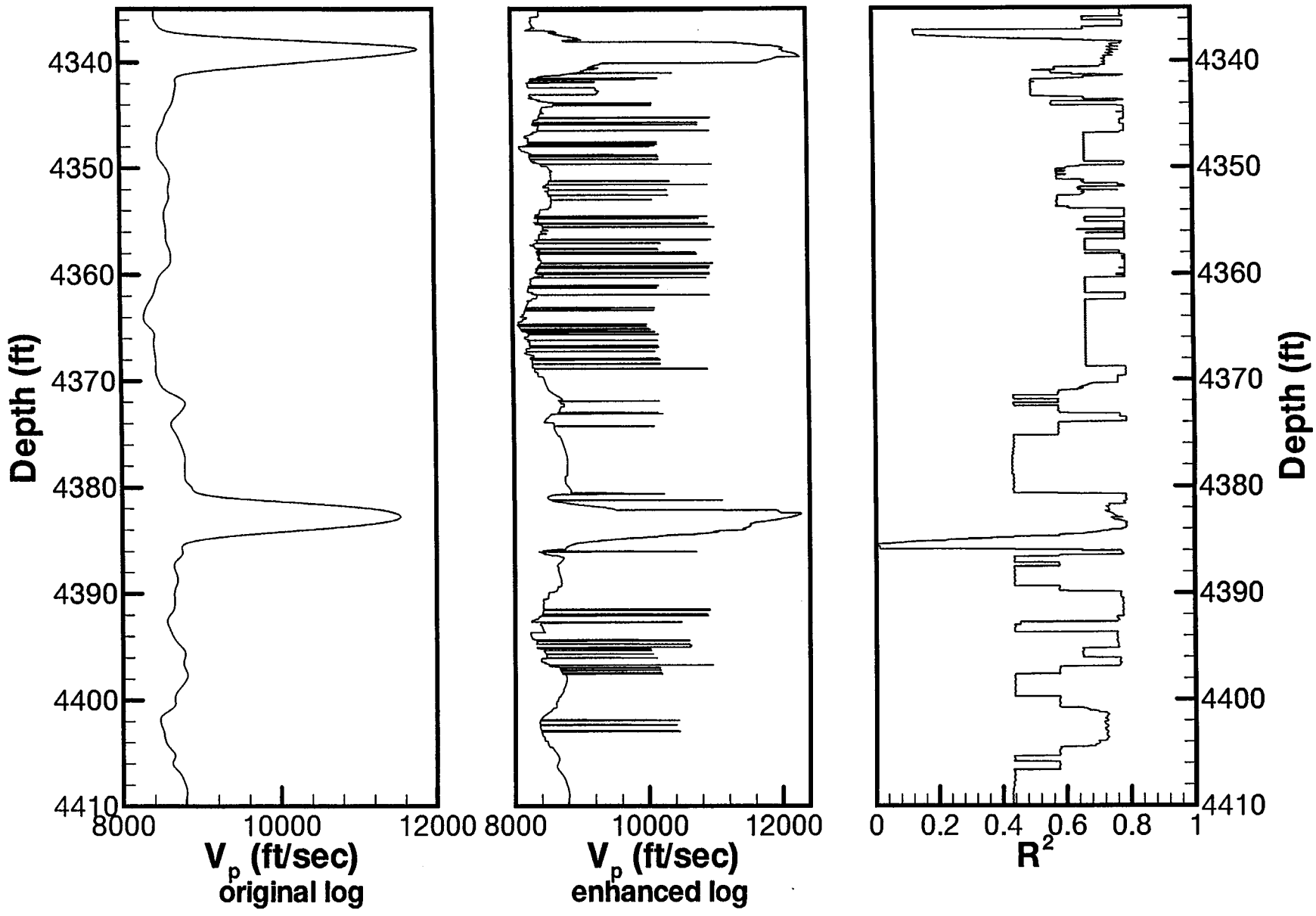

Figure IV-4. Velocity log enhanced with lithology.

V. ESTIMATING THE CONTRIBUTION OF ELASTIC SCATTERING AND INTRINSIC ATTENUATION TO VELOCITY DISPERSION USING WELL CONTROL

A. Introduction

This section outlines a technique for employing velocity dispersion to map intrinsic attenuation. It is well known (Aki and Richards, 1980) that dispersion and attenuation are closely related. The attenuation of seismic waves in a reservoir may be closely related to the type of saturating fluid, porosity, permeability and other important parameters. Methods of estimating the dispersion from crosswell data and commonly available logs are discussed in this section, and the technique is applied to the Buena Vista Hills field. The lithology of this field is very complex, however, which makes it difficult to interpret the results. Forward modeling is used to demonstrate the fundamental validity of the approach.

B. Outline of Technique, with Field Data

Dispersion is the difference in propagation velocity of waves of different frequencies. To estimate the dispersion in a reservoir, therefore, requires velocity measurements with at least two different frequencies. The velocity measurements available to us are the sonic log (roughly 10 kHz) and crosswell seismic data (with a center frequency of about 1,000 Hz). Tomographic inversion of the crosswell data provides us with a velocity profile for the lower frequency. To properly make a detailed comparison of the two velocity measurements, however, we must deal with two problematic issues. The first is anisotropy in the medium. Anisotropy is known to be very important at the Buena Vista Hills field because observed crosswell (horizontal) velocities have been found to be about 20 percent higher than observed sonic (vertical) velocities. The second issue is the effective resolution of the data. The vertical resolution of the crosswell seismic data is limited by the 5-foot vertical spacing of the sources and receivers and also by the approximately 8-foot wavelength of the propagating wave. In contrast, the vertical resolution of the sonic data is as small as 18 inches.

The effective anisotropy can result from two sources. One source is actual, intrinsic anisotropy of the host medium. Another is layering-induced anisotropy, the result of thin, high velocity layers embedded in a slower host rock. A concern with anisotropy is having to reconcile the vertical sonic log data with the horizontal crosswell data. If we employ low frequency vertical data, such as from a VSP, anisotropy will not be an issue.

1. Resolution Enhancement

The initial part of this method lies in creating high resolution well logs. Resolution greater than the 6-18 inches commonly found in density and velocity logs is important in resolving thin beds and also in estimating the layering induced anisotropy. Figure V-1 shows the original resolution well logs. At this resolution, most of the thin beds observed in the core samples are not visible in the density and velocity curves. The FMI resistivity data, sampled every 0.1 inch, does reflect the presence of the thin sands and carbonates. By finding a statistical relationships between the density, velocity, and resistivity logs, we can create a full set of high resolution well logs, as in Figure V-2.

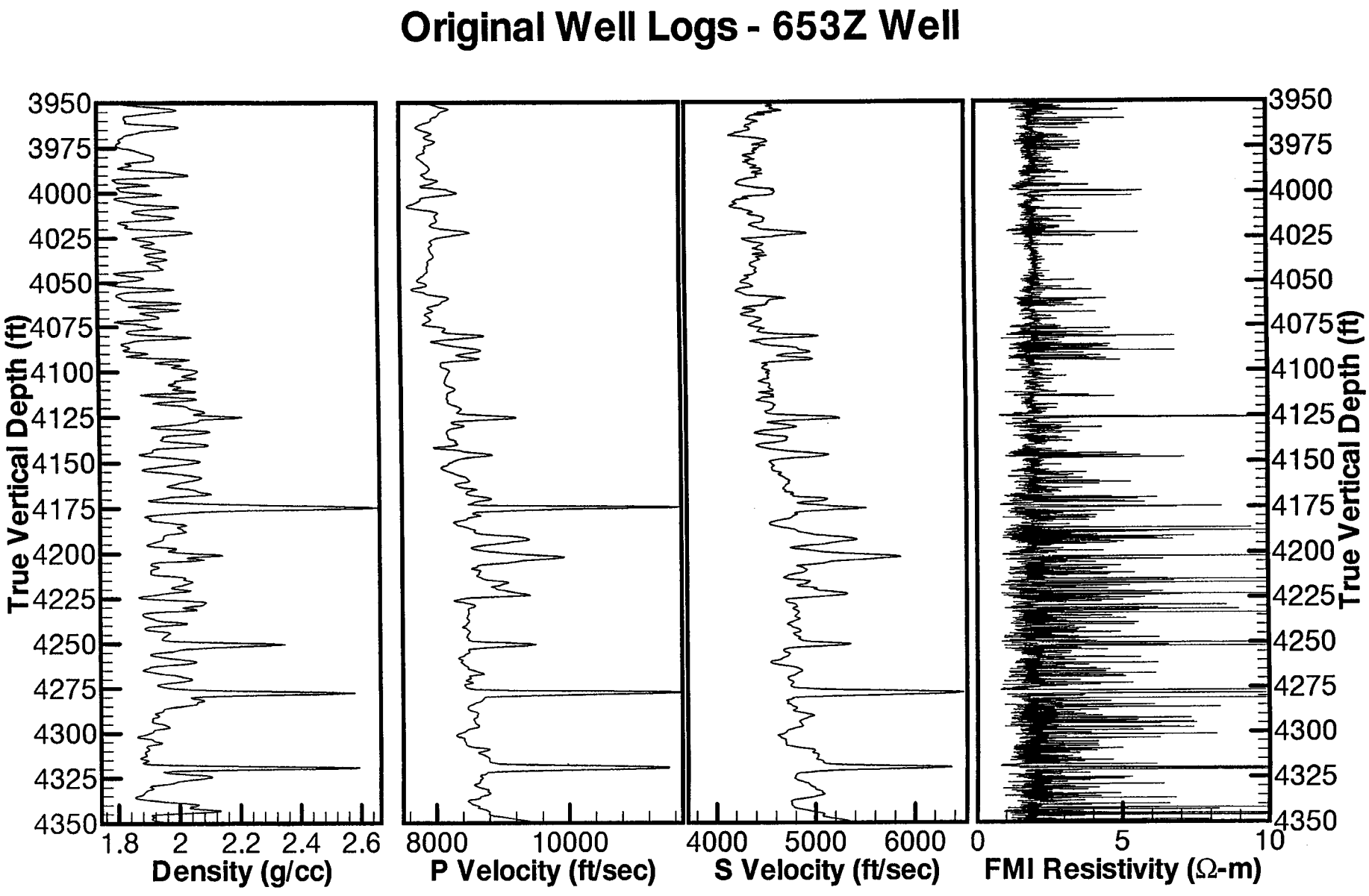

Figure V-1. Density, Vp, Vs, and FMI curves at original scale.

The high resolution FMI curve is used as a guide to predict layering and ultimately to increase the resolution of the Vp, Vs and density logs. The reason for doing this is to account for the component of dispersion caused by thin beds below the resolution of the sonic logs. Because these beds are so small, a close up of a 25-foot section is shown in Figure V-2. Compare the bed size and spacing with the lithology images derived from core samples (see the geological characterization of the Buena Vista Hills reservoir in Section II).

A high resolution log (in this case the FMI) can be used to estimate high resolution versions of logs typically recorded with a lower resolution capability (in this case the sonic and density logs). The basic idea is to first filter the high resolution FMI log to predict how the FMI would appear if it had the same vertical resolution as the sonic or density logs. Next, a regression relationship is determined between the sonic-resolution version of the FMI curve and the actual sonic (or density) curve. The regression curve is assumed to also be valid when applied at the FMI scale of resolution. Application of the regression curve to the original FMI data leads to the prediction of a high resolution version of the sonic (or density) curve. This prediction is then modified to be closer or equal to the original sonic curve depending on the confidence in the regression. The degree of correlation varies with depth, but the average R^2 value is greater than 0.7 for all three logs. See the paper by Nelson and Mitchell (1991) for further details on this technique.

2. Creation of Elastic Constants

After a high resolution set of well logs has been formed, we must transform the logs into a high resolution set of elastic constants. We chose to model the Buena Vista Hills field as a vertically transversely isotropic medium. To fully predict the elastic constants, the presence of intrinsic anisotropy in the medium must be considered. The crosswell seismic shows velocity anisotropy of about 20 percent in thick shale regions where no sands or carbonates were identified from the core samples. In the apparent absence of contributing high velocity laminae, we were forced to consider this anisotropy to be an intrinsic property of the shale.

The intrinsic anisotropy of shales cannot be estimated directly from well logs. Empirical equations have been developed to predict the anisotropy (assumed to be transversely isotropic) of the shales from vertical Vp and Vs measurements in the well. Only four of the five constants estimated are plotted in Figure V-3, and only a 25-foot section is shown in order to bring out the detail.

Correct prediction of the intrinsic anisotropy of the shales is an important part of predicting the seismic responses of formations at lower frequencies. The model of the formation is a sequence of layers made up of transversely isotropic layers. The shale content is used to estimate the degree of transverse isotropy. The resultant model parameters are assumed to be representative of sonic frequencies. In essence, we assume that elastic scattering is the only mechanism acting to make the sonic velocities slower than very high frequency measurements (which have wavelengths more closely comparable to the thickness of the thin beds). We therefore neglect high frequency intrinsic mechanisms that apply to sonic and higher frequencies, e.g., the Biot mechanism, and assume that a different low-frequency intrinsic mechanism is responsible for the velocity dispersion between sonic and crosswell or surface seismic frequencies.

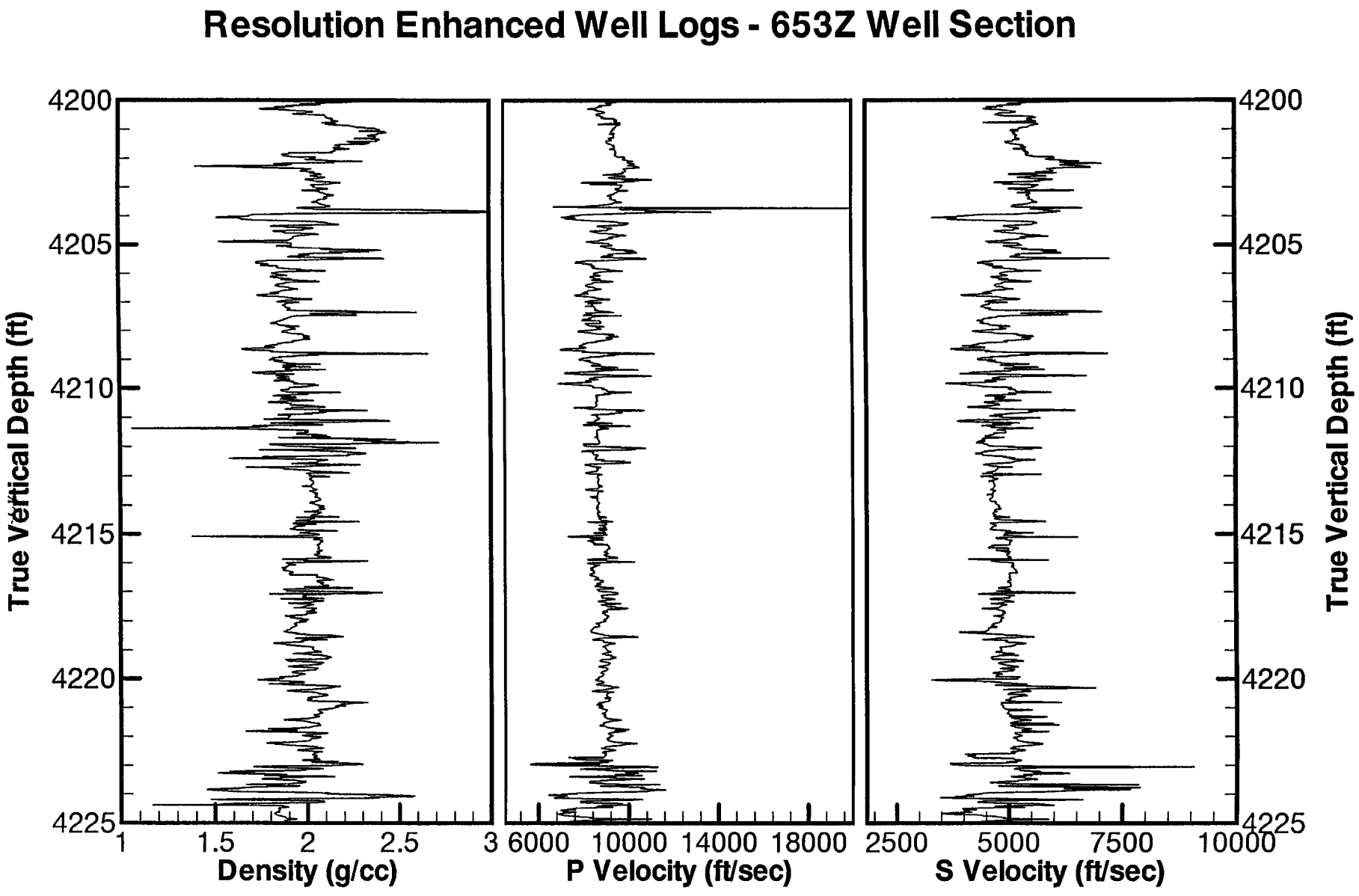

Figure V-2. Density, Vp, and Vs (predicted) curves at FMI scale.

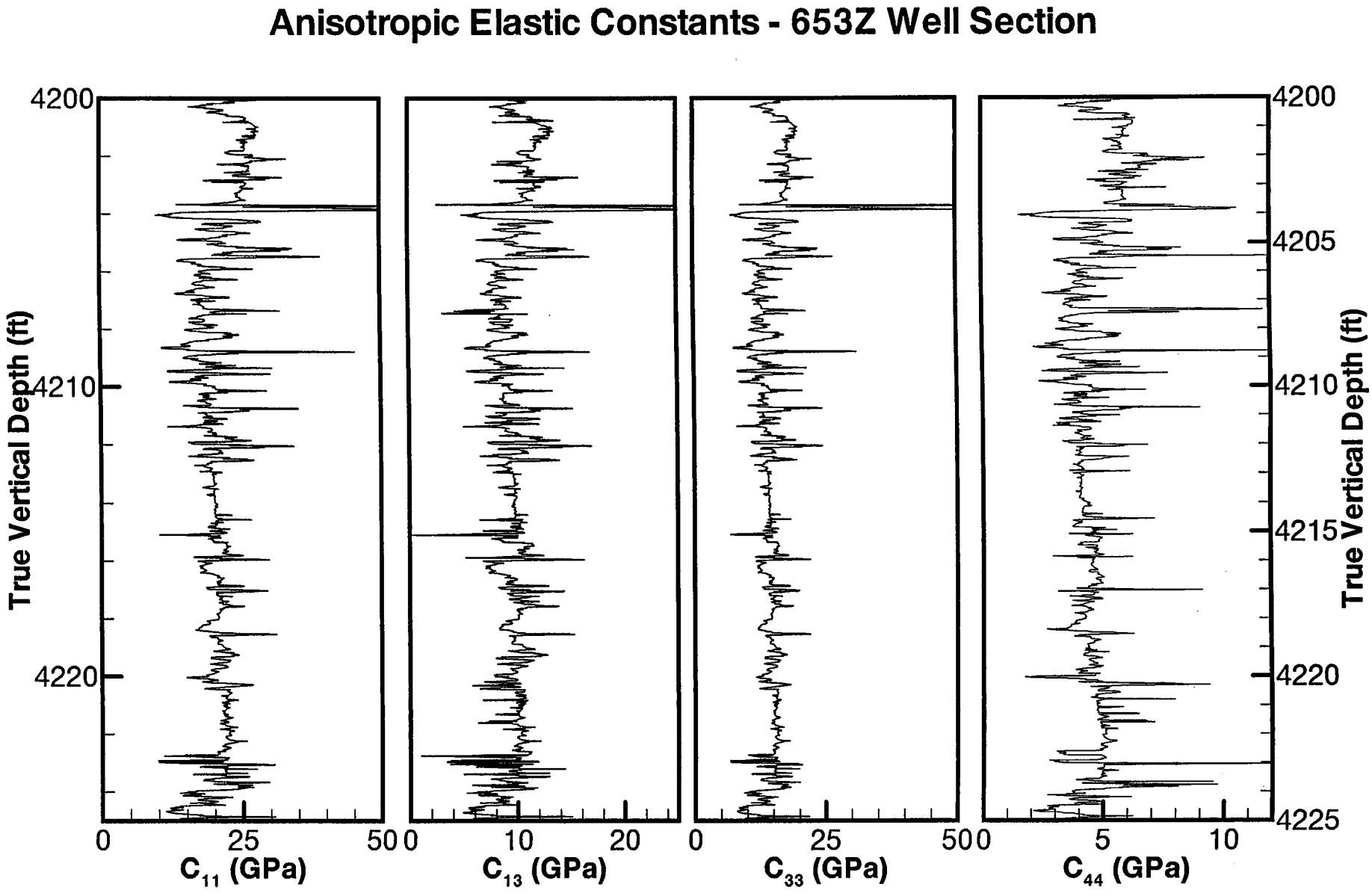

Figure V-3. Predicted elastic constants at the FMI scale.

It is apparent by comparing the sonic well logs with the crosswell velocities that there is significant anisotropy in the formations under study. This is not surprising, since the formations are predominantly shale, and shales frequently exhibit anisotropies of 20 percent or more. To resolve this, we expanded on the technique outlined in the paper by Ryan-Grigor (1997) and used statistical correlations to predict the local anisotropic constants in the form of parameters defined by Thomsen (1986).

We assumed that the shales are transversely isotropic (TI) while the sandstones and carbonates are isotropic. Using information on shales available in the literature, a set of statistical correlations for the Thomsen parameters in shales was found. These correlations were sufficient to predict the TI set of elastic constants when used with the standard Thomsen relations and sonic measurements of Vp and Vs in the shales.

3. Prediction of Sonic Frequency Horizontal Velocity

Having established a set of elastic constants based on the sonic frequency data, we may now attempt to predict a sonic frequency horizontal velocity. In contrast to the high resolution elastic constants, however, the predicted horizontal velocity must correspond to the resolution in the observed crosswell data. In other words, the predicted horizontal velocity must behave as if it had a wavelength of roughly 8 feet and a correspondingly large region of influence. In these circumstances it is known that the effective elastic constants are a particular kind of weighted average of the "true" elastic constants.

Two effects contribute to making a high frequency measurement different from a low frequency measurement: elastic scattering and an intrinsic attenuation. The elastic scattering component of velocity dispersion can be viewed as the result of the interference of multiples and interface modes. Thus, any velocity measurement can be written in the following form:

$$V_{OBS} = V_{ES} - V_I \qquad (1)$$

where

V_{OBS} = observed velocity (crosswell seismic)

V_{ES} = predicted velocity accounting only for the effects of elastic scattering at the selected crosswell frequency (this velocity should be slightly distorted from the measurement at sonic frequencies but will be faster than the actual observed crosswell velocity).

V_I = component of velocity dispersion between sonic and crosswell frequencies accounting for intrinsic attenuation.

Our goal is to estimate the elastic scattering component of a velocity measurement (V_{ES}) and subtract it from the actual measurement in order to estimate the intrinsic attenuation component of dispersion.

$$V_I = V_{ES} - V_{OBS} \quad (2)$$

The intrinsic component of dispersion is of interest because it can potentially be related to the fluids within a reservoir.

An approximate method of predicting the elastic scattering component of velocity dispersion (V_{ES}) is to use Backus averaging (Backus, 1962) over a layered system. Backus averaging is a quasistatic approximation of the long-wavelength apparent anisotropy of a formation. The problem with using Backus averaging is selection of the window length and weighting function with which to perform the average. We tried different window lengths and chose an averaging length scale of one wavelength (based on an average crosswell frequency of 1000 Hz and an average medium vertical velocity of 2.5 km/sec) or roughly 8 feet (2.5 m). This averaging length scale seemed to reproduce the resolution of the tomographic data.

Note in Figure V-4 that the observed horizontal velocity (V_{OBS}) is generally slower than the predicted horizontal velocities accounting for elastic scattering (V_{ES}). Both logs are shown at a lower resolution than the sonic V_P log and are faster than the sonic Vp log because of intrinsic anisotropy. There are a few depths at which the predicted V_{ES} is less than the observed V_{OBS}. This results in a negative V_I, which is a non-physical result of residual errors in the model. This effect is generally confined to a few particularly fast layers made up predominantly of sandstone or dolomite.

Figure V-5 compares the velocity dispersion and predicted quality factor Q_I (intrinsic attenuation). Predicted values of Q_I range from 5 up, with most values lying in the range of 10 to 20.

Our long term goals are to:

- Predict the frequency-dependence and anisotropy of velocities adjacent to boreholes for enhanced imaging capabilities,
- Relate intrinsic attenuation to important reservoir properties, and
- Map the intrinsic attenuation throughout a reservoir.

C. Results with Synthetic Data

Because of the difficulty in obtaining sufficiently accurate information to make a confident Q prediction, synthetic data have been generated to further demonstrate the basic validity of the technique. Using synthetic data gives the advantage of exact knowledge of the model parameters, which both improves the accuracy of the method and allows for evaluation of the results.

Forward modeling was undertaken for the region between 4,100 and 4,200 ft. MD. The model is of a plane layered medium, with alternating layers of shale, sandstone, and dolomite at intervals corresponding to the known lithology in well 653Z. For purposes of the model, however, each rock type was assigned a unique set of elastic constants similar to the known field values for that type. In the absence of other information, the Q for the model shale was set to 34, the Q for the model sandstone was set to 66, and the Q for the model dolomite was set to 88. The characteristics

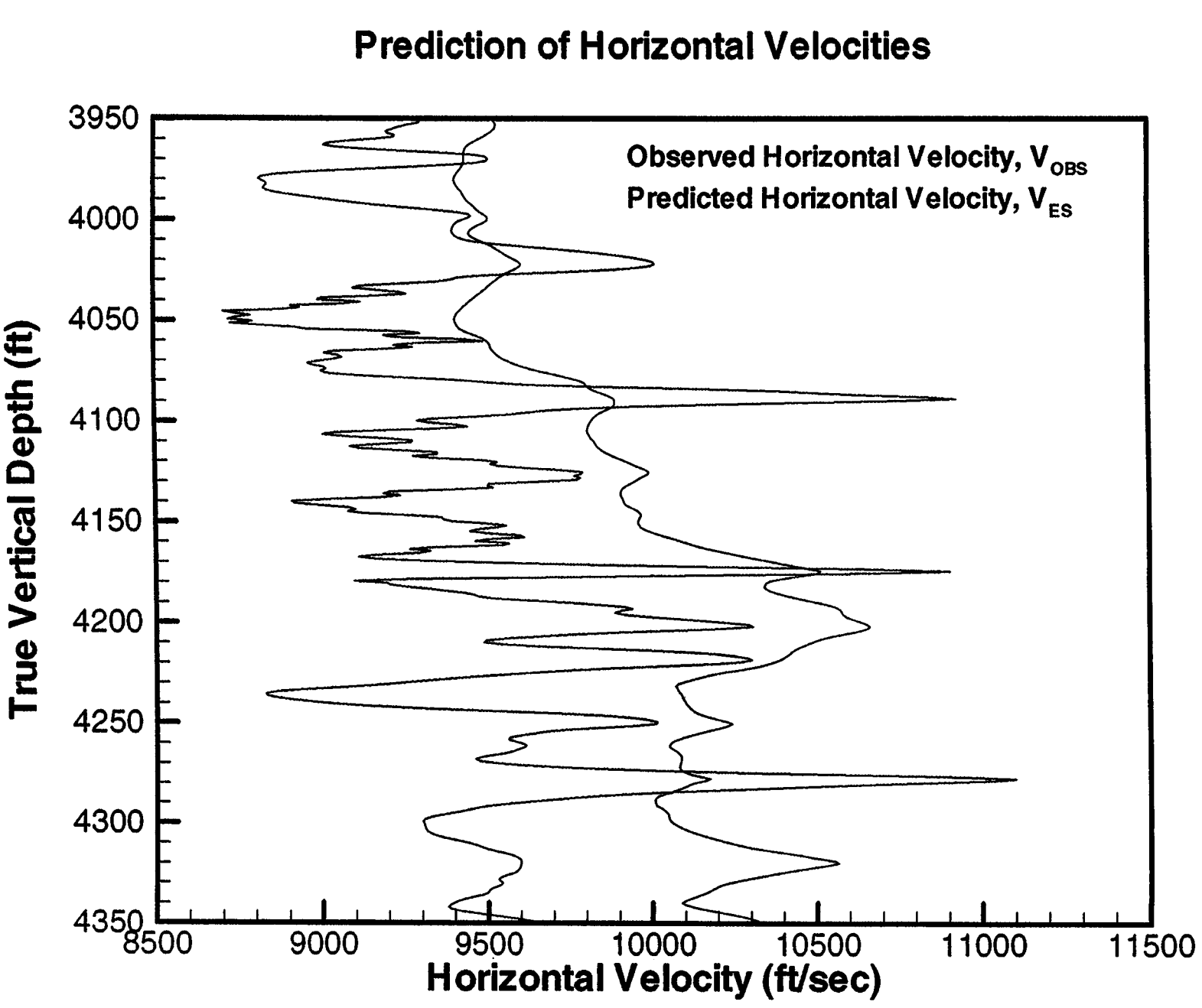

Figure V-4. Prediction of velocities accounting for elastic scattering at crosswell frequencies compared to observed crosswell horizontal velocities.

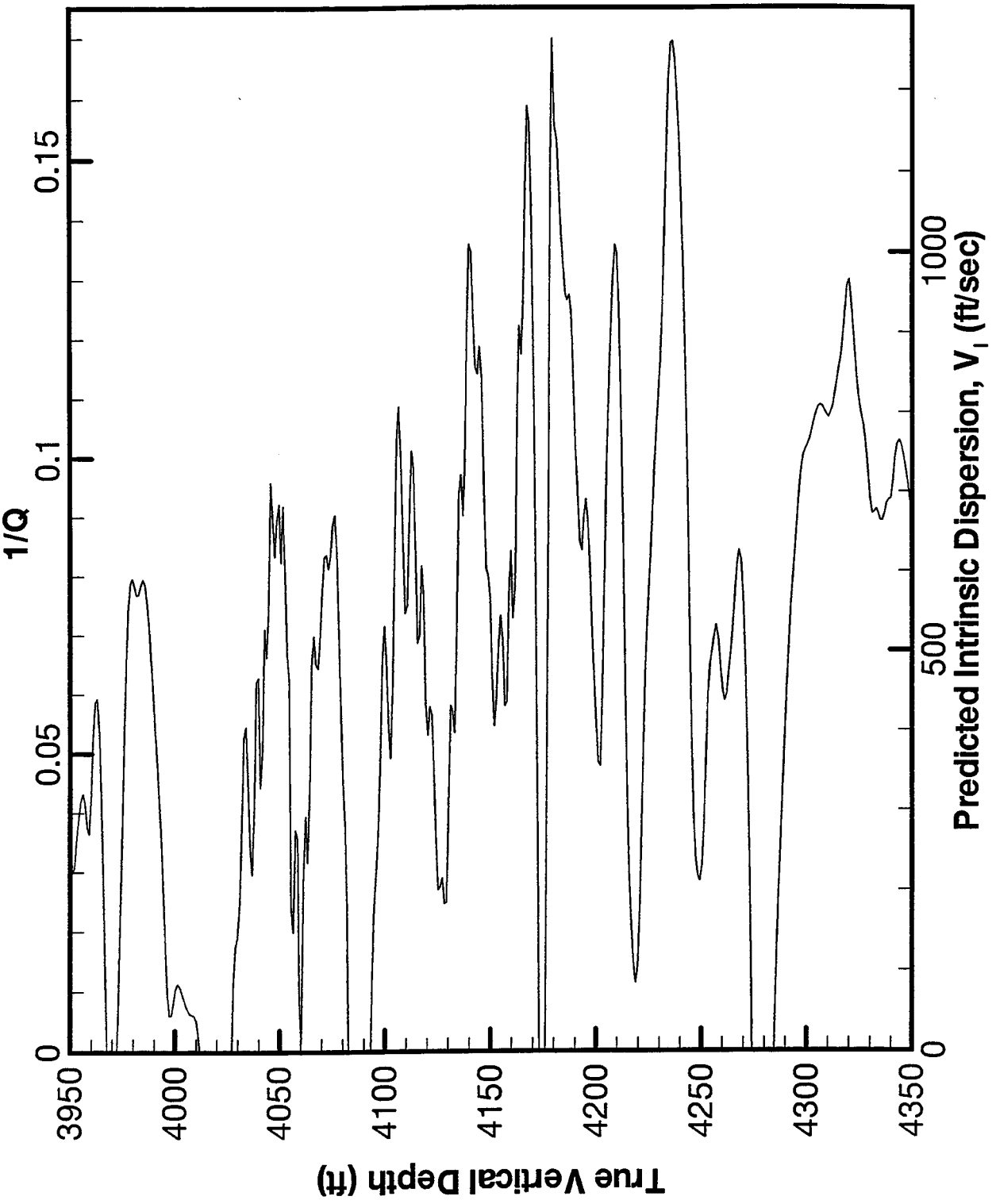

Figure V-5. Intrinsic velocity dispersion and quality factor.

of the underlying elastic model are shown in blue in Figure V-6. Seismograms were generated using a boundary element point source program and represent waves propagated to 166 meters horizontal distance. This corresponds to the approximate interval between the 653Z and 564 wells at the depths of interest. Dispersion between the 1,000 Hz seismogram frequency and the 10,000-Hz sonic frequency at which the model parameters are defined is governed by a constant Q relationship.

The V_{OBS} is found by arrival time picking from the zero vertical offset synthetic seismograms. The sonic frequency V_{ES} is generated by Backus averaging of the model input parameters. It may be seen from Figure V-6 that these two curves are similar in shape. The difference between the two, the V_I, generates a Q profile that is well related to the input profile. The Q values of the bulk shale and the single thicker sandstone are recovered with fair accuracy. The resolution of the computed Q roughly corresponds to the wavelength of the lower frequency, which is far greater than the actual layer thickness. For this reason, the thinnest laminations are not well resolved.

D. Summary

We have taken steps to predict the effective anisotropy and dispersion based on well control. With some refinement, we expect our methods will lead to improved imaging of reservoir properties. However, in the long term, we hope to use the intrinsic velocity dispersion to map reservoir properties. The forward modeling shows the basic feasibility of the technique. To be successful, however, we must be able to obtain precise and accurate well log and anisotropy information from field measurements. We also expect this method to be better suited to reservoirs where the scale of the structure is more comparable to the seismic wavelength.

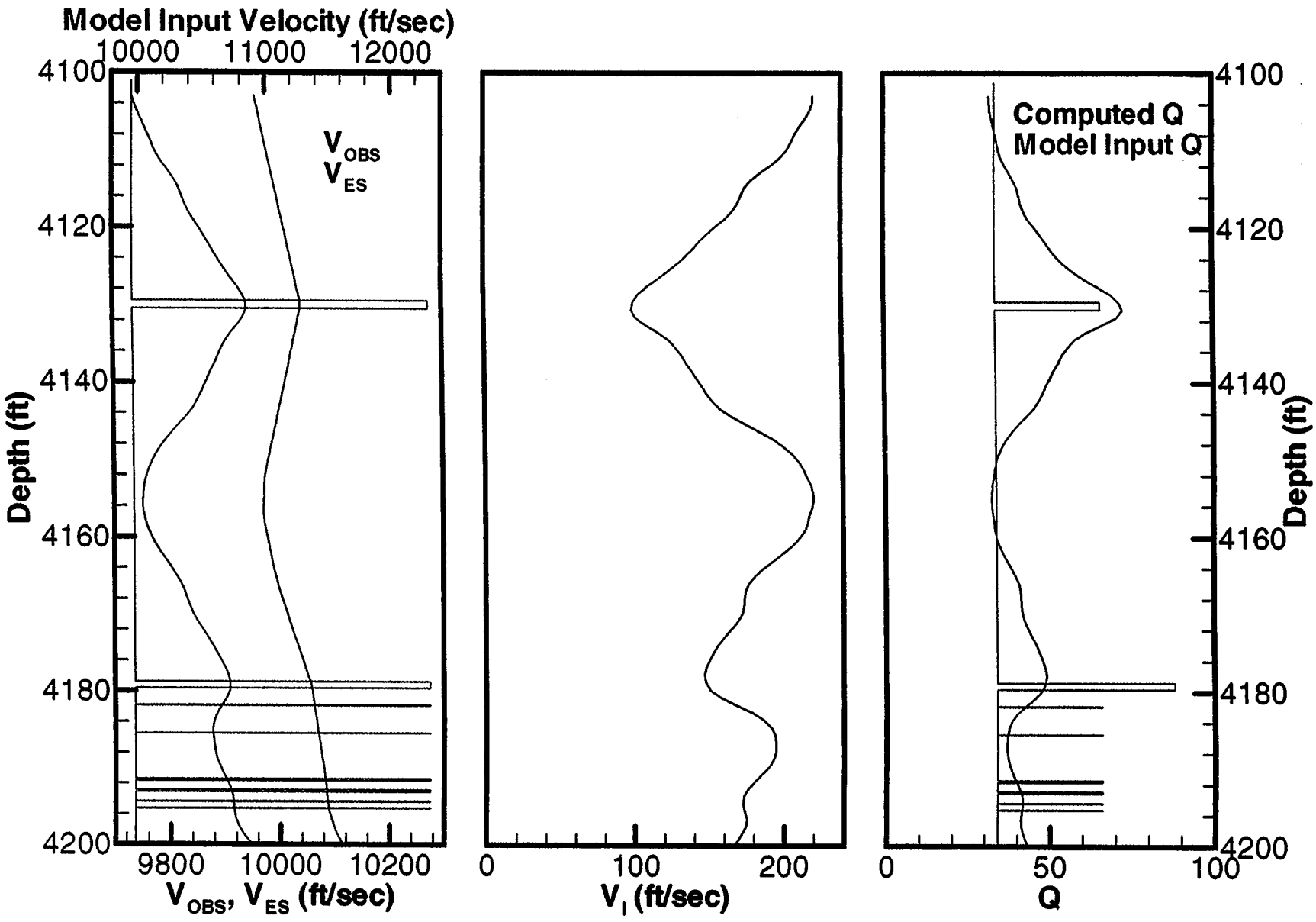

Figure V-6. Forward modeling of intrinsic dispersion.

VI. RELATION OF ATTENUATION AND DISPERSION TO PERMEABILITY IN POROELASTIC ENVIRONMENTS WITH AZIMUTHAL ANISOTROPY

A. Introduction

A qualitative evaluation of the preferential directions of fluid flow in formations containing hydrocarbons is of great importance in the characterization of fractured reservoirs. Such preferential directions are related to the permeability anisotropy of the reservoir. Reservoirs are considered to be anisotropic when they possess significant variation in physical properties (porosity, permeability, wettability, etc.) in three dimensions. The permeability field at a given point in the rock can be treated as a second-order tensor in directions coincident with the principal permeability planes. In particular, the presence of vertical parallel cracks and fractures in an isotropic rock matrix leads to azimuthal anisotropy, which can be described by a transversely isotropic model with a horizontal axis of symmetry. Azimuthal and incidence variations in P-wave attenuation as well as phase velocity from reverse VSP, crosswell, and acoustic logging data have the potential to reveal parameters associated with the fracture conditions of a reservoir.

Recently, analytical studies to relate tensor permeability to attenuation and dispersion of seismic waves was reported by Parra (1997). This work led to the development of an analytic solution that estimates the elements of tensor permeability by modifying the constitutive relation of the stress tensor in the pore fluid (Biot, 1955 and Biot, 1962). This constitutive equation was extended to describe the Biot and squirt-flow mechanisms (Dvorkin and Nur, 1993) for transversely isotropic poroelastic media. In addition, a field example was presented to test the model and to relate permeability to seismic waves propagating between wells at the Gypsy test site, Oklahoma (Parra et al., 1996). This work relates to our efforts at Buena Vista Hills because it represents early effort to develop techniques with which to characterize fractured reservoirs. Another project, at the Buckhorn Test Site in Illinois, provided an example of fractured reservoir characterization and proved valuable in the current investigation. The objective of the Buckhorn project as to demonstrate whether attenuation and dispersion of acoustic waves propagating in the frequency range of cross well and RVSP would predict direction of fluid flow in reservoirs. The objective was accomplished using numerical modeling and crosswell seismic data. The model, based on the Biot and squirt-flow mechanisms, was represented by a transversely isotropic poroelastic medium with a horizontal axis of symmetry perpendicular to the vertical z-axis. The results of the Buckhorn project are presented in this section.

B. Method of Computation and Analysis

The calculations of dispersion and attenuation curves were accomplished using the solution of the transversely isotropic poroelastic wave equation including the Biot and squirt-flow mechanisms (BISQ) given in Parra (1998). Here, the Biot constitutive equation (stress in the pore fluid) was extended to include the BISQ mechanisms. This new equation was expressed such that the axis of anisotropy is in the horizontal direction (x), and the axis of symmetry is in the vertical direction (z). Thus, the poroelastic differential equation was established in terms of the vector wave displacement and the fluid pressure using the new extended equation and the Biot constitutive relations (total stress, momentum balance equation, and generalized Darcy's law).

The poroelastic coupled system of equations was solved using a plane harmonic wave propagating in an arbitrary (x,y,z) plane. The determinant of the system of linear equations was expressed by the product of two polynomials. The solution of the polynomials gives the wave numbers, from which the phase velocity and attenuation of the quasi P-waves and the quasi SV-waves can be determined. For a wave number (k) the phase velocity and attenuation are calculated by:

$$V = \omega / \text{real}(k) \quad \text{and} \quad Q\text{-}1 = 2\,\text{imag}(k) / \text{real}(k).$$

To determine the dispersion from the zero-vertical offset waveforms, the spectral ratio method was used (Ganley and Kanasewich, 1980).

Two different types of poroelastic environments are considered: (1) one in which sandstone is saturated with water, and (2) one in which a limestone formation is saturated with oil. The second environment exists at the Kankakee oil reservoir at the Buckhorn test site, Illinois.

C. Parametric Study

Attenuation and dispersion curves were produced for the model parameters of a sandstone given in Table VI-1. The curves, as a function of azimuth angle (measured from the horizontal x-axis as shown in Figure VI-1) and the angle of propagation or incident angle (measured from the z-axis), were calculated for a large range of frequencies and horizontal permeabilities.

1. Effect of Frequency and Horizontal Permeability on the Attenuation

In Figures VI-2 and VI-3, attenuation and phase velocity curves are characterized by peak frequencies and velocity transition zones, respectively. For example, at a frequency of 1,500 Hz, attenuation is less for a permeability greater than 2.5 md. On the other hand, for a peak frequency near 10,000 Hz, the attenuation peak is at 17.5 md, and attenuation is less for permeability values lower than 17.5 md.

In addition, these curves show that for low permeability values attenuation peaks and velocity transition zones are shifted toward the low frequency region. In general, each curve shows that at low frequency (large wavelengths) the fluid in the porous medium is relaxed in the presence of a compression wave motion. This effect is opposite to that predicted by the Biot theory. At high frequency (short wavelengths) the fluid in the porous medium becomes stiff in the presence of a compression wave motion. The motion of the fluid (or squirt) occurs at intermediate frequencies.

Viscoelastic materials respond to wave excitation differently, depending on the frequency of the wave. At low frequencies, fluid is relaxed (low attenuation), causing small induced fluid pressure. At high frequencies, fluid is unrelaxed (low attenuation) and the induced fluid pressure is large. At an intermediate critical frequency, a transition of the fluid phase from relaxed to unrelaxed modes takes place. This transition is usually accompanied by a peak in attenuation and a velocity transition zone in the phase velocity.

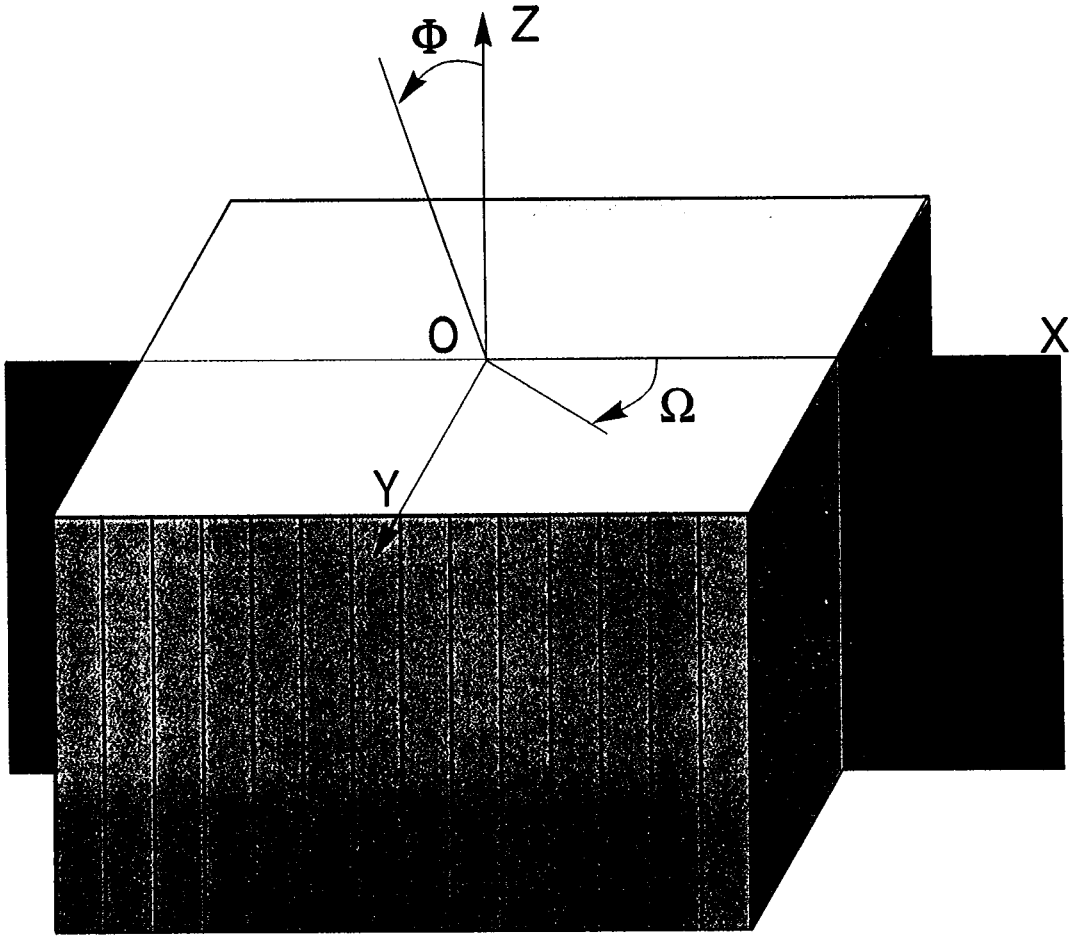

PAR024B

Figure VI-1. 3D view of an anisotropic medium with axis of symmetry perpendicular to the vertical z-axis, showing orientation of azimuthal and propagation angles.

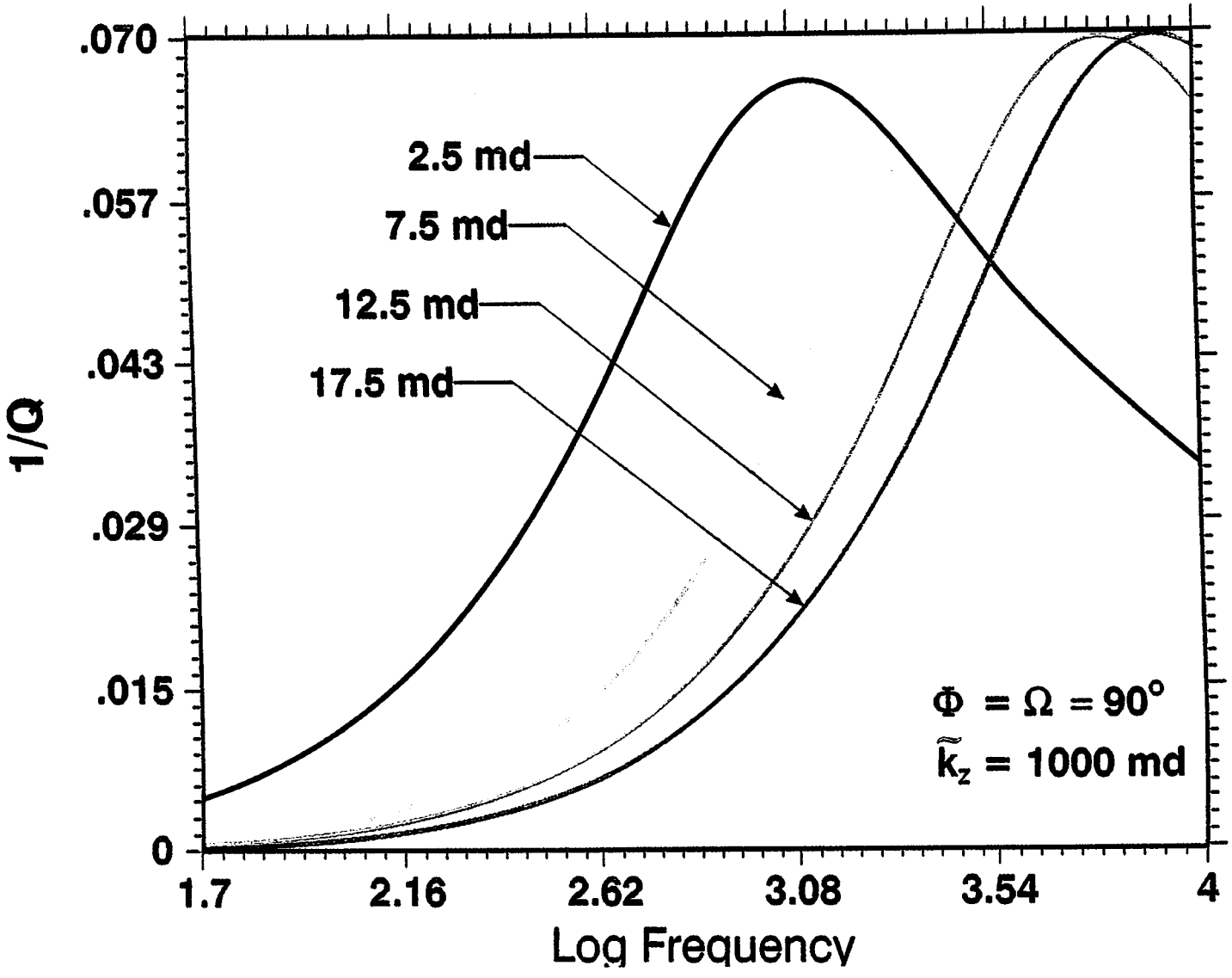
.070
.057
.043
.029
.015
0
1/Q
2.5 md
7.5 md
12.5 md
17.5 md
Φ = Ω = 90°
k̃z = 1000 md
1.7
2.16
2.62
3.08
3.54
4
Log Frequency

PAR018B

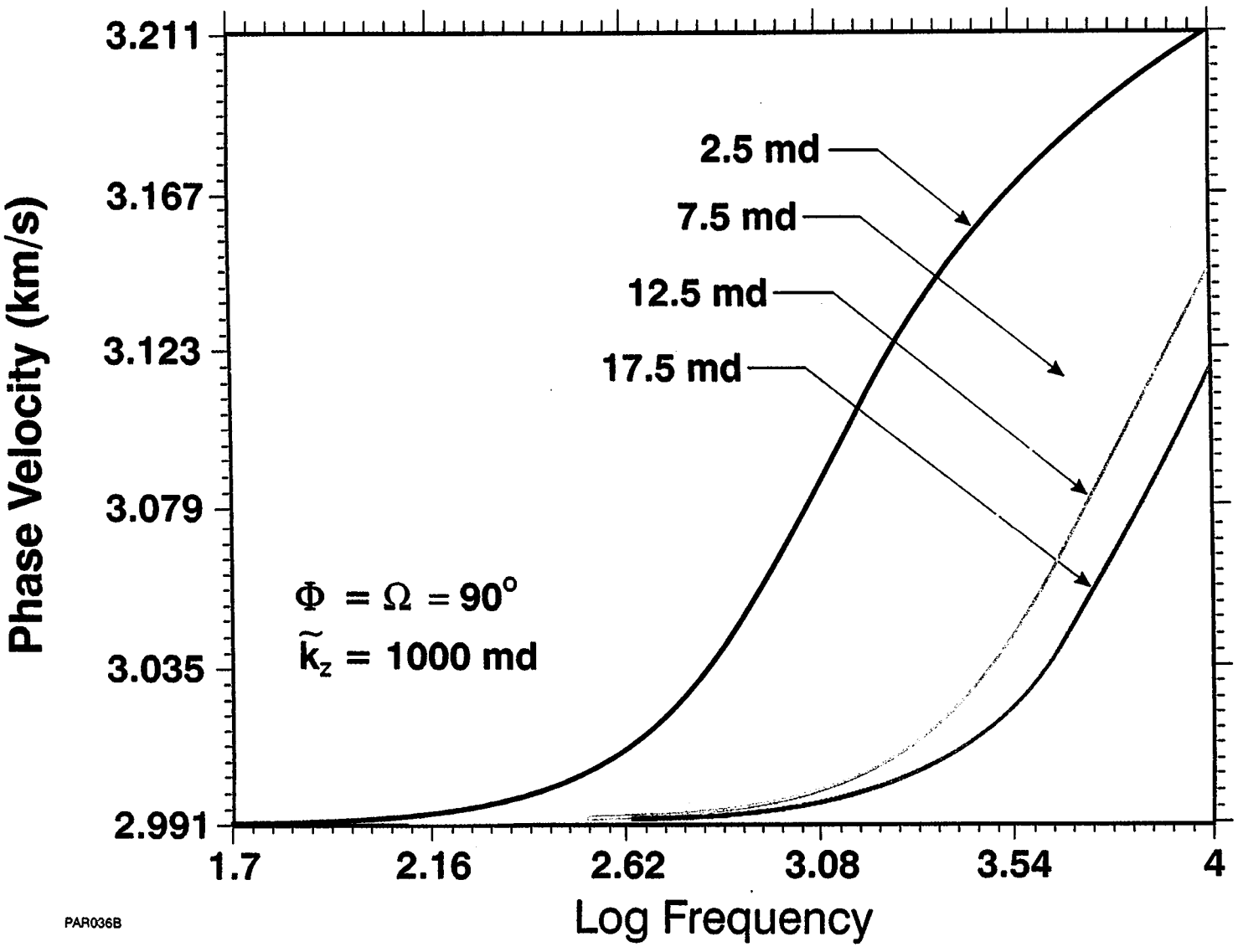

Figure VI-3. Effect of frequency and horizontal permeability on dispersion.

2. *Effect of Azimuthal Angle, Propagation Angle, and Frequency on Dispersion*

Figure VI-4 shows phase velocity curves produced for propagation angles of 15 and 90 degrees. For small propagation angles the wave travels near the vertical z-axis. For angles of propagation near 90 degrees the wave travels parallel to the x-axis. The frequency range is that of reverse VSP and crosswell seismic measurements (i.e., 500-2,500 Hz). The medium is a sandstone saturated with water having a porosity of 23 percent. We assume that the vertical permeability (kz) is much greater than the horizontal permeability (kx) (i.e, kx = 2.5 md and kz = 1,000 md). The curves show that as the azimuthal angle approaches 90 degrees (i.e., the wave propagates in the direction of maximum permeability) the velocity increases (high dispersion). In particular, when the angle of propagation is 90 degrees the dispersion is 14 percent. At a 15-degree angle of propagation, the dispersion is about 1 percent. For waves traveling perpendicular to the minimum permeability the phase velocity is proportional to the bulk modulus c11 (or the velocity in the direction of the z-axis), and the dispersion/attenuation is controlled by the squirt-flow associated with minimum permeability. Furthermore, the theory demonstrated that, for a 0-degree angle of propagation, the solution is independent of the azimuthal angle. The cubic equation becomes a quadratic equation. The phase velocity of the P-wave is a solution of a biquadratic equation for vertical propagation, and the P-wave propagates with velocity proportional to c11 (i.e., the quasi body waves become uncoupled). The computer models indicate that attenuation is more sensitive than phase velocity to the orientation of the azimuthal angle and permeability. As a result, the following examples are based on attenuation effects.

3. *Effect of Azimuthal Angle and Horizontal Permeability on Attenuation*

To illustrate the effect of horizontal permeability on attenuation we selected a frequency of 1,500 Hz for the same type of sandstone used in the previous example. In Figure VI-5 we vary the azimuthal angle from 0 to 90 degres and the horizontal permeability from 0.1 md to 2.2 md. We use a 90-degree angle of propagation. As the waves travel perpendicular to the minimum permeability, the attenuation increases 65 times for a horizontal permeability of 2.2 md, and about 14 times for a permeability of 0.1 md. That is, as the permeability increases from 0.1 md to 2.2 md, the attenuation increases about 51 times. This figure shows an attenuation peak value of about 0.067 for a permeability of 2.5 md, which decreases to about 0.027 for a permeability of 17.5 md.

Why is attenuation maximum when the horizontal permeability is 2.5 md? The reason is that attenuation distribution as a function of frequency for a horizontal permeability of 2.5 md has a peak at 1,500 Hz (see Figure VI-2). Each attenuation distribution is characterized by a horizontal permeability parameter. For example, if we produce a similar set of parametric curves for a frequency of about 10,000 Hz, the curve associated with 17.5 md will have the maximum values of attenuation for the different azimuthal angles.

In Figure VI-6, we show how attenuation varies as a function of permeability for azimuth angles of 15, 30, 60, and 90 degrees for a frequency of 1,500 Hz. These curves show a distinct relation between attenuation and permeability: attenuation is small at small permeabilities,

Effect of Azimuth Angle, Propagation Angle, and Frequency on Dispersion

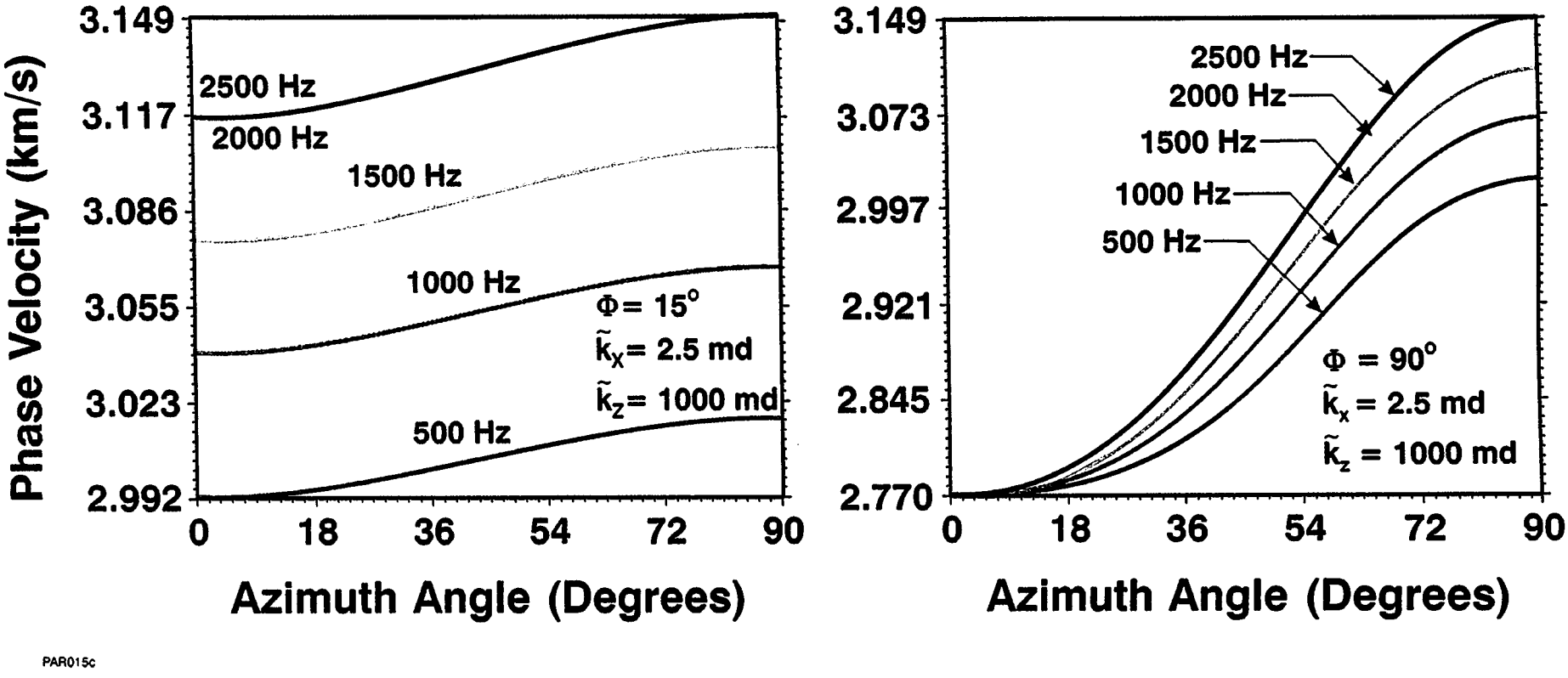

Figure VI-4. Effect of azimuth angle, propagation angle, and frequency on dispersion.

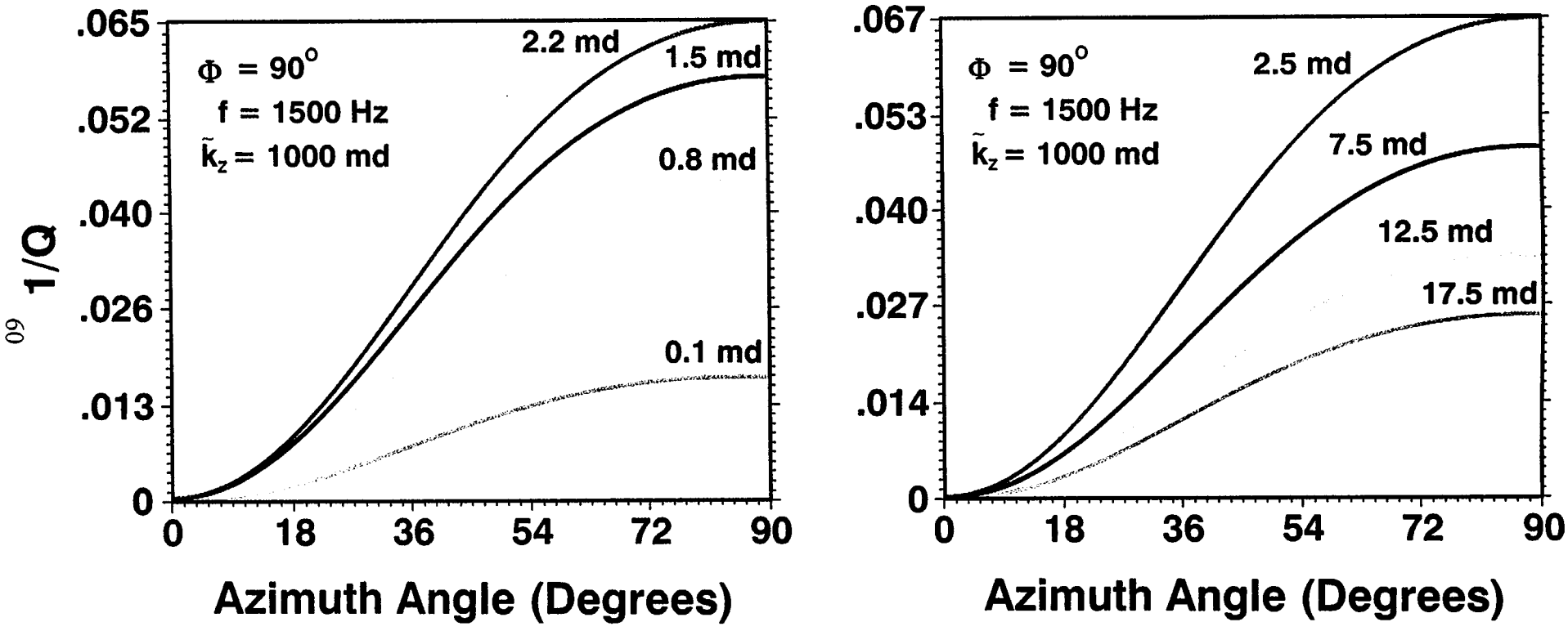

Figure VI-5. Effect of horizontal permeability and azimuth angle on attenuation.

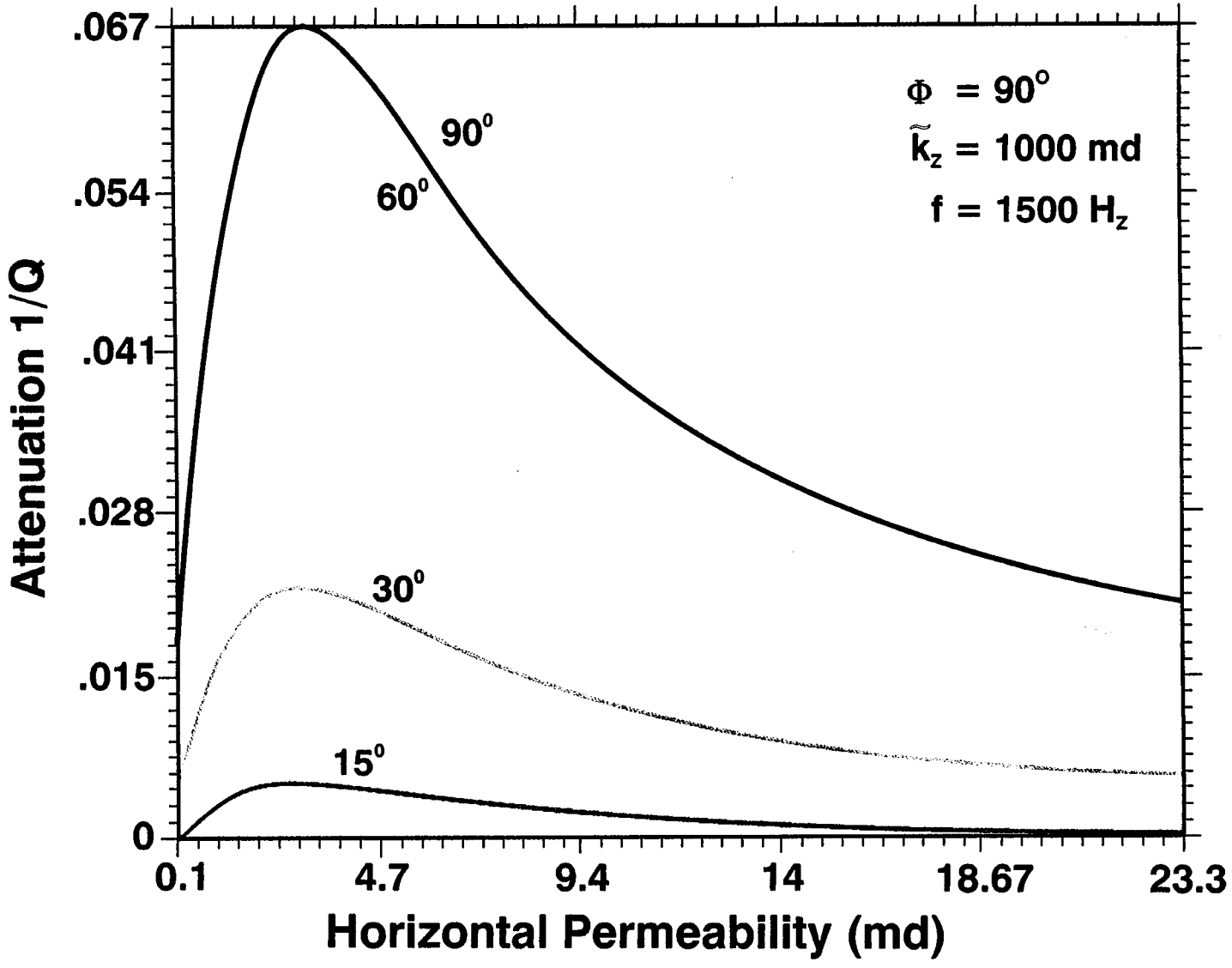

PAR019B
Figure VI-6. Attenuation as a function of horizontal permeability for azimuth angles of 15, 30, 60, and 90 degrees.

increases to a maximum at intermediate permeabilities, and decreases sharply at large permeabilities. In addition, these curves show that as the waves propagate perpendicular to minimum permeability, attenuation is maximum. For this angle ($\Omega = 90$), motion is controlled by the squirt-flow associated with the minimum permeability. In fact, for azimuth and propagation angles of 90 degrees, the cubic equation is reduced to a biquadratic equation that contains only the element of squirt-flow tensor associated with the horizontal (minimum) permeability. In this case, attenuation is controlled by the horizontal permeability.

On the other hand, when the wave travels perpendicular to the maximum permeability, attenuation is controlled by the element of the squirt-flow tensor associated with the maximum permeability. For 1,000 md, the attenuation peak occurs at a very high frequency that is beyond the range of reverse VSP and crosswell seismic measurements.

D. Dispersion of Seismic Waves in the Kankakee Limestone Formation

Interwell seismic techniques and well logs were used to characterize structure and rock physical parameters in a hydrocarbon-bearing formation at the Buckhorn test site (Parra, 1995). In this area, the oil reservoir is in the porous zone of the Silurian Kankakee limestone formation, which is horizontally distributed at about 200 m and is less than 8 m thick. Several logging measurements recorded just after drilling indicated a good correlation of the formation from well to well. However, the logs also suggested significant lateral changes in porosity within the formation, which is believed to be a thin high-velocity layer in a low-velocity background shale (Saito, 1991). Figure VI-7 shows the lithology column depicting the limestone and shale formation, and Figure VI-8 is a 3D view of the wells at the site.

Interwell seismic measurements have become an extremely efficient technique for determining rock physical parameters and detecting heterogeneity in hydrocarbon bearing formations. In particular, travel-time tomography inversion was successfully used to estimate the P-wave velocity distribution within the Kankakee limestone. Two 24-element hydrophone arrays (streamers) were used to acquire the data. The source was placed in well A and the streamers were placed in wells D and B. The hydrophone data was recorded by moving the source in increments of 2 m in well A (Parra, 1995).

Zero-vertical offset seismograms recorded in wells D and B were selected to extract dispersion and attenuation curves from interwell seismic data taken at depths ranging from 154 m to 200 m in well A. Figure VI-9 illustrates zero-vertical offset seismograms produced at 20 m and 46 m separation distances from well A. Both seismic sections show strong first arrivals for waves traveling in the shale formation and weak first arrivals for waves traveling in the Silurian Kankakee formation. To compare the vertical velocity distribution with zero-vertical offset waveforms, P-wave velocity logs are also presented in Figure VI-9. A low-velocity zone within the limestone is observed in the logs. This zone starts in well D and extends to well B; it is located along well D at a depth between 196 and 198 m.

The shale/Kankakee limestone interface is clearly defined by a sharp reflection in both seismograms. The horizontal compressional wave velocity in the shale varies between 2.7 km/s and

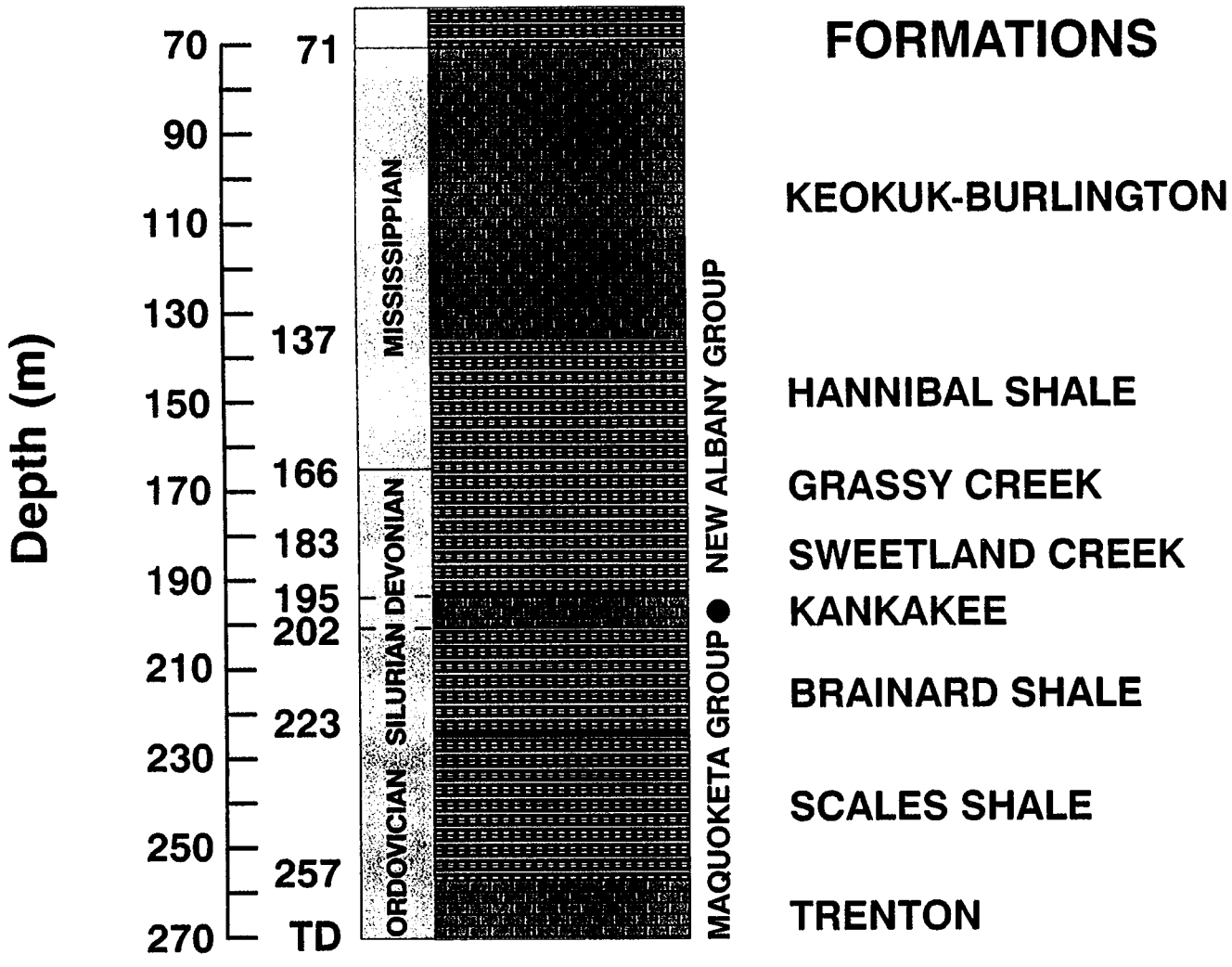

Figure VI-7. Lithologic column at the Buckhorn test site.

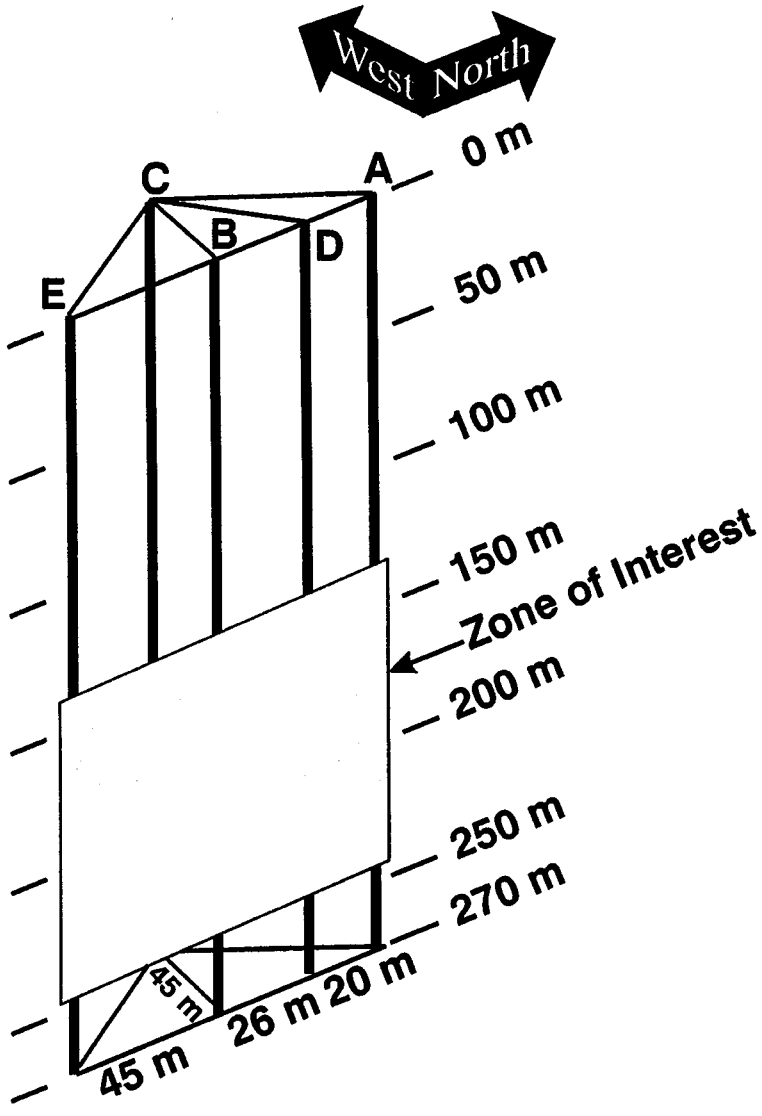

PAR028B Figure VI-8. 3D view of five boreholes at the Buckhorn test site.

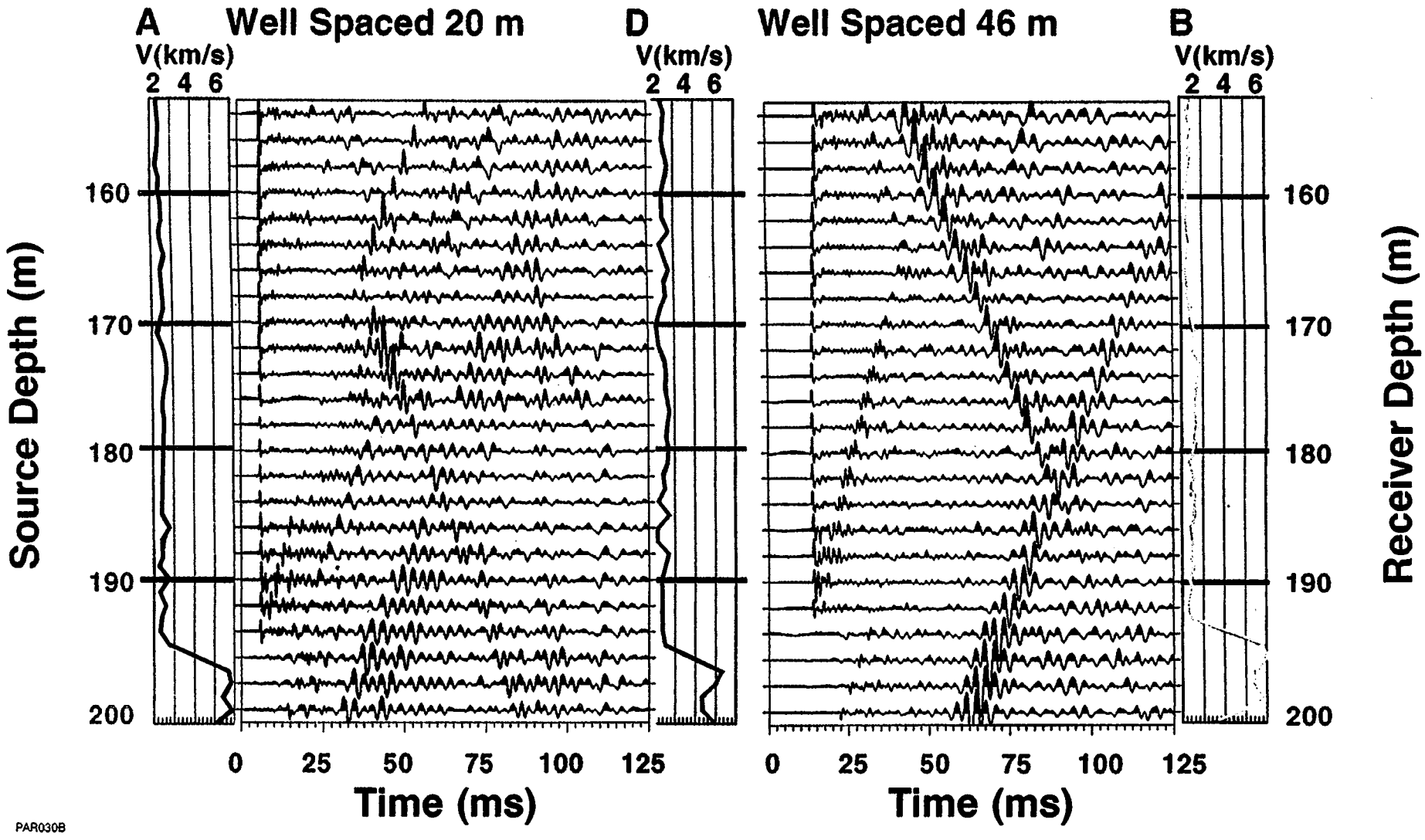

Figure VI-9. Zero-vertical offset seismograms.

3.5 km/s, and the P-wave velocity in the Kankakee varies between 4 km/s and 6 km/s. Several waveforms were selected to determine attenuation and dispersion effects in the shale and the Kankakee limestone. Figures VI-10 and VI-11 illustrate in detail the waveforms used to extract quality factors, Q, and dispersions between wells D and B. The direct P-waves associated with the limestone formation are clearly shown by the detectors in well D. Alternatively, the direct P-waves observed in well B have been decreased in amplitude and broadened by the attenuated medium between wells D and B. The waveforms in Figures VI-10 and VI-11 are used extract the quality factors for the shale and the Kankakee formation. Figure VI-12 shows an example of dispersion and attenuation for the shale. In this case the quality factor was determined to be Q = 28 and the phase velocity was found to reach its asymptotic value at 3 km /s, corresponding to the horizontal velocity of the shale (estimated using travel-time tomography).

Similarly, attenuation and phase velocities were calculated for the Kankakee limestone formation. The quality factors were 4.5, 7 and 4.4. As expected, the low quality factors and low phase velocities of the limestone are associated with the high-porosity and low-velocity heterogeneity delineated by Saito (1991). In addition, core information from well D indicated that the Kankakee limestone is formed by vertical fractures, vugs, and a porous matrix saturated with oil and water.

To correlate permeability to seismic waves, two seismic traces recorded in the Kankakee formation were selected. The first trace was recorded in receiver well D, 20 m from source well A, and the second trace was recorded in receiver well B, 46 m from source well A. The source and the two receiver wells were located in the same vertical plane. The receivers and source were placed at a depth of 196 m. The spectra of the seismic signatures are given in Figure VI-13. The phase velocity dispersion curves obtained using the spectra ratio method are plotted, together with theoretical phase velocity curves, in Figure VI-14. Theoretical curves were produced for azimuthal angles of 0, 30, 40, and 90 degrees based on the model parameters derived from well log data (Parra, 1995). The dispersion curve calculated at an azimuthal angle of 90 degrees fit the observed curve best at frequencies greater than 2,000 Hz. This suggests that the waves travel in the direction of maximum permeability, parallel to the fractured Kankakee formation, which surrounds the low-velocity heterogeneity.

The modeling demonstrates that flow is controlled by vertical fractures in the host rock matrix. On the other hand, the observed dispersion curve (for frequencies less than 2,000 Hz) shows that flow is controlled by porosity in the low-velocity heterogeneity within the Kankakee. Here the phase velocity varies from about 3,500 m/s to 4,500 m/s, a range consistent with the low-velocity anomaly delineated with travel-time tomography and P-wave velocity logs (Saito, 1991).

E. Summary

Modeling shows that in the frequency range of crosswell and reverse VSP measurements, the attenuation and phase velocity of the P-wave is sensitive to azimuth and propagation angles as well as permeability. To predict preferential directions of fluid flow in a reservoir, data regarding changes in attenuation and dispersion of seismic waves will be useful if measurements are conducted at different azimuth and incident angles.

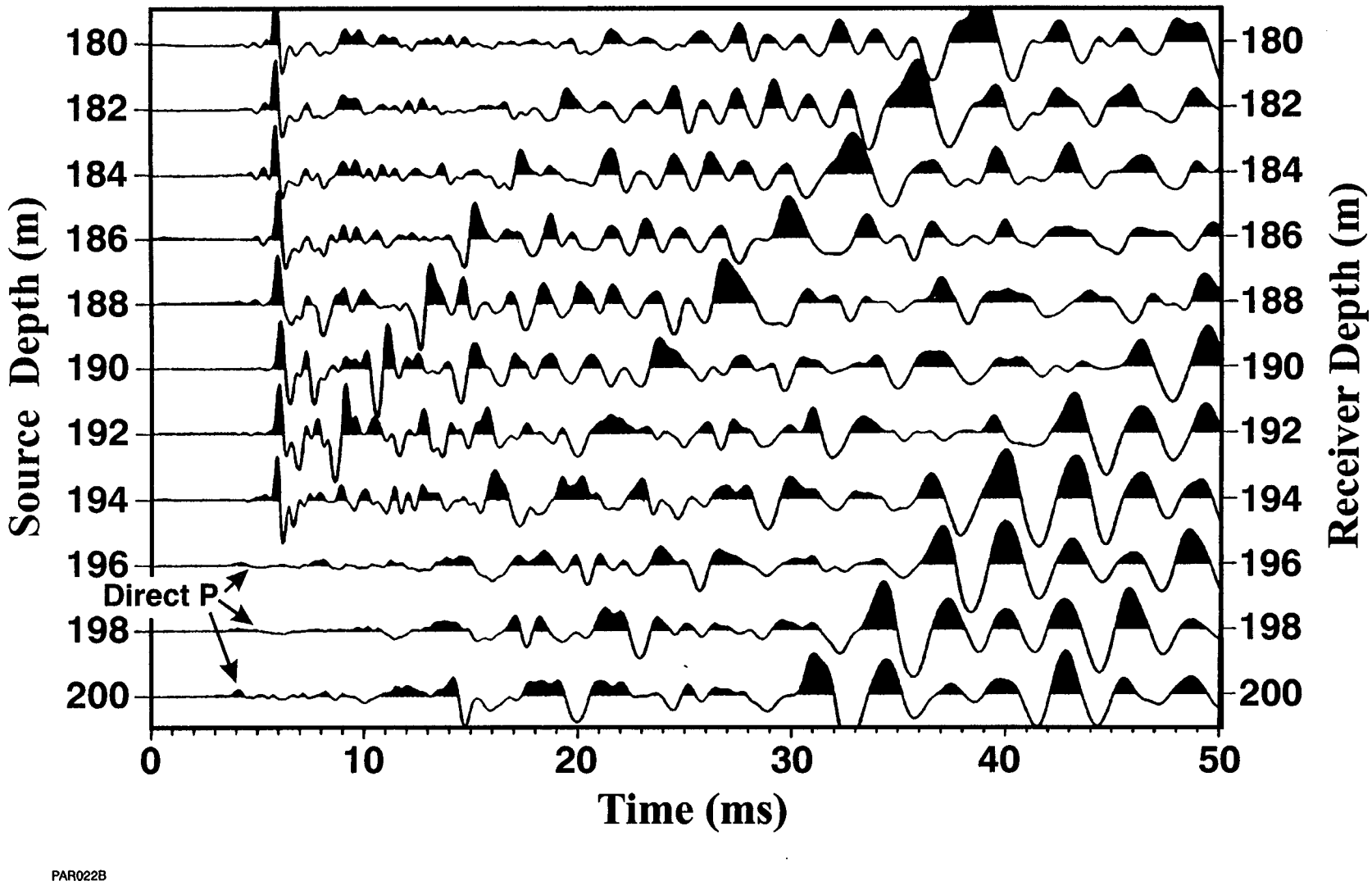

Figure VI-10. Zero-vertical offset waveforms recorded between wells A and D. Wells spaced 20 m apart.

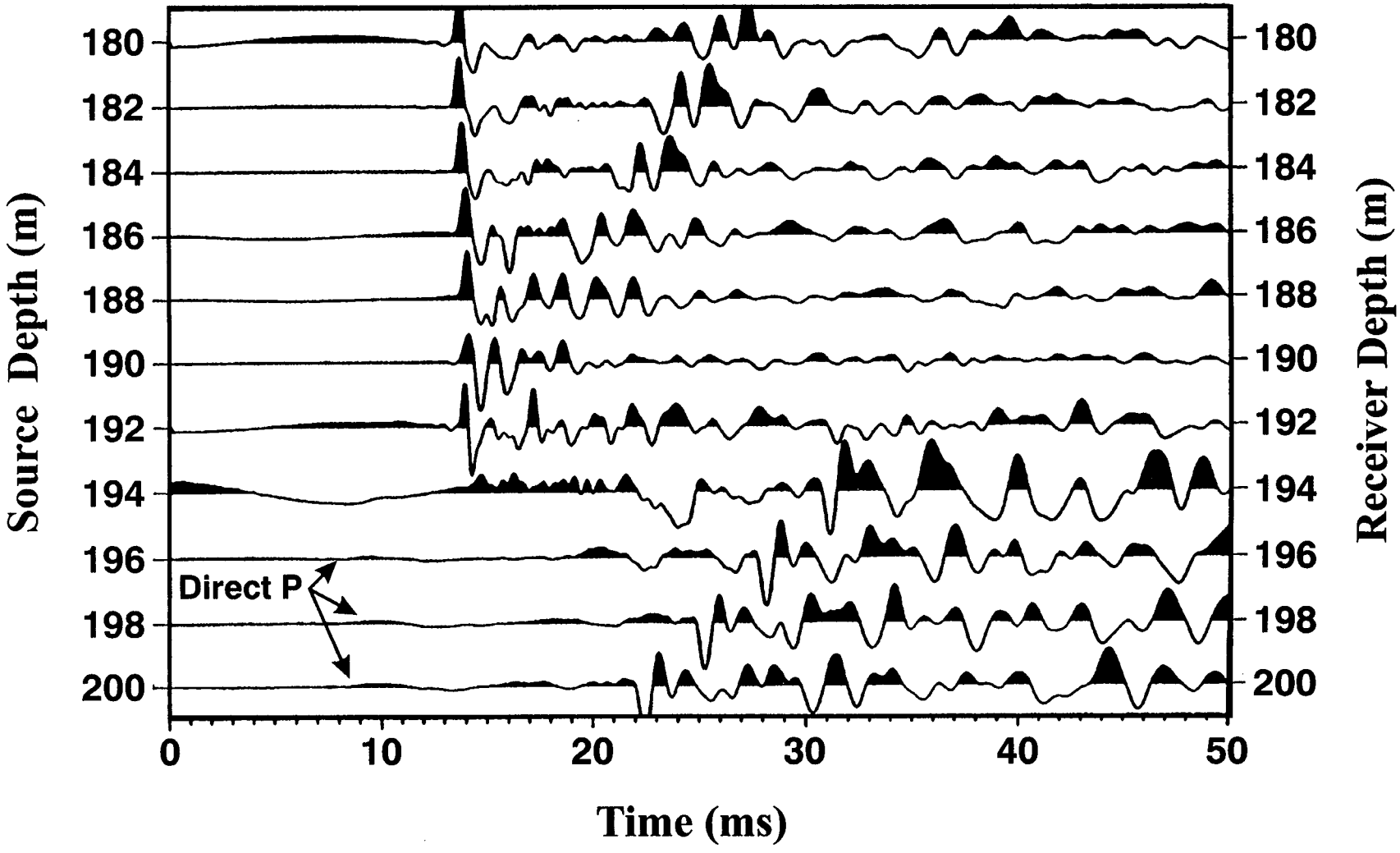

Figure VI-11. Zero-vertical offset waveforms recorded between wells A and B. Wells spaced 46 m apart.

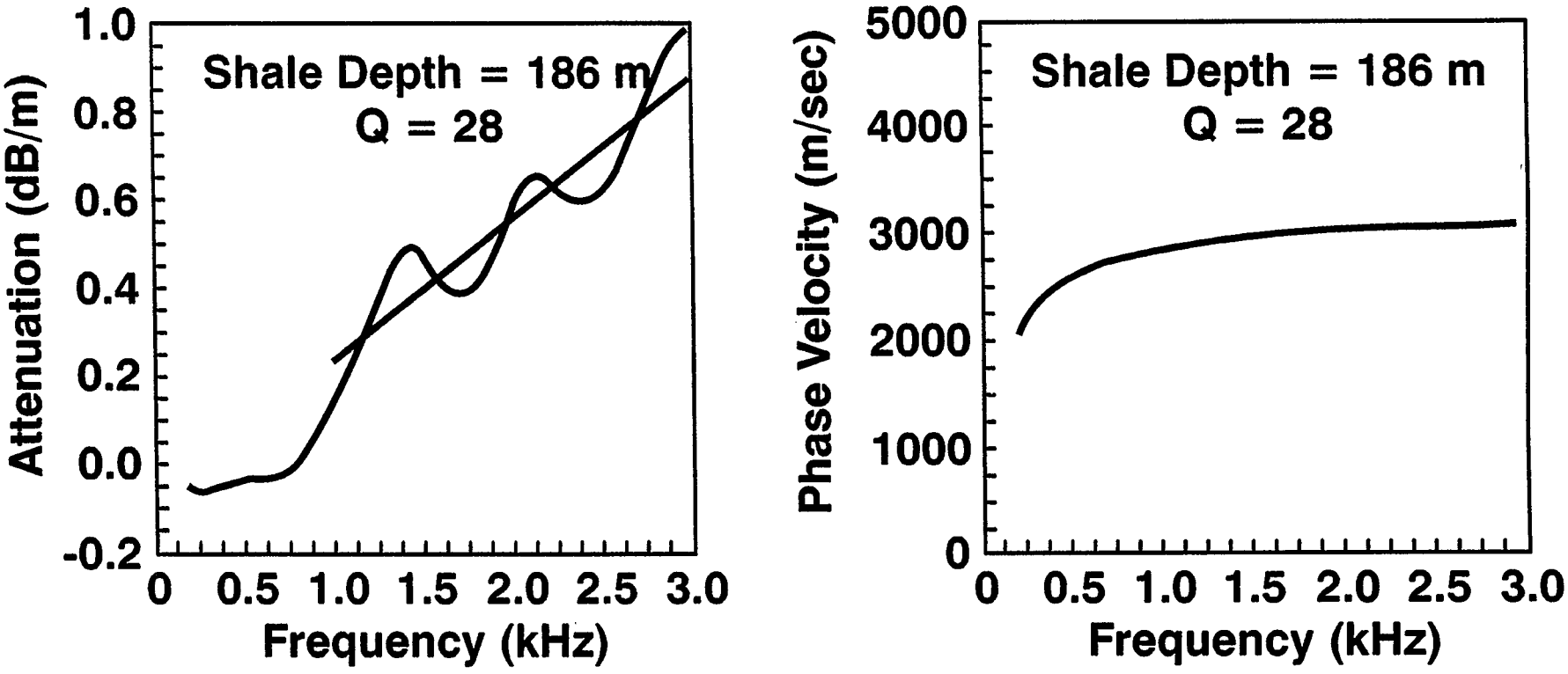

PAR027B

Figure VI-12. Dispersion and attenuation curves for a shale formation between wells D and B at a depth of 186 m.

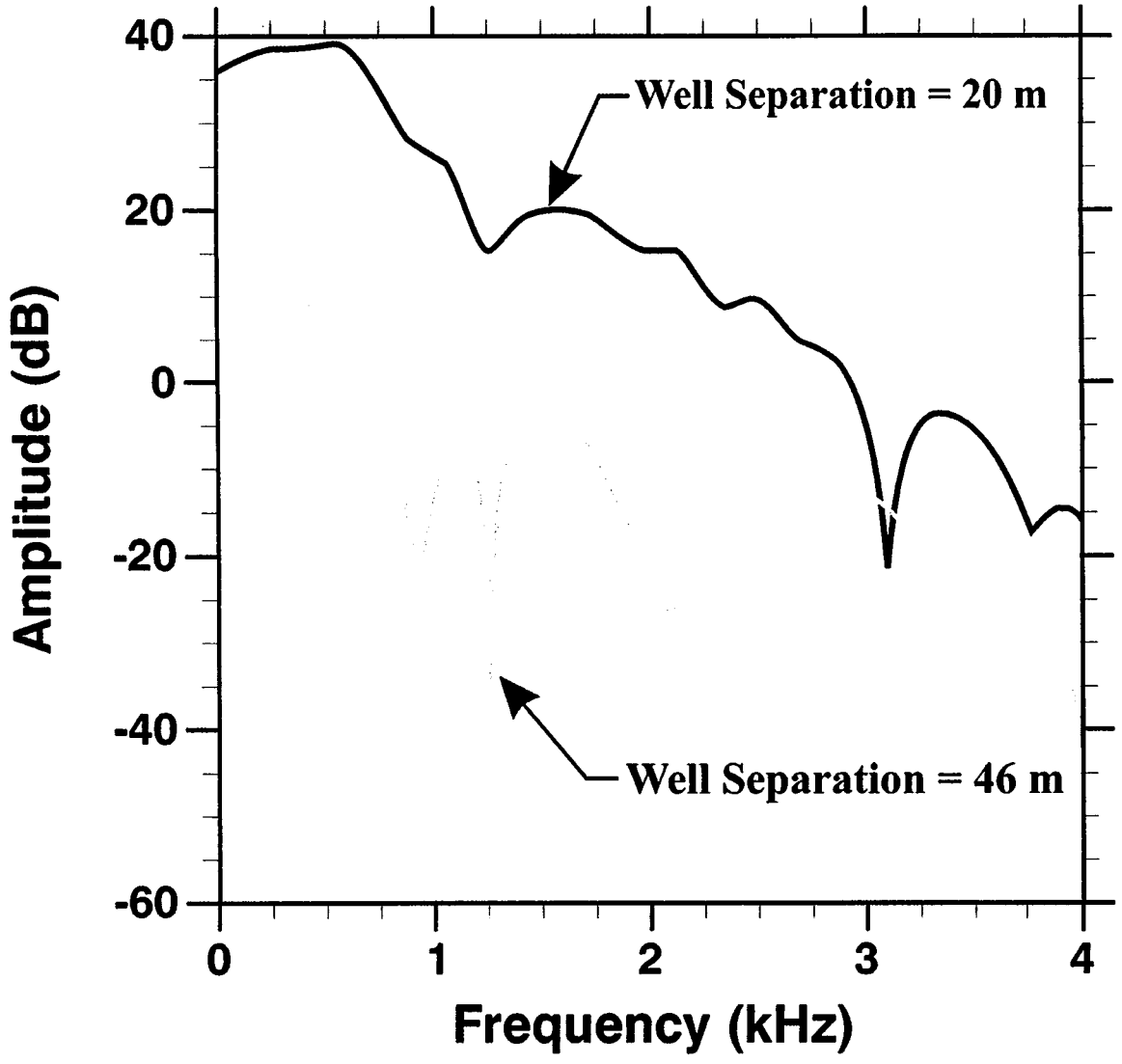

PAR025B

Figure VI-13. Spectra of common source waveforms recorded at 20 m and 46 m in well A.

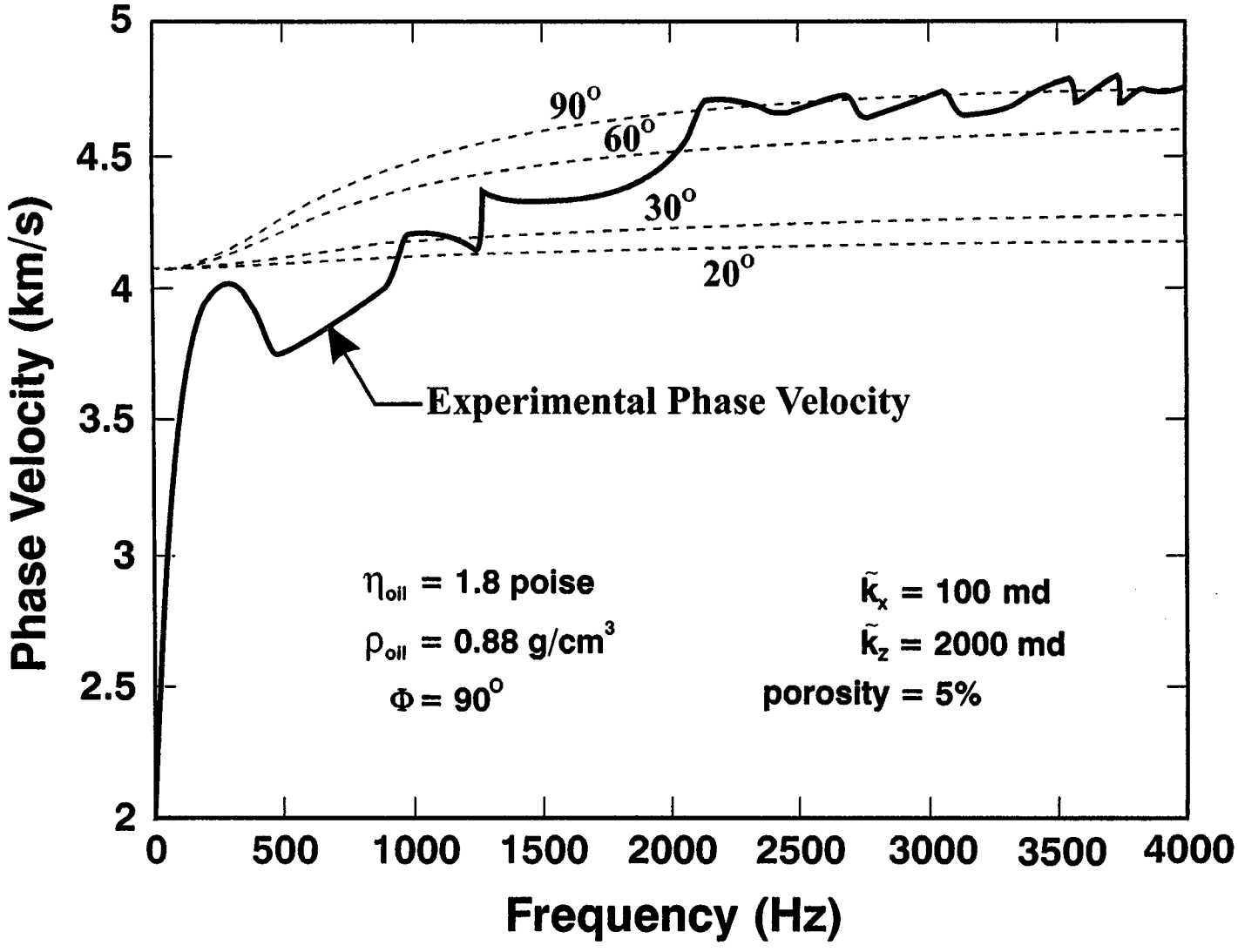

PAR026B

Figure VI-14. Comparison between experimental and theoretical phase velocity curves produced at several azimuthal angles.

When a plane P-wave propagates perpendicular (azimuth angle = 90 degrees) to the direction of minimum (horizontal) permeability, attenuation is always higher than when a wave propagates perpendicular to maximum permeability (yz-plane).

Modeling of dispersion data suggests that fluid flow in the rock matrix surrounding a low-velocity heterogeneity is controlled by fractures. Alternatively, flow in the low velocity zone is controlled by porosity.

Table VI-I. Transversely Isotropic Poroelastic Formation Parameters

Parameter	Unit	Formation Values
c_{11}	(GPa)	21
c_{13}	(GPa)	8.1
c_{33}	(GPa)	18
c_{44}	(GPa)	5
c_{66}	(GPa)	6
ϕ	%	23
K_s	(GPa)	37.9
ρ_s	(g/cm^3)	2.75
v_f	(km/s)	1.5
ρ_f	(g/cm^3)	1
η	(poise)	0.01
k_h	Darcy	0.0025
k_v	Darcy	1
Sqh	(mm)	4
Sqv	(mm)	6

VII. CHARACTERIZATION OF FRACTURES USING PETROPHYSICS AND 2D SEISMIC IN THE TWIN CREEK RESERVOIR, LODGEPOLE FIELD, UTAH-WYOMING OVERTHRUST BELT

An important approach to characterizing the fracture orientation and fracture permeability of reservoirs is one based on the effects of fractures on the propagation of acoustic and seismic waves in the rock. For this method to succeed, however, it is imperative to relate the petrophysical properties and distribution of fractures within the reservoir to the seismic signatures. This approach was used to study the Twin Creek Formation in Lodgepole field, northeast Utah. Integration of cuttings petrography, well logs, a synthetic seismogram, and the migrated 2D surface seismic data identified seismic events associated with geological features of interest. The surface seismic delineated the major geological boundaries between members of the Twin Creek Formation. The petrographic and petrophysical analyses demonstrated that most fracturing occurs in dolomitic mudstone rocks of the Watton Canyon and Rich Members. The high-velocity anomaly observed in the velocity inversion image correlates with a fracture zone in the Watton Canyon Member intercepted by a horizontal well. In the Lodgepole field, crosswell seismic measurements may be useful for delineating the high velocity anomalies associated with small fracture zones.

A. Introduction

In low porosity reservoirs, natural fractures are the primary source of permeability, controlling both production and injection of fluids. The open fractures do not contribute significantly to total porosity, but they provide an increased drainage network for the matrix porosity. Delineation of the fracture network is essential to successful exploration and development of such reservoirs.

Well logs and thin sections of cuttings from both horizontal and vertical boreholes were used to quantify petrophysical parameters and fracture distribution. Cuttings were substituted for cores because the Twin Creek has never been cored either in Lodgepole or in any of the neighboring fields. Thin section analysis was integrated with formation microscanner logs (FMS) to delineate fracture distribution in the horizontal wells. Fracture distribution was then correlated to anomalies in the 2D migrated seismic section velocity distribution. The 2D seismic section was also used to delineate the major boundary surfaces between members of the Twin Creek formation. The data were also used to determine the feasibility of using interwell seismic measurements at Lodgepole (Parra et al. 1997).

B. Location And Geology of Study Area

1. Location

Lodgepole field is one of a series of oilfields in the Overthrust Belt of northeast Utah (Figure VII-1). Union Pacific Resources (UPRC) has three fields in the play in Summit County, Utah: Lodgepole, Elkhorn, and Pineview. Lodgepole field extends over six sections (see Figure VII-2). The field has produced 1,132 MBO from the Twin Creek and Nugget formations.

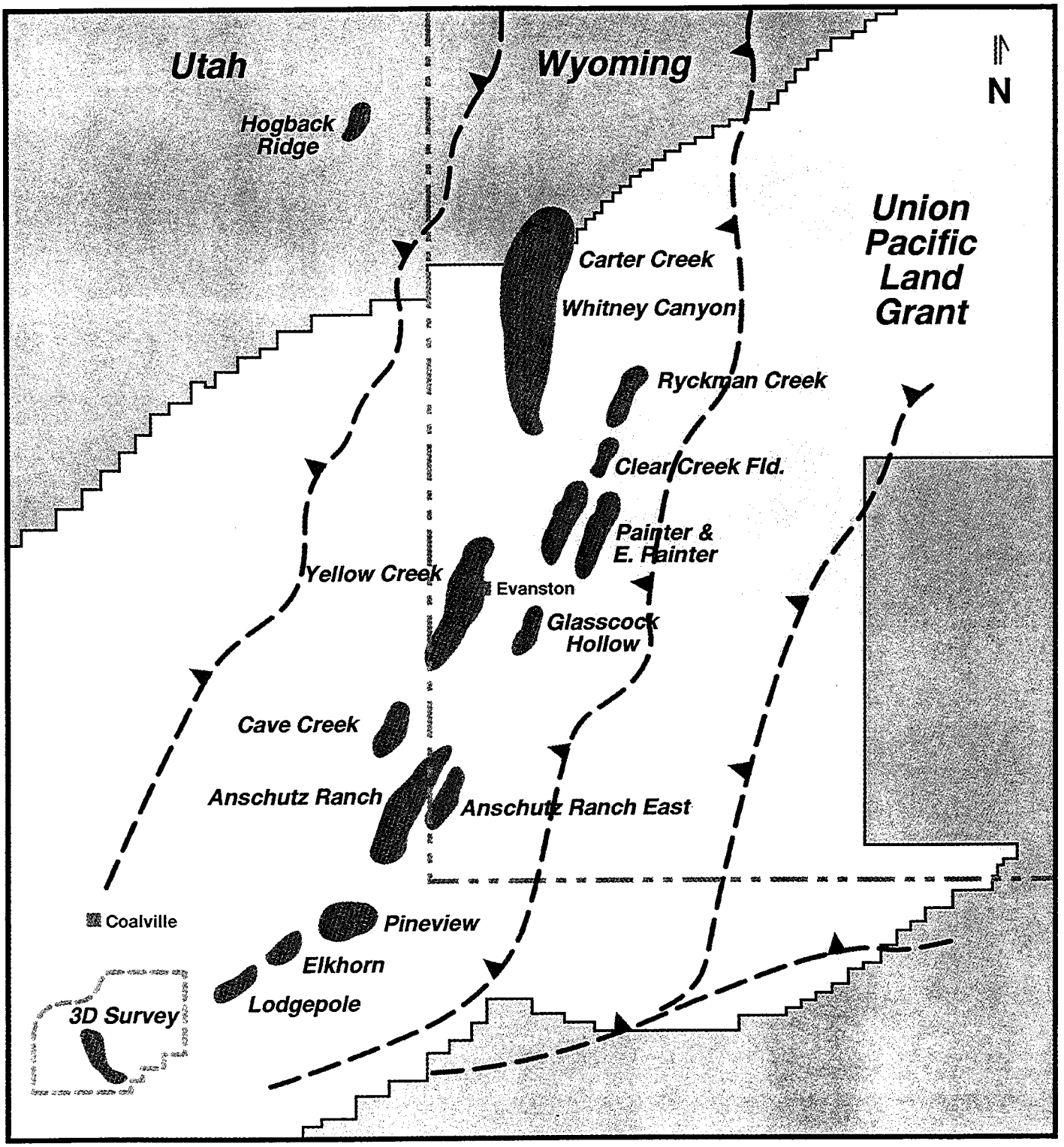

Figure VII-1. Regional map showing location of Utah-Wyoming Overthrust Belt fields.

LODGEPOLE FIELD

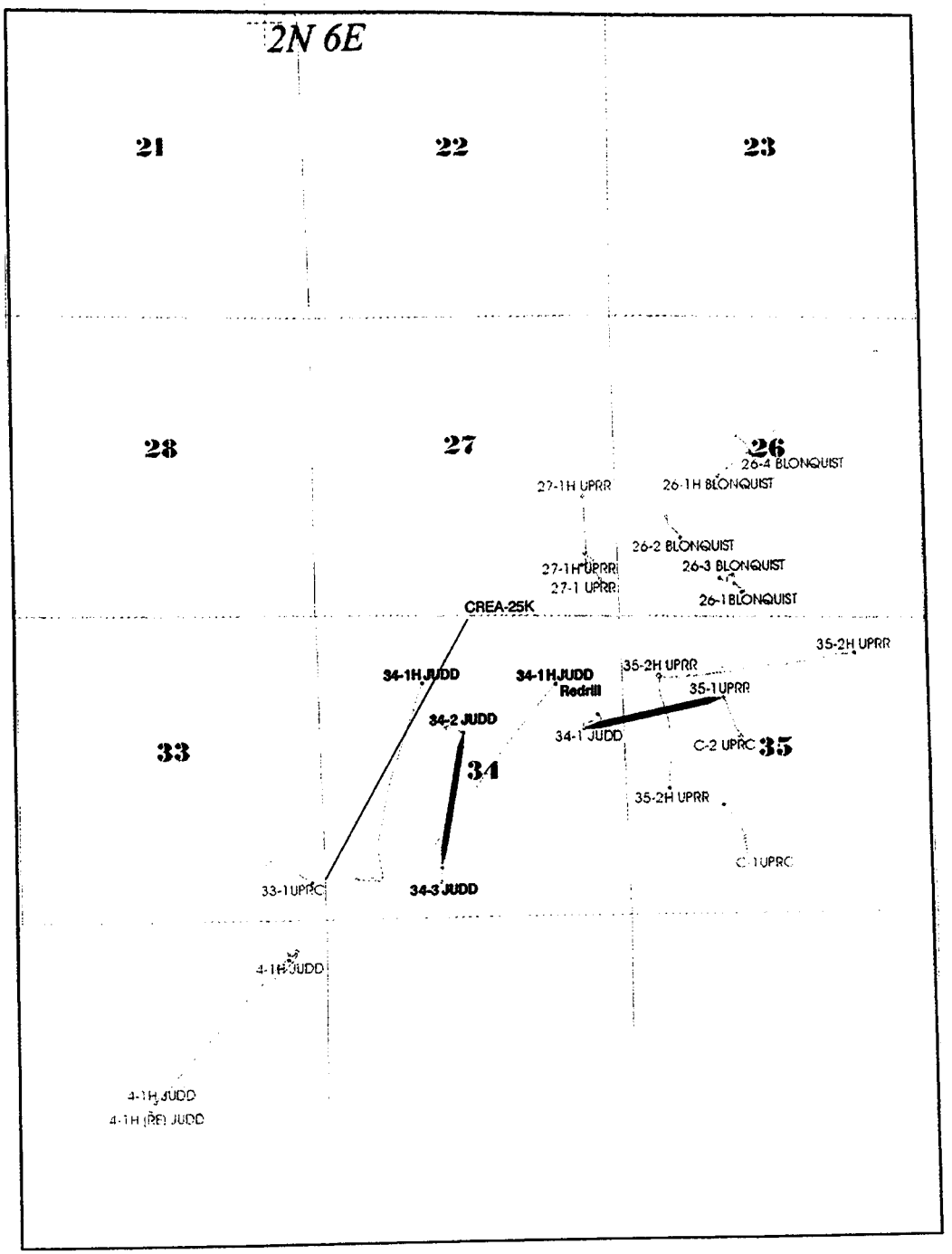

VII-2. Map showing the horizontal path of Judd 34 -1H and 34-1H Redrill wells and location of petrophysical cross section.

Section 34 was chosen as the study area (see Figure VII-2). It contains three vertical and two horizontal wells. Induction, gamma ray, density, neutron, and sonic are the only logs available for the vertical wells. FMS and gamma ray are the only logs for any of the horizontal wells. The study used horizontal wells Judd 34-1H and Judd 34-1H Redrill and the 2D seismic line (CREA-25K) that parallels them. The quality of the seismic data is decent.

2. Stratigraphy

The Twin Creek Formation is approximately 1,500 feet thick in Lodgepole Field and is divided into seven members. The following description of each member, beginning at the base, is adapted from Bruce (1988):

Gypsum Springs. Approximately 50 feet of sabkha evaporites, red beds, and minor carbonates. It serves as a detachment surface between the Nugget and Twin Creek for thrust faulting. In most places it also creates a barrier to hydrocarbon migration between the Nugget and Twin Creek Formations.

Sliderock. Approximately 90 feet of micritic limestone with thin beds of oolitic grainstone and thin shaly zones. No primary porosity has been preserved, but calcite-filled fractures are present.

Rich. Approximately 250 feet of argillaceous limestone that cleans upward. The upper 20 to 50 feet has some intergranular porosity and may be dolomitized. The Rich was the target zone in the 34-1H Judd Redrill.

Boundary Ridge. Approximately 50 feet of red siltstones and claystones with a sabkha character. It serves as a good marker bed in the Twin Creek Formation.

Watton Canyon. Approximately 250 feet of limestone with thin, tightly cemented oolitic zones. The limestones of the Watton Canyon are thinner bedded and more terrigenous than the Rich Member. An interval approximately 20 feet thick near the base of the Watton Canyon is the primary target for most horizontal wells, including the 34-1H Judd.

Leeds Creek. Approximately 300 feet of interbedded argillaceous and relatively clean limestones. A highly radioactive unit near the top of the member is a devitrified tuff.

Giraffe Creek. Approximately 450 feet of micritic and oolitic carbonates. It is sandy toward the top. It is the uppermost member of the Twin Creek.

The Basal Preuss Silt, a 30- to 100-foot interval of tightly cemented quartz siltstone, overlies the Twin Creek Formation. The Preuss Salt, in turn, overlies the siltstone. It varies from 20 to 300 feet in thickness. The Twin Creek Formation overlies the Nugget Formation, which

is eolian sandstones. The Nugget is one of the primary hydrocarbon producing reservoirs in the Overthrust Belt.

Structural cross sections parallel and perpendicular to the trace of Judd 34-1H were constructed with the logs from the vertical wells in Section 34. The cross sections center on the Watton Canyon and Boundary Ridge Members, which contain the fractured intervals in the Twin Creek Formation. The cross sections include the acoustic velocity, bulk density, gamma ray, caliper, and lithology curves. Figure VII-3 is the cross section parallel to the horizontal wells.

3. Geologic Controls on Fracture Distribution

To understand the nature of fracturing in the Twin Creek, thin sections of 10-foot cutting samples were made in the largely unfractured Giraffe Creek and Leeds Creek Members and in both fractured and unfractured intervals of the Watton Canyon and Rich, the two main fractured members. The Judd 34-1H (10,400 to 13,470 ft.) provided sample coverage from the top of the Twin Creek through the fractured lower part of the Watton Canyon. The Judd 34-1H Redrill (12,780 to 13,180 ft.) provided sample coverage of the fractured upper part of the Rich. Unfortunately, because of lack of returns in the Judd 34-1H Redrill, no samples were available for the lower Watton Canyon and Boundary Ridge Members.

The thin sections were impregnated with blue epoxy for identification of porosity and open fractures. Selected thin sections were stained with Alizarin Red S to distinguish calcite from dolomite.

Only scattered traces of porosity were found in the thin sections, which is consistent with low porosity values on the density log. Fracturing, however, is common. It is selectively controlled by lithology, with significant fracturing mainly confined to dolomitized mudstones where silt and sand are minor constituents (see Figure VII-4). The favorable facies for fracturing is a backbank low energy brackish environment (based on the absence of pellets). Petrographic analysis of the cuttings reveals that lithologic changes control fracture distribution:

Giraffe Creek Member. Fractures are very rare in the Giraffe Creek. It contains two distinct units, an upper siltstone-dominated unit and a lower pellet-packstone-dominated unit. Clastics are abundant in the Giraffe Creek from 10,440 to 10,600 ft, while mudstone and fracturing are rare. The clastics are composed of argillaceous to calcareous pelletal siltstones with minor amounts of sandstones and mudstones. Only traces of vuggy, moldic intercrystalline and microporosity are present from 10,460 to 10,610 ft. The lower part of the Giraffe Creek consists of interbedded pelletal siltstones and silty pellet packstones with significant silty mudstones. Its base is marked by increasing amounts of interbedded mudstones.

Leeds Creek Member. The Leeds Creek Member, starting at 10,921 ft, can be divided into an upper oolitic to pellet-packstone-dominated facies and a lower slightly silty to slightly dolomitic mudstone (top at 11,180 ft). The

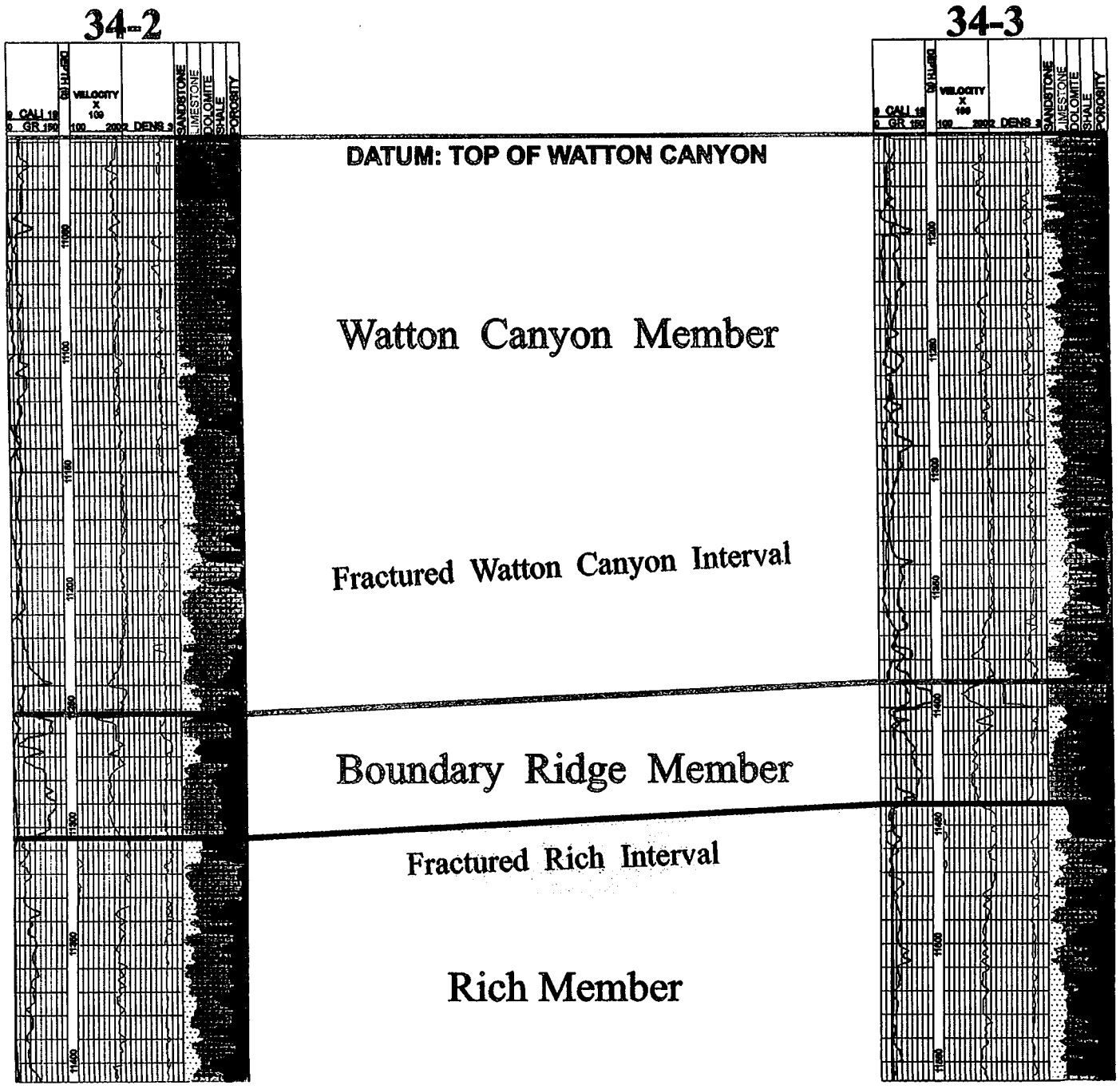

Figure VII-3. A structural cross section through vertical wells 34-2 and 34-3 at the Lodgepole field.

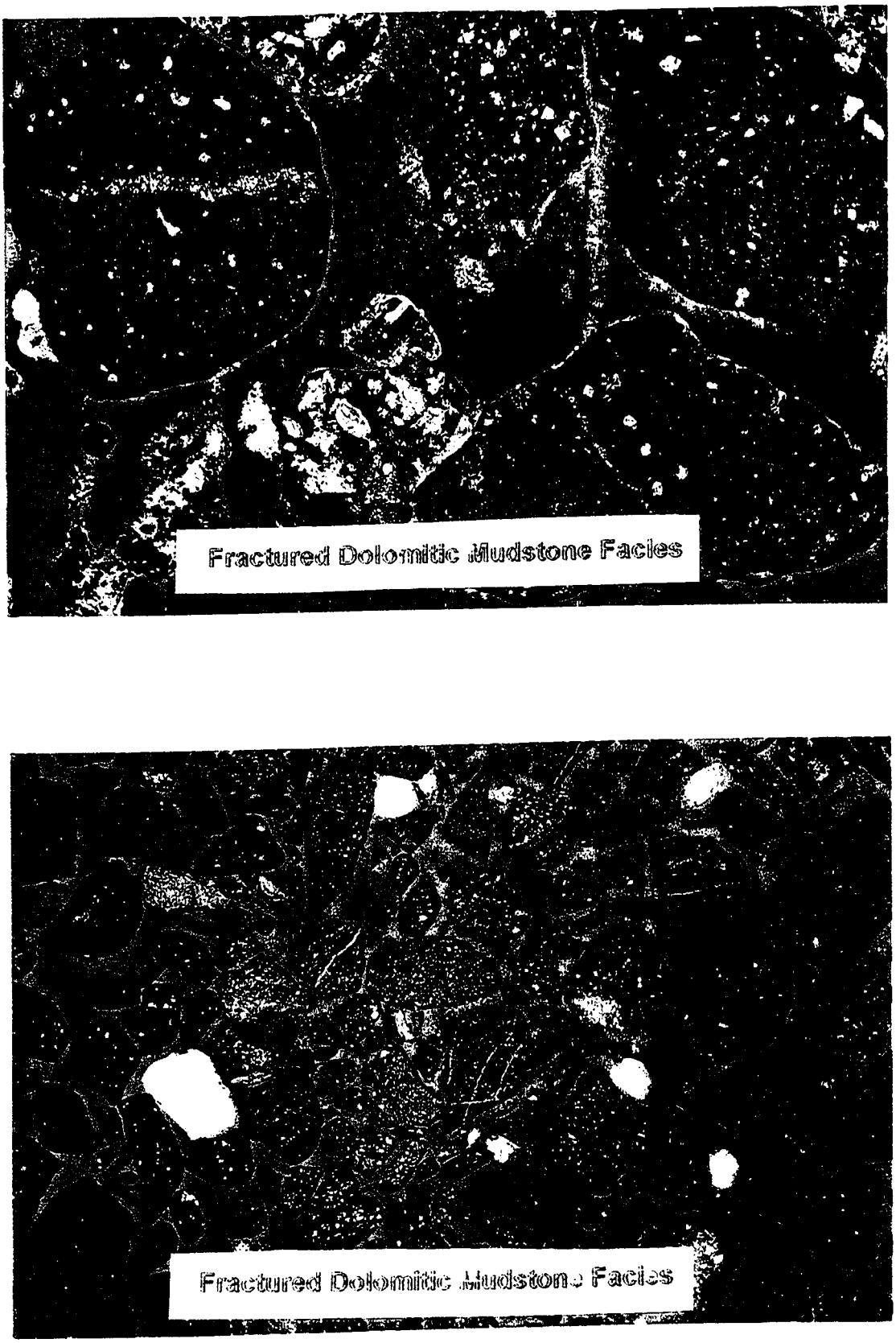

Figure VII-4. Thin section photomicrograph of the fractured dolomitic mudstone lithofacies.

mudstones at 11,180 ft. are slightly silty and slightly dolomitic with increased fracturing. The fracture interval occurs between 11,180 ft. and into the top of the Watton Canyon Member. An increase in fracturing to five percent occurs at 11,190 to 11,200 ft. in slightly to very dolomitic mudstone. Fracturing is rare in the upper part of the Leeds Creek Member, increasing at the base of the member where dolomitization and mudstone content increase.

Watton Canyon Member. The Watton Canyon Member (top at 11,260 ft.) differs little from the base of the Leeds Member. The upper part of the Watton Canyon is predominately dolomitic mudstone. Overall, the Watton Canyon is dominated by dolomitic mudstones with scattered zones of pellet packstone. Dolomitic mudstone is the main host rock for fracturing (Figure VII-4). The Watton Canyon mudstones range from slightly to very silty and slightly to very dolomitic. Some scattered, slightly calcareous dolomites are interbedded with the very dolomitic mudstones. An increase in dolomitization and decrease in silt corresponds to an increase in fracturing. Where interbedded silty pellet packstones abound, fracturing is rare to absent (Figure VII-5). Good fractured intervals in the Watton Canyon occur at 11,180 - 11,360 ft., 11,400 - 11,470 ft., 11,730 - 11,900 ft., 11,990 - 12,540 ft., 12,960 - 13,050 ft., and 13,260 - 13,470 ft. (sample depths).

The fracturing in the Watton Canyon is recognized on the basis of five to 20 percent healed fractures in the mudstone and a corresponding occurrence of free crystalline calcite (trace to 20 percent). Most healed fractures show little open porosity. The open fracture porosity may be represented by the free crystalline calcite. One Watton Canyon interval (11,510 to 11,610 ft.) contains five to 30 percent free crystalline calcite and only traces of healed fractures. The top of this interval is pellet-packstone-dominated while the base of the interval is mudstone-dominated. This is the only packstone interval with fracturing. Figure VII-6 shows the correlation between fracturing and the mudstone facies. In the figure, mudstones are present in the intervals where pellets and ooids are absent.

Rich Member. Thin sections of the Rich were made from 12,780 to 13,180 ft. in the Judd 34-1 Redrill from cutting samples caught after mud returns were established at 12,780 ft. From the available Rich samples, two units were recognized, an upper pellet-dominated packstone and a lower ooid-dominated packstone. Fracturing was rare to absent in both units and only occurred at 12,900 to 12,920 ft. and 12,960 to 12,980 ft. in the pellet-dominated unit where mudstones were present. A zone of free crystalline calcite was observed at 12,920 to 12,980 ft., which may indicate a fractured interval in the base of the interbedded pellet and mudstone unit. No fracturing was found below 12,980 ft. or in the ooid-dominated packstone.

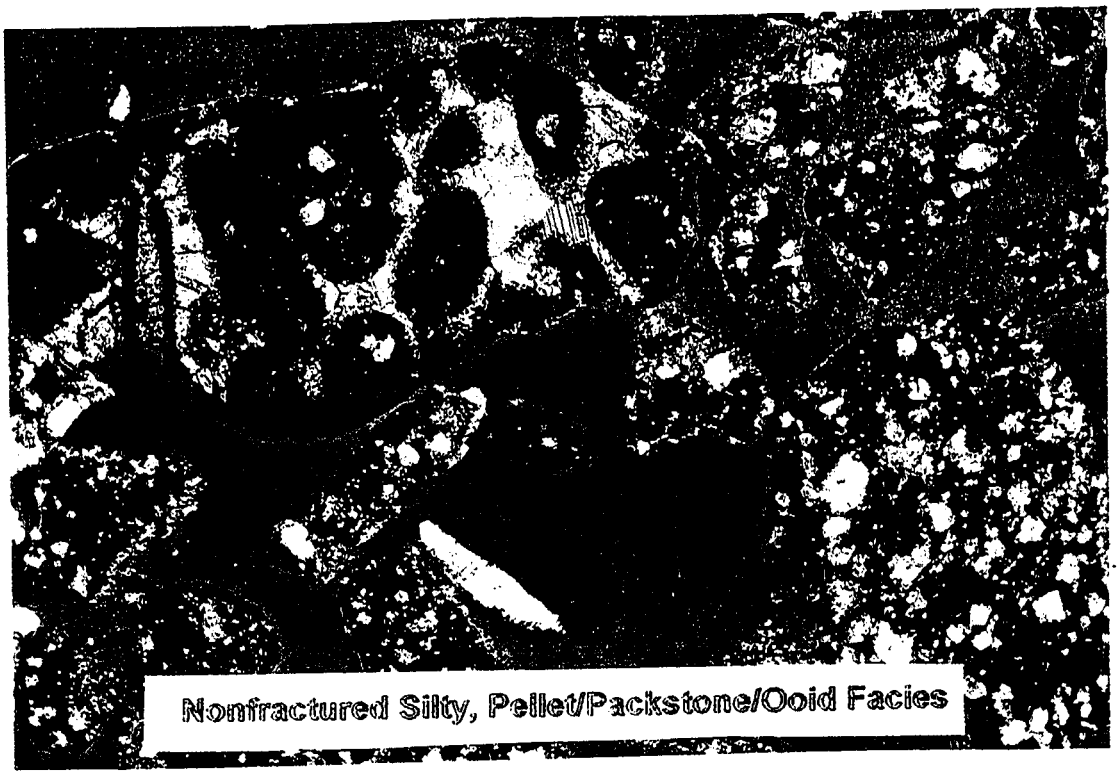

Figure VII-5. Thin section photomicrograph of the nonfractured silty, pellet/packstone/ooid lithofacies.

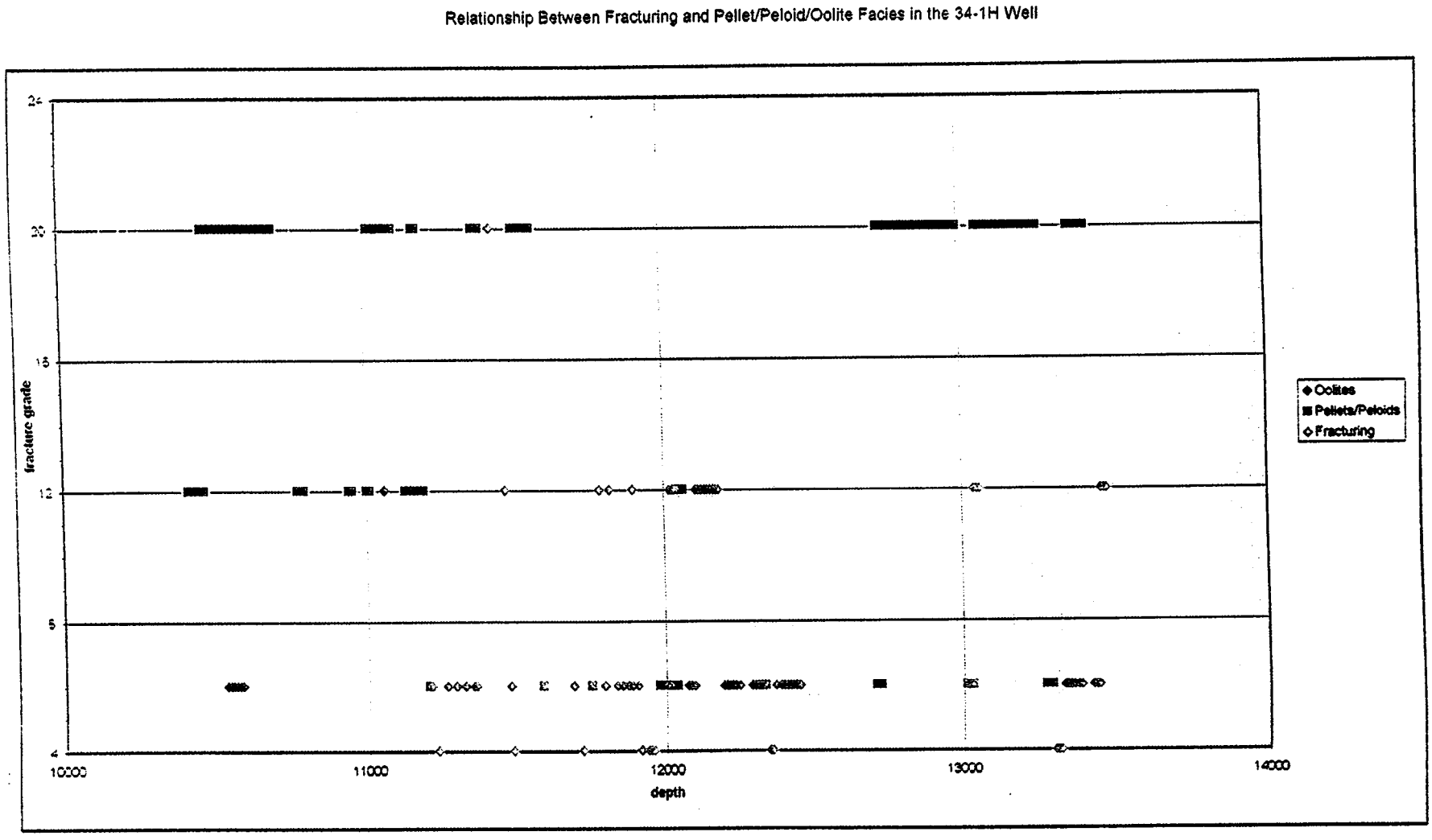

Figure VII-6. Relationships between fracturing and lithofacies in the 34-H well. Mudstones are present in the intervals where oolites and pellets/peloids are absent.

4. Geologic Controls on Hydrocarbon Production

Virtually all the effective porosity in the Twin Creek Formation is from fractures. Vertical wells produce from five members of the Twin Creek, while horizontal wells produce from fractured intervals in only the Rich and Watton Canyon members. In the Rich the upper 30 feet is the fractured interval.

The Watton Canyon is the most prolific hydrocarbon-producing member of the Twin Creek and it is also the most intensely fractured. The bottom 100 ft. of the Watton Canyon contains fractures. A zone approximately 20 ft. thick near the base of the Watton Canyon is the primary target for most of the horizontal wells, including the 34-1H.

Based on outcrop studies, FMS logs, and production data, the fractures run NW-SE. Fracturing was produced by faulting and tight folding of the hanging wall of the Absaroka Thrust sheet (Bruce, 1988). The Gypsum Springs Member served as a detachment surface between the Nugget and Twin Creek in the thrusting process. The trapping mechanism is structural closure on asymmetrical anticlines in the hanging wall.

C. Data Analysis and Interpretation

1. Seismic Interpretation

Seismic line CREA-25K was selected because it follows the horizontal path of the Judd 34-1H. This well and well 34-2 are plotted in the migrated seismic section given in Figure VII-7. A synthetic seismogram was produced using the compressional wave velocity log and the density log from well 34-2. The seismogram was superimposed on the migrated seismic line in Figure VII- 7, together with the geological boundaries defined by the well logs in Figure VII-3. Figure VII-7 shows the horizontal path of well 34-1H intercepting the fracture zone in the Watton Canyon (refer to the cross-section in Figure VII-3). The Watton Canyon Member is the most prominent geologic unit in the seismic section of Figure VII-7. Its upper and lower boundaries correlate with the sonic, density, and gamma logs, and the seismic events on the seismic sections. In fact, the synthetic seismogram fits reasonably well at the position of the Judd 34-1H in " time-depth" on the seismic section. For example, the top of the Watton Canyon is at 1,600 ms and the top of the Rich Member is at 1,640 ms.

In general, the petrophysical boundaries defined by the well logs correlate with the seismic events in the seismic section. The seismic signatures associated with the Watton Canyon suggest lateral velocity changes between wells 34-1H and 34-2. There is a change on the seismic signature associated with this region of interest between the trace at position 2190 and well 34-1H. This event may be associated with the petrophysical characteristics of the Rich Member in the region below the Watton Canyon.

The fractured zones are located in the bottom part of the Watton Canyon Member and in the top of the Rich Member, where these fractured zones are intercepted by well 34-2. Both fractured zones are associated with low gamma ray counts, indicating shale-free intervals. The

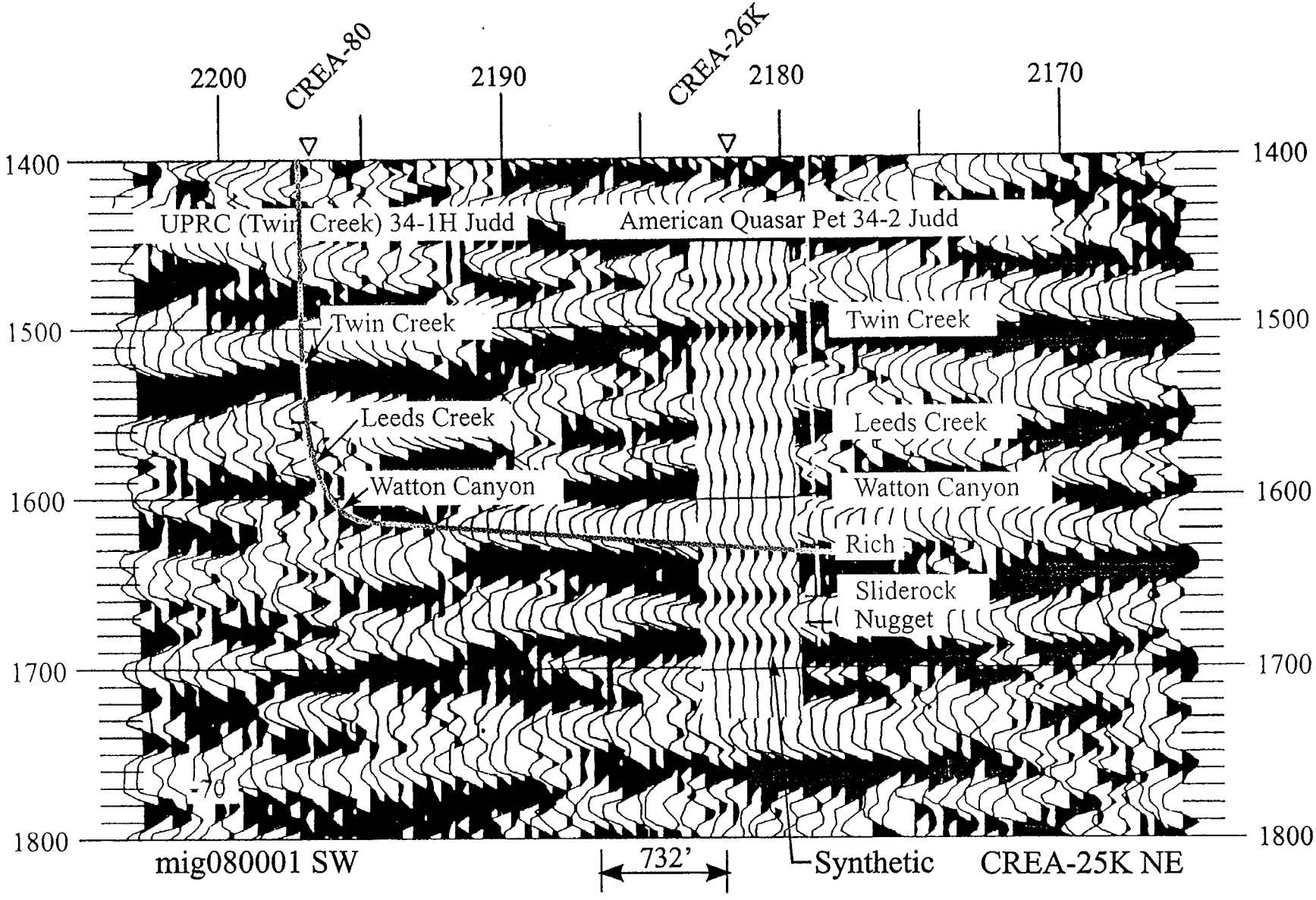

Figure VII-7. Migrated seismic section CREA-25K along horizontal well path of well 34-1H Judd with synthetic seismogram inserted at well location 34-2 Judd.

fracture zone in the Watton Canyon is separated from the fracture zone in the Rich by the 50-foot thick Boundary Ridge Member, which consists of siltstones and claystones. A reflection event associated with this boundary is observed in the seismic section of Figure VII-7 and is below the horizontal path of well 34-1H. This analysis suggests that the Watton Canyon, in the region between both wells under consideration, is associated with a "trough"- reflection response, which may be caused by the presence of a fractured zone containing vertical fractures. This fractured zone is intercepted by the horizontal well in the bottom part of the Watton Canyon. The FMS log recorded in the horizontal well intercepted vertical fractures having a variable fracture density distribution.

2. Petrophysical Analysis

Lithologic calculations from the logs in the vertical wells, shown in Figure VII-3, confirm the mixture of lithologies seen in the cuttings and show that fracturing in the Rich Member is in the dolomitic facies. A similar pattern is seen in the Watton Canyon fractured interval in the 34-3 well. The fractured interval in the Rich has more shale than the fractured interval in the Watton Canyon.

Union Pacific Resources' horizontal well fracture index (RFI) was used to quantify the significance of the fracturing seen on the FMS log (Svor and Meehan, 1991a and 1991b). This weighted grading system is based on visual correlation of the fractures by comparing the fracture's excess conductivity to high end/low end calibration points in the borehole. This process gives a quick and easy estimation of fracture aperture and distribution. For the 34-1H well, the calibration points are the unfractured target zones and an uphole shale bed.

The FMS tool used in the Judd 34-1H is a four-pad microresistivity device. Each pad has 16 buttons, and the resistivity trace of each button is recorded on the log (see Figure VII-10a, Raw Buttons column). Fractures appear on the traces as low resistivity deflections (deflections to the right). Fractures are graded and assigned a numerical value based on the number of pads that show a deflection and the magnitude of the deflection. The higher the number, the more significant and larger the fracture.

Grading the FMS log revealed two main fracture intervals along the horizontal path of the 34-1H well: 11,800-12,000 ft. and 12,300-13,200 ft. (see Figure VII-8). The fractured interval from 12,300-13,200 ft. shows up as an anomaly on the velocity inversion of the migrated seismic section as shown in Figure VII-9. A velocity high correlates with the 900-foot long, high fracture density interval, and a lower velocity anomaly correlates with the second fractured zone (11,800-12,000 ft.). Figure VII-10a shows an example of the FMS log over a fractured interval within the velocity inversion anomaly. In this figure the high resistivity signatures correspond to a high density distribution. In contrast, Figure VII-10b is the FMS log of an interval outside the velocity inversion anomaly that has little fracturing. Here, few resistivity anomalies are observed, corresponding to a low fracture density.

The sonic and density logs from the vertical wells were also examined to determine their correlations with fracture intervals. The fractured interval within the Watton Canyon has a high velocity and is dolomitic: sonic velocity ranges from 18,500-20,000 ft/s and bulk density

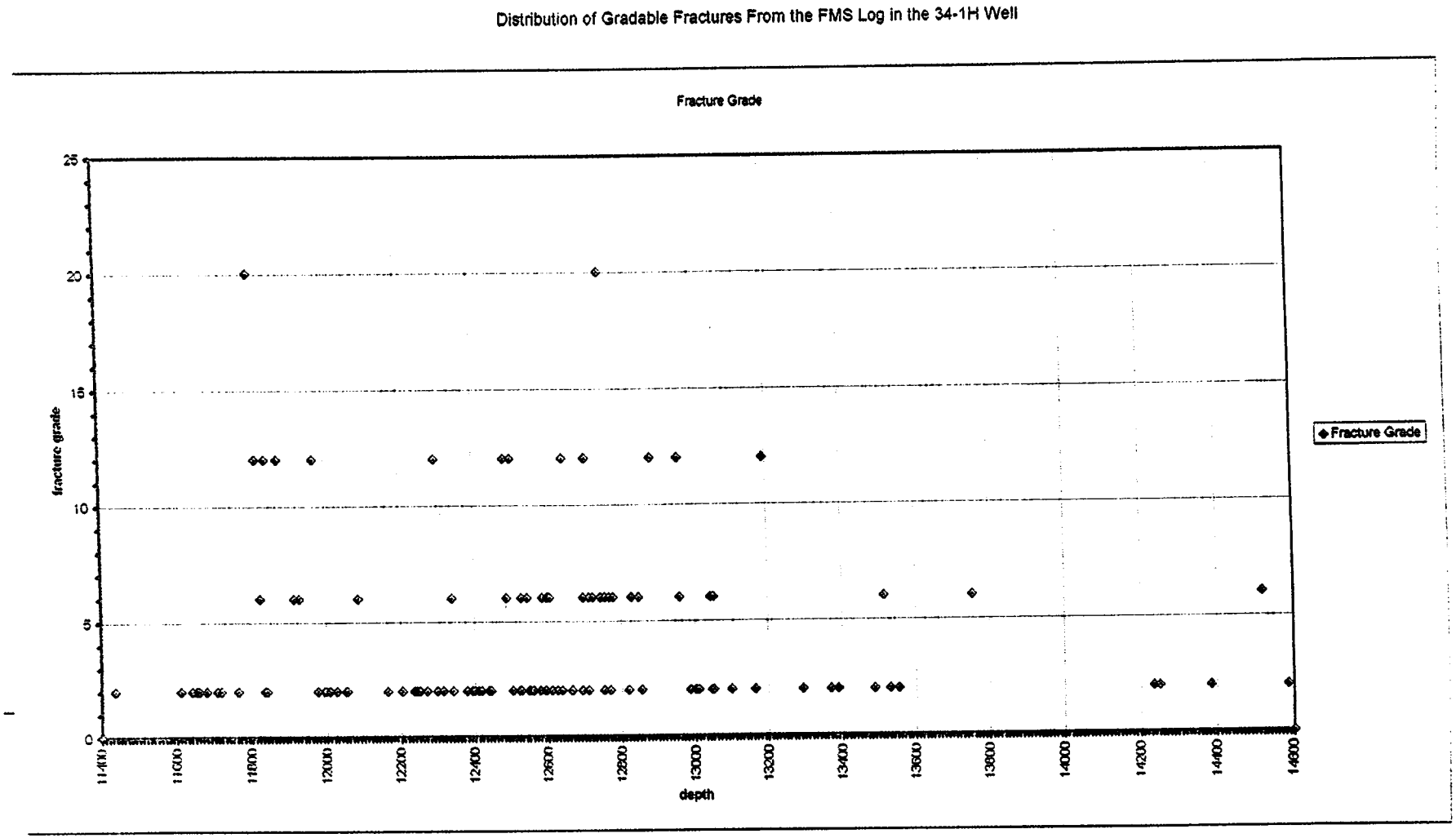

Figure VII-8. Distribution of gradable fractures from the FMS log in the 34-1H well.

VELOCITY INVERSION OF MIGRATED SEISMIC SECTION CREA-25K
ALONG HORIZONTAL WELL PATH 34-1H

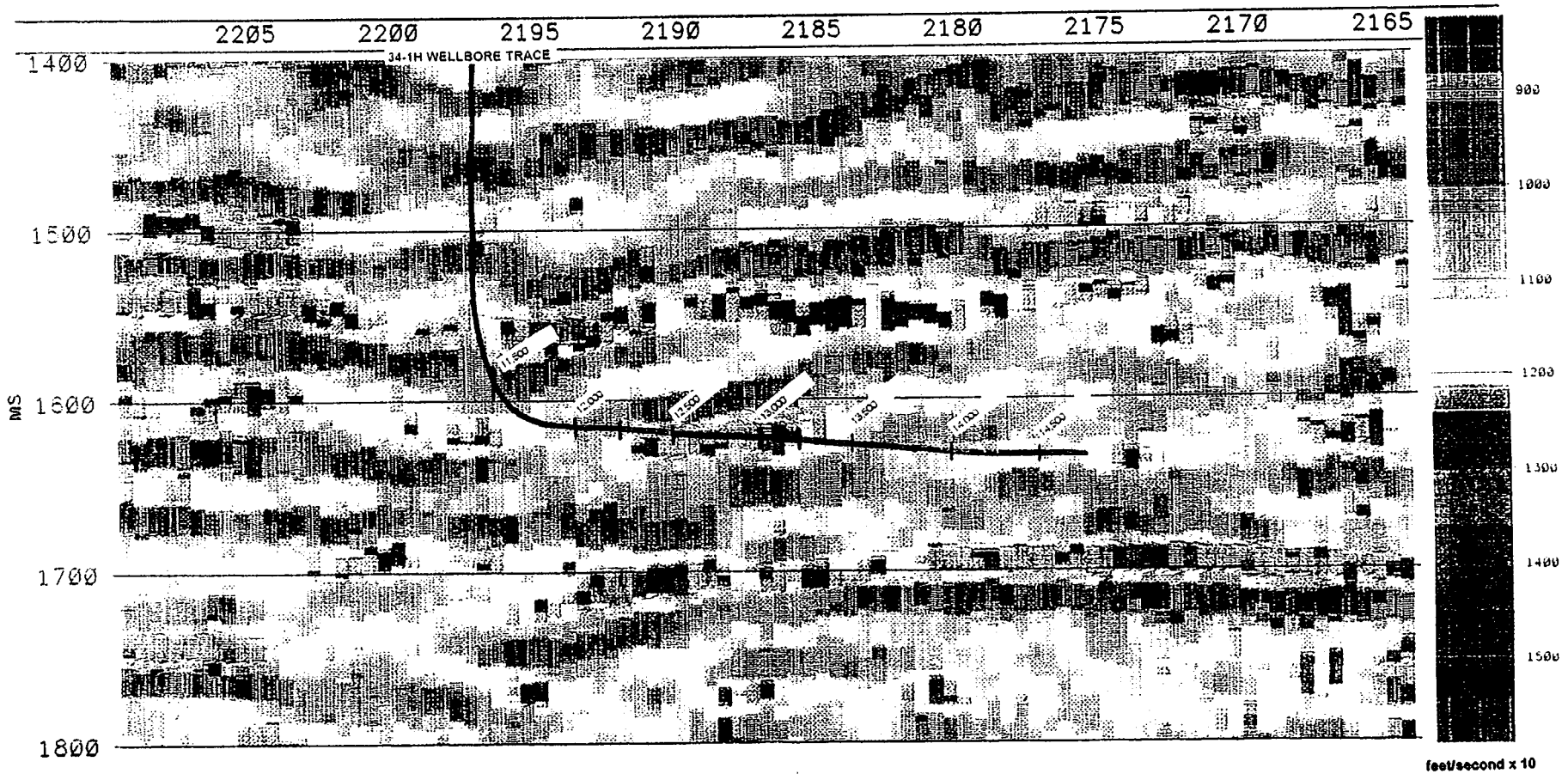

Figure VII-9. Velocity inversion of migrated seismic section CREA-25K along horizontal well path 34-1H.

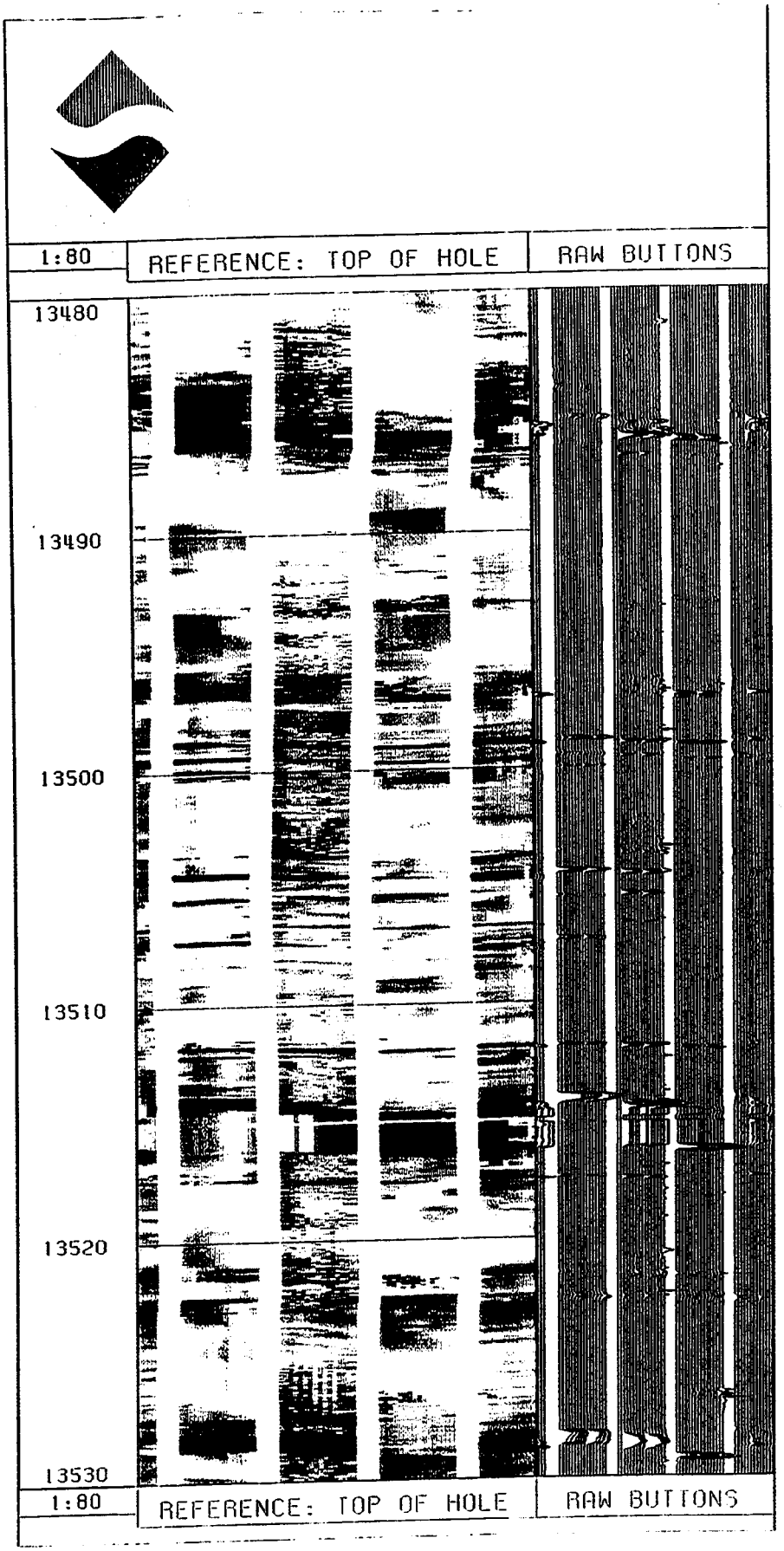

Figure VII-10(a). FMS image of an interval with high-grade fractures within the inversion velocity anomaly.

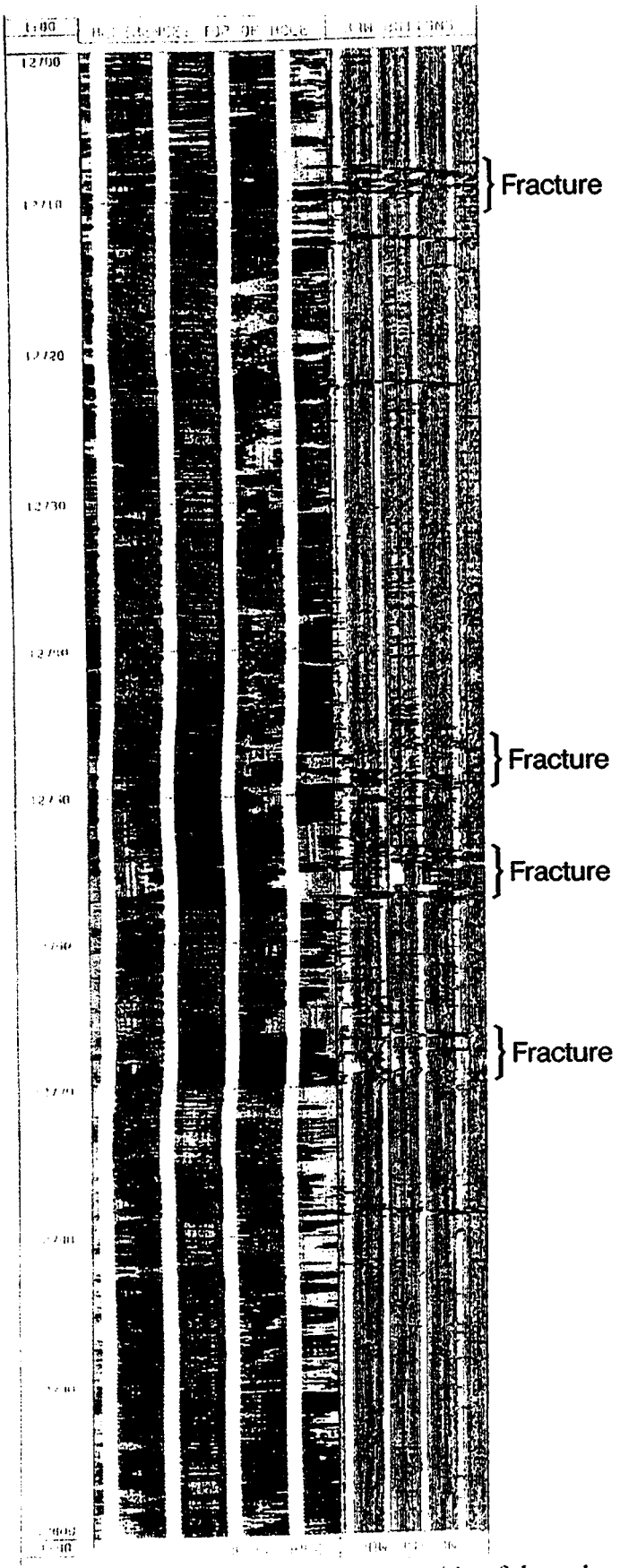

VII-10(b). FMS image of an interval with (b) low-grade fractures outside of the velocity anomaly.

ranges from 2.6 to 2.80 g/cm^3. The Watton Canyon above the fractured interval does not have a significant change in sonic velocity, but the lower boundary is an unfractured shale with a sonic velocity of 16,000-17,000 ft/s.

For most of the fractured interval in the Rich, sonic velocities range from 18,800 to 21,000 ft/s and bulk density ranges from 2.65 to 2.8 g/cm^3. The interval is bounded above by a shale with a sonic velocity of 16,000 ft/s and below by a shaly limestone with a velocity of approximately 18,000 ft/s. The fractured interval is relatively shale-free. The upper 15 feet of the fractured interval contains a significant percent of dolomite, which may explain, at least in part, the higher sonic velocities.

To map fracture zones in the Watton Canyon and the Rich Members, we recommend crosswell seismic measurements (Parra et al., 1997). This method is appropriate for mapping the small fracture zones that appear to be common in Lodgepole field.

D. Summary

Correlations between the cuttings description, the well logs, a synthetic seismogram, and the migrated 2D surface seismic data identified seismic events associated with geological units of interest. The surface seismic delineated the major geological boundaries between members of the Twin Creek Formation. The surface seismic section showed a reflection at about 1,640 ms (at the bottom of the Watton Canyon) that was interpreted as a boundary surface between the Watton Canyon Member and the Rich Member. In this case, the fracture zones (in the Watton Canyon and the Rich members) and the Boundary Ridge Member were interpreted to be part of this boundary surface. In addition, the petrographic and petrophysical analyses demonstrated that most fracturing occurs in dolomitic mudstone rocks and that an increase in dolomitization and a decrease in silt content correspond to an increase in fracturing. In addition, the high-velocity anomaly observed in the velocity inversion image correlates with a fracture zone in the Watton Canyon intercepted by the horizontal well. It suggests that high-velocity anomalies in the Watton Canyon may be associated with fracture zones. This can be confirmed by analyzing additional horizontal wells and their parallel seismic lines. In addition, we recommend crosswell seismic measurements to better delineate the high velocity anomalies associated with small fracture zones.

VIII. DISPERSION AND ATTENUATION OF ACOUSTIC WAVES IN RANDOMLY HETEROGENEOUS MEDIA: THEORY

A. Background

In this section we formulate the effective displacement relation that applies in a spatially random heterogeneous 1D medium. The relationship is expressed in terms of parameters σ_R and σ_A, which represent the standard deviations of the randomly varying medium density $\rho(x)$ and the randomly varying Young's modulus $\alpha(x)$, respectively. In this way, we build the contributions into the displacement relationship that arises from the spatially random heterogeneous medium. This analysis allows us to determine the attenuation and dispersion of acoustic waves propagating in a random heterogeneous medium.

B. Introduction

As geophysicists obtain increasingly accurate information about acoustic velocities, the dispersion, or frequency dependence of these velocities becomes more important. Dispersion is known to fall into two basic classes: intrinsic, which is based on anelasticity; and scattering, which is based on local, wavelength-scale variations in the rock formation. Intrinsic dispersion is a local property of the rock. Scattering dispersion is a property of a rock region and it includes the effects of reflections, refractions, and the law requiring displacement continuity.

Different approaches to scattering dispersion have been taken in the past. Backus (1962) derived the effective elastic constants of a layered medium in the long wavelength (low frequency) limit, and showed that this resulted in generally slower velocities than geometrical optics (high frequency limit) would imply. O'Doherty and Anstey (1971) showed that in a medium with many reflecting surfaces, multiply reflected waves tend to overtake the direct wave in amplitude. This results in an apparent decrease in velocity, as the multiples necessarily arrive later than the direct wave.

Here the effects of inhomogeneities in the medium are treated as a perturbation to the one-dimensional wave equation. The solution is obtained in the Fourier transformed coordinates, so heterogeneities of varying length scale may be included as a perturbation spectrum in the wave number domain. In contrast to an earlier work (Parra *et al.,* 1998), the present derivation is taken in an ensemble average sense, which facilitates the inclusion of second-order effects.

C. Theory

To develop a vector wave displacement solution associated with a heterogenous medium, we form a relation for the wave displacement in terms of second-order displacements, the variances and products of standards deviations of the rock physical properties. The second order terms are associated with the Gaussian random functions $R(x)$ and $A(x)$. The next step in the analysis is to insert the second-order solution in the 1D heterogeneous wave equation, which contains the randomly varying density $\rho(x)$ and randomly varying Young's modulus $\alpha(x)$. These functions are exponential forms of the zero-mean fluctuations $R'(x)$ and $A'(x)$, and standard deviations σ_R and σ_A.

The exponential forms of these physical properties are expressed in second-order Taylor expansion and substituted into the heterogeneous wave equation. Thus, the first part of the theory derives explicit expressions for the second-order forcing functions of the heterogeneous wave equation. The second part derives wave displacement in terms of the varying propagation vector and explicit expressions for the effective wave propagation vector. The last part of the analysis derives wave displacement using an alternate method to determine the effective wave propagation vector.

1. General Formulation

We write the displacement field u(x,t) as an expansion in standard deviation parameters σ_R and σ_A, dropping terms higher than second order in σ_R and σ_A. In Parra *et al.* (1998), equation (14) shows such an expansion, but where second-order terms are also dropped. Here we keep the second-order terms. Thus, Taylor expansion of $u(\sigma_R, \sigma_A)$ about $(\sigma_R, \sigma_A) = (0,0)$ gives:

$$u(\sigma_R, \sigma_A) = u_0 + u_1 + u_2 + 0(\sigma^3) \ , \tag{1}$$

where the zero, first, and second-order parts are:

$$\begin{aligned} u_0 &= u(0, 0) \\ u_1 &= u_R\sigma_R + u_A\sigma_A \\ u_2 &= u_{RR}\sigma_R^2 + u_{RA}\sigma_A\sigma_R + u_{AA}\sigma_A^2 \, . \end{aligned} \tag{2}$$

In Parra *et al.* (1998), the first-order solution has zero-mean (in the sense of ensemble mean):

$$\langle u_1 \rangle = 0 \, . \tag{3}$$

However, this is not true in general for the second-order solution; thus we must write *a-priori* the mean displacement as:

$$\begin{aligned} \langle u(x,t) \rangle &= u_0 + \langle u_2 \rangle + 0(\sigma^3) \\ &= u_0 + \langle u_{RR} \rangle \sigma_R^2 + \langle u_{RA} \rangle \sigma_R\sigma_A + \langle u_{AA} \rangle \sigma_A^2 + 0(\sigma^3) \, . \end{aligned} \tag{4}$$

To accomplish our objectives we introduce the heterogeneous wave equation

$$\rho(x)\frac{\partial^2 u}{\partial t^2} = \frac{\partial}{\partial x}\left(\alpha(x)\frac{\partial u}{\partial x} \right), \tag{5}$$

which in terms of the log-coefficients $\alpha(x)$ and $\rho(x)$ (see Parra *et al.* 1998) can be written as

$$\bar{\rho}_G \, e^{\sigma_R R'(x)} \frac{\partial^2 u}{\partial t^2} = \frac{\partial}{\partial x}\left(\bar{\alpha}_G e^{\sigma_A A'(x)} \frac{\partial u}{\partial x} \right). \tag{6a}$$

After expanding the exponential functions in equation (6a) using Taylor series expansion and including second-order terms such as

$$\begin{aligned} e^{\sigma_R R'(x)} &= 1 + \sigma_R R'(x) + \frac{\sigma_R^2}{2}(R'(x))^2, \\ \text{and} \quad e^{\sigma_A A'(x)} &= 1 + \sigma_A A'(x) + \frac{\sigma_A^2}{2}(A'(x))^2, \end{aligned} \tag{6b}$$

we insert equation (6b) into equation (6a) to obtain

$$\begin{aligned} &\left[1 + \sigma_R R'(x) + \frac{\sigma_R^2}{2}(R'(x))^2 \right] \frac{\partial^2 u}{\partial t^2} \\ &= V_0^2 \left\{ \frac{\partial^2 u}{\partial x^2} + \sigma_A \left(\frac{\partial A'}{\partial x}\frac{\partial u}{\partial x} + \frac{\partial^2 u}{\partial x^2} \right) + \sigma_A^2 \left[A' \frac{\partial A'}{\partial x}\frac{\partial u}{\partial x} + \frac{(A')^2}{2}\frac{\partial^2 u}{\partial x^2} \right] \right\}. \end{aligned} \tag{6c}$$

In equation (6c), V_o , $R'(x)$ and $A'(x)$ are given in Parra *et al.* (1998). These two functions are defined as normalized Gaussian random fields with zero means and unit variances.

Next, we are required to obtain explicit expressions for the second-order displacement. The perturbation expansion can be pushed further to obtain equations for the second order displacement terms, u_{RR}, u_{AA}, u_{RA} (respectively, σ_R^2, σ_A^2, $\sigma_R \sigma_A$). If we Fourier-transform with respect to time, and put equation (4) into equation (6c), we have for the second-order terms:

Order $(\sigma_R)^2$:

$$\begin{aligned} \left(\omega^2 + V_0^2 \frac{\partial^2}{\partial x^2} \right) u_{RR} &= f_{RR} \\ &= -\omega^2 \left(R' u_R + \frac{1}{2} R'^2 u_0 \right). \end{aligned} \tag{7}$$

Order $(\sigma_A)^2$:

$$\left(\omega^2 + V_0^2\frac{\partial^2}{\partial x^2}\right) u_{AA} = f_{AA}$$
$$= -V_0^2\left\{\frac{\partial}{\partial x}\left(A'\frac{\partial u_A}{\partial x} + \frac{1}{2}\frac{\partial}{\partial x}\right)\left((A')^2\frac{\partial u_0}{\partial x}\right)\right\} \tag{8}$$

Order $\sigma_R\,\sigma_A$:

$$\left(\omega^2 + V_0^2\frac{\partial^2}{\partial x^2}\right) u_{RA} = f_{RA}$$
$$= -\left\{\omega^2 R'u_A + V_0^2\frac{\partial}{\partial x}\left(A'\frac{\partial u_R}{\partial x}\right)\right\}. \tag{9}$$

Since we are only interested here in the ensemble means of u_{RR}, u_{AA}, u_{RA} we restrict ourselves to the mean equations obtained by applying ensemble mean operator to both sides of equations (7) - (9). Taking into account that R′ and A′ are normalized to unit variance:

$$\langle R'^2\rangle = \langle A'^2\rangle = 1$$

this yields, respectively:

$$\left(\omega^2 + V_0^2\frac{\partial^2}{\partial x^2}\right)\langle u_{RR}\rangle = \langle f_{RR}\rangle$$
$$= -\omega^2\left(\langle R'u_R\rangle + \frac{1}{2}u_0\right) \tag{10}$$

$$\left(\omega^2 + V_0^2\frac{\partial^2}{\partial x^2}\right)\langle u_{AA}\rangle = \langle f_{AA}\rangle$$
$$= -V_0^2\left\{\frac{\partial}{\partial x}\left\langle A'\frac{\partial u_A}{\partial x}\right\rangle + \frac{1}{2}\frac{\partial^2 u_0}{\partial x^2}\right\} \tag{11}$$

$$\left(\omega^2 + V_0^2 \frac{\partial^2}{\partial x^2} \right) \langle u_{RA} \rangle = \langle f_{RA} \rangle$$

$$= -\left\{ \omega^2 \langle R' u_A \rangle + V_0^2 \frac{\partial}{\partial x} \left\langle A' \frac{\partial u_R}{\partial x} \right\rangle \right\}. \tag{12}$$

We now recognize on the right-hand sides some terms that can be easily computed. Such terms are:

$$\langle R' u_R \rangle, \quad \langle R' u_A \rangle, \quad \left\langle A' \frac{\partial u_R}{\partial x} \right\rangle, \quad \text{and} \quad \left\langle A' \frac{\partial u_A}{\partial x} \right\rangle. \tag{13}$$

Since the derivations of the statistical average of these terms are similar in nature, we present the development of only two of the terms. The derivations of these terms are:

$$\langle R' u_R \rangle = \int\int e^{j(k'-k)x} \langle d\hat{U}_R(k') d\hat{R}^*(k) \rangle. \tag{13a}$$

Thus, using the expression of the stochastic solution in terms of random Fourier-Stieltjes increments shown in Parra *et al.* (1998), we can derive the statistical average of the product

$$\langle R' u_R \rangle = \int\int e^{j(k'-k)x} U_0(\omega) \frac{k_0^2}{k'^2 - k_0^2} \langle d\hat{R}(k' + k_0) d\hat{R}^*(k) \rangle,$$

$$= U_0(\omega) \int\int e^{j(k'-k)x} \frac{k_0^2}{k'^2 - k_0^2} S(k) \delta(k_0 + k' - k) dk\, dk',$$

$$= U_0(\omega) e^{-jk_0 x} \int_{-\infty}^{+\infty} \frac{k_0^2}{(k - k_0)^2 - k_0^2} S(k)\, dk, \tag{13b}$$

$$= \frac{1}{2} u_0(x,\omega) \int_{-\infty}^{+\infty} \frac{k_0^2}{k^2 - 2k_0 k} S(k) dk,$$

$$= \frac{1}{2} u_0(x,\omega) \int_{-\infty}^{+\infty} k_0 \left(\frac{1}{k - 2k_0} - \frac{1}{k} \right) S(k)\, dk,$$

In equation (13b) the odd integrand S(k)/k has been eliminated. Similarly, the statistical average of the product $R'u_A$ is given by

$$\langle R'u_A \rangle = \int\int e^{j(k'-k)x} \langle d\hat{U}_A(k') d\hat{R}^*(k) \rangle . \tag{14a}$$

Its derivation is as follows,

$$\begin{aligned}
\langle R'u_A \rangle &= U_0(\omega) \int\int e^{j(k'-k)x} \frac{k_0^2}{k'^2 - k_0^2} \frac{k'}{k_0} \langle d\hat{A}(k' + k_0) d\hat{R}^*(k) \rangle , \\
&= U_0(\omega) \int\int e^{j(k'-k)x} \frac{k_0^2}{k'^2 - k_0^2} \frac{k'}{k_0} \tilde{r} S(k) \delta(k_0 + k' - k) dk\, dk' , \\
&= \tilde{r}\, U_0(\omega) e^{-jk_0 x} \int_{-\infty}^{+\infty} \frac{k_0^2}{(k-k_0)^2 - k_0^2} \frac{k - k_0}{k_0} S(k)\, dk , \\
&= \frac{1}{2} \tilde{r} u_0(x,\omega) \int_{-\infty}^{+\infty} \left[\frac{k_0}{k - 2k_0} + \frac{k_0}{k} \right] S(k) dk ,
\end{aligned} \tag{14b}$$

or, again noting that the odd integrand pass is zero. Thus, the statistical average of the above product is reduced to

$$\langle R'u_A \rangle = \frac{1}{2} \tilde{r} u_0(x,\omega) \int_{-\infty}^{+\infty} \left[\frac{k_0}{k - 2k_0} \right] S(k) dk. \tag{14c}$$

In equation (14c), $\tilde{r}$ is the cross-correlation coefficient (i.e., $-1 \le \tilde{r} \le 1$) as introduced in Parra *et al.* (1998).

Collecting all results into equations (10)-(12) gives the following equations. These are written first for a general random medium with spectrum S(k). To obtain the equations It should be noted that we use the identities:

$$u_0(x,\omega) = U_0(\omega) e^{-jk_0 x}; \text{ for } (k_0 = \omega/V_0) , \tag{15a}$$

$$\frac{\partial u_0}{\partial x} = -jk_0 u_0 , \tag{15b}$$

$$\frac{\partial^2 u_0}{\partial x^2} = -k_0^2 u_0 . \tag{15c}$$

We also define, for a general random medium,

$$C(\omega) = \int_{-\infty}^{+\infty} \frac{k_0(\omega)}{k - 2k_0(\omega)} S(k)dk, \tag{16}$$

where $k_0(\omega)$ is a complex variable that includes the intrinsic attenuations, and S(k) is the spectral density.

Thus we can write the right-hand sides of equations (10) - (12) in terms of integral $C(\omega)$:

$$\langle f_{RR} \rangle = -\frac{1}{2}\omega^2(C + 1)u_0 , \tag{17}$$

$$\begin{aligned} \langle f_{AA} \rangle &= +\frac{1}{2}V_0^2(C + 1)\frac{\partial^2 u_0}{\partial x^2} , \\ &= -\frac{1}{2}\omega^2(C + 1)u_0 , \end{aligned} \tag{18}$$

and

$$\begin{aligned} \langle f_{RA} \rangle &= -\left\{\omega^2 \tilde{r} u_0 C/2 + V_0^2 \frac{\partial}{\partial x}(-\tilde{r}\varepsilon_0 C/2)\right\}, \\ &= -\left\{\omega^2 \tilde{r} u_0 \frac{C}{2} + \omega^2 \tilde{r} u_0 \frac{C}{2}\right\}, \\ &= -\omega^2 \tilde{r} C u_0 . \end{aligned} \tag{19}$$

Equations (17), (18) and (19) are relationships for the second-order forcing functions of the heterogeneous wave equation. These equations are used in Section VIII.C.2 to determine explicit expressions for the heterogeneous wave displacement and the effective wave propagation vector.

2. *The Displacement Wave in a Randomly Heterogeneous Medium*

Now we have all the ingredients to determine an expression of the average displacement in the frequency domain. The average coefficient of the displacement associated with a combination of the random material properties as indicated below

$$\langle u(x,\omega)\rangle = u_0(x,\omega) + \langle u_{RR}(x,\omega)\rangle \sigma_R^2 + \langle u_{RA}(x,\omega)\rangle \sigma_R \sigma_A + \langle u_{AA}(x,\omega)\rangle \sigma_A^2 + 0(\sigma^3)\,. \tag{20}$$

can be obtained by a solution of the wave equations that are formed by equations (10), (11), and (12). In this case we use the source functions given by equations (17), (18), and (19). Thus, these new equations are given by:

$$\left[\omega^2 + V_0^2 \frac{\partial^2}{\partial x^2}\right]\langle u_{RR}(x,\omega)\rangle = \langle f_{RR}(x,\omega)\rangle = -\frac{1}{2}\omega^2(C(\omega)+1)\,u_0(x,\omega), \tag{21a}$$

$$\left[\omega^2 + V_0^2 \frac{\partial^2}{\partial x^2}\right]\langle u_{AA}(x,\omega)\rangle = \langle f_{AA}(x,\omega)\rangle = -\frac{1}{2}\omega^2(C(\omega)+1)\,u_0(x,\omega), \tag{21b}$$

$$\left[\omega^2 + V_0^2 \frac{\partial^2}{\partial x^2}\right]\langle u_{RA}(x,\omega)\rangle = \langle f_{RA}(x,\omega)\rangle = -\omega^2 \tilde{r} C(\omega)\,u_0(x,\omega)\,. \tag{21c}$$

The most appropriate method to solve equations (21a), (21b), and (21c) is to decompose each term as a product of plane wave U_o times an amplitude, as:

$$\langle u_{RR}(x,\omega)\rangle = U_{RR}(x,\omega)u_0(x,\omega)\,, \tag{22a}$$

$$\langle u_{AA}(x,\omega)\rangle = U_{AA}(x,\omega)u_0(x,\omega)\,, \tag{22b}$$

$$\langle u_{RA}(x,\omega)\rangle = U_{RA}(x,\omega)u_0(x,\omega)\,. \tag{22c}$$

It follows from equation (21) that

$$V_0^2\left[\frac{\partial^2 U_{RR}}{\partial x^2} - 2j\frac{\omega}{V_0}\frac{\partial U_{RR}}{\partial x}\right] = -\frac{1}{2}\omega^2\big(C(\omega)+1\big), \tag{23a}$$

$$V_0^2\left[\frac{\partial^2 U_{AA}}{\partial x^2} - 2j\frac{\omega}{V_0}\frac{\partial U_{AA}}{\partial x}\right] = -\frac{1}{2}\omega^2\big(C(\omega)+1\big), \tag{23b}$$

$$V_0^2\left[\frac{\partial^2 U_{RA}}{\partial x^2} - 2j\frac{\omega}{V_0}\frac{\partial U_{RA}}{\partial x}\right] = -\omega^2\tilde{f}C(\omega). \tag{23c}$$

Let us define

$$F_1(\omega) = -\frac{1}{2}\omega^2(C(\omega)+1), \tag{24a}$$

$$F_2(\omega) = -\omega^2\tilde{f}C(\omega). \tag{25}$$

If we further define

$$E_{RR}(x,\omega) = \frac{\partial U_{RR}}{\partial x}, \tag{26a}$$

$$E_{AA}(x,\omega) = \frac{\partial U_{AA}}{\partial x}, \tag{26b}$$

$$E_{RA}(x,\omega) = \frac{\partial U_{RA}}{\partial x}. \tag{26c}$$

then it follows that equation (23) may be written as

$$V_0^2\left(\frac{\partial E_{RR}}{\partial x} - 2j\frac{\omega}{V_0}E_{RR}\right) = F_1(\omega) \tag{27a}$$

$$V_0^2\left(\frac{\partial E_{AA}}{\partial x} - 2j\frac{\omega}{V_0}E_{AA}\right) = F_1(\omega) \tag{27b}$$

$$V_0^2\left(\frac{\partial E_{RA}}{\partial x} - 2j\frac{\omega}{V_0}E_{RA}\right) = F_2(\omega). \tag{27c}$$

The solutions to these equations are found to be

$$U_{RR}(x,\omega) = U_0^{RR}(\omega) + U_1^{RR}(\omega)e^{2jk_0x} + \frac{jF_1(\omega)}{2\omega V_0}x, \tag{28a}$$

$$U_{AA}(x,\omega) = U_0^{AA}(\omega) + U_1^{AA}(\omega)e^{2jk_0x} + \frac{jF_1(\omega)}{2\omega V_0}x, \tag{28b}$$

$$U_{RA}(x,\omega) = U_0^{RA}(\omega) + U_1^{RR}(\omega)e^{2jk_0x} + \frac{jF_2(\omega)}{2\omega V_0}x. \tag{28c}$$

We set the term containing e^{2jk_0x} to zero, and require therefore that

$$U_1^{RR}(\omega) = U_1^{AA}(\omega) = U_1^{RA}(\omega) = 0. \tag{29}$$

We also choose that

$$U_0^{RR}(\omega) = U_0^{AA}(\omega) = \frac{F_1(\omega)}{2\omega^2}, \tag{30a,b}$$

$$\text{and} \quad U_0^{RA}(\omega) = \frac{F_2(\omega)}{2\omega^2}. \tag{30c}$$

This produces the solution

$$U_{RR}(x,\omega) = \frac{F_1(\omega)}{2\omega^2}\left[1 + j\frac{\omega}{V_0}x\right] = U_{AA}(x,\omega), \tag{31a,b}$$

$$U_{RA}(x,\omega) = \frac{F_2(\omega)}{2\omega^2}\left[1 + j\frac{\omega}{V_0}x\right], \tag{31c}$$

which is the same as

$$U_{RR}(x,\omega) = -\frac{1}{4}(C(\omega) + 1)\left[1 + jk_0x\right] = U_{AA}(x,\omega), \tag{32a,b}$$

$$U_{RA}(x,\omega) = -\frac{1}{2}\rho C(\omega)\left[1 + jk_0x\right]. \tag{32c}$$

Substituting into equations (22) and (20) gives

$$\langle u(x,\omega)\rangle = u_0(x,\omega) - \frac{1}{4}(C(\omega)+1)\left[1+jk_0x\right]\left(\sigma_R^2+\sigma_A^2\right)u_0(x,\omega)$$

$$-\frac{1}{2}\tilde{r}C(\omega)\left[1+jk_0x\right]\left(\sigma_R\sigma_A\right)u_0(x,\omega)$$

$$= u_0(x,\omega)\left\{1-\left[\frac{1}{4}(C(\omega)+1)\,(\sigma_R^2+\sigma_A^2)+\frac{1}{2}\tilde{r}C(\omega)\sigma_R\sigma_A\right]\right.$$

$$\left.-jk_0x\left\{1-\left[\frac{1}{4}(C(\omega)+1)\,(\sigma_R^2+\sigma_A^2)+\frac{1}{2}\tilde{r}C(\omega)\sigma_R\sigma_A\right]\right\}\right\} \tag{33}$$

The solution expressed by equation (33) is unphysical in this form, in the sense that it contains "secular" terms proportional to x. However, recognizing that the terms $O(\sigma_R^2)$, $O(\sigma_A^2)$, and $O(\sigma_R\sigma_A)$ were all obtained by perturbation (Taylor expansion), we may in turn regard equation (33) as a Taylor expansion. The more natural such expansion would be that of an exponential. Similar reasonings were made by Landau *et al.* (1984) to improve the estimate of the effective dielectric constant of mixture. This procedure may be called the "Landau extrapolation" or more specifically in the present case, the "exponential extrapolation." Thus, using the exponential extrapolation technique, we have

$$\langle u(x,\omega)\rangle = u_0 e^{-jk_0x}\left\{e^{-d(\omega)(1+jk_0x)}\right\}, \tag{34}$$

where

$$d(\omega) = \frac{1}{4}(C(\omega)+1)\,(\sigma_R^2+\sigma_A^2)+\frac{1}{2}\tilde{r}C(\omega)\,\sigma_R\sigma_A\,. \tag{35}$$

We recognize that the integral $C(\omega)$ given by equation (16) has real and imaginary parts,

$$C_R(\omega) = \mathrm{Re}\{C(\omega)\} = P\int_{-\infty}^{\infty}\frac{k_0(\omega)}{k-2k_0(\omega)}S(k)dk\,, \tag{36a}$$

$$C_I(\omega) = \mathrm{Im}\{C(\omega)\} = -\pi k_0(\omega)S(2k_0(\omega))\,. \tag{36b}$$

It follows that

$$d_R(\omega) = \frac{1}{4}\left(C_R(\omega) + 1\right)(\sigma_R^2 + \sigma_A^2) + \frac{1}{2}\tilde{r}C_R(\omega)\sigma_R\sigma_A\,, \tag{37a}$$

$$d_I(\omega) = \frac{1}{4}\left(C_I(\omega)\right)(\sigma_R^2 + \sigma_A^2) + \frac{1}{2}\tilde{r}C_I(\omega)\sigma_R\sigma_A\,. \tag{37b}$$

and equation (34) is written as

$$\langle u_0(x,\omega)\rangle = \left\{u_0 e^{-d(\omega)}\right\} e^{-jk_0x(1+d(\omega))}\,, \tag{38a}$$

or

$$\langle u_0(x,\omega)\rangle = \left\{u_0(\omega) e^{-d(\omega)}\right\} e^{-jk_0x(1+d_R(\omega)+jd_I(\omega))}\,, \tag{38b}$$

or

$$\langle u_0(x,\omega)\rangle = \left\{u_0(\omega) e^{-d(\omega)}\right\} e^{+d_I(\omega)k_0x}\, e^{-jk_0x(1+d_R(\omega))}\,. \tag{39}$$

In equation (39) we noted that $d_I(\omega)$ is negative because $C_I(\omega) < 0$. It follows that the attenuation coefficient of the displacement wave is

$$\eta_d = k_0 |d_I(\omega)| = \frac{k_0^2\pi}{4} S(2k_0(\omega))\left[(\sigma_R^2 + \sigma_A^2) + 2\tilde{r}\sigma_R\sigma_A\right]. \tag{40}$$

This form for the attenuation coefficient is quite similar to that derived by Shapiro *et al.* (1994) and Shapiro and Zien (1993), who also report attenuation proportional to k^2 S(2k). The exact form of the other results must vary because of different notation and assumptions in the two approaches.

The real part of the effective wave vector for the displacement wave is

$$\mathrm{Re}\left[K_d\right] = k_0(1 + d_R(\omega))\,, \tag{41}$$

which after substituting equation (37) is

$$\mathrm{Re}\left[K_d\right] = k_0\left\{1 + \frac{1}{4}(1 + C_R(\omega))(\sigma_R^2 + \sigma_A^2) + \frac{1}{2}\tilde{r}C_R(\omega)\sigma_R\sigma_A\right\}. \tag{42}$$

Thus, the effective wave number is shown to change in a frequency dependent manner by an amount proportional to σ^2. The effective velocity for a given frequency must correspondingly change by a proportional amount. It is known (Aki and Richards, 1980) that the Hilbert transform of the attenuation must yield the frequency times the slowness dispersion. Inspection of equations (36a) and (36b) shows that C_R is the Hilbert transform of C_I, and thus the dispersion behavior inherent in equation (42) is the causal complement to the attenuation behavior of equation (40).

3. *Alternate Method of Solution for the Effective Wave Vector*

An alternate method of solution is as follows. By combining equations (21), an expression is found for the expected value of the perturbed wave:

$$\left[\omega^2+V_o^2\frac{\partial^2}{\partial x^2}\right]\left\langle u(x,\omega)\right\rangle = \sigma_R^2\left\langle f_{RR}(x,\omega)\right\rangle + \sigma_A^2\left\langle f_{AA}(x,\omega)\right\rangle + \sigma_R\sigma_A\left\langle f_{RA}(x,\omega)\right\rangle. \tag{43}$$

Recall from equation (21) that the various $\langle f(x,\omega)\rangle$ include a factor of $u_o(x,\omega)$. Accordingly, g_{RR}, g_{AA}, and g_{RA} are defined such that

$$g_{ij}u_o = \sigma_i\sigma_j\langle f_{ij}\rangle, \tag{44}$$

where ij can take on the values of RR, AA, or RA. Then, since

$$\langle u\rangle = u_o + O(\sigma^2), \tag{45}$$

it must be true that

$$\sigma^2 u_o = \sigma^2\langle u\rangle + O(\sigma^4). \tag{46}$$

Thus, all instances of $u_o(x,\omega)$ in equation (21) may be replaced with instances of $\langle u(x,\omega)\rangle$ without affecting the $O(\sigma^2)$ accuracy of equation (43). This allows all terms to be placed inside the square brackets, as

$$\left[\omega^2+V_o^2\frac{\partial^2}{\partial x^2} - g_{RR} - g_{AA} - g_{RA}\right]\left\langle u(x,\omega)\right\rangle = 0. \tag{47a}$$

Or, taking the Fourier transform with respect to x as well,

$$\left[\omega^2 - V_o^2 k^2 - g_{RR} - g_{AA} - g_{RA}\right]\langle u(k,\omega)\rangle = 0. \tag{47b}$$

Expanding the g terms,

$$\left[\omega^2 - V_o^2 k^2 + \frac{1}{2}\omega^2\left(\sigma_R^2 + \sigma_A^2\right)\left(C(\omega)+1\right) + \omega^2\sigma_R\sigma_A\tilde{r}C(\omega)\right]\langle u(k,\omega)\rangle = 0. \tag{47c}$$

Like the standard wave equation, this equation has a solution of the form exp(-jkx), but the velocity is no longer V_0. The new phase velocity $V = \omega/k$ may be found by requiring that the term in square brackets equal zero. This results in a perturbed velocity given by

$$\left(\frac{\omega}{k}\right)^2 = \frac{V_0^2}{1 + \frac{1}{2}\left(\sigma_R^2+\sigma_A^2\right)\left(C(\omega)+1\right) + \sigma_R\sigma_A\tilde{r}C(\omega)}. \tag{48}$$

It is convenient to express this in an alternate form, equivalent to that above with order σ^2:

$$\frac{\omega}{k} = V_0\left[1 - \frac{1}{4}\left(\sigma_R^2+\sigma_A^2\right)\left(C(\omega)+1\right) - \frac{1}{2}\sigma_R\sigma_A\tilde{r}C(\omega)\right].$$

As previously noted, $C(\omega)$ is complex [equation (36)]. This results in a complex wave number, which may be interpreted [with the notation of equation (37)] as yielding a velocity of $V = V_0[1 - d_R]$ and an attenuation of $\eta_d = k_0|d_I|$.

The effective wave propagation vector is used to produce practical expressions for the attenuation and phase velocity for predicting scattering and intrinsic effects. These expressions are applied to calculate attenuation and phase velocity for different correlation lengths and standard deviations of material properties. Also, the solution is applied to interpret phase velocity curves obtained from interwell acoustic waveforms recorded at the Buckhorn test site, Illinois. In addition, an example is presented to describe the effect on the phase velocity of a heterogeneity within the reservoir.

D. Summary

In this section, a method for deriving a second-order accurate perturbation solution to the ensemble-averaged inhomogeneous wave equation was presented. Results of this solution have been shown to exhibit both dispersion and attenuation in a manner consistent with other work.

In particular, an analytical solution of the wave propagation vector was obtained. This relation was produced in terms of standard deviations of the density and Young's modulus, respectively, as well as the cross-correlation coefficient and an integral that includes the spectral density and a kernel function. The present solution has been applied to predict attenuation and dispersion curves for synthetics and real examples. These applications are presented in Section X.

Finally, a solution of the displacement and wave propagation vector can be extended to model 2D heterogeneities by including the compressional and shear wave velocities of the medium.

IX. DISPERSION AND ATTENUATION OF ACOUSTIC WAVES IN RANDOMLY HETEROGENEOUS MEDIA: APPLICATIONS

A. Background

Attenuation and dispersion of waves propagating in media with randomly varying properties has been the subject of much study. Most of this work has neglected the effects of intrinsic dispersion and attenuation to concentrate on the effects of the medium inhomogeneities. We demonstrate how intrinsic attenuation may easily be included in a recent theoretical development, and we explore the combined effects of scattering-based and intrinsic attenuation and dispersion on wave propagation. We apply the solution to model interwell acoustic waves propagating in the Kankakee formation at the Buckhorn test site, Illinois. The modeling results show that a strong dispersion in the frequency range of 500-2,000 Hz is due to the reservoir heterogeneity. Alternatively, the velocity dispersion for frequencies greater than 2,000 Hz corresponds to the intrinsic properties of the reservoir.

B. Introduction

This work is based on Parra *et al.* (1998b), which is an extension of Parra *et al.* (1998a). This is an ensemble averaged, perturbation based, second-order theory of one-dimensional wave propagation in randomly varying media. It is readily shown that this particular theory gives results consistent with those of many others, including Backus (1962), O'Doherty and Anstey (1971), and Shapiro *et al.* (1994).

The key results are outlined here. The wave field for a plane wave passing through the stochastic region is given by

$$\left\langle u(x,\omega)\right\rangle = u_0(\omega)e^{-jk_o x}e^{-jd(\omega)k_o x} \tag{1}$$

where k_o is the unperturbed wave number, ω/V_o, and d has real and imaginary parts given by

$$d_R(\omega) = \frac{1}{4}\left(1 + C_R(\omega)\right)\left(\sigma_R^2 + \sigma_A^2\right) + \frac{1}{2}C_R(\omega)\sigma_R\sigma_A,$$

$$\text{and } d_I(\omega) = \frac{1}{4}C_I(\omega)\left(\sigma_R^2 + \sigma_A^2\right) + \frac{1}{2}\tilde{r}C_I(\omega)\sigma_R\sigma_A. \tag{2}$$

In equation (2), σ_R and σ_A are the nondimensionalized standard deviations of the density and stiffness distributions, and $C_R(\omega)$ and $C_I(\omega)$ are the real and imaginary parts of the integral

$$C(\omega) = \int_{-\infty}^{\infty} \frac{k_0}{k - 2k_0} S(k)dk. \tag{3}$$

The function S(k) is the spectral density of perturbations in the density and stiffness.

C. Theory

1. Addition of Intrinsic Attenuation

One of the main conceptual difficulties in the theory development is the solution of the $C(\omega)$ integral in equation (3). While the principal value formulation seems to provide useful results, having a complex integral $C(\omega)$ creates difficulties in understanding the basic concept of attenuation. In this section, we show that the inclusion of intrinsic (an elastic, or non-scattering-based) attenuation to the problem resolves this difficulty.

Intrinsic attenuation may be added to the wave equation by considering that k_o is complex. That is,

$$k_0 = k_R - jk_I, \tag{4}$$

where $k_R = \omega/V_o$ and $k_I = \omega/(2V_oQ)$ are real numbers. The intrinsic attenuation Q is allowed to vary with frequency, but must be positive. Given this definition, equation (3) may be rewritten as

$$C(\omega) = \int_{-\infty}^{\infty} \frac{k_R - jk_I}{k - 2(k_R - jk_I)} S(k)dk. \tag{5}$$

This form is separable into real and imaginary parts of $C(\omega)$:

$$\begin{aligned} C_R(\omega) &= \int_{-\infty}^{\infty} \frac{k_R\left(k - 2k_R\right) - 2k_I^2}{\left(k - 2k_R\right)^2 + 4k_I^2} S(k)dk, \\ \text{and } C_I(\omega) &= -\int_{-\infty}^{\infty} \frac{kk_I}{\left(k - 2k_R\right)^2 + 4k_I^2} S(k)dk. \end{aligned} \tag{6}$$

These two integrals have finite, real integrands and are readily integrable on a computer for reasonable choices of S(k). An analytical solution for a particular choice of S(k) is presented later. It is possible to show that for even, well-behaved functions S(k),

$$C_R(\omega \to 0) = C_I(\omega \to 0) = 0\,,$$
$$C_R(\omega \to \infty) = -1/2\,, \tag{7}$$
$$C_I(\omega \to \infty) = 0\,.$$

Furthermore, it may be shown that for $\omega > 0$, $C_I(\omega) < 0$.

Equations (1) and (2) represent the original displacement wave solution given in Parra *et al.* (1998a). Substituting in the real and imaginary parts of k_o yields a new equation in terms of k_R k_I

$$\langle u(x,\omega)\rangle = u_o e^{-j(k_R + d_R k_R + d_I k_I)x_e - (k_I + d_R k_I - d_I k_R)x}\,. \tag{8}$$

Recall that k_R and k_I are both defined to be positive numbers, and d_I is negative because C_I is negative. From this equation, it is apparent that the effective wave number is given in the first exponential, while the effective attenuation is given in the second exponential. The total dispersion then has the form

$$V_{eff}(\omega) = \frac{V_0(\omega)}{1 + d_R(\omega) + d_I(\omega)/2Q(\omega)}, \tag{9}$$

where $V_o(\omega)$ includes the effects of intrinsic dispersion due to $Q(\omega)$. At the same time, the total attenuation is given by

$$Q_{eff}(\omega) = \frac{1}{2}\frac{2Q(\omega)\left(1 + d_R(\omega)\right) + d_I(\omega)}{\left(1 + d_R(\omega)\right) - 2Q(\omega)d_I(\omega)}, \tag{10}$$

where again $Q(\omega)$ represents the effects of intrinsic dispersion only. In the limiting case where intrinsic dispersion is negligible (i.e., $Q \to \infty$), the effective properties reduce to

$$V_{eff}(\omega) = V_o\left(1 - d_R(\omega)\right),$$
$$Q_{eff}(\omega) = \frac{1 + d_R(\omega)}{2\left|d_I(\omega)\right|}, \tag{11}$$

in the limit of second-order accuracy, and recalling that $d_I < 0$.

2. *Influence of Second-Order Average Properties and Limiting Behavior*

The exponential form for the density and stiffness fluctuations is a convenient, compact, and positive definite form for the medium properties. It is worth noting, however, that the mean density and stiffness are not ρ_o and α_o, but are affected by the exponential skew in the fluctuation distribution. Since the density and stiffness have the same functional form, only the density will be examined. The actual mean density is given by

$$\langle \rho \rangle = \rho_o \int_{-\infty}^{\infty} P(R') e^{\sigma_R R'} dR', \tag{12}$$

where P(R') is the probability density of a zero mean, unit variance, Gaussian variable. Expanding equation (12), we obtain

$$\langle \rho \rangle = \rho_o \int_{-\infty}^{\infty} \frac{1}{\sqrt{2\pi}} e^{-R'^2/2} e^{\sigma_R R'} dR'. \tag{13}$$

To evaluate this integral we employ the method of completing the square, and make the substitution $z = R' - \sigma_R$. Now,

$$\langle \rho \rangle = \rho_o e^{\sigma_R^2/2} \int_{-\infty}^{\infty} \frac{1}{\sqrt{2\pi}} e^{-z^2/2} dz. \tag{14}$$

The integrand is now simply P(z), and the integral of any probability density function over its entire range must be unity. Thus, the mean density, and by similar reasoning the mean stiffness, are

$$\begin{aligned} \langle \rho \rangle &= \rho_o e^{\sigma_R^2/2}, \\ \langle \alpha \rangle &= \alpha_o e^{\sigma_A^2/2}. \end{aligned} \tag{15}$$

It is known that in an inhomogeneous medium, the high frequency (or ray theoretical) slowness is equal to the mean slowness. That is,

$$V_{RT}^{-1} = \langle V^{-1} \rangle = \left\langle \frac{\rho^{1/2}}{\alpha^{1/2}} \right\rangle. \tag{16}$$

This may also be evaluated analytically given the assumed exponential property distributions. Using the joint probability distribution function for a bivariate Gaussian distribution (Kalbfleisch, 1985) with covariance $\tilde{r}$ $(\tilde{r}^2 < 1)$,

$$V_{RT}^{-1} = \frac{\rho_0^{1/2}}{\alpha_0^{1/2}} \int_{-\infty}^{\infty}\int_{-\infty}^{\infty} \frac{1}{2\pi}\frac{1}{\sqrt{1-\tilde{r}^2}} \exp\left(-\frac{1}{2(1-\tilde{r}^2)}\left[R'^2 + A'^2 + 2\tilde{r}R'A'\right]\right) \exp\left(\frac{1}{2}\left(\sigma_R R' - \sigma_A A'\right)\right) dR'dA'. \tag{17}$$

Holding A′ constant in equation (17) for the moment, we make the substitution

$$z = \frac{R'}{\sqrt{1-\tilde{r}^2}} + \sqrt{1-\tilde{r}^2}\left(\frac{\tilde{r}A'}{1-\tilde{r}^2} - \frac{1}{2}\sigma_R\right), \tag{18}$$

to yield

$$V_{RT}^{-1} = V_o^{-1} \int_{-\infty}^{\infty}\int_{-\infty}^{\infty} \frac{1}{2\pi} \exp\left(-\frac{A'^2}{2(1-\tilde{r}^2)} - \frac{\sigma_A A'}{2}\right) \exp\left(-\frac{z^2}{2}\right) \exp\left(\frac{1}{2}(1-\tilde{r}^2)\left(\frac{\tilde{r}A'}{1-\tilde{r}^2} - \frac{\sigma_R}{2}\right)^2\right) dz dA'. \tag{19}$$

The integral in z is now straightforward. The integral in A′ may be evaluated by making the substitution

$$y = A' + \frac{1}{2}\left(\sigma_A + \tilde{r}\sigma_R\right). \tag{20}$$

After some algebra, the remaining expression simplifies to

$$V_{RT}^{-1} = V_0^{-1} \exp\left(\frac{1}{8}\sigma_R^2 + \frac{1}{8}\sigma_A^2 + \frac{1}{4}\sigma_R\sigma_A\right) \int_{-\infty}^{\infty}\int_{-\infty}^{\infty} \frac{1}{2\pi} \exp\left(-\frac{1}{2}z^2 - \frac{1}{2}y^2\right) dy dz \,. \tag{21}$$

The double integral evaluates to unity. By taking a series expansion (to second order) of the remaining exponential, we find

$$V_{RT}^{-1} = V_0^{-1}\left(1 + \frac{1}{8}\sigma_R^2 + \frac{1}{8}\sigma_A^2 + \frac{1}{4}\tilde{r}\sigma_R\sigma_A\right). \tag{22}$$

This is in exact correspondence with the perturbation theory development, given that in the high frequency limit $C_R(\omega) = -\frac{1}{2}$ and $C_I(\omega) = 0$.

The low frequency (effective medium theory) limiting velocity for a statistically stationary medium was determined by Backus (1962). For the one-dimensional case considered here, it is given simply by

$$V_{EMT}^{-2} = \langle \rho \rangle \left\langle \frac{1}{\alpha} \right\rangle . \tag{23}$$

The expression for the mean value of ρ is given above and the mean value of $1/\alpha$ may be calculated similarly. Then,

$$V_{EMT}^{-1} = V_o^{-1} e^{\sigma_R^2/4} e^{\sigma_A^2/4}, \tag{24}$$

which is equivalent with second-order accuracy to

$$V_{EMT}^{-1} = V_o^{-1} \left(1 + \frac{\sigma_R^2}{4} + \frac{\sigma_A^2}{4} \right) . \tag{25}$$

This is itself equivalent to the perturbation theory prediction in the low frequency limit of $C_R(\omega) = C_I(\omega) = 0$. Thus, we have shown that in the limiting cases of high frequency and low frequency, the perturbation theory of wave propagation produces the correct dispersive velocities.

3. *Influence of the Spectral Density and Relations with Other Random Medium Theories*

The intermediate frequency results of the perturbation theory depend on an integral over the spectral density, and so are intimately tied to the functional form of S(k). Accordingly, it is worth examining the physical meaning of the spectral density, as well as geologically appropriate forms of S(k). Furthermore, the spectral density (or a similar function) has been employed in previous work on wave propagation through random media, and comparisons between the perturbation theory results and results in the literature can be made.

First, the autocorrelation function for R′ and A′ will be defined as

$$\chi(a) = \langle R'(x) R'(x+a) \rangle = \langle A'(x) A'(x+a) \rangle . \tag{26}$$

Recall that R′ and A′ are defined as zero mean random variates with identical spatial statistics. The requirement for statistical stationarity ensures that χ is not a function of x and only depends on the absolute value of *a*. It is not difficult to show that the spectral density, S(k), is the Fourier transform of the autocorrelation function. This leads to two immediate restrictions on S(k). First, since $\chi(a)$

is an even, real valued function, S(k) must be an even, real valued function. Secondly, at k=0, S is given by

$$S(k=0) = \int_{-\infty}^{\infty} \chi(a)da, \tag{27}$$

which implies that S(k=0) is positive and a maximum of S(k) for most reasonable correlation functions χ.

The most common and most reasonable choice of correlation function is the exponential

$$\chi(a) = e^{-a/\ell}. \tag{28}$$

This form has both experimental justification (based on examination of velocity logs, Velzeboer, 1981; White *et al.* 1990) and theoretical justification (considering cyclical sedimentary transition as a Markov process, Velzeboer, 1981; Kerner, 1992). For this choice of correlation function, the spectral density has the simple form

$$S(k) = \frac{\ell}{\pi} \frac{1}{1+k^2\ell^2}. \tag{29}$$

This is particularly convenient for two reasons. First, this form leads to a straightforward analytic solution of the C(ω) integral (equation 3). Secondly, it leads to good correspondence with results from other techniques.

A brief solution to the C(ω) integral using the technique of contour integration is given here. The equation to solve is

$$C(\omega) = \frac{1}{\pi} \int_{-\infty}^{\infty} \frac{k_o}{z-2k_o} \frac{1}{1+z^2\ell^2} dz\ell, \tag{30}$$

with k_o complex and the integration to take place along the real axis. This integrand has three poles at $z = 2k_o$, and $z = \pm j/\ell$. It may be seen by inspection that the integrand goes to zero as z goes to infinity regardless of the phase. Therefore, we may close the integration path in either the positive or negative j directions. The same result is obtained in either case, but since there is only one pole above the real axis (see equation 4), we will close it in that direction. The result of the integral is then quite simply $2\pi j$ times the residue of the pole, or

$$C(\omega) = 2\pi j \frac{1}{\pi}\left(\frac{k_o}{\frac{j}{\ell} - 2k_o}\frac{1}{2j}\right). \tag{31}$$

Simplifying,

$$C(\omega) = -\frac{k_o \ell(2k_o\ell + j)}{4k_o^2\ell^2 + 1}. \tag{32}$$

In the limit of no intrinsic attenuation ($k_I \ll k_R$), we can write this in terms of the spectral density,

$$\begin{aligned} C_R(\omega) &= -2\pi k_R^2 \ell S(2k_R), \\ C_I(\omega) &= -\pi k_R S(2k_R). \end{aligned} \tag{33}$$

Expressions for velocity and attenuation in the limit of no intrinsic attenuation may be obtained by substituting equations (29) and (33) into equations (2) and (11). Now, since we have a solution valid in the limit of no intrinsic attenuation, it should be examined in comparison to other solutions. For this purpose note that the attenuation coefficient $\eta = k / 2Q$ is proportional to $k\, C_I$. The exact constants of proportionality are dependent on the definitions made in the derivation, and so will not compare exactly with other work.

O'Doherty and Anstey (1971) state that the attenuation coefficient η is equal to the power spectrum of the autocorrelation function. In other words, $\eta \sim k^2 S(k)$. Shapiro *et al.* (1994) put this on a more mathematical footing, deriving an expression for η which is proportional to $k^2\, S(2k)$. This result has the identical functional form to that derived here. Furthermore, Shapiro and Zien (1993) combined this with the localization results of White et al. (1990), showing that η behaves as $\omega^2/(c_1\omega^2 + c_2)$. This implies that S(k) has the form $1/(c_1 + c_2k^2)$, which is the same as that desired.

D. Results

1. Numerical Modeling

The following sample results will be based on a case with the following arbitrary parameters: $\sigma_R = 0.15$, $\sigma_A = 0.15$, $\tilde{r} = 0.3$, and characteristic length scale ℓ. Changes in σ and $\tilde{r}$ generally only result in changes in magnitude rather than fundamental changes in the results. The exponential autocorrelation function is chosen, and wavenumbers (or frequencies) are nondimensionalized by the correlation length to preserve generality. Since the correlation length only appears in the solution as a product of the wave number, the effect of changing the correlation length is only to move features to higher or lower frequencies. Figure IX-1 shows the scattering part of dispersion and attenuation (as Q^{-1}) for the basic case with a constant intrinsic Q of 80. The lower part

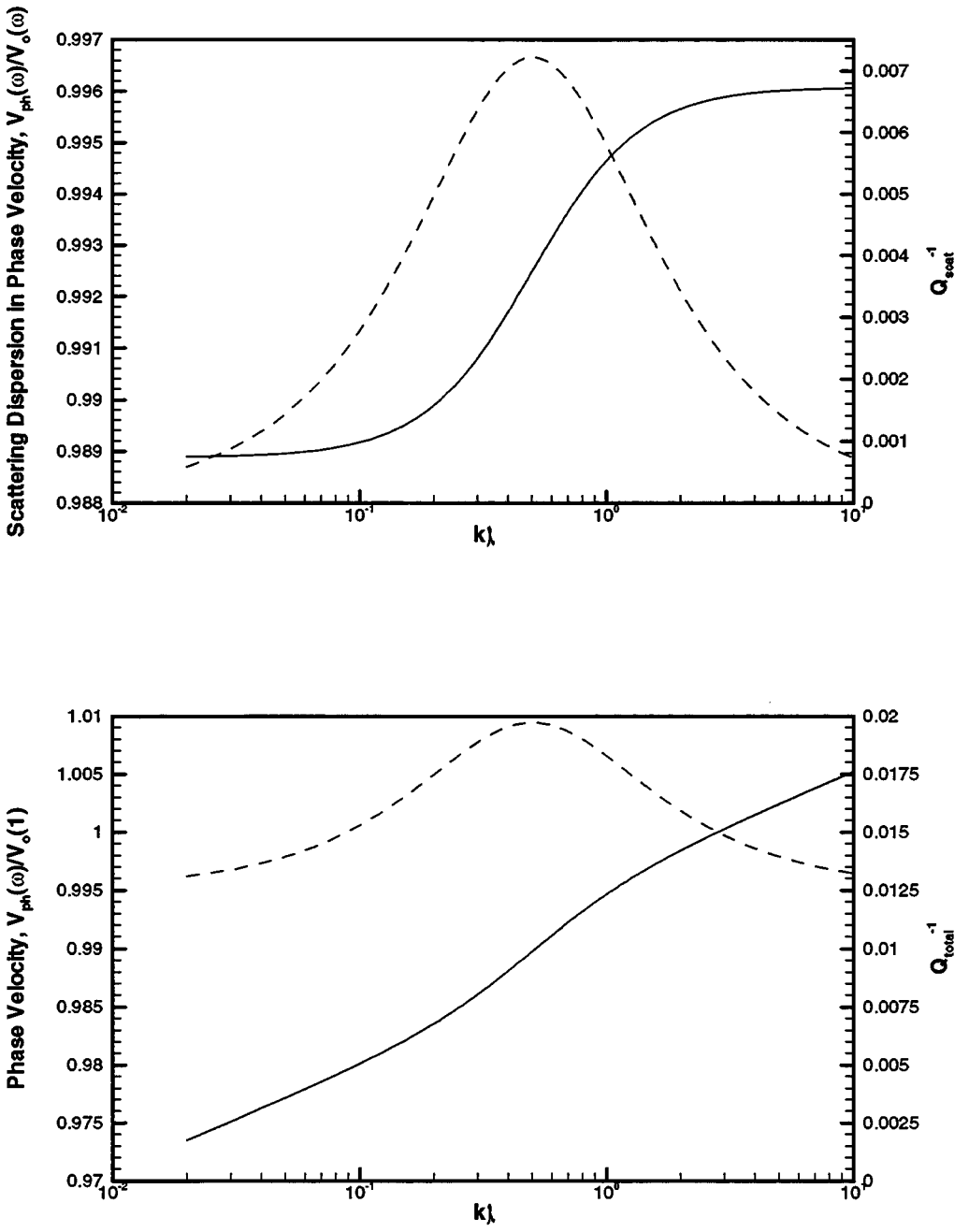

Figure IX-1: Top: Part of dispersion (solid line) and attenuation (dashed line) due only to scattering for a case with intrinsic attenuation corresponding to $Q(\omega) = 80$. Bottom: Total dispersion and attenuation due to both scattering and intrinsic effects. The scattering part of dispersion and attenuation appears superimposed on the uniform (linear) background.

of the figure shows the combined effects of both scattering and intrinsic dispersion and attenuation for this same case.

More interesting results come about when a frequency-dependent intrinsic Q is introduced. This can be the result of a relaxation-type phenomenon as outlined in Aki and Richards (1980) or the Biot or squirt-flow mechanism (Parra, 1997). The mechanism introduced here will be of the general relaxation type. In this mechanism, the intrinsic Q is given by

$$\frac{1}{Q} = \frac{\omega\left(\tau_\varepsilon - \tau_\sigma\right)}{1 + \omega^2 \tau_\varepsilon \tau_\sigma}, \tag{34}$$

where τ_ε and τ_σ are characteristic relaxation time constants of the medium. Attenuation is at a maximum for $\omega = (\tau_\varepsilon\, \tau_\sigma)^{-½}$.

For a hypothetical medium with the base parameters above and a single attenuation peak of Q = 80 centered on $k\ell = 10$, the scattering-based dispersion and attenuation is shown in Figure IX-2. With the intrinsic part included, both components clearly show up independently in the combined dispersion and attenuation plot. As the correlation length varies, the center frequency of the scattering attenuation peak ($\omega = V/\ell$) will change with respect to the center frequency of the intrinsic attenuation peak. Thus, at times the scattering attenuation and dispersion may overlap the intrinsic attenuation and dispersion. At other times they may be sufficiently separable that an analyst can determine the type and magnitude of the underlying attenuation mechanism.

2. *Intrinsic and Scattering Dispersion of Seismic Waves in the Kankakee Oil Reservoir*

To illustrate the applicability of the present solution, we use crosswell seismic data recorded in the Kankakee Limestone Formation at the Buckhorn Test Site, Illinois. A heterogeneity that corresponds to the oil reservoir in the Kankakee Limestone Formation was detected using travel-time tomography by Saito (1991). The same heterogeneity was analyzed using well logs and dispersion and attenuation data by Parra (1995). Furthermore, the phase velocity data was modeled using the Biot and squirt-flow mechanisms by Parra (1998) to predict the azimuthal permeability anisotropy. Although this model study predicted the fracture orientation in the formation, it did not explain the presence of a heterogeneity in the experimental phase velocity curve associated with the reservoir.

We attempt to explain the effect of the heterogeneity using the present solution. In fact, we have obtained a reasonable fit to the experimental dispersion curve that was derived by Parra (1995) using the spectral ratio method. Figure IX-3 shows the phase velocity data with theoretical model responses produced using a constant Q intrinsic model with Q = 20. The scattering response was obtained using a correlation length of about 0.5 m. I t is important to note that while the model qualitatively has a good fit to the experimental data, many factors not present in the model do affect the field result. These include other sources of intrinsic dispersion such as squirt flow or spatially variable Q, as well as multidimensional effects. In addition, in the

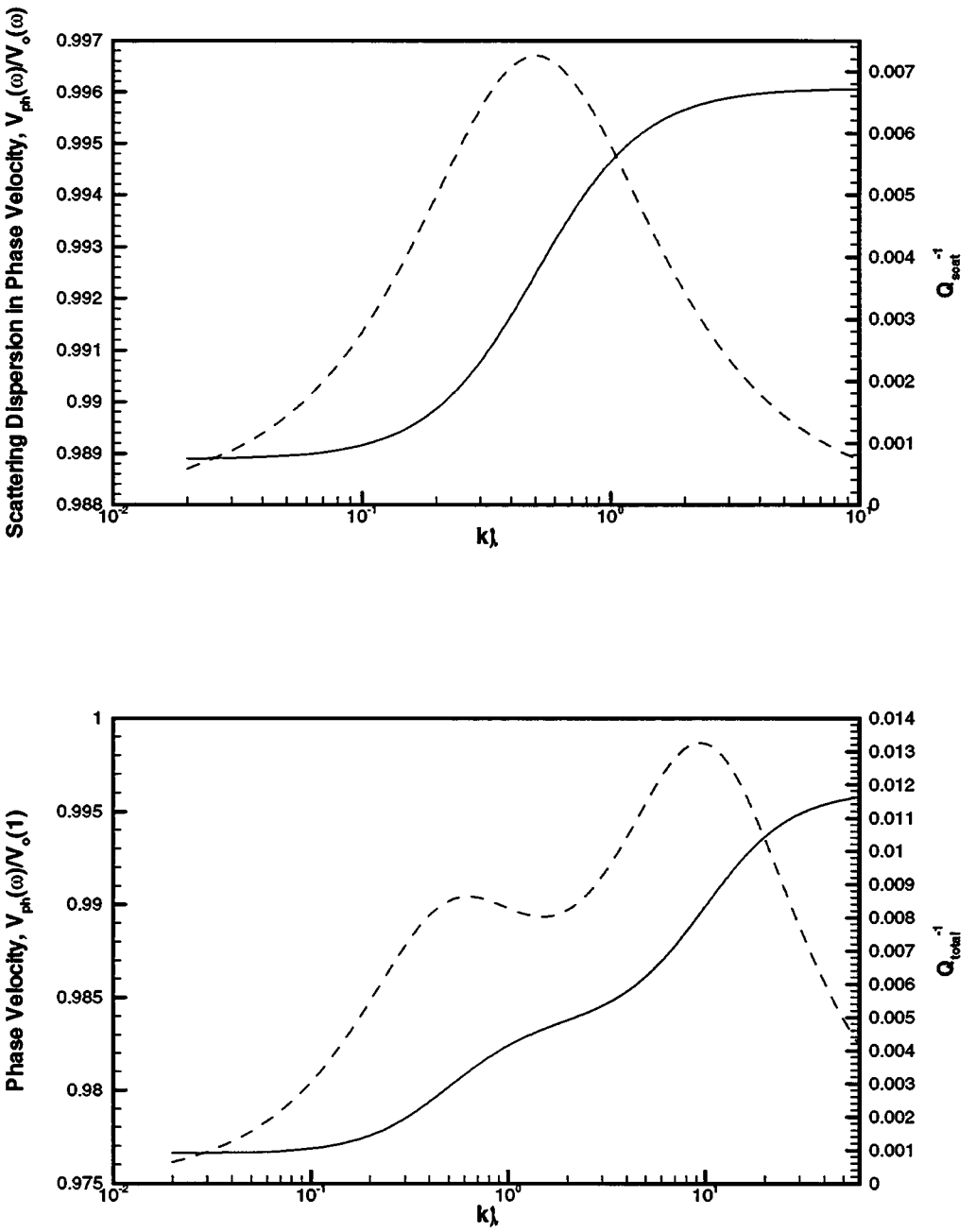

Figure IX-2: Top: Part of dispersion (solid line) and attenuation (dashed line) due only to scattering for a case with intrinsic attenuation only from a relaxation mechanism centered on $k\ell = 10$. Bottom: Total dispersion and attenuation due to both scattering and intrinsic effects. Note that scattering and intrinsic attenuation are easily distinguishable for this choice of parameters.

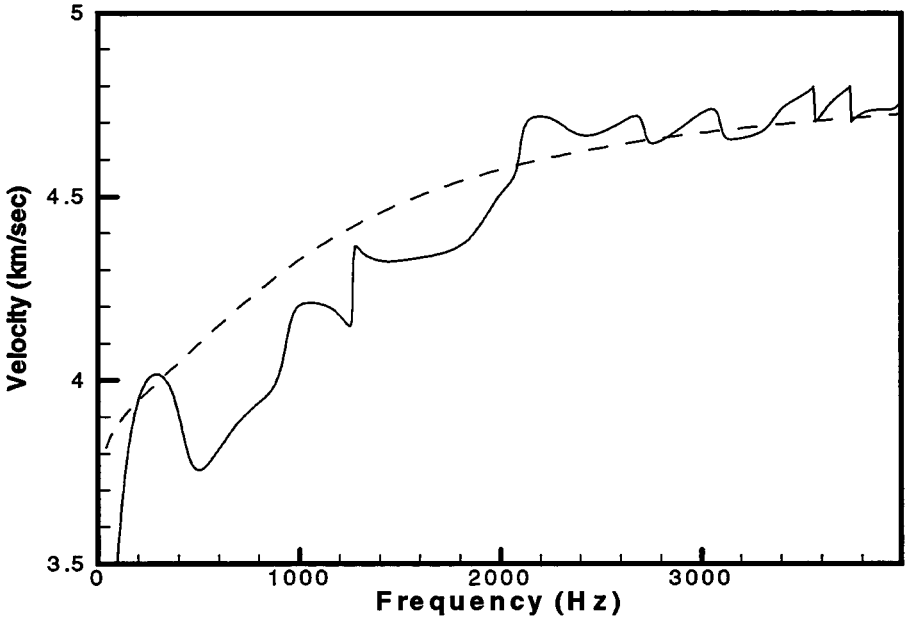

Figure IX-3: Experimentally determined dispersion (solid line) and fitted random medium model dispersion (dashed line) for the Kankakee reservoir in Illinois.

determination of phase velocity from the spectral ratio method, there may be some unresolved effect from multiple arrivals, head waves, or mixed modes of propagation. The computed model Q (Figure IX-4), however, matches the experimentally observed Q quite well with attenuation ranging from Q = 5 to Q = 7 over frequencies 500 to 4,000 Hz. This suggests that the strong dispersion observed for frequencies less than 2,000 Hz is caused by the reservoir heterogeneity in the Kankakee Limestone Formation. On the other hand, the velocity distribution for frequencies greater than 2,000 Hz is associated with the intrinsic properties of the reservoir (e.g., viscoelastic properties).

E. Summary

We have presented a extension of the random medium theory to intrinsically attenuating media. Our results show that inclusion of intrinsic attenuation in a random medium theory is straightforward, and that computation of the combined dispersion and attenuation can be readily performed. In addition, we give an analytical solution for a special case of the spectral density which is expected to correspond to a real sedimentary sequence. The relationship of a physical earth to the parameters underlying the theory is also discussed. Computed model results are shown, and comparisons are drawn to field data and other previously published theoretical work. Correspondence between the present work and previously established theoretical limiting behavior is within the expected second-order accuracy. Finally, modeling experimental phase velocity data shows the scattering effects caused by reservoir heterogeneity and the intrinsic effects caused by the viscoelastic property of the reservoir.

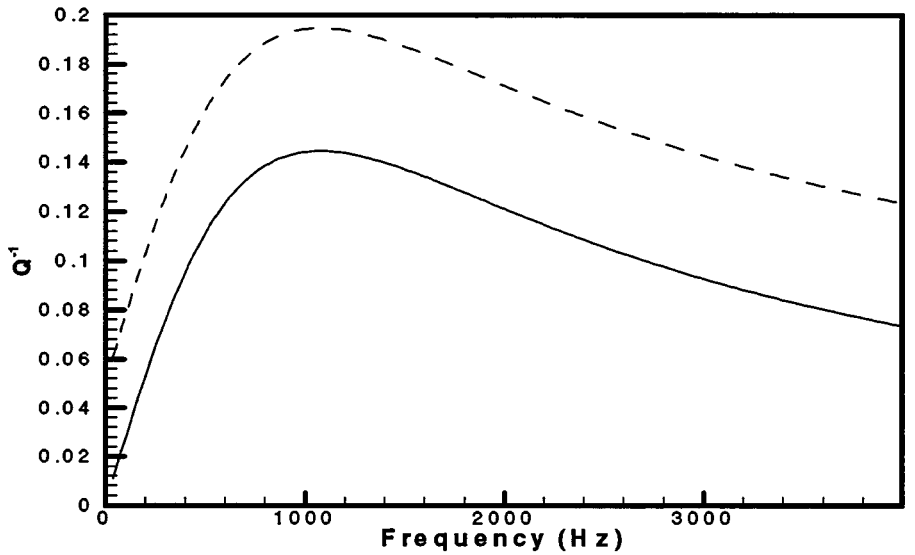

Figure XI-4: Attenuation for the model in Figure XI-3: attenuation due only to scattering (solid line) and combined scattering and intrinsic attenuation (dashed line). Intrinsic attenuation is modeled here by a frequency independent Q of 20. The resulting combined Q of 5 to 7 over the range of 500 to 4,000 Hz is in good agreement with field measurements.

X. METHODS DEVELOPED TO ACCOUNT FOR SCATTERING AND ANISOTROPY AT THE BUENA VISTA HILLS FIELD

The project as a whole has been devoted to accounting for the effects of velocity dispersion in order to integrate seismic measurements at different frequencies. One mechanism for velocity dispersion is referred to as elastic scattering. The other mechanisms for velocity dispersion are referred to collectively as intrinsic attenuation mechanisms. The work described in this section is pointed specifically toward estimating the elastic scattering component of velocity dispersion. This work is important because it is the first step toward understanding the nature of the intrinsic attenuation mechanisms, which may be useful for mapping fluids within the Buena Vista Hills reservoir. Once the elastic scattering component of dispersion has been quantified, the intrinsic attenuation can be quantified and studied.

A. Building a High Resolution Velocity Model

To predict the elastic scattering component of velocity dispersion, an accurate elastic model of the formation has to be constructed. By accurate elastic model, we mean a model capable of predicting elastic scattering effects to a desired degree of accuracy.

Predicting an accurate elastic model of a formation originates with the low resolution of the available logs. For example, sonic logs often have a resolving power of two feet. This is unfortunate because there is evidence that small beds below the resolution of the sonic log can affect the total dispersion. In other words, the small-scale heterogeneity that is missed by the low-resolution logs can play a major role in the estimation of the effects of elastic scattering. However, when a high-resolution log is available, e.g., the Formation Micro Scanner, it can be used to estimate a high-resolution version of other lower resolution logs. Section X.A.1, "Predicting High Resolution Logs from Low Resolution Logs," includes an algorithm designed for accomplishing this task.

One of the remaining problems facing efforts to build an accurate elastic model of the Buena Vista Hills formation is the estimation of the elastic constants which characterize the elastic anisotropy of the formation. The problem arises because most of our log measurements reveal a vertical fracture through the formation. To completely characterize seismic anisotropy, a series of measurements would have to be made at different angles through the formation, and this task is impractical.

To overcome these problems, we developed an approach for estimating the anisotropy based upon available log measurements. The method, which assumes that all anisotropy is a result of shales present in the formation, is described in Section X.A.3, "Prediction of Intrinsic Anisotropy for Shales."

1. Predicting High Resolution Logs from Low Resolution Logs

This section gives a review of the article titled "Improved Vertical Resolution of Well Logs by Resolution Matching," which was written by Richard J. Nelson and William K. Mitchell of Oryx Energy Company. The article was published in the July-August 1991 issue of *The Log Analyst.* The paper describes the basic ideas used to predict high-resolution versions of low-resolution logs, e.g., the sonic and density logs. For the purposes of this project, we changed the notation to ease interpretation of the equations. The emphasis here is to develop the equations necessary to write a program that implements resolution matching ideas.

Two logs are required to implement the ideas of Nelson and Mitchell: a low-resolution log (e.g., a sonic log) and a high-resolution log (e.g., an FMI resistivity log). Each of these logs should be digitized at an interval small enough to capture the highest frequency information from the high-resolution log. The digitization interval may be as small as one inch or less. Each log is assumed to be influenced by the formation directly adjacent to the depth of interest and some portion of the surrounding formation. The degree to which the surrounding formations influence the logs determines the vertical resolution of the logs. We begin by describing the response of the high-resolution log.

a. High Resolution Log

High Resolution Log Measurement = H
High Resolution Log Measurement at depth point i = H_i

Each measurement on the high-resolution log, H, can be written as a linear combination of the adjacent points to the measurement point.

$$H = \sum_{i=1}^{M_H} g_i H_i \tag{1}$$

The response function coefficients g_i represent the fractional contribution of each adjacent sample to the measurement. They are constructed so that

$$\sum_{i=1}^{M_H} g_i = 1 \tag{2}$$

For the sampling used, only M_H adjacent points are considered to influence the measurement of the high-resolution log.

b. Low Resolution Log

Low Resolution Log Measurement = L
Low Resolution Log Measurement at depth point i = L_i

Each measurement on the low-resolution log, L, can be written as a linear combination of the adjacent points to the measurement point.

$$L = \sum_{i=1}^{N_L} j_i L_i \ . \tag{3}$$

The response function coefficients j_i represent the fractional contribution of each adjacent sample to the measurement. They are constructed so that

$$\sum_{i=1}^{N_L} j_i = 1. \tag{4}$$

For the sampling used, only N_L adjacent points are considered to influence the measurement of the low-resolution log. However, the number of adjacent points N_L that influence the low resolution measurement will always be greater than the number of adjacent points M_H that influence the high resolution log measurement.

$$N_L > M_H . \tag{5}$$

c. *Filtering the High Resolution Log*

The first step toward predicting a high resolution version of a sonic log is to filter the high resolution log, in this case the FMI log, and produce an FMI curve that has the same vertical response as the sonic. We assume that the j_i (sonic) and g_i (FMI) are known or can be approximated for both logs. The problem then is to find the filter, i.e., the series of coefficients, a_i, that can be applied to the samples of the high resolution log to obtain H_f, a filtered version of the high resolution log H.

$$H_f = \sum_{i=1}^{M_H} a_i H_i \ . \tag{6}$$

Now the H_i on the right hand side of the equation can be expanded using equation (1). The low-resolution version of the high-resolution log, Hf, can be expanded using the low-resolution response coefficients

$$H_f = \sum_{i=1}^{N_L} j_i H_i \ . \tag{7}$$

Equating and collecting terms, the following matrix equation is obtained for determining the coefficients

$$\begin{bmatrix} j_1 \\ j_2 \\ j_3 \\ \cdots \\ j_{N_L} \end{bmatrix} = \begin{bmatrix} g_1 & 0 & N_L - M_H Zeroes \\ g_2 & g_1 & \\ \cdots & g_2 & g_1 \\ g_{M_H} & \cdots & g_2 \\ & g_{M_H} & \cdots \\ N_L - M_H Zeroes & N_L - M_H - 1 Zeroes & g_{M_H} \end{bmatrix} \begin{bmatrix} a_1 \\ a_2 \\ \cdots \\ a_{M_H} \end{bmatrix} \tag{8}$$

or, in matrix notation,

$$J = G\,A. \tag{9}$$

The above equation can be solved using the least squares method. The rows of the G matrix can be constructed by sliding the vertical response function for the high-resolution curve to the right by one column as each new row in the matrix is constructed. A Do-Loop over the rows of the G matrix can be used to define the matrix elements in terms of the vertical resolution coefficients for the high-resolution log (g_i). For example, if g(1), g(2).....g(M_H) are the coefficients for the vertical response of the high resolution log and G(i,j) are the coefficients of the G matrix, we can write the following algorithm to construct the G matrix:

Loop Over i (rows of the G matrix) i=1,....N_L

Loop Over j (cols of the G matrix) j=1,..... M_H

If(a) (i is less than or equal to M_H), then do the following:

If(b) (j greater than i) then
G(i,j)=0
else
G(i,j)=g(i-(j-1))
endif(b)

Else (if i greater than M_H)

If(c) (j less than or equal to i- M_H) then
G(i,j)=0
else
G(i,j)=g(i-(j-1))
endif(c)
endif(a)

Given the matrix G and J, we can use a least squares matrix inversion algorithm to predict the filter coefficients (a_i) in the A matrix (see equation 9). The a_i can be used to predict the filtered response of the high-resolution log H_f (equation 6).

d. Linear Regression of the Low Resolution Log, L, with the Filtered Version (equation 6) of the High Resolution Log, H_f

Next, the filtered version of the high-resolution log, H, and the low-resolution log, L, are assumed to be linearly related. A least squares estimate of the line through a group of points within an optimum window is selected. Within the selected window, the following equation is obtained by least squares fitting

$$L_e = m*H_f + b, \tag{10}$$

where L_e is the estimated value of the actual value L_a of the low-resolution log, and H_f is the filtered version of the high-resolution log. The low resolution estimation error for the process will be referred to as E_L where

$$E_L = L_e - L_a \ . \tag{11}$$

The slope and intercept in equation (10) can be retained and used with the values of the high resolution log, H, to estimate what the low resolution log value would be if it had a high resolution capability, L_{eh}:

$$L_{eh} = m*H + b, \tag{12}$$

where L_{eh} is the estimated high-resolution version of the actual low-resolution log at a higher resolution, L_{ah}. The error in this estimate is referred to as E_h where

$$E_h = L_{eh} - L_{ah} . \tag{13}$$

Admitting that the estimate given in equation (12) is a rough estimate, Nelson and Mitchell look for an additional perturbation to correct the estimate. They suggest two approaches to correct the value of L_{eh} to a better estimate, L_a, which are described in the next two sections.

e. Method 1 Correction

In this approach, Nelson and Mitchell assume

$$E_L = E_H . \tag{14}$$

Substituting from equations (11) and (13) yields

$$L_e - L_a = L_{eh} - L_{ah} . \tag{15}$$

Solving this for the actual high-resolution version of the low-resolution log yields

$$L_{ah} = L_{eh} - L_e + L_a . \tag{16}$$

Equation (16) is most appropriate for curves that can go negative or positive.

f. Method 2 Correction

In this approach, errors are assumed to vary directly with the measurement:

$$\frac{E_L}{L_a} = \frac{E_H}{L_{ah}}. \tag{17}$$

Solving for the actual value of the high resolution version of the low resolution log, L_{ah}, yields

$$L_{ah} = \frac{L_{eh} L_a}{L_e}, \tag{18}$$

where

L_a = actual value of low resolution log
L_e = estimate of low resolution log value made from equation (10) using the filtered version of the high resolution log, H_f
L_{eh} = estimate of a high resolution version of the low resolution log (equation 12 using the high resolution log as input)
L_{ah} = actual value of high resolution version of the low resolution log

Equation (18) is most appropriate for curves that cannot go to zero and have large changes in value, e.g., the resistivity logs.

g. Accounting for the Correlation Between Logs

To reduce problems where the filtered high resolution log and the low resolution log have a very low correlation, Nelson and Mitchell suggest using the following equation to estimate a high resolution version of the low resolution log, L_{hr}:

$$L_{hr} = R^2 L_{ah} + (1 - R^2) L_a, \tag{19}$$

where R is the correlation coefficient computed for the least squares fit described in equation (10). This equation favors the estimated value of the high-resolution version of the low-resolution log when the correlation coefficient is high. Otherwise, the value is near that of the original low-resolution log.

h. Determination of the Optimum Window

To complement the above approach in estimating what a high-resolution version of a low-resolution log would look like, Nelson and Mitchell suggest moving

the window to find an optimum window (assuming a fixed window length). The optimum interval is determined for a point when the least estimation error (E_L in equation 11) and the best correlation are obtained. This interval is determined by finding the interval with the lowest value of W where

$$W = \left[\frac{L_e - L_a}{\delta}\right]^2 + \left(1 - R^2\right). \tag{20}$$

The δ appears as a normalization factor and must depend on the type of log.

i. Summary

In summary, a method has been described for predicting a high-resolution version of a low-resolution log using information from a high-resolution log. The steps are as follows:

(1) Filter the high-resolution log (using equation 6).

$$H_f = \sum_{i=1}^{M_H} a_i H_i .$$

(2) Perform linear regression between the filtered high resolution log and the low resolution log on a fixed interval about each point and store the results (m,b and R) for equation (10).

$$L_e = m*H_f + b.$$

The following steps will be repeated for each sample point.

(1) Determine the optimum window for the output sample point by checking adjacent window values of equation (20) [using the regression factors computed in step 2 above].

$$W = \left[\frac{L_e - L_a}{\delta}\right]^2 + \left(1 - R^2\right).$$

(2) Using m,b and R determined for the optimum window, compute the high-resolution estimate of the low-resolution log (equations 16 or18 along with equation 19).

equation (16) $L_{ah} = L_{eh} - L_e + L_a$

equation (18) $L_{ah} = \frac{L_{eh} L_a}{L_e}$

equation (19) $L_{hr} = R^2 L_{ah} + (1 - R^2) L_a$

2. *Testing the Algorithms Used to Predict a High Resolution Sonic Log*

To evaluate the ideas (Nelson and Mitchell, 1991) used to predict high resolution logs, the following test is proposed. Portions of the preceding section will be referred to in this section.

a. Generate a Function, R(z), Representing Resistivity

First generate an analytic function, R(z), which can be imagined to represent the resistivity reading. This function will be a function of the depth (z) and will represent the actual distribution of the resistivity as a function of depth.

Suggested Function - We can initially assume that the resistivity profile is made up of the sum of two sine functions using the following functional form of R(z):

$$R(z) = A\sin(\frac{2\pi}{L_R}Z) + B\sin(\frac{2\pi}{H_R}) \tag{21}$$

where

A = amplitude of low resolution portion of the resistivity curve
B = amplitude of high resolution portion of the resistivity curve
L_R = wavelength of low resolution portion of the resistivity curve
H_R = wavelength of high resolution portion of the resistivity curve

The idea is to vary these parameters so the trial resistivity curve will have a low-resolution component with a wavelength of feet and a high resolution with a wavelength of a few inches. This curve should be a low-resolution trend with a high frequency variation added to it. Any other function can be used, even real data from a log. The idea is to use a known function as a function of depth.

b. Simulate the FMI Reading of the Resistivity Curve

To simulate how the FMI resistivity log will appear, the vertical response function for the FMI will be approximated using the following equation:

$$FMI(z) = \sum_{i=1}^{M_R} g_i R_i . \tag{22}$$

R_i represents the values of the sampled resistivity function at depth points over a range including the depth point z. We assume that this function is sampled at a rate ΔZ_R that is much smaller than the FMI log sample rate ΔZ_{FMI}. It will be convenient to have ΔZ_{FMI} as an integral multiple of ΔZ_R. Although we can adjust the sizes, it might be practical to have $2\Delta Z_{FMI\,R}$ be approximately equal to the vertical length of the response for the FMI (which we will assume is known. Some guessing may be necessary since the vertical response seems to be proprietary information). If we

use $\Delta Z_{FMI} = 10\Delta Z_R$, then 21 vertical response coefficients, g_I, will be used to compute the FMI log value at each depth.

We approximate the vertical response function as a triangular-shaped function [see Figure 1a in Nelson and Mitchell (1991)], since the FMI measurement is effectively a shallow resistivity measurement. The only variable (to be guessed) is the vertical resolution length L_{VR}. This length represents the vertical distance over which the vertical response function is applied. The actual distance will be slightly smaller because the function is sampled at a rate equal to ΔZ_R. The triangular function about the point Z_i where we are attempting to predict the FMI response for the resistivity can be written in the form

$$h(Z) = \frac{-A}{\left(\frac{L_{VR}}{2}\right)}(Z - Z_i) + A, \tag{23}$$

where the function is evaluated for $Z\text{-}Z_i$ within the range $+L_{VR}$ to $-L_{VR}$.

To use the above function as a response function, we have to normalize the function so that the coefficients sum to one. We use L_{VR} to describe the distance over which the response coefficients are non-zero. L_{VR} in the above equation describes the distance between zeroes. By adding a sample width to L_{VR} in the above equation, the zeroes for the function are shifted half a sample width, which has the effect of placing all the non-zero samples for the function with the window length = L_{VR}. Setting the A=1, we obtain the following modified equation:

$$h(Z) = \frac{-(Z - Z_i)}{\left(\frac{L_{VR} + \Delta Z_R}{2}\right)} + 1. \tag{24}$$

This equation reaches a maximum value of 1 at the point where we predict the log response (the FMI response in this case). We now need to compute this function at all the points and sum the values to compute the normalization value.

The most shallow depth Z at which the above equation will have a non-zero value will be ZSTART = Z_i - $L_{VR}/2$. The first non-zero point of the vertical response function will be the above function evaluated at this value of Z. The second point of the response function will be evaluated at ZSTART+ΔZ_R. The process will be repeated for

$M_H = \frac{L_{VR}}{\Delta Z_R} + 1$ times (remember to specify the vertical resolution length L_{VR} as an integral number of sample intervals, e.g., L_{VR}=10 ΔZ_R).

Now assume that we have made the above computations of the function h at the M_H non-zero points of the filter, and call these computed values h_i (where the index goes from 1 to M_H). The normalization value of the function is simply the sum of these h's:

$$N = \sum_{i=1}^{M_H} h_i \tag{25}$$

Normalize the values of the h_i by dividing them by N to obtain the g_i, the components of the vertical response function for the FMI log.

$$g_i = \frac{h_i}{N} \tag{26}$$

Using the response function described above, we can compute the resistivity determined by the FMI using

$$FMI(Z_i) = \sum_{i=1}^{M_H} g_i R_i \,, \tag{27}$$

where the R_i are evaluated at the same depths that the h_i were computed. The above equation can then be repeated for each depth Z_i. The distance between output samples can be varied to any desired level. The result of this process is an estimate of what the FMI log output will be given the actual values of the resistivity, R_i, at nearby points.

c. Simulate the FMI Measurement with a Low Resolution Response

The concepts described above can be used to predict what the FMI log response would be if the log had a different vertical response function. In particular, we can evaluate what the FMI would yield if it had a vertical response much like that of a sonic. However, it seems physically justifiable to assume that each interval within the zone sampled by the sonic log will make an equal contribution to the measurement. We then assume that the vertical response function is a perfect rectangle over the specified zone of the sonic measurement. Thus, using the same notation as that used in the log filtering equations, the normalization constant N = M_L number of points over the window specified by L_{VR} (sonic resolution). In the case of a lower resolution response, we will use L_{VR} (sonic resolution) > L_{VR} (FMI resolution). For example, sonic logs make measurements over distances of 60 cm all the way down to 6 cm. We must find the distance L_{VR} (sonic resolution) that applies to the sonic measurements made in the wells at Buena Vista Hills field. Over the interval where the sonic applies, the low-resolution response of the FMI can be modeled using

$$FMI_{LowRes}(Z_i) = \frac{\sum_{i=1}^{M_H} R_i}{M_L} \,. \tag{28}$$

In other words, the estimated low resolution response of the FMI with a vertical response similar to a sonic is essentially a running average of the resistivity measurements over a window equivalent in width to the distance over which the sonic measurements are made. The curve generated using this assumed method is approximate, but it can be used as a check during efforts to design a filter to predict the same low resolution curve (see the following section).

d. Design Filter to Predict a Low Resolution Version of the FMI Log

We need to design a filter to see how well we can predict the low-resolution version of the FMI given the high-resolution version of the FMI. The low-resolution filter coefficients have been referred to as j_i. Using the running average described in the previous section, the coefficients for the low resolution FMI are

$$j_i = \frac{1}{M_L}, \tag{29}$$

where M_L is the number of points contained within the low-resolution window. Using the defined values of the j's and g's, equation 8 can be used to determine the filter that can be applied to the FMI (high resolution) to estimate the FMI (low resolution - same resolution as sonic). The output can be compared to the actual low-resolution curve predicted. Agreement means that we are on the right track.

e. Predict a Low Resolution Sonic Log from the Low Resolution FMI

Assume that the resistivity predicted from the low-resolution version of the FMI is linearly related to the velocities or delta-t's in the sonic.

$$Sonic\Delta T_{LowRes}(Z_i) = A * FMI_{LowRes}(Z_i) + B \tag{30}$$

The values of the constants can be estimated from experience in correlating resistivity to sonic measurements.

f. Predict a High Resolution Sonic Log from the High Resolution Version of the FMI

Using the log filtering equations, we predicted a high-resolution version of the FMI using a triangular shaped curve. Now we use this curve to predict a high resolution sonic (using the same constants used in the previous section).

$$Sonic\Delta T_{HighRes}(Z_i) = A * FMI_{HighRes}(Z_i) + B \tag{31}$$

This curve is what we hope to obtain using the methods of Nelson and Mitchell (1991).

g. Predict a High Resolution Sonic Log Given the FMI and the Sonic

We can now pose the problem of predicting a high-resolution version of a sonic log given: (1) a low-resolution sonic log, and (2) a high resolution FMI log. We can implement the prediction scheme outlined in Nelson and Mitchell (1991) and compare the results with the curve predicted in the previous section. All of this should produce a rather self-consistent approach to predicting high-resolution sonics. Later, we can add challenge to the task by adding random noise to the assumed correlation between the sonic and the FMI.

h. Summary

At this point, we should be ready to move the application to real logs. We should be able to compute the vertical response functions for logs as well as the filter that we will apply to the high-resolution version of the FMI to obtain the low-resolution version of the FMI. It is this low-resolution version of the FMI that we assume correlates with the low-resolution version of the sonic log. We will need to be able to change the assumed vertical resolutions of the FMI and the sonic to get the best filter responses for jumping from the high resolution version of the FMI to the low resolution version of the FMI.

3. Prediction of Intrinsic Anisotropy for Shales

This section describes an approximate method of predicting the Transversely Isotropic (TI) elastic parameters of shale formations adjacent to a borehole using sonic measurements of Vp and Vs. Only shales are considered here since they are assumed to represent the majority of the intrinsic anisotropy in sedimentary rocks. The method described can be used to characterize the shales in the study area at the Buena Vista Hills field. In particular, we will be able to make more accurate high-resolution velocity models of the formations adjacent to wells. Neglecting the intrinsic anisotropy of the shales leads to erroneous predictions of crosswell and surface seismic responses. A major problem for the future will be making a distinction between the effects of intrinsic anisotropy, as predicted using techniques such as those described here, and effects due to elastic scattering. Once this problem is solved, the intrinsic attenuation of a formation can be studied.

The estimation of the TI properties of shales is based on empirical relations between Vp, Vs and the TI parameters used by Thomsen (1986) for a weak TI medium. Once the Thomsen (1986) parameters are estimated, they are used to solve for the classic elastic parameters of the TI medium. The advantage of this approach is that it can be accomplished with log measurements instead of expensive core measurements.

a. Thomsen Parameters

As luck would have it, many sedimentary rocks can be characterized as weak TI media. In this case, the five classic elastic constants (C_{11}, C_{33}, C_{44}, C_{13},

C_{66}) can be replaced by the vertical P- (α_0) and S- (β_0) wave velocities through a formation and three new constants: δ, ε and γ (Thomsen, 1986). The new parameters are defined in terms of the classic elastic parameters as follows:

$$\varepsilon = \frac{C_{11} - C_{33}}{2C_{33}} \approx \frac{V_P(\frac{\pi}{2}) - \alpha_0}{\alpha_0} \tag{32}$$

$$\gamma = \frac{C_{66} - C_{44}}{2C_{44}} \approx \frac{V_{SH}(\frac{\pi}{2}) - \beta_0}{\beta_0} \tag{33}$$

and

$$\delta = \frac{(C_{13} - C_{44})^2 - (C_{33} - C_{44})^2}{2C_{33}(C_{33} - C_{44})} \tag{34}$$

where V_P ($\pi/2$) and V_{SH} ($\pi/2$) are the horizontal P- and SH-wave velocities, respectively. The Thomsen (1986) parameters are used here because they can be used to describe useful relationships for shales and they offer a more intuitive system of parameters than the classic elastic parameters. For example, the parameter ε can be viewed as a frequently used measure of P-wave anisotropy. Similarly, the parameter γ is a measure of S-wave anisotropy. The parameter δ is less familiar, but may be viewed as controlling the velocity at oblique angles through the TI medium.

If the Thomsen (1986) parameters (α_0, β_0, δ, ε and γ) and the density (ρ) of a formation are known, the following sequence of equations can be used to solve for the classic elastic parameters.

First use α_0 and β_0 to obtain C_{33} and C_{44}.

$$C_{33} = \rho\alpha_0^2 \tag{35}$$

$$C_{44} = \rho\beta_0^2 \tag{36}$$

Next, ε and γ can be used to compute C_{11} and C_{66}.

$$C_{11} = 2C_{33}(\varepsilon + 1) \tag{37}$$

$$C_{66} = 2C_{44}(\gamma + 1) \tag{38}$$

Finally, C_{13} is obtained using

$$C_{13} = \sqrt{2\delta C_{33}(C_{33} - C_{44}) + (C_{33} - C_{44})^2} - C_{44}. \tag{39}$$

Using the above equations we can switch back and forth between the Thomsen (1986) parameters and the classic elastic parameters.

b. Ryan-Grigor (1997) Empirical Relations for the δ Parameter

In addition to the intuitive description provided by the Thomsen (1986) parameters, they are also easier to relate to rock properties. For example, Ryan-Grigor (1997) used the Vp/Vs ratio (measured vertically) of rocks to predict Thomsen's (1986) δ parameter, which is important for surface seismic studies. She expressed the δ parameter in the following form:

$$\delta = \frac{\left[1 + (C_{13}/C_{44})\right]^2 - \left[\left(\frac{V_p}{V_s}\right)^2 - 1\right]^2}{2\left(\frac{V_p}{V_s}\right)^2\left[\left(\frac{V_p}{V_s}\right)^2 - 1\right]}. \tag{40}$$

Since the δ parameter can be expressed in terms of the vertical P- and S-wave velocities and the ratio C_{13}/C_{44}, she plotted the ratio C_{13}/C_{44} for numerous lithologies published in the literature and found a straight line relationship between the C_{13}/C_{44} ratio and Vp/Vs.

$$\frac{C_{13}}{C_{14}} = 3.61\left[\frac{V_p}{V_s}\right] - 5.06. \tag{41}$$

Using equation (41) in equation (40), a value of the δ parameter can be obtained using Vp/Vs ratios determined from sonic measurements.

As stated earlier, Ryan-Grigor's (1997) work was devoted to predicting the effects of intrinsic anisotropy on surface seismic measurements. As a result, she was not interested in a complete description of intrinsic anisotropy. In addition, her work was based on a variety of lithologies. To adapt her findings to the studies at Buena Vista Hills field, we determined that shales should be the only lithology involved. In addition, Ryan-Grigor's work was extended so as to predict all of the TI parameters for the shales.

c. *Modified Ryan-Grigor Empirical Relation for the δ Parameter of Shales Only*

We modified the approach taken by Ryan-Grigor (1997) by studying the relationship between Vp/Vs and the δ parameter for shales. A subset of the data used by Ryan-Grigor is used here. The data were selected from the original data of Ryan-Grigor using the following criteria:

- Only data from shales were used.
- The Vp values of the shales fall with the range (2.7-3.9 km/sec), since this range brackets the velocities at Buena Vista Hills field.
- The measurements were made on shales *in situ* or in a laboratory condition simulating *in situ* conditions.

Table X-1 lists the data selected for this study. The figures in the last column were computed by substituting the appropriate values of Vp/Vs and the δ parameter into equation (40) and solving for (C_{13}/C_{44}).

Table X-1

Source/ Sample	Vp (km/sec)	Vs (km/sec)	Vp/Vs	δ	ε	C_{13}/C_{44} (Computed)
Leaney (1994)						
Java Sea-1a	2.73	1.15	2.36	0.01	0.18	4.515
Java Sea-1b	2.43	0.97	2.49	0.03	0.16	5.289
Java Sea-2	2.46	1.08	2.25	-0.07	0.06	3.553
South China Sea	2.35	0.97	2.41	-0.18	0.12	3.473
West Africa	2.93	1.50	1.96	-0.05	0.20	2.446
Greenhorn	3.06	1.49	2.05	-0.05	0.20	2.812
Vernik and Nur (1993)	3.41	2.07	1.65	0.12	0.24	1.758
Vernik and Nur (1993)	4.21	2.52	1.67	0.02	0.20	1.549
Vernik and Nur (1993)	3.72	2.25	1.65	0.03	0.19	1.499
Vernik and Nur (1993)	3.85	2.40	1.60	0.15	0.26	1.622
Thomsen (1986) Mesa Verde clayshale	3.794	2.074	1.83	0.204	1.89	2.779

Following Ryan-Grigor's (1997) approach, a linear regression has been completed of the values of (C_{13}/C_{44}) against the values of (Vp/Vs).

$$\frac{C_{13}}{C_{14}} = 3.51\left[\frac{V_p}{V_s}\right] - 4.15 \text{ (modified for shales only)} \tag{42}$$

$$\frac{C_{13}}{C_{14}} = 3.61\left[\frac{V_p}{V_s}\right] - 5.06 \quad \text{[original Ryan-Grigor (1997); mixed lithologies]}$$

Figure X-1 illustrates the regression line and the data. Given measurements of the Vp/Vs ratio within a shale, equation (42) can be used to estimate the C_{13}/C_{44} ratio for the shale. Once this ratio has been computed, the δ parameter can be computed using equation (40).

Although equation (42) represents only data for shales within a restricted P-wave velocity range, corresponding to a presumed state of compaction, the validity of the equation should be tested. For example, when exploring a new area, an equation of the sort given should be constructed for the shales in the region being explored. Since we do not have a great deal of control over the intrinsic properties of the shales at Buena Vista Hills, equation (42) should give us a good starting value for the δ parameter of the shales.

d. Empirical Relation for the ε Parameter

Ryan-Grigor (1997) was primarily interested in surface seismic data and did not require the ε parameter, i.e., the P-wave anisotropy, for her study. However, to estimate all the properties of the shales involved in crosswell studies at Buena Vista Hills, an estimate of the ε parameter had to be made.

Although shales are difficult to characterize with simple equations, we made the assumption that the ε parameter for shales could be characterized over a limited range of P-wave velocities using a linear relationship between the Vp/Vs ratio and the ε parameter. Figure X-2 illustrates the linear regression and the data from Table X-2. The regression equation for the ε parameter is

$$\varepsilon = 0.365 - 0.0865(Vp / Vs) \tag{43}$$

Note that the correlation coefficient (see Figure X-1) for equation (43) is not as high as that for equation (42) used to determine the δ parameter. This indicates that the estimate for the ε parameter is not as reliable as the estimate for the δ parameter.

e. Empirical Relation for the γ Parameter

The last parameter that needed to be estimated for shales is the γ parameter as defined by Thomsen (1986), which effectively describes the shear wave anisotropy. Unfortunately, the γ parameter measurements for many of the shales used in the determination of equations (42) and (43) were not available. As a result, we were forced to use a different set of

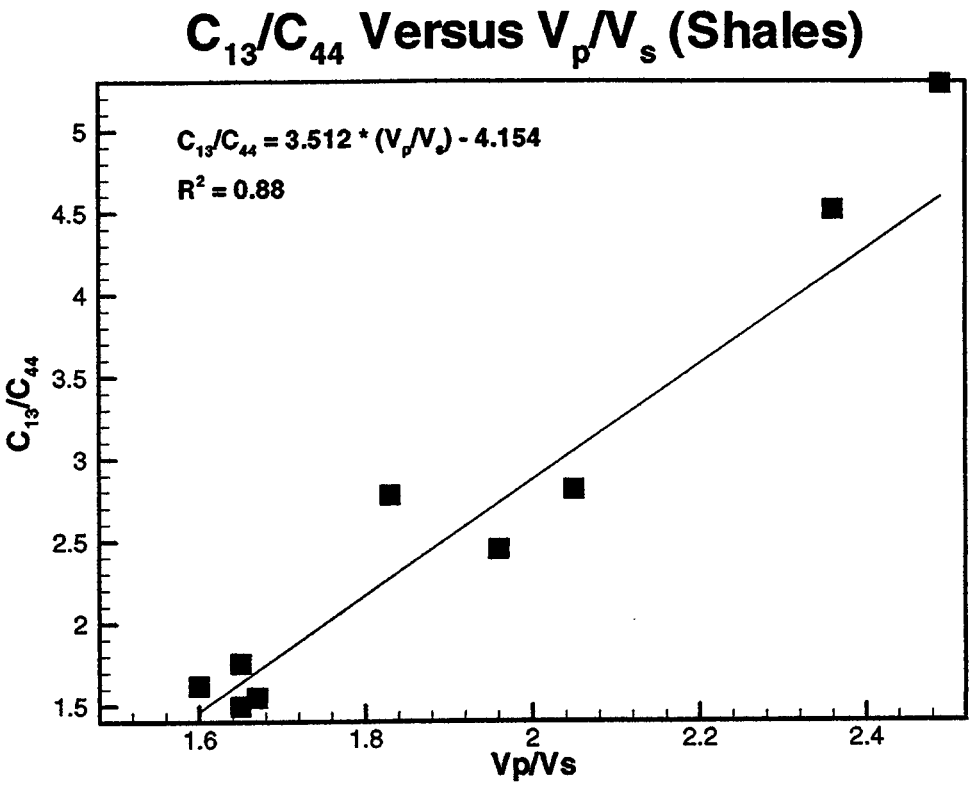

Figure X-1. Plot of C_{13}/C_{44} versus Vp/Vs for selected shales from Ryan-Grigor (1997). Line represents the best fitting equation for the data.

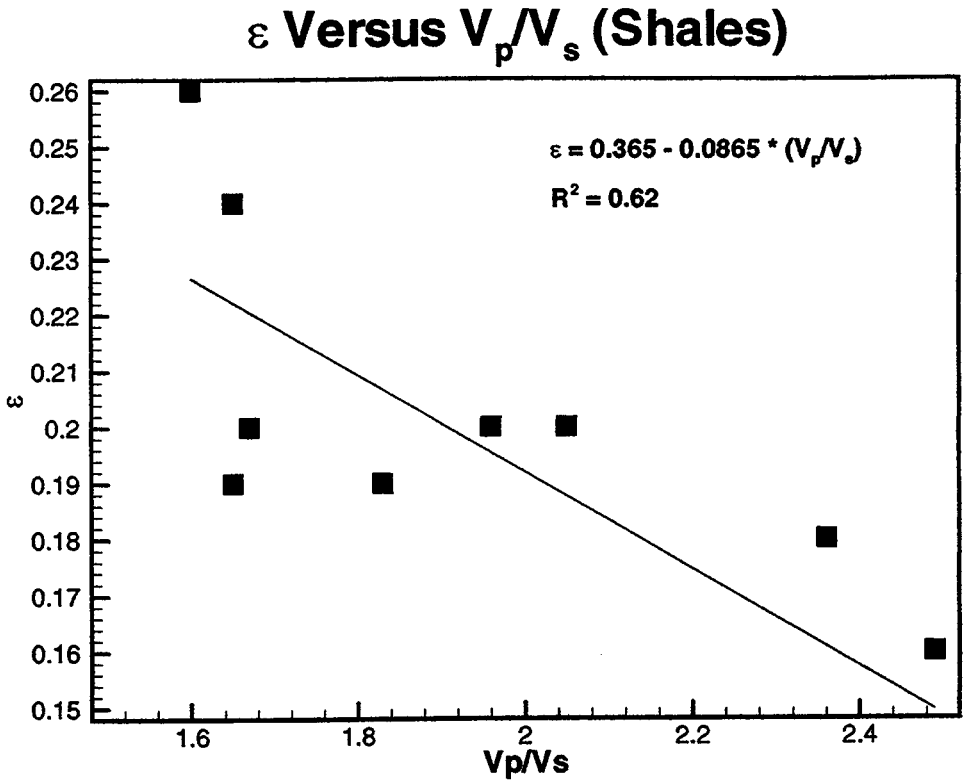

Figure X-2. Plot of ϵ parameter versus Vp for selected shales from Ryan-Grigor (1997). Line represents the best fitting equation for the data.

shales. All of the shales used are listed in Table X-2 and have been taken from the data listed by Thomsen (1986).

Table X-2. Selected Shales from Thomsen (1986)

References*	Sample	Epsilog	Delta	Gamma
Kelly (1983)	Mesa Verde mudshale	0.034	0.211	0.046
Kelly (1983)	Mesa Verde clayshale	0.189	0.154	0.175
Kelly (1983)	Mesa Verde mudshale	0.010	0.012	-0.005
Kelly (1983)	Mesa Verde mudshale	0.081	0.129	0.048
Robertson et al. (1983)	Dog Creek Shale	0.225	0.100	0.345
Robertson et al. (1983)	Wills Point Shale	0.215	0.315	0.280
Tosaya (1982)	Cotton Valley Shale	0.135	0.205	0.180
Podio et al. (1968)	Green River Shale	0.025	0.055	0.020

* See Thomsen (1986) for references.

In Figure X-3, the γ parameter is plotted against the ε parameter for the shales listed in Table X-2. The straight line through the data is the best fit to the data and is described by the following equation

$$\gamma = (1.399)\varepsilon - 0.0237 \tag{44}$$

f. Summary

Three empirical equations were set up to help assign the Thomsen elastic parameters to shales:

$$\frac{C_{13}}{C_{14}} = 3.51\left[\frac{V_p}{V_s}\right] - 4.15 \tag{45}$$

$$\varepsilon = 0.365 - 0.0865(Vp / Vs) \tag{46}$$

$$\gamma = (1.399)\varepsilon - 0.0237 \tag{47}$$

Equation (45) was used in

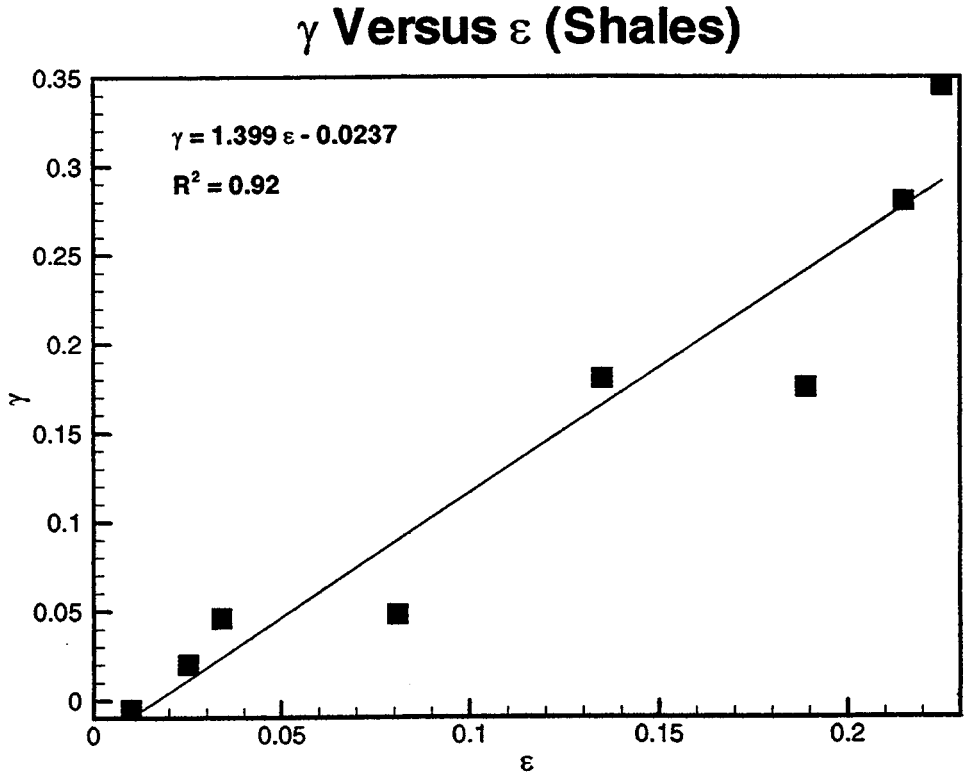

Figure X-3. Plot of γ parameter versus ϵ parameter for shales from Thomsen (1986). Line represents the best fitting equation for the data.

$$\delta = \frac{\left[1+(C_{13}/C_{44})\right]^2 - \left[\left(\frac{V_p}{V_s}\right)^2 - 1\right]^2}{2\left(\frac{V_p}{V_s}\right)^2\left[\left(\frac{V_p}{V_s}\right)^2 - 1\right]} \tag{48}$$

to obtain the δ parameter for the shale. Equations (45) and (46) were obtained for shales that resemble shales at Buena Vista Hills. Equation (47) has been obtained, out of necessity, from shales listed by Thomsen. In spite of the uncertainties, the above system of equations should give a useful approximation of the TI properties of Buena Vista Hills shales (given the vertical measurements of the P- and S-wave velocities) in terms of the Thomsen (1986) parameters.

The procedures described here will be used in predicting the intrinsic anisotropy of shales at Buena Vista Hills. This should remove some of the discrepancy between the crosswell and sonic measurements. However, one of the lessons to be learned from this work is the importance of being able to predict the anisotropy of formations in order to scale seismic measurements.

Building a high-resolution elastic model of a formation based upon log measurements cannot be accomplished directly from the log measurements. Instead, we found it necessary to develop software to account for the effects of deviated boreholes, dip of formations, low resolution of sonic and density logs, and restrictions on the measurement geometry within the borehole. This software gave us the capability to assemble realistic elastic models that can be used to predict the frequency and directional dependence of velocity measurements through a formation.

B. Quantifying the Elastic Scattering Component

There are two general categories of velocity dispersion – elastic scattering and intrinsic attenuation. This section describes methods for estimating the elastic scattering component of velocity dispersion. The basic idea will be to use the high-resolution elastic models determined from well control using the techniques described earlier as a reference high frequency elastic model. Our goal then will be to predict the effective elastic parameters at lower frequencies due only to the effects of elastic scattering.

Several approaches can be designed to estimate the elastic parameters at lower frequencies by using some form of Backus (1962) averaging. Sections X.B.1 and X.B.2 describe a variety of approaches using the Backus averaging methods, while section X.B.3 describes a more direct method of computing the effective elastic parameters of a medium at different frequencies using a special approach to ray tracing and plane-wave modeling.

1. *Basics of Backus Averaging*

This section describes the equations necessary for computing the Backus (1962) average elastic properties for a layered medium. The resulting elastic constants represent an effective transversely isotropic medium. Once the effective elastic constants for a layered system have been computed, the phase velocity, i.e., the velocity of a plane wave in that direction, can be computed using results given by White (1965, 1983).

First, we introduce some notation describing elastic constants. Next, the Backus (1962) average and phase velocity equations are described. Finally, a brief outline of a computer program to compute the Backus average elastic constants will be included.

a. Notation Describing Elastic Constants

Hooke's Law for elastic media can be written in the form:

$$\tau_{ij} = c_{ijkl}\varepsilon_{kl} \tag{49}$$

(implicit sum over repeated indices)

$$\tau_{ij} = Stress \tag{50}$$

$$\varepsilon_{kl} = Strain \tag{51}$$

$$c_{ijkl} = 81\_elastic\_constants \tag{52}$$

The most general linear relationship between stress and strain requires 81 elastic constants. However, because of symmetry in the stress and strain tensors, the number of possible elastic constants required can be reduced to 36. This symmetry has led to frequent use of the following equation:

$$\begin{pmatrix} \tau_{xx} \\ \tau_{yy} \\ \tau_{zz} \\ \tau_{xy} \\ \tau_{xz} \\ \tau_{yz} \end{pmatrix} = \begin{bmatrix} c_{11} & c_{12} & c_{13} & c_{14} & c_{15} & c_{16} \\ c_{21} & c_{22} & c_{23} & c_{24} & c_{25} & c_{26} \\ c_{31} & c_{32} & c_{33} & c_{34} & c_{35} & c_{36} \\ c_{41} & c_{42} & c_{43} & c_{44} & c_{45} & c_{46} \\ c_{51} & c_{52} & c_{53} & c_{54} & c_{55} & c_{56} \\ c_{61} & c_{62} & c_{63} & c_{64} & c_{65} & c_{66} \end{bmatrix} \begin{pmatrix} \varepsilon_{x} \\ \varepsilon_{y} \\ \varepsilon_{z} \\ \gamma_{xy} \\ \gamma_{xz} \\ \gamma_{yz} \end{pmatrix}. \tag{53}$$

The usual definition of C_{ij} is such that the indices i and j of C_{ij} vary from 1 to 6 if the pairs of indices (i,j) or (k,l) of elastic tensor C_{ijkl} take values (1,1), (2,2), (3,3), (2,3), (1,3) and (1,2), respectively.

Some additional symmetry is introduced into the problem by considering the strain energy function. As a result, only 21 of the above elastic constants are required for the most general type anisotropy (referred to as triclinic symmetry). Another important point is that equation (53) no longer represents a tensor equation, i.e., equation (53) does not hold after a rotation of the coordinate system. However, equation (49) is a tensor equation. If we ever need to rotate the coordinate systems, equation (49) will be the form to use.

Introducing symmetry axes and planes into the problem allows further simplification of equation (53). For a transversely isotropic material the following form is given by Helbig (1983, p. 87):

$$\begin{pmatrix} \tau_{xx} \\ \tau_{yy} \\ \tau_{zz} \\ \tau_{xy} \\ \tau_{xz} \\ \tau_{yz} \end{pmatrix} = \begin{bmatrix} c_{11} & c_{12} & c_{13} & 0 & 0 & 0 \\ c_{12} & c_{11} & c_{13} & 0 & 0 & 0 \\ c_{13} & c_{13} & c_{33} & 0 & 0 & 0 \\ 0 & 0 & 0 & c_{55} & 0 & 0 \\ 0 & 0 & 0 & 0 & c_{55} & 0 \\ 0 & 0 & 0 & 0 & 0 & c_{66} \end{bmatrix} \begin{pmatrix} \varepsilon_x \\ \varepsilon_y \\ \varepsilon_z \\ \gamma_{xy} \\ \gamma_{xz} \\ \gamma_{yz} \end{pmatrix} \tag{54}$$

where

$$C_{44} = \frac{1}{2}(C_{11} - C_{12}) \tag{55}$$

A difficulty in working with this topic is the diversity of notation and vocabulary. In addition, several authors give a different version of equation (54). For our purposes, we reconciled the notation of Helbig (1983), Backus (1962) and White (1965, 1983) for the case of a transversely isotropic medium. The correspondence between the expressions is given in Table X-3.

Table X-3

Helbig (1983)	Backus (1962)	White (1983)
C_{11}	A	A
C_{12}	B	(A-2N)
C_{13}	F	F
C_{33}	C	C
C_{55}	L	L
C_{66}	M	N

b. Backus Averaging Equations

Backus (1962) gives the following equations for determining the effective long wavelength elastic constants for a vertically heterogeneous medium:

$$A = \left\langle a - f^2 c^{-1} \right\rangle + \left\langle c^{-1} \right\rangle \left\langle f c^{-1} \right\rangle^2 \tag{56}$$

$$B = \left\langle b - f^2 c^{-1} \right\rangle + \left\langle c^{-1} \right\rangle \left\langle f c^{-1} \right\rangle^2 \tag{57}$$

$$C = \left\langle c^{-1} \right\rangle^{-1} \tag{58}$$

$$F = \left\langle c^{-1} \right\rangle^{-1} \left\langle f c^{-1} \right\rangle \tag{59}$$

$$L = \left\langle l^{-1} \right\rangle^{-1} \tag{60}$$

$$M = \langle m \rangle \tag{61}$$

The capital letters represent the effective medium properties while the lower case letters are used to describe the transverse isotropy in the individual layers. We can therefore use the above equations to compute the effective transversely isotropic elastic constants for layers made up of isotropic and intrinsic transversely isotropic materials.

Note that a = b + 2m and A = B + 2M. The brackets represent averages over the interval of interest. The wavelengths are assumed to be much longer than the interval of interest. In addition to the above average elastic properties, the average density is used to represent the effective medium.

c. *Phase Velocity Equations of White (1983)*

Once the elastic constants for a medium have been computed, the phase velocity as a function of angle with respect to the vertical can be computed using the following equations found in White (1983, page 41):

P-wave velocity

$$V_P = \left[\frac{(p+q)}{2\rho} \right]^{\frac{1}{2}} \tag{62}$$

SV-wave velocity

$$V_{SV} = \left[\frac{(p-q)}{2\rho} \right]^{\frac{1}{2}} \tag{63}$$

where

$$p = A \sin^2 \gamma_z + C \cos^2 \gamma_z + L \tag{64}$$

and

$$q = \left\{\left[(A-L)\sin^2\gamma_z - (C-L)\cos^2\gamma_z\right]^2 + 4(F+L)^2\sin^2\gamma_z\cos^2\gamma_z\right\}^{\frac{1}{2}} \qquad (65)$$

SV-wave velocity

$$V_{SH} = \left\{\frac{\left[N\sin^2\gamma_z + L\cos^2\gamma_z\right]}{\rho}\right\}^{\frac{1}{2}} \qquad (66)$$

d. Design of a Computer Program to Compute the Effective Elastic Constants and Phase Velocity as a Function of Direction Through a Vertically Heterogeneous Medium

Using the preceding equations, a computer program can be written to compute the effective elastic properties of a layered medium. The program should be designed to accept input for two kinds of layers – isotropic layers (Vp, Vs, ρ) and anisotropic layers (a,c,m,f,l, ρ).

The input density ρ for layer i should be designated as rho(i) and should be in gm/cm^3. Inside the program, this density will be converted to kgm/m^3 using

rhoc(i)=rhoc(i)*1000.

The c on the back of the variable indicates that it has been converted to the appropriate units for the computations.

e. Isotropic Layers

For the special case of isotropic layers, the process can be made easier by simply inputting the p-wave velocity Vp and the shear wave velocity Vs. Since many of our studies are for data measured in feet/second, it is handy to allow the layer velocities in these units. One approach would be to assign a value to a variable = iunit that would signal how the velocity is to be treated (iunit=1 implies velocities in feet/sec, iunit=2 implies velocities in m/sec). Then a test could be placed inside the program such as the following:

```
if (iunit.eq.1) then
        vpc(i)=vp(i)/3.28
        vsc(i)=vs(i)/3.28
Endif
```

to convert the parameters to SI (mks system), which should be used inside the program. Once the velocities for an isotropic layer have been converted or input in meters/second, we can compute the product of the density times the respective velocities to obtain:

```
rhovp2=rhoc(i)*vpc(i)*vpc(i)
rhovs2=rhoc(i)*vsc(i)*vsc(i)
```

These products will be used in the computation of the elastic constants for the layer using the following equations:

```
ba(i)=rhovp2              (=a in Backus notation)
bc(i)=rhovp2              (=c in Backus notation)
bm(i)=rhovs2              (=m in Backus notation)
bf(i)=rhovp2-(2.*rhovs2)  (=f in Backus notation)
bl(i)=rhovs2              (= l (small L) in Backus notation)
```

f. Anisotropic Layers

For anisotropic layers, the elastic parameters for the individual layers will have to be implemented. For example, a file containing rho(i), ba(i), bc(i), bm(i), bf(i), and bl(i) could be read. It is probably easiest to input the elastic parameters in giga (10^9) pascals and then convert them into pascals as required for the computation. Time and experience should reveal more efficient techniques for the input of parameters.

g. Intermediate Computation

After the layer parameters have been specified, a series of intermediate results is required. These results are basically the averages required to compute the effective elastic constants. We can zero 5 constants as follows:

```
ak1=0
ak2=0
ak3=0
ak4=0
ak5=0
rhoavg=0
```

Next, the following do-loop can be used to compute the required averages:

```
do 25 j=1,nlayers

    rhoavg=rhoavg+fk(j)*rhoc(j)

    temp1=(bf(j)*bf(j))/bc(j)
```

```
        AK1=AK1+fk(j)*(ba(j)-temp1)
        AK2=AK2+fk(j)*(bf(j)/bc(j))
        AK3=AK3+fk(j)*(1./bc(j))
        AK4=AK4+fk(j)*(1./bl(j))
        AK5=AK5+fk(j)*(bm(j))
25 Continue
```

The fk(j) represent the weights in the weighted average, e.g., the thickness of the layer divided by the thickness of the interval being considered.

Now the effective elastic parameters can be computed using the following equations:

```
c11e=AK1+ (AK2*AK2/AK3)      (effective a in Backus notation)
c33e=1./AK3                  (effective c in Backus notation)
c13e=AK2/AK3                 (effective f in Backus notation)
c44e=1./AK4                  (effective l (small L) in Backus notation)
c66e=AK5                     (effective m in Backus notation)
```

The above results can be used to compute the phase velocities (equations 45, 46 and 49) as a function of angle of the direction of travel measured from the vertical. The following segment of code starts at an angle of theta = zero degrees (vertical propagation) and increments the angle (rad is used to convert the angle from degrees to radians).

```
do 11 i=1,10
        thetar=theta*rad
        snt2=sin(thetar)*sin(thetar)
        cst2=cos(thetar)*cos(thetar)
        tempp=c11e*snt2+c33e*cst2+c443
        tempqa=(c11e-c44e)*snt2-(c33e-c44e)*cst2
        tempqb=4*(c13e+c44e)*(c13e+c44e)*snt2*cst2
        tempq=sqrt(tempqa+tempqb)
        vp=sqrt((tempp+tempq)/(2.*rhoavg))
        vsv=sqrt((tempp-tempq)/(2.*rhoavg))
        theta=theta+dtheta
11 continue
```

In summary, an algorithm was developed for predicting the Backus average or effective elastic parameters for a layered medium made up of transversely isotropic layers. This algorithm will be used for computing the effective elastic constants in an interval that is short compared to the wavelength of the signal. After the elastic constants have been computed, the phase velocities for arbitrary angles can be computed. The material presented in this report can potentially be used in a scheme to make rapid computations of the effects of elastic scattering. Several approaches to using Backus averaging are described in the following section.

2. *Calibrated Backus Averaging to Predict Low Frequency Velocities Through High Resolution Velocity Models*

a. Introduction

Sonic measurements augmented by higher resolution well logs such as the FMI can be combined to predict finely layered velocity models of the formations surrounding the borehole. These high-resolution velocity models can then be used to predict elastic scattering effects over the range of available seismic frequencies. Direct solution of wave propagation through a layered model is a time consuming approach to predicting all possible velocities through a finely layered formation. This section describes three ideas, which need to be tested, for using Backus (1963) averaging to predict the velocities for a transversely isotropic medium at different frequencies.

Backus averaging over long windows will naturally tend to smooth the velocity profile for lower frequencies. To make higher resolution versions of the low frequency velocity curves obtained by Backus averaging, we will use the techniques described in Sams et al. (1994) and Nelson and Mitchell (1991). Thus, our low frequency velocity curves should be useful for predicting reflection as well as transmission responses.

The Backus averaging schemes proposed in this section should allow a prediction of the vertical velocities at lower frequencies. The basic idea proposed here is to calibrate the vertical velocity predicted using the proposed Backus averaging techniques to the velocity predicted using a plane wave solution for the layered medium at a specified frequency. Once the calibration has been accomplished, i.e., a characteristic frequency has been assigned to a particular length for the averaging window, the transversely isotropic elastic parameters for the formation layers surrounding the borehole will have been established and the velocity of propagation can be computed through all angles. Our major goal is to describe the transmitted signals. However, using the resolution matching technique, we intend to predict high-resolution velocity models that can also be used to predict the low frequency reflection response.

Backus (1962) averaging is a straightforward method of estimating the long wavelength average velocity of a finely layered medium. The Backus average assumes that the wavelength is long compared to the interval being studied (a quasistatic approximation). In this way the problem of finding the effective velocity through the interval can be treated using static rather than dynamic elastic theory. The Backus averaging equations yield the effective long wavelength elastic constants (an effective transversely isotropic medium) for a vertically heterogeneous interval.

There are some conceptual problems in directly applying Backus averaging to obtain the velocity at some lower frequency. The first question is regarding the frequency at which the Backus average applies. Certainly part of the answer lies in the thickness of the interval being averaged (so that the static assumption applies). For example, Helbig (1984) found that the long wavelength average applies to SH propagation when the wavelength is three times the spatial period of the periodic sequence.

However, still another portion of the answer depends on the vertical heterogeneity within the interval (Carcione et al., 1991; Marion et al., 1994; Melia and Carlson, 1984). Vertical heterogeneity, or distribution of rock properties, controls the intra- and inter-bed multiples that constructively interfere to cause the apparent slowing of velocities at lower frequencies. If the averaging interval is made up of beds with a thickness d, then Marion et al. (1994) suggest that the long wavelength limit applies at approximately a wavelength-over-bed thickness ratio (λ/d) of 10. Melia and Carlson (1984) indicate that that the ratio (λ/d) at which the long wavelength limit applies varies from 10-100. More importantly, Melia and Carlson (1984) emphasize that the frequency dependence of the anisotropy is a function of the proportions of the materials as well as the effective thickness of the layers. Sams et al. (1994) examine the vertical variability within the averaging interval using statistical arguments and approximate transmission models [O'Doherty and Anstey (1971) and Shapiro and Zien (1993)].

In summary, the application of Backus averaging is desirable because it represents a simple computation for predicting the transverse isotropy of the formations around the borehole. However, an interpretation of Backus averaging requires some form of independent checking, at least in the initial stages of the application, so that the maximum effective frequency at which the Backus average applies can be estimated. Three approaches to Backus averaging, each of which is expected to yield different results, are described in the following, along with a technique for producing high-resolution versions of the curves.

b. Single-Window Backus Averaging

The simplest approach to using Backus averaging is to simply Backus average over some interval within the borehole. Since the effective frequency at which this averaging is expected to apply depends, at least in part, on the averaging interval, longer averaging intervals can be expected to predict velocities at lower frequencies. This basic idea has been exploited by Hsu et al. (1988a). They used longer and longer windows until the drift between their sonic and VSP measurements was matched. They also used proprietary deconvolution methods to produce a high-resolution version of the sonic log (Hsu et al., 1988b). Sams et al. (1994) also used window length to predict the velocities at lower frequencies and suggested using a window length proportional to the wavelength squared.

Because the frequency at which Backus averaging applies is difficult to predict, we follow Hsu et al. (1988a) and use plane wave modeling of the vertical transmission velocities to see which frequencies agree with windows of different lengths. The following approach is suggested:

- **Plane Wave Transmission**. First, compute the plane wave transmission time through the high-resolution model using a desired frequency to find the vertical travel time through the model. The desired frequency will usually be the dominant frequency for either crosswell or surface seismic studies that have been conducted near the well control.

- **Backus Average**. Next, compute a running Backus average of the log using increasing window lengths until the travel time through the interval is matched. From an intuitive point of view, the dimension of the averaging interval should be short compared to the wavelength in order to satisfy the quasistatic conditions (Backus, 1962). For example, the averaging interval should be at least one third (or less) of the wavelength (Helbig, 1984). However, the Backus average really carries no information on the thickness of the averaging interval. All that is produced are some average elastic constants. This reasoning may have been used by Esmersoy et al. (1989) as a justification for using a 250-foot window. Although we would prefer to use a window length of approximately 1/3 of a wavelength or less, we may have to consider longer windows to match the plane wave velocities at specific frequencies. Some experimentation will be required to find the correct window size for each frequency.

The resulting Backus average elastic constants, which have been calibrated vertically for specific frequencies (e.g., crosswell and surface seismic) using plane wave solutions, can then be used to predict crosswell seismic velocities (accounting only for the effects of elastic scattering). The crosswell velocities predicted using Backus averaging should be compared to those obtained via plane wave solutions. If there is agreement, then the Backus averaging is doing a good job of predicting the horizontal velocities. In general, all directions of transmission through the formation should be modeled.

c. Backus Averaging Using Cascaded Windows

In some respects, the single window averaging described above could be misrepresentative of the scaling that actually takes place. The scaling could be the result of multiple length scales associated with the log data. For example, if we start at the FMI log scale and use Backus averaging to step up to the next level scale using an averaging window one foot long, the Backus velocities should apply when the wavelengths are much longer than the thickness of the beds at the FMI scale. For the sake of discussion, assume that the dispersion ceases when the wavelengths are three times the averaging interval. Beyond this wavelength, the Backus average properties of the interval do not change. However, as the wavelengths increase, adjacent beds, which have also been averaged over one-foot intervals, begin to contribute to the effective velocity. Thus, the Backus average computed at the first length scale is the input to the Backus average at the next length scale. This process should be repeated until the length scales necessary to explain the vertical drift are obtained. The resulting transversely isotropic elastic constants can then be used to predict crosswell or surface seismic velocities.

The first step to building a cascaded Backus average for a log will be to directly block adjacent samples as shown in Figure X-4. In Figure X-4 we are showing the FMI model of the formation with a sample interval of (d). Each set of three FMI-scale model samples is Backus averaged and the result is placed at the center of the averaging window. The parameters of the layers at the FMI scale can be those of isotropic or transversely isotropic materials. However, all the samples with primed numbers, e.g., 1', 2', 3', represent the location of Backus averages that will generally be transversely isotropic. The separation between the primed sample points is 3d. Next, we Backus average the adjacent 3 samples at the primed scale to predict values at the center of windows with a length equal to 9d. We refer to this approach to

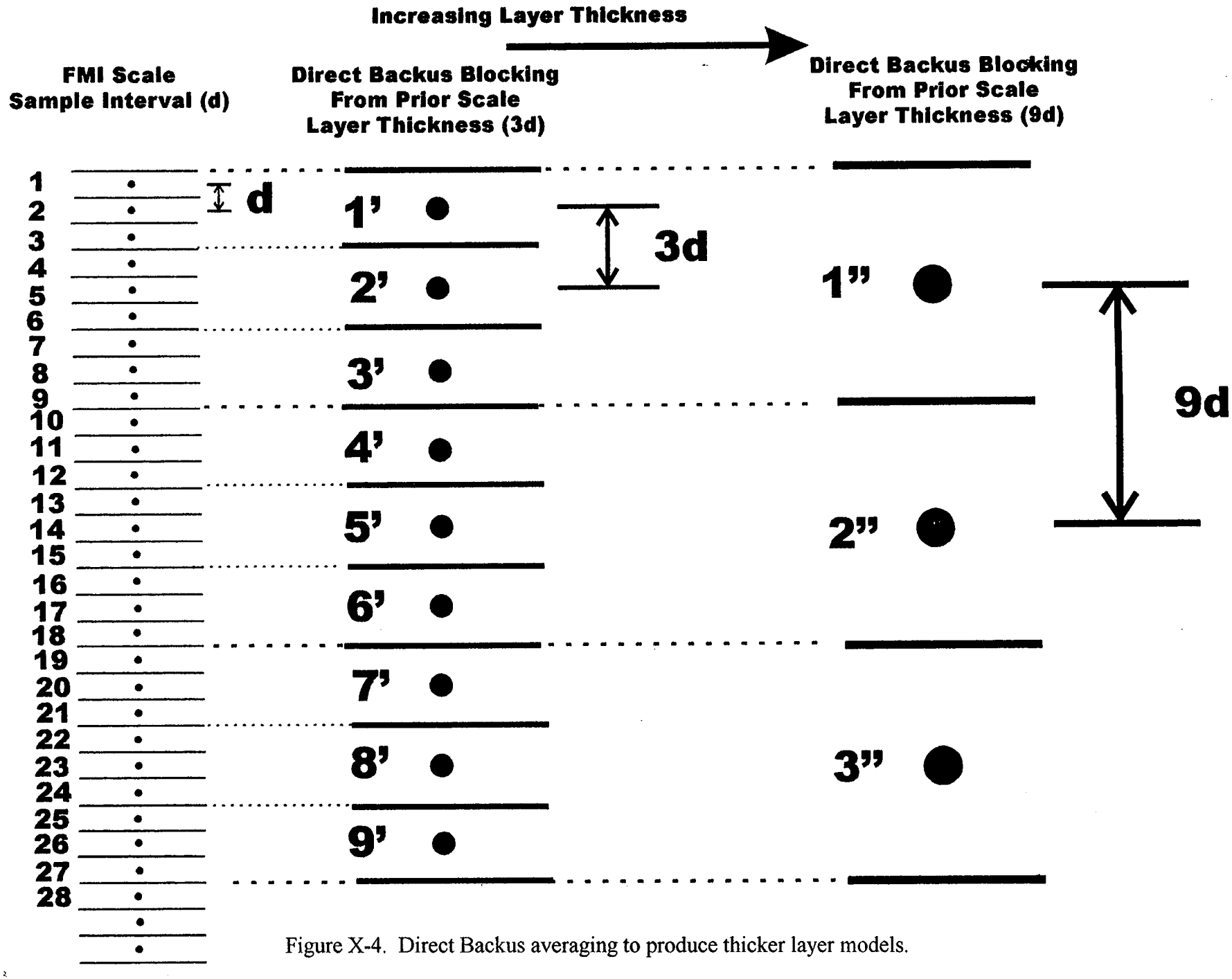

Figure X-4. Direct Backus averaging to produce thicker layer models.

windowing as direct Backus averaging with a fixed window. A moving window average produces a smoother curve, but we want to isolate different length scales in the data using this direct blocking. Once we have created different data curves in which the logs have been directly blocked to different length scales in the cascading manner shown in Figure X-4, we have the foundation for predicting velocity curves at different frequencies. We shall refer to these curves as directly blocked curves because there is no sliding window involved. Of course as the averaging lengths get longer, a great deal of information on bed boundaries is lost (true for the single window averaging approach as well). When we are inside a thick layer compared to the averaging interval, we expect direct blocking to give a good representation of the velocities.

To produce a smoothed Backus estimate at a particular level (each higher level is believed to apply to a lower frequency), a running Backus average (3 points) is applied on the prior level of direct blocking. We have chosen to block in units of three because Backus (1962) suggested that the most general type of transverse isotropy due to layering could be constructed using three constituents.

Cascaded window averaging has the same disadvantage that was described for single window averaging. The frequency that applies to the result for any particular level (or length scale) is unknown. There are too many variables, such as bed spacing and lithological variations, to allow us to use the same scaling relationships all the time. Our goal, as with single window averaging, is to calibrate the Backus averaging by finding the frequency, via plane wave modeling, that yields a vertical velocity closest to the Backus average predictions. Once this is accomplished, the crosswell velocities predicted via cascaded averaging and single-window averaging can be compared to plane wave solutions.

As we go from high frequencies toward lower frequencies, the beds at each preceding high-frequency level begin to look like the Backus average over thicker zones. Thus the individual beds in Figure X-5 can be viewed as direct Backus averages of thin beds at an even finer scale. To produce a smooth Backus average (and to predict velocities at the next window scale), we use a three-sample Backus moving average over the prior scale of direct blocking (Figure X-6).

d. Backus Average/Ray Theory Cascade

The cascading described above steps directly from one low frequency estimate to the next low frequency estimate using Backus averaging. This large-scale jump may bypass some of the physics of what takes place as the wavelengths get longer. When we start with a high-resolution model of a formation, we have implicitly assumed that this is the high frequency or ray theoretical model of the formation, and we apply Backus averaging to the ray theoretical model of the formation. However, as the wavelength gets longer, the Backus average of the previous level becomes the ray theoretical model for the next level. The approach described below attempts to simulate this process using a combination of Backus averaging and ray tracing.

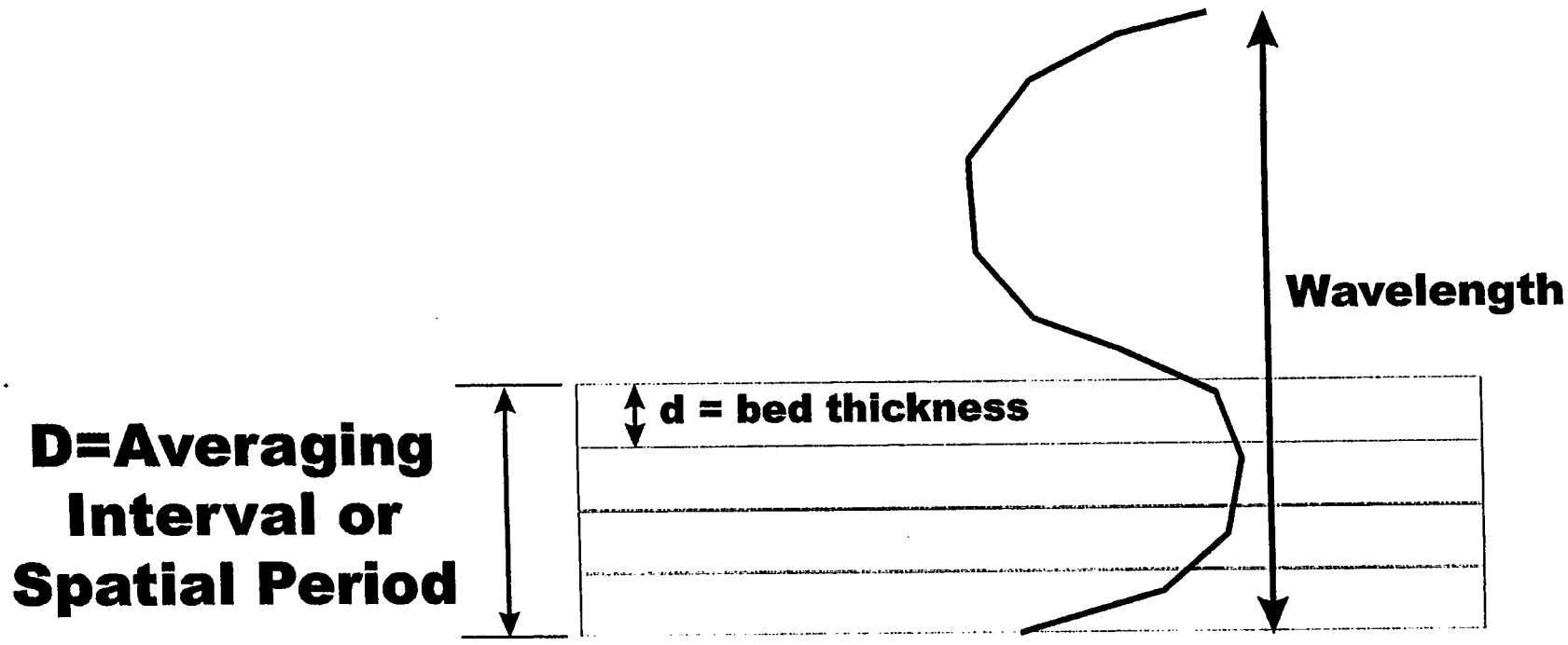

Figure X-5. Wavelength, averaging interval thickness, and bed thickness are parameters which can be used to estimate when Backus averaging applies.

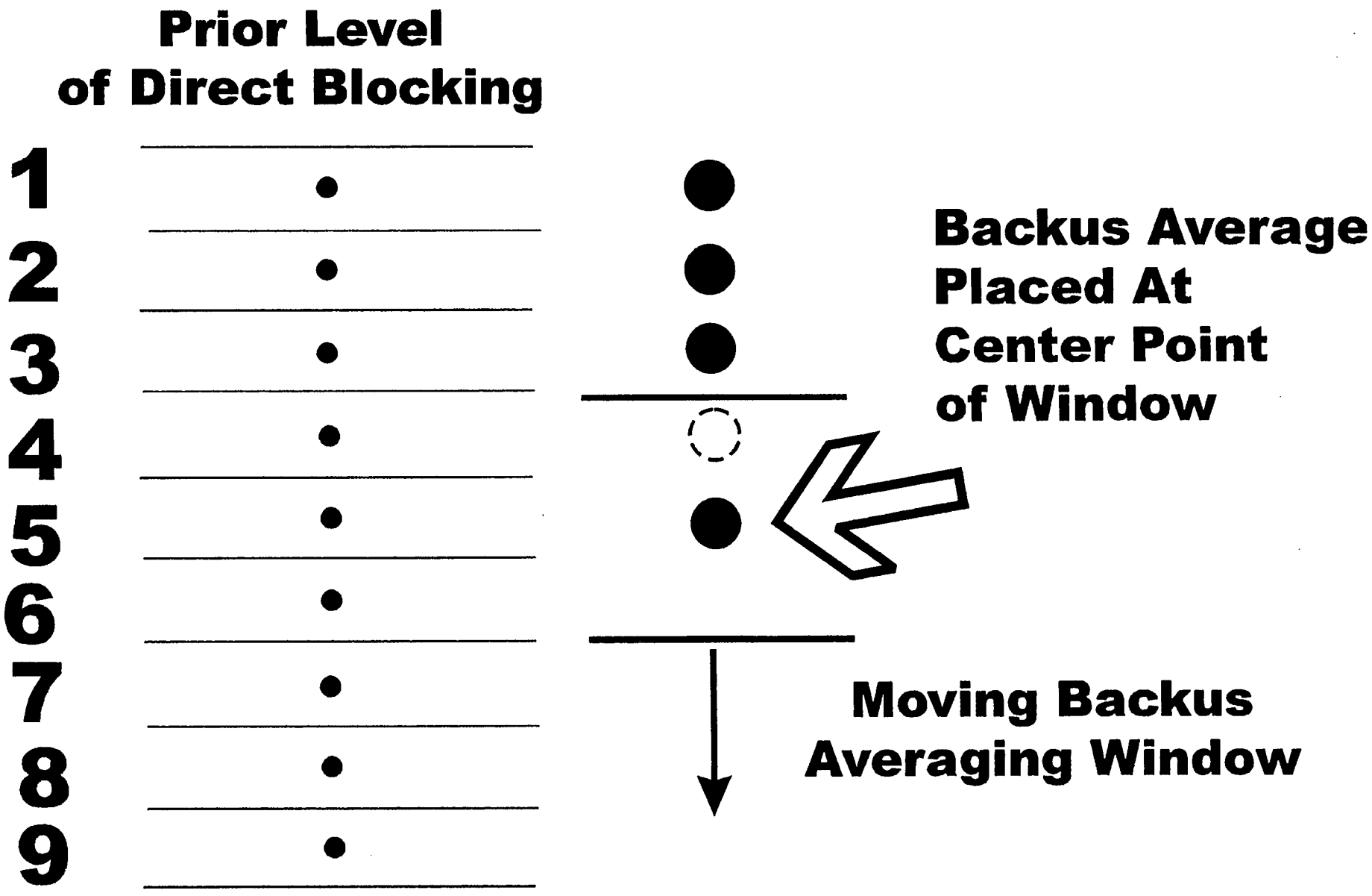

Figure X-6. A moving Backus average window is used to predict a smoothed curve representing the low frequency velocity (compared to the previous level of blocking) at a sample rate equal to the prior Level Direct Blocking.

Assume that the averaging intervals shown in Figure X-4 apply. Now Backus averaging over the FMI scale model will produce the long wavelength averages shown with primed numbers. Each of these averages is expected, for this discussion, to apply at a wavelength that is longer than the averaging interval, e.g., three times longer than the averaging interval (Helbig, 1984). However, we expect the ray theoretical model for the next level of dispersion to have dimensions comparable to the wavelength. Using the sampling shown in Figure X-4, this implies that the Backus averaging of the FMI data applies at a wavelength equal to 9d (comparable to the 10d of Marion et al., 1994).

The ray theoretical models (regardless of how long the wavelengths are) should be specified in blocks that are large or comparable to the wavelengths. So we need to construct the ray theoretical model for the next level of Backus averaging. To do so, we must compute the ray theoretical average of adjacent Backus averaging blocks. In this way, we use an effective ray calculation to estimate the effective ray theoretical model. For example, the Backus averages obtained in intervals 1', 2', and 3' in Figure X-4 will be averaged using the effective ray travel times through the formation. The results will be placed into the 1" interval and the process repeated for the other double prime intervals. The 1", 2", 3"... intervals will then represent the ray theory model for the next level of Backus averaging.

To compute the ray theory average of the elastic parameters through the three layers 1', 2', and 3', simple ray tracing will be implemented (through the three transversely isotropic layers). The effective travel times for various wave types (quasi-P, quasi-SV and quasi-SH) transmitted through the three layers will be computed. These travel times will then be used to compute the five effective elastic constants of a homogeneous, transversely isotropic interval that spans the three intervals (1', 2', and 3') obtained by Backus averaging of the FMI data. At this point we have a model that is described at wavelengths comparable to the bed thickness (sample interval) of the model. Thus the transversely isotropic intervals 1", 2", and 3", computed using ray theory averaging of the previous level of Backus averaging results, will be used as the input for computation of the next level of Backus averaging. As a result, the approach is intended to honor some physical details that are ignored in an approach based strictly on Backus averaging.

The type of ray tracing we want to accomplish involves finding the phase velocity rather than the group velocity (which is determined for standard ray tracing). At each interface, the horizontal component of wave motion will be assumed to be the same. A series of equations will be used to find the new velocity and the direction of the wave in the new medium. Once the direction and velocity of the wave in the second medium have been computed, the ray travel time through the interval can be computed. The process is repeated for all the intervals.

Once the necessary effective phase velocities have been computed, the effective elastic constants of the ray theoretical model can be computed. These elastic constants will be used as input for the next level of Backus averaging to predict elastic constants at even lower frequencies.

e. High Resolution Models of Low Frequency Velocity Curves

A traditional problem with any form of averaging is the low resolution of the output. This is not a serious problem when the curves are used to predict transmission velocities, since transmission is not as sensitive to small-scale changes. However, when the velocity models are being used to compute reflections at lower frequencies, the resolution of the velocity model has to be sufficient to identify and analyze important reflectors. A solution to this problem is the use of resolution matching methods described by Nelson and Mitchell (1991).

Each long wavelength estimate of the transversely isotropic parameters that apply at a particular frequency can be viewed as a different log reading. The long wavelength curves can be viewed as logs that have a low-resolution vertical response function (Nelson and Mitchell, 1991). The FMI-scale model can be viewed as the high-resolution log (comparable in resolution to the FMI). Using resolution matching, we can obtain a high-resolution estimate of the low frequency velocity curves. In this way, we will be able to predict low frequency velocity models that should preserve the character of the reflections as well as the transmissions.

Because both the high resolution (corresponds to a high frequency velocity) and low-resolution (low frequency velocity) "curves" represent the five transversely isotropic elastic constants, we may have to develop some special resolution matching techniques. For example, we may want to experiment with the way the high resolution log is filtered to predict the low-resolution estimate of the high-resolution log. One suggestion is the ray theory averaging described above.

f. Summary

Three methods of applying Backus averaging to the prediction of low frequency seismic velocities (surface and crosswell) have been described. All of the windowing approaches depend on calibration of the vertical velocities using plane wave solutions. However, the three approaches are not expected to yield the same relationship between crosswell velocities (even when their vertical velocities are forced to agree). Experimentation with plane wave solutions should be used to decide between the basic approaches.

Resolution matching will be used to develop a high-resolution model capable of accurately predicting reflections for low frequency velocity models. This allows us to bypass a major objection to long window averaging methods that effectively eliminate any information on reflected signals.

3. Direct Computation Methods

The methods based on Backus averaging described above offer some computational advantages, but it is difficult to know exactly what constitutes a long wavelength in

the Backus average. The best way to remove this uncertainty is by a direct computation of the elastic parameters of a formation using both ray theory and plane wave modeling. Ray theory can be used to estimate the elastic parameters of a formation that apply at high frequency. Plane wave modeling can be used to predict the elastic parameters at lower frequencies. First, we describe the computation of ray theoretical velocities (phase velocities) through a formation. Next, we describe how ray theoretical velocities and plane wave modeling at specific frequencies can be used to estimate the elastic parameters of a formation at other frequencies. The methods described in this section should be used when computer speed is not an issue.

a. Ray Theoretical Velocity

We will now discuss the ray theoretical or high frequency estimate of elastic parameters for a layered medium. Although the discussion applies to the particular case of computing ray theoretical velocity through a layered medium made up of isotropic layers, the same ideas can be extended to layered anisotropic media. Some aspects of the general problem will be mentioned in the summary of this section.

The ray theoretical velocity through a medium is defined here to be the high frequency (short wavelength) velocity through a layered medium, while the velocities obtained using Backus (1962) averaging represent a case where the wavelengths are much longer than the interval being considered. The value of computing the ray theoretical velocity and the Backus averaging velocity is that they give limiting values for the amount of elastic scattering expected through a formation.

Figure X-7 illustrates a layered medium bounded above and below by infinite half-spaces. The velocities of the layers and half-spaces are assumed to be known. The wavelengths are assumed to be comparable to or smaller than the thickness dimensions of the bed.

A ray is shown incident in the upper half-space at an incident angle θ. Snell's law applies at each interface within the layered medium

$$\frac{\sin\theta_0}{V_0} = \frac{\sin\theta_1}{V_1} = \frac{\sin\theta_2}{V_2} = \frac{\sin\theta_3}{V_3} = \ldots\ldots\ldots = \frac{\sin\theta_n}{V_n} = p \qquad \text{(Snell's Law),} \tag{67}$$

where p is referred to as the ray parameter.

The travel time $\Delta t(p)$ through the layered medium can be computed using (Kleyn, 1983):

$$\Delta t(p) = \sum_{i=1}^{Nlayers} \frac{\Delta D_i}{V_i \sqrt{1 - p^2 V^2{}_i}}. \tag{68}$$

The horizontal distance $\Delta X(p)$ traveled through the layered system is

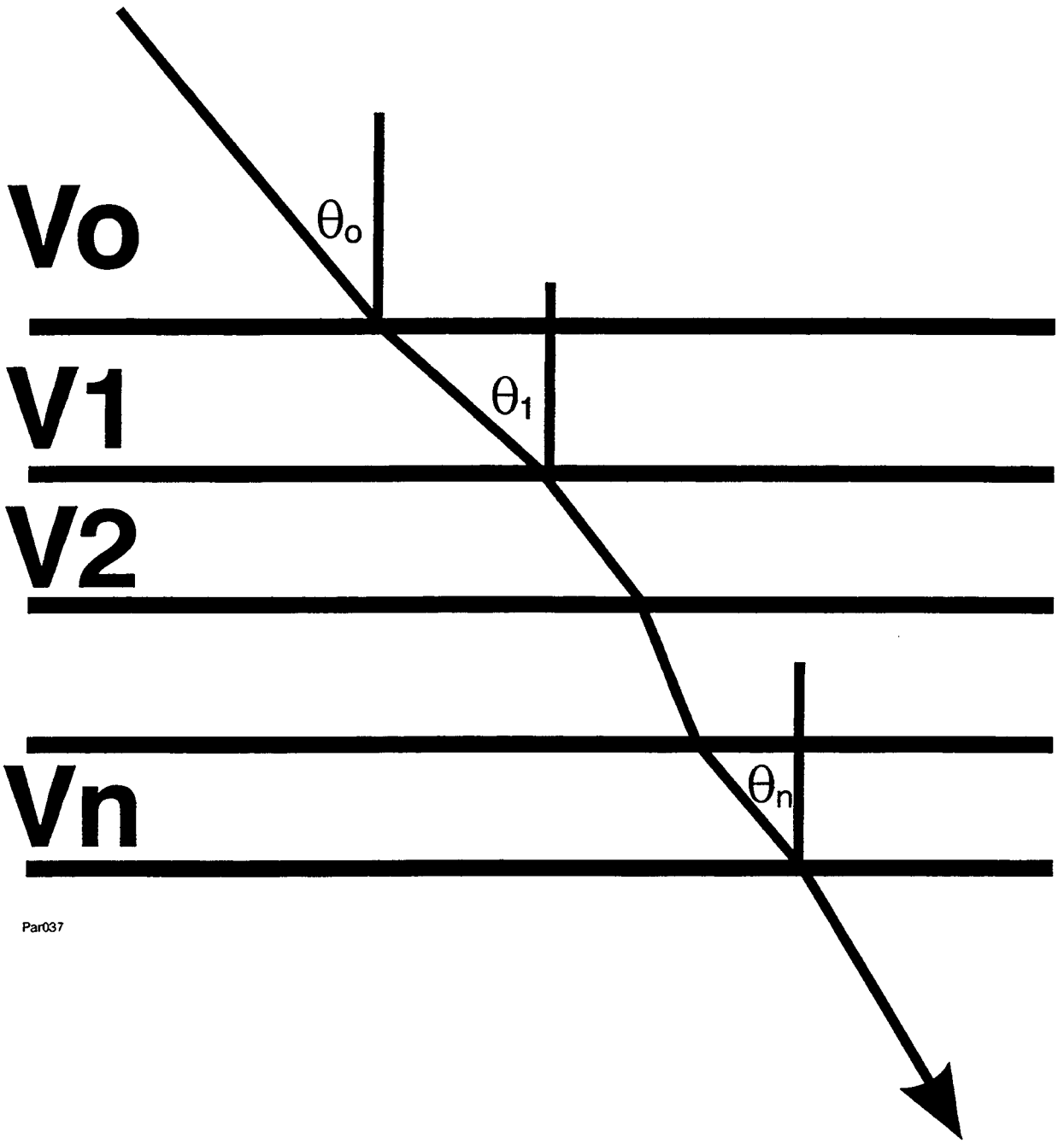

Figure X-7. Ray through layered medium.

$$\Delta X(p) = \sum_{i=1}^{Nlayers} \frac{pV_i \Delta D_i}{\sqrt{1 - p^2 V^2{}_i}}. \tag{69}$$

If D_{ist} = the total distance traveled through the system of layers and ΔD_{Total} is defined as the sum of the interval thickness,

$$\Delta D_{Total} = \sum_{i=1}^{Nlayers} \Delta D_i \tag{70}$$

then

$$D_{ist} = \sqrt{\left(\left(\Delta D_T\right)^2 + \left(\Delta X_T{}^2\right)\right)} \tag{71}$$

The ray theoretical velocity through the system of layers is simply the distance divided by the velocity (the average velocity through the layers)

$$V_{RT}(p) = \frac{D_{ist}}{\Delta t(p)} \tag{72}$$

The above equations can be used to compute the ray theoretical velocity through a layered formation as a function of the ray parameter p. Ultimately, the velocity at a certain angle of propagation through the formation is desired. The "ray theoretical velocity" is therefore open to interpretation, because the incident ray parameter depends on both the angle of incidence and the velocity of the upper half-space. Perhaps the best way to find the ray theoretical velocity would be in a self-consistent manner. The velocity of the bounding half-space can be chosen to be equal to the average velocity of the system of layers. Using this assumption, the direction of propagation through the formation can be determined uniquely.

b. Summary

The ray theoretical and Backus averaging velocities represent the high and low frequency velocities through a layered formation. These end-limit velocities allow a quick and easy estimate of the role of elastic scattering in a formation. Armed with these two velocities, it is possible to estimate the elastic scattering component at intermediate frequencies. The potential benefit of this study could be a fast and easy approach to estimating the role of elastic scattering without having to solve a complete wave equation problem. The ray theoretical ideas presented here can be extended to layered anisotropic media by tracing to find the phase velocity as would be measured in different directions through the formation. The resulting phase velocities represent the high frequency velocities through the formation and can be used to estimate important elastic constants for the medium using methods described in the next section.

C. Conclusions

During this portion of the study, funded by the Department of Energy, we developed: (1) methods for estimating accurate high resolution elastic models of the formations surrounding a borehole, and (2) methods for quantifying elastic scattering in the formation adjacent to a borehole.

To build an elastic model for the formation adjacent to the borehole, we developed software that could be used for the following purposes:

- To account for the dip of the borehole,
- To account for the dip of the formation, and
- To account for the low resolution of the logs.

Next, to estimate the effects of elastic scattering in the formation adjacent to the borehole, we developed the following algorithms:

- Multiple approaches for using Backus averaging,
- Ray theoretical methods for determining effective elastic constants, and
- Plane-wave modeling methods for determining effective elastic constants.

The results of this portion of the study give us the foundation for properly estimating the frequency-dependent elastic scattering velocities near a borehole. In particular, we can now estimate the component of elastic scattering dispersion and assume that the rest is due to intrinsic attenuation. In this way, we can study and model the intrinsic attenuation mechanisms that play a role in different lithologies.

XI. FIELD APPLICATION OF DATA INTEGRATION TECHNIQUES AT THE BUENA VISTA HILLS FIELD

A. Introduction

A 3D geostatistical reservoir model for the Buena Vista Hills field was built. A detailed cross sectional model was generated for the pilot area as shown in Figure XI-1 using the parameters from the field-scale model. The reservoir model for the pilot area incorporated geophysical data in the form of crosswell seismic velocity. The well locations for the entire field are shown in Figure XI-2. For this project, the steps followed for geophysical data integration are as follows:

- Construct full field model using well log and petrophysical data,
- Use variogram information from the full field model to generate a cross sectional model for the pilot area,
- Correlate porosity with sonic velocity as well as resistivity, and
- Generate resistivity distribution in the cross section using collocated cokriging.

B. Full Field Model

The available information was loaded in RC^2, a commercial software for geostatistical reservoir characterization, and a 3D porosity model was constructed. In Figure XI-3, a typical well log of the Buena Vista Hills field is shown. Figures XI-4 to XI-6 display the variograms used in construction of the 3D-kriged model between markers NA and P1A. Figure XI-4 shows the marker variograms for NA and P1A. Figure XI-5 shows the isotropic vertical variogram and Figure XI-6 presents the directional XY (surface) variogram. All these variograms were fitted to spherical models. After the 3D model was complete, cross sections were constructed. Figure XI-7 shows a cross section NW-SE and Figure XI-8 a cross section SW-NE for the whole field. Figure XI-9 shows a cross section NW-SE for the pilot area.

C. Correlation Porosity-Velocity at the Injector Well

Before discussing the process of trying to find the best possible correlation between the compressional wave velocity (delta of time, ms/ft), or DTCO, and porosity, it is important to mention the source of the porosity information. Porosity curves were generated via a transform from the Spontaneous Potential (SP) log to V_{shale} and subsequently from V_{shale} to porosity. The correlation coefficient was 0.649[1].

GRACE[2], a non-parametric correlation package developed at Texas A&M University, was used to complete the task of finding the best possible correlation between porosity and sonic velocity. The results are summarized in Table 1.

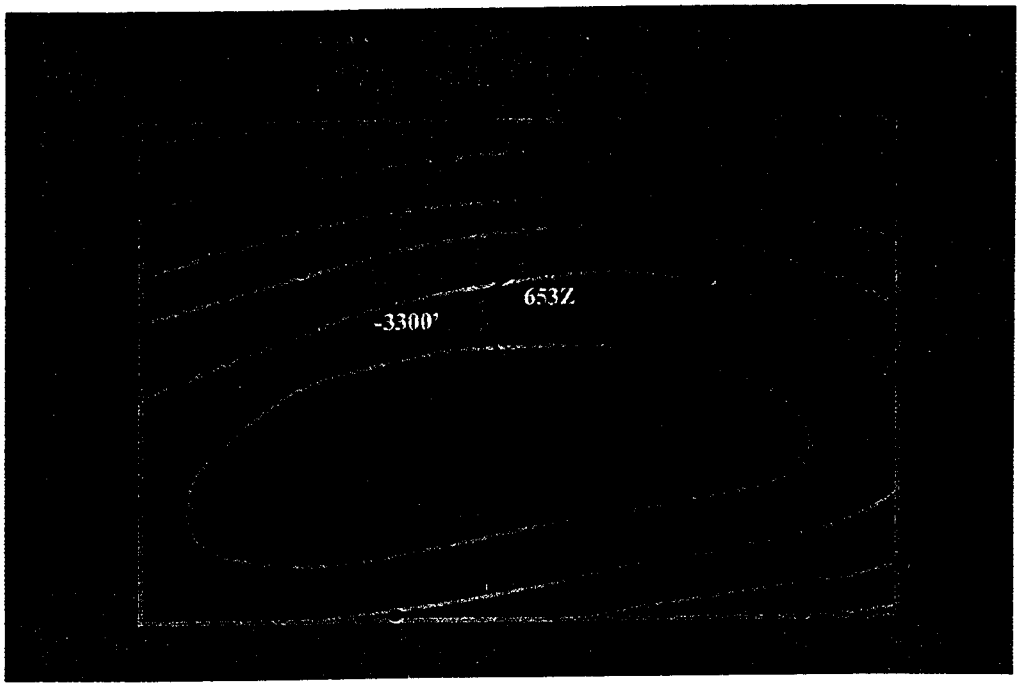

Figure XI-1. Structure contour at point "P," Buena Vista Hills Field.

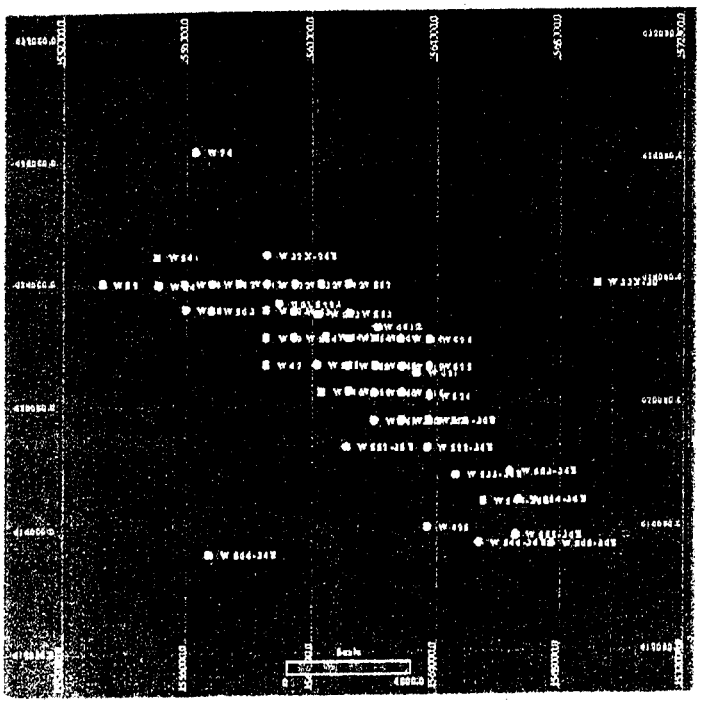

Figure XI-2. Buena Vista Hills Field.

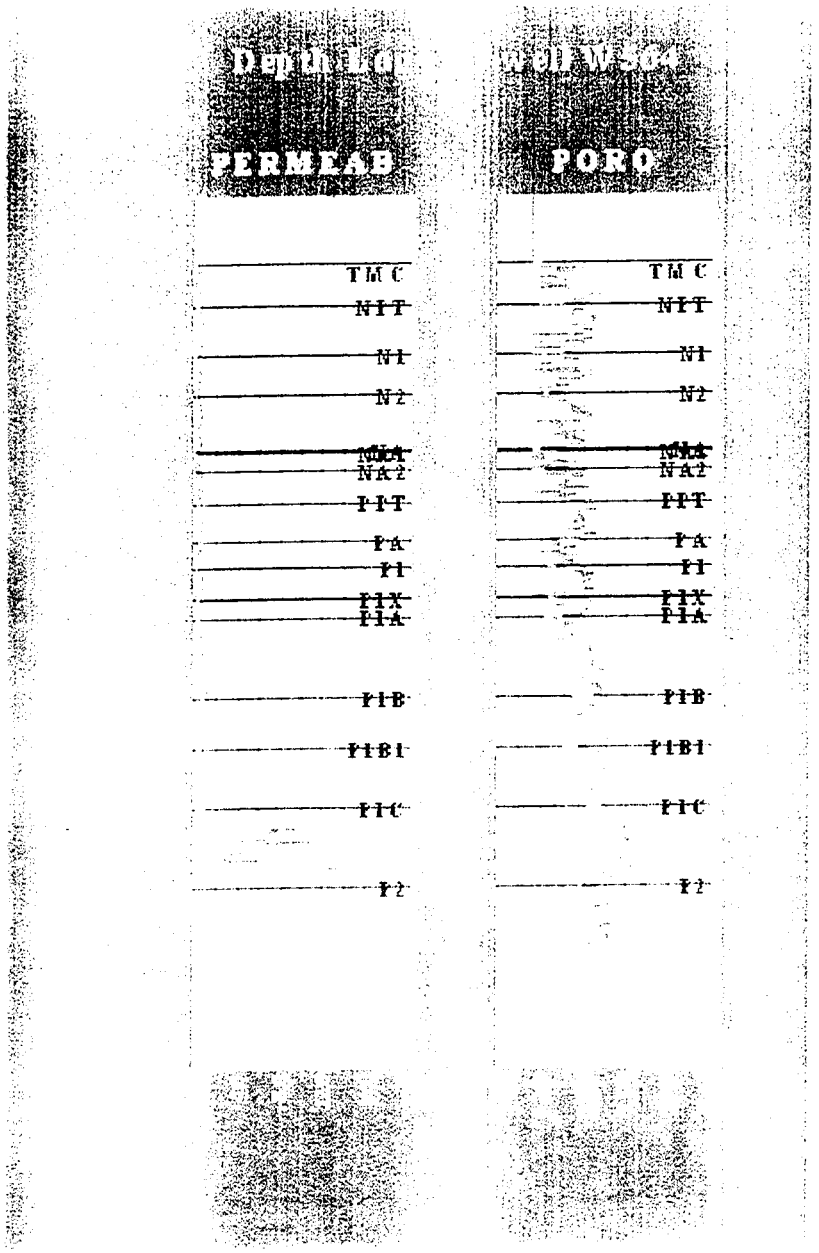

Figure XI-3. Typical well log from Buena Vista Hills Field.

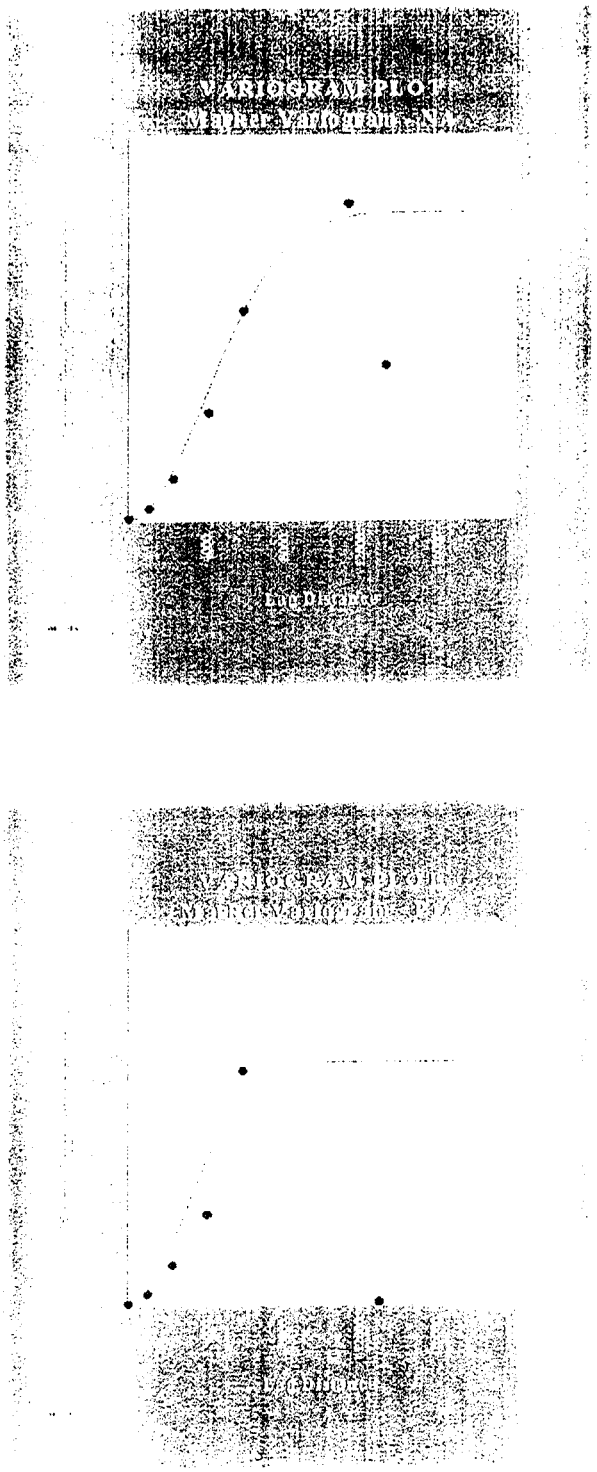

Figure XI-4. Marker variograms for NA and PAT.

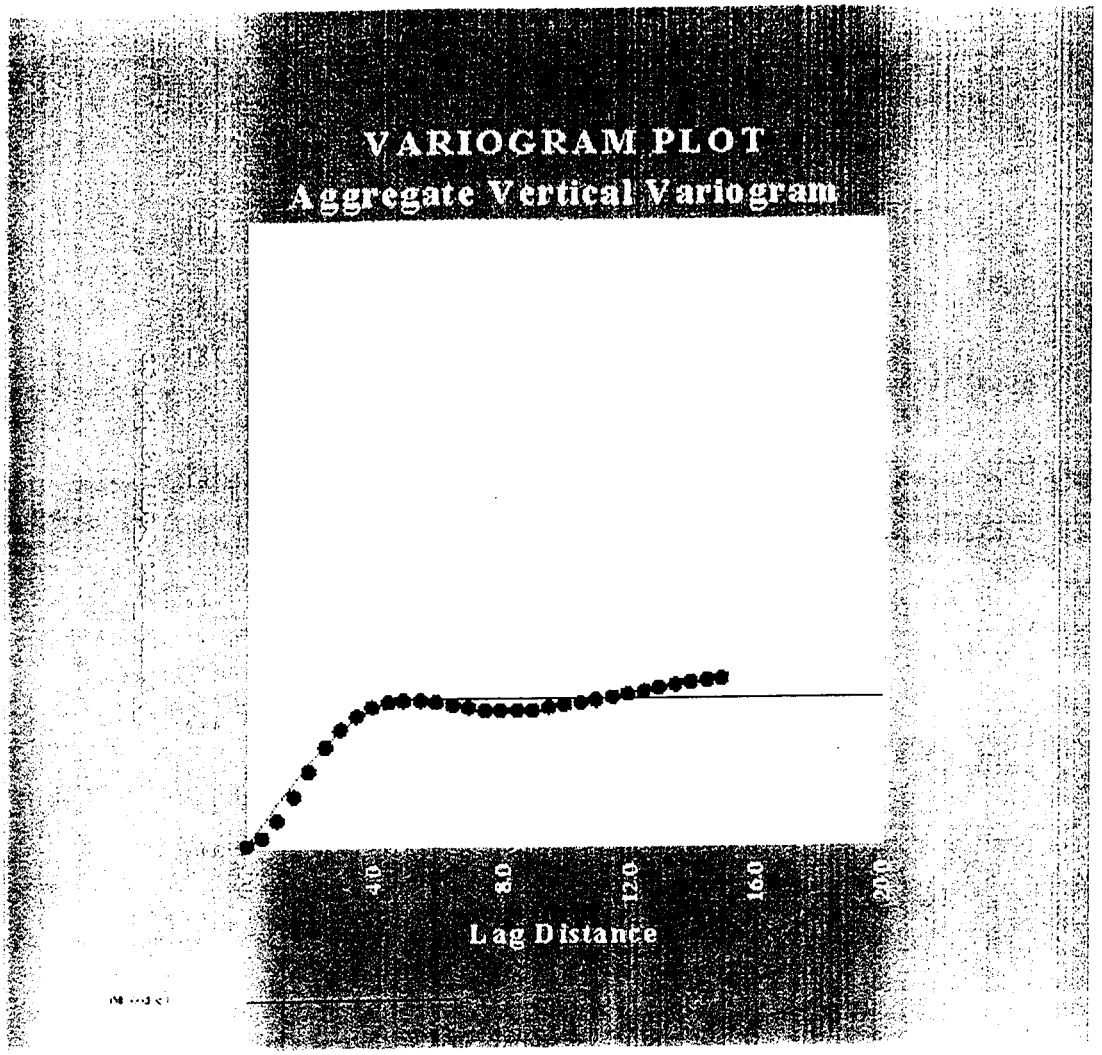

Figure XI-5. Isotropic vertical variogram.

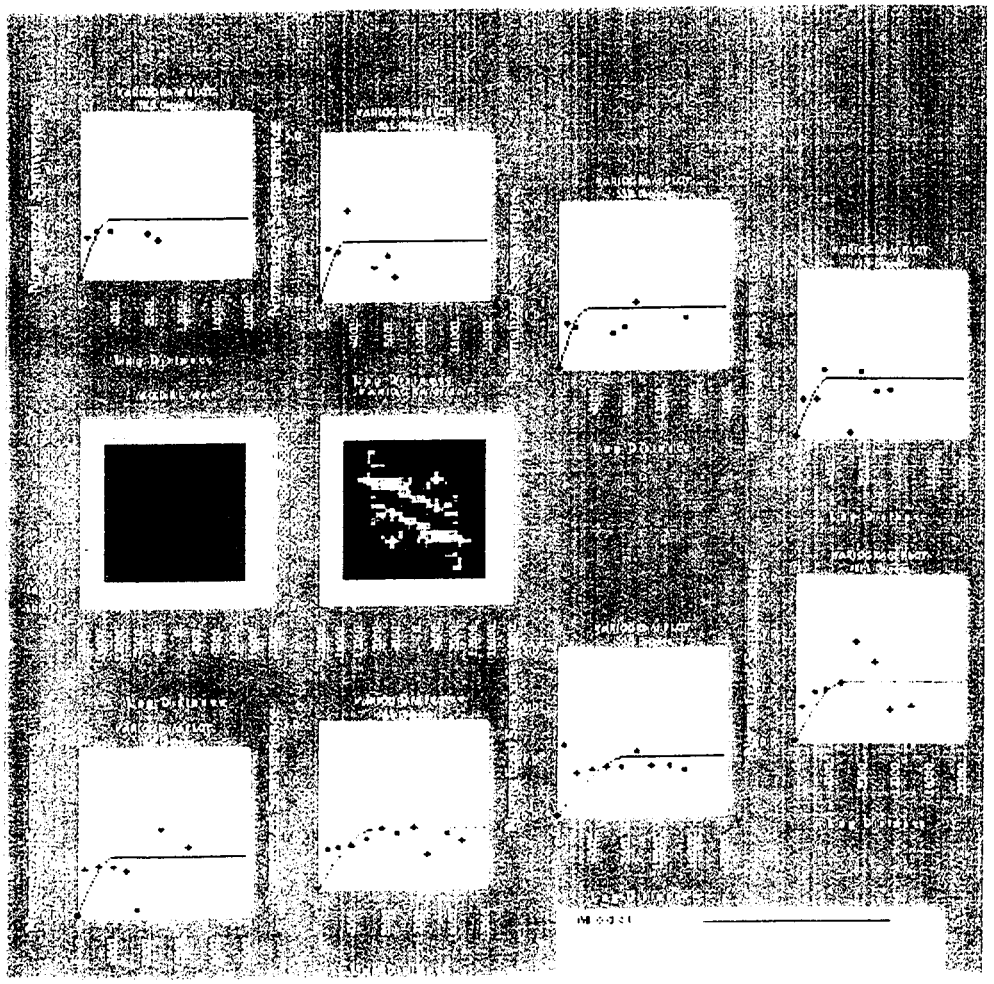

Figure XI-6. Directional surface variogram.

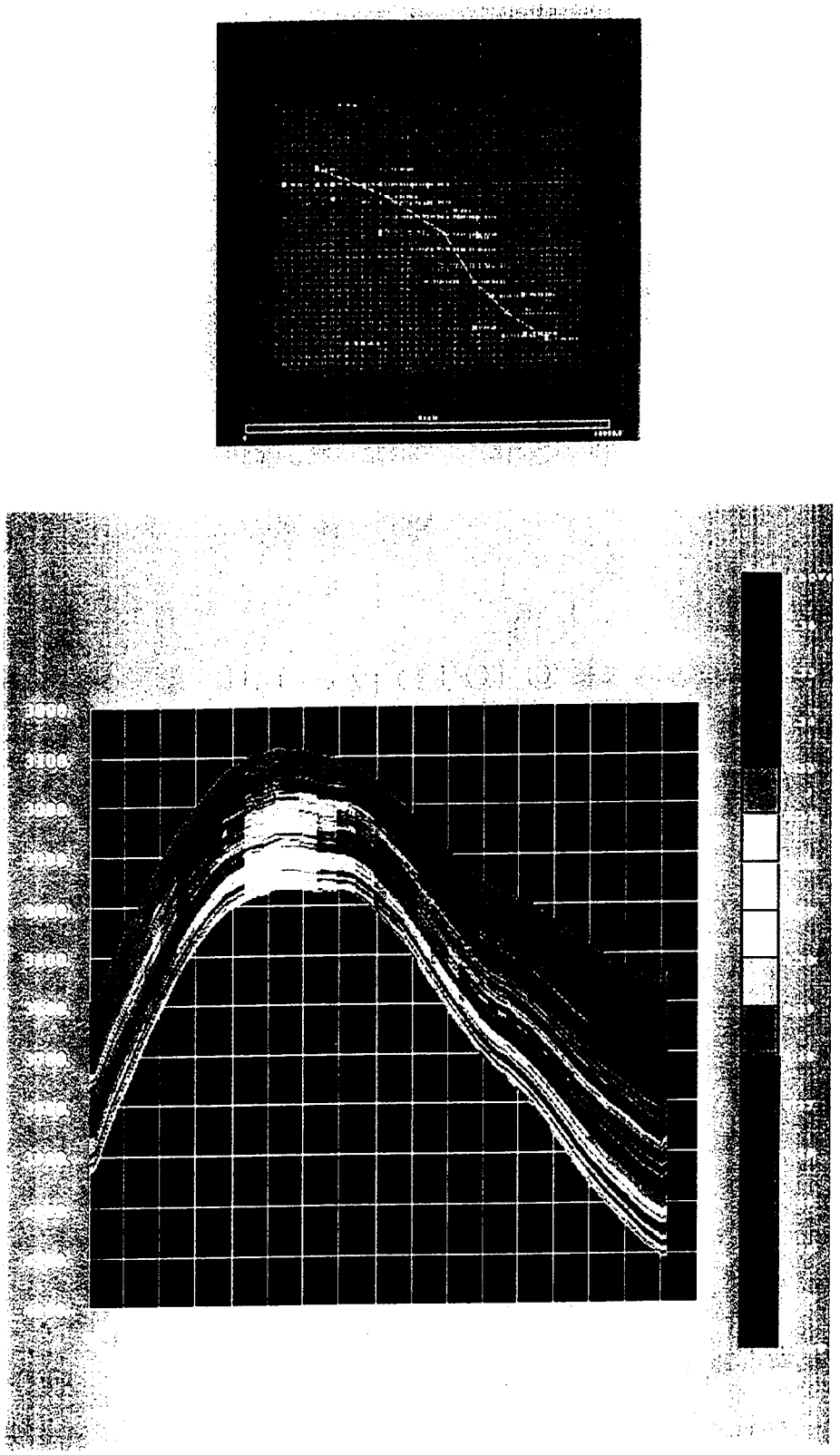

Figure XI-7. NW-SE cross-section for the whole field.

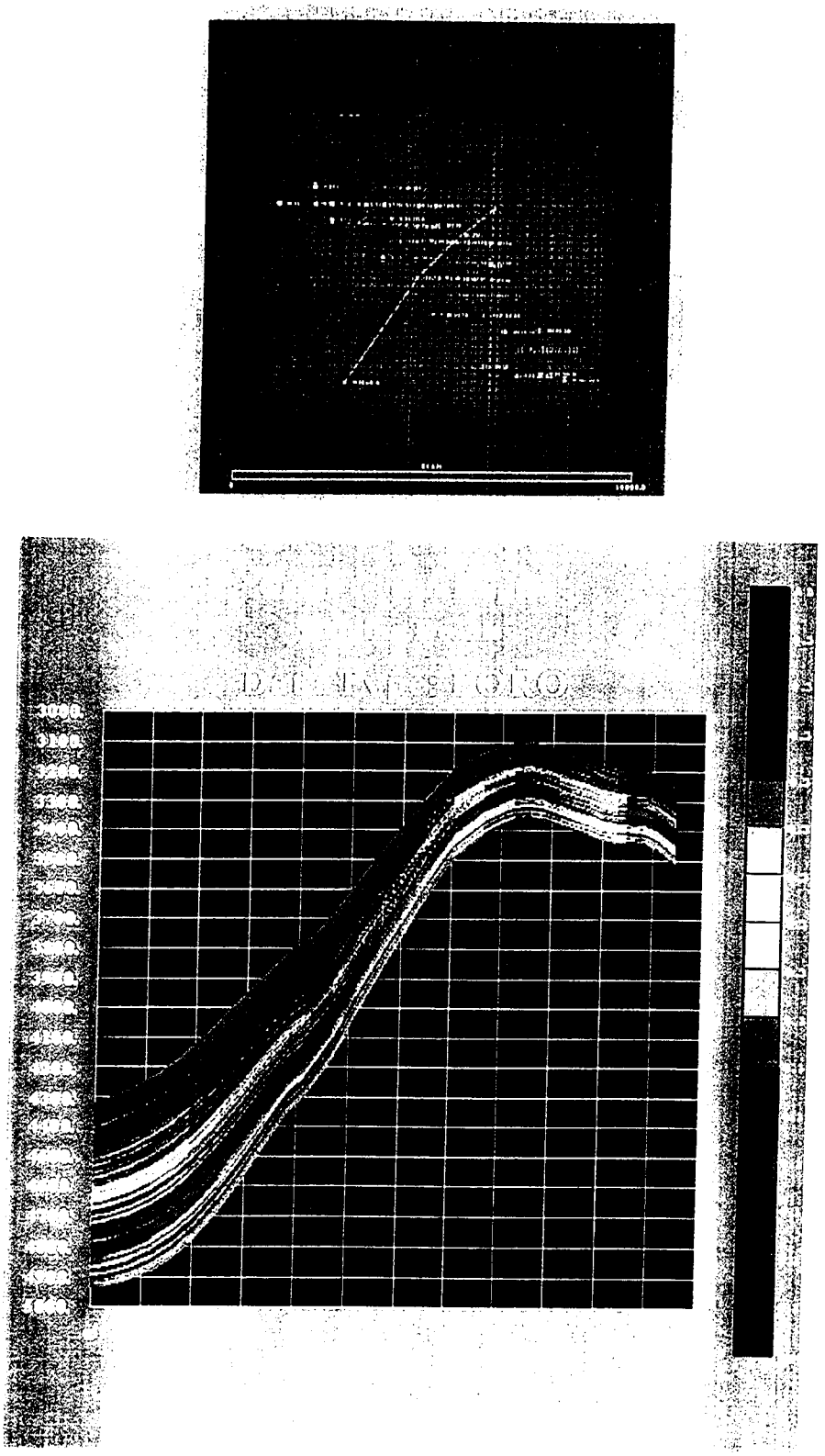

Figure XI-8. SW-NE cross-section for the whole field.

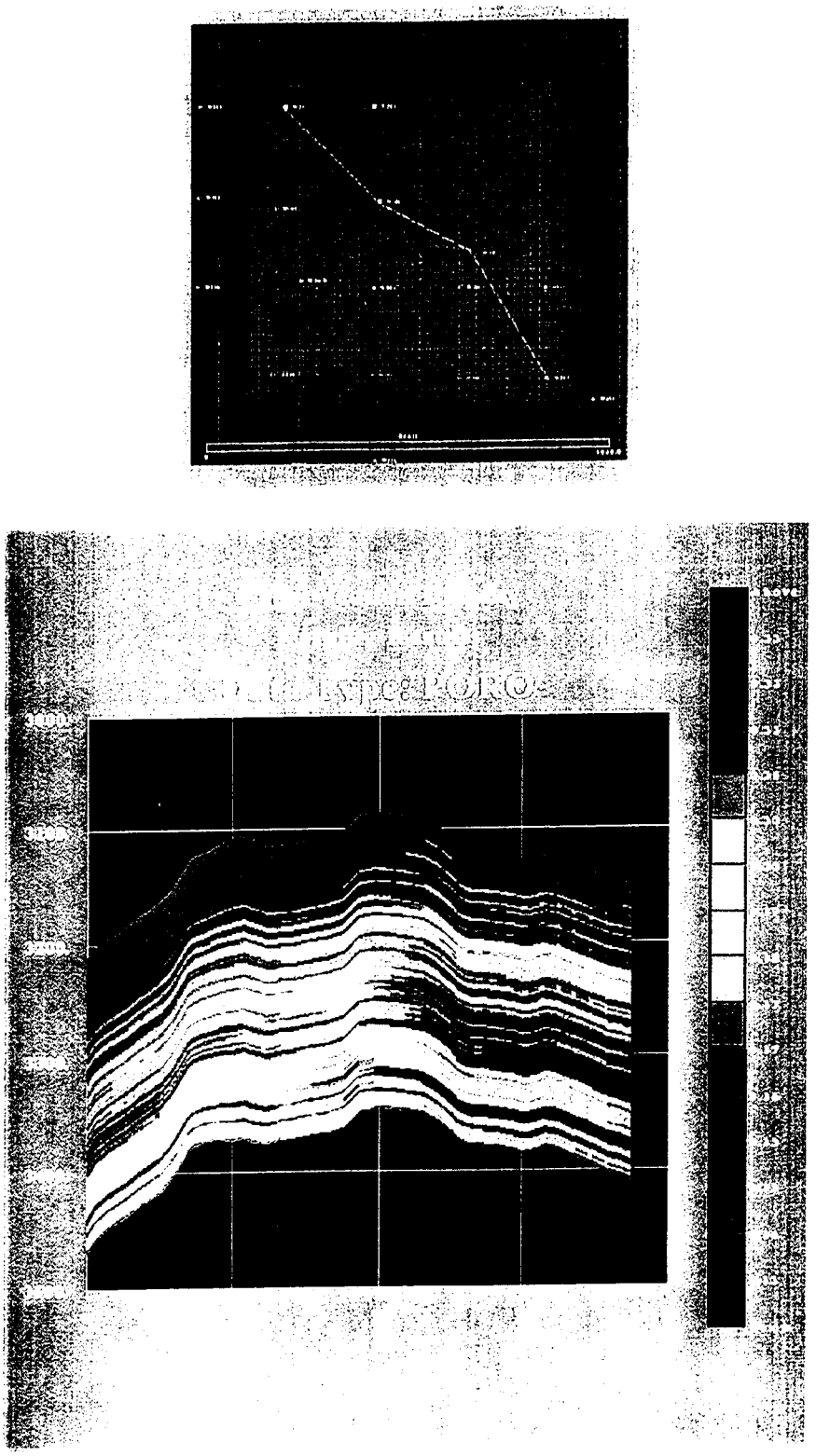

Figure XI-9. NW-SE cross-section for the pilot area.

Table1

	Procedure	Scatterplot ϕ-Vel	*GRACE*
1	Data without default values	0.010	0.041
2	Data, taking out velocities > 9500	0.118	0.211
3	Data, taking out porosities > 0.3	0.119	0.309

Figures XI-10 and XI-11 show the scatterplot porosity-velocity and porosity and velocity vs depth, respectively, for the last case. Figure XI-12 shows the fit achieved with ***GRACE***.

D. Correlation Resistivity-Velocity at Injector Well

The correlation obtained at well 653Z was unsatisfactory. For this reason an attempt at correlating sonic velocity and resistivity was made. The first step of this procedure was to choose from among *AF10, AF20, AF30, AO10, AO20,* and *AO30* (estimators of *Rxo*) the one that exhibits the best relationship with ***DTCO***. Figure XI-13 shows that *AF30* achieved the best fit. The next step is to improve this relationship by adjusting depth. Table 2 shows the depth intervals of shifting sonic velocity.

Table 2

Interval	Shifting Up
3970-4125	5
4125-4173	1
4281-4283	1
4835-4845	2

In Figure XI-14, a significant improvement in the resistivity-sonic velocity relationship is shown. The final step was to run the adjusted data in ***GRACE***. The results are shown in Figure XI-15. A summary of the correlation coefficient (R^2) calculated by simply plotting the scatterplot and by running ***GRACE*** is reported in the Table 3.

Table 3

Case	R^2	Correlation Coefficient
Raw data	0.053	0.230
Shifting	0.384	0.620
GRACE	0.555	0.745

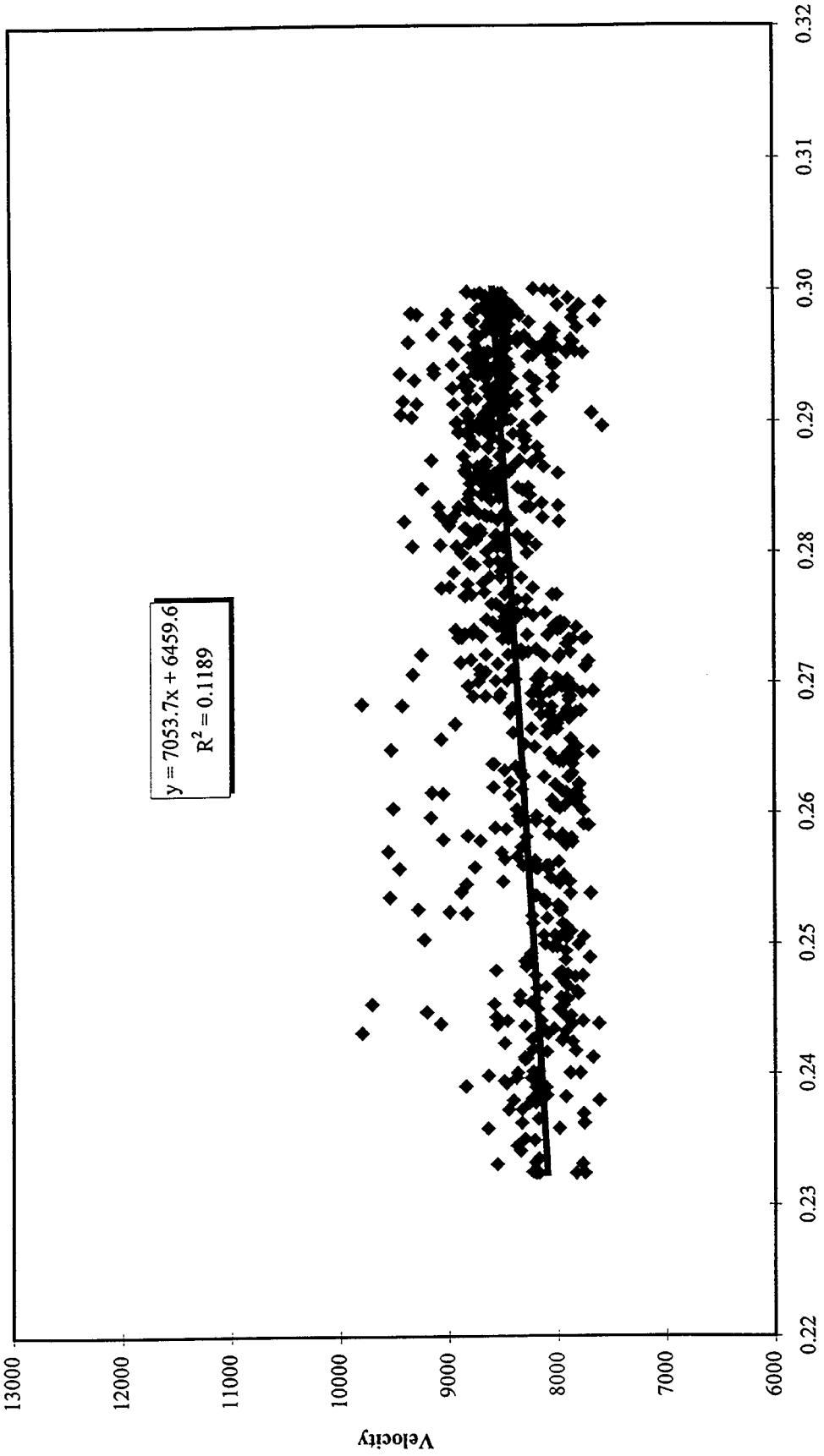

Figure X-10. Scatterplot porosity-velocity.

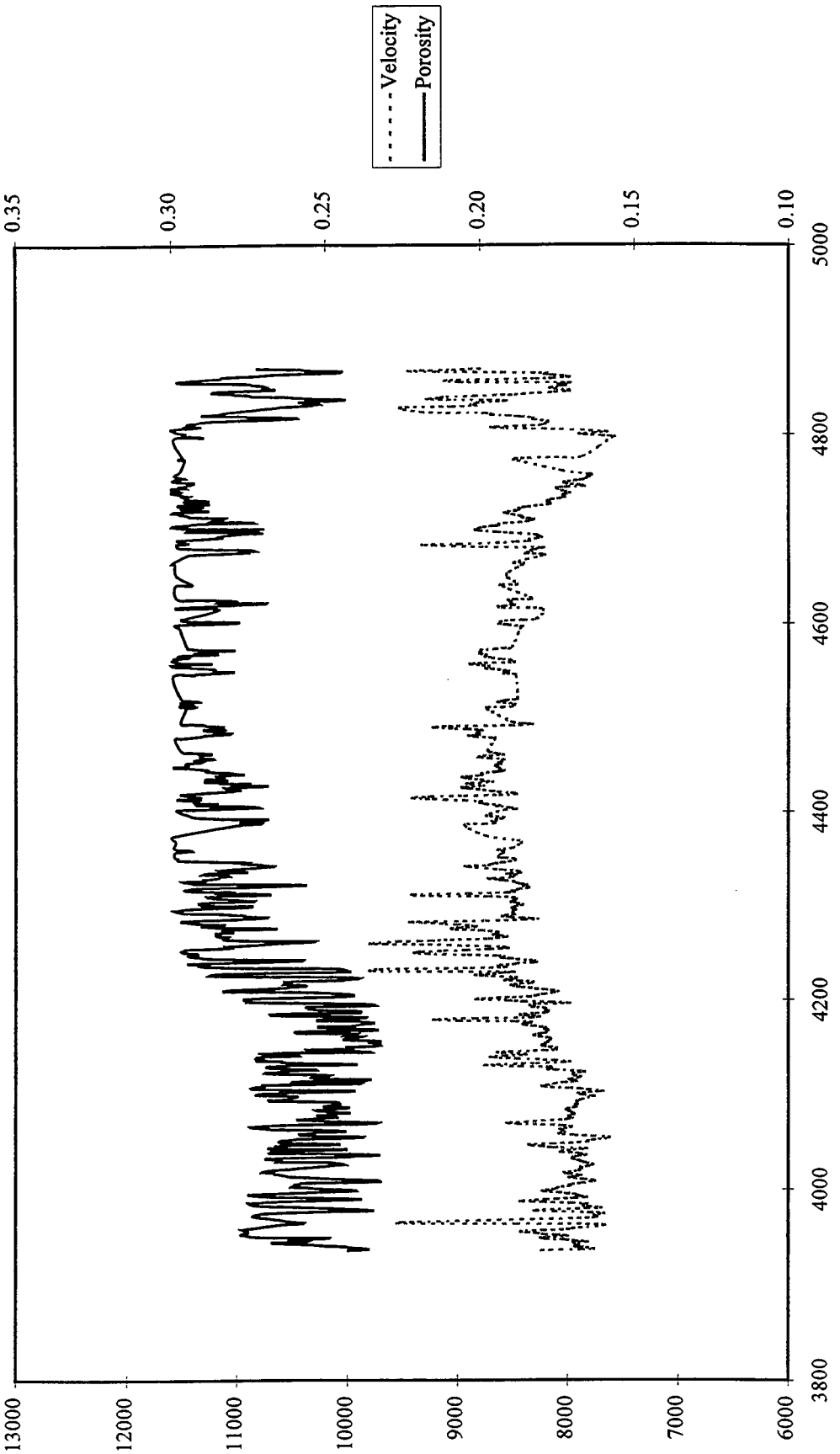

Figure X-11. Porosity and velocity vs depth.

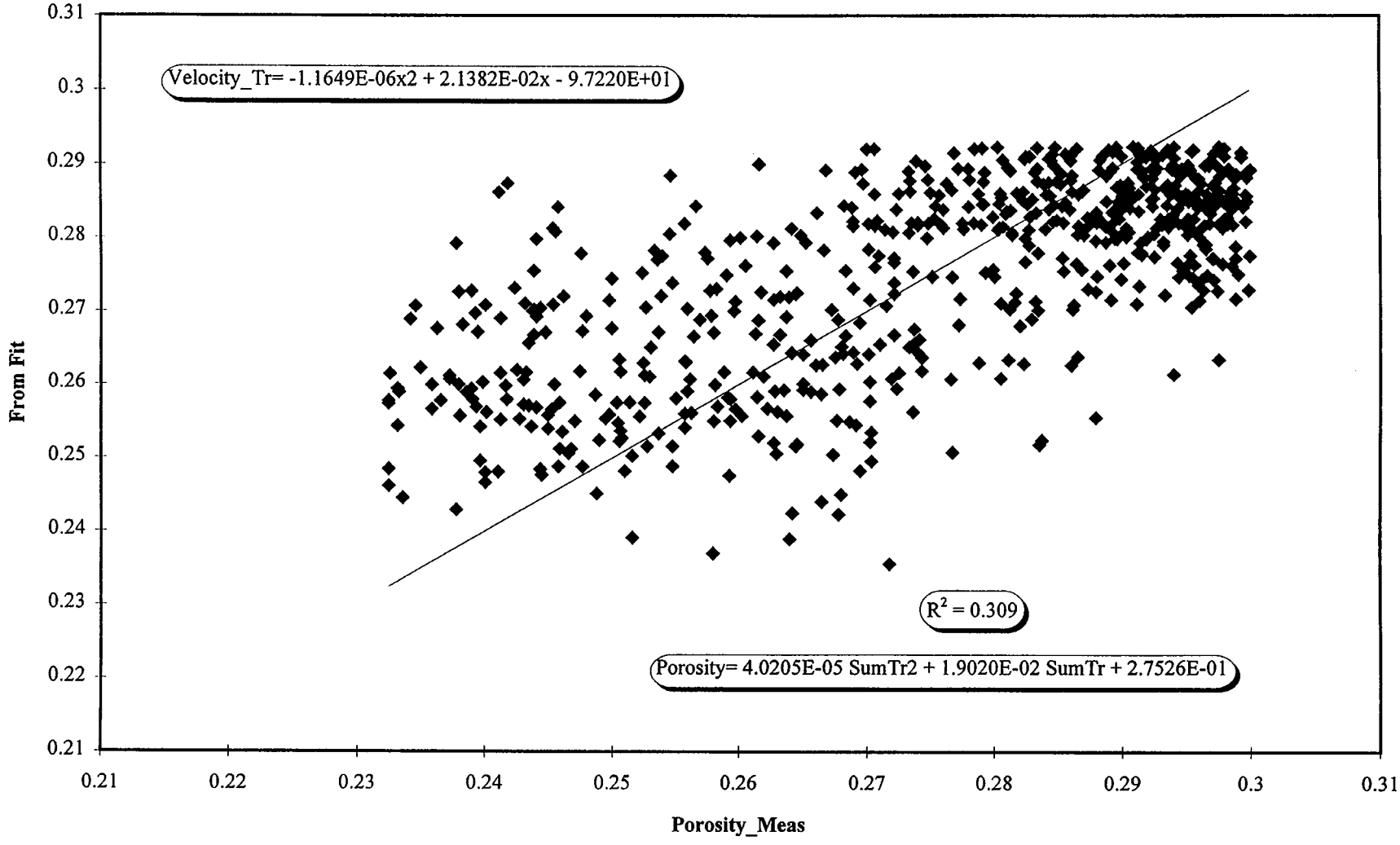

Figure X-12. Porosity measurement obtained by using GRACE.

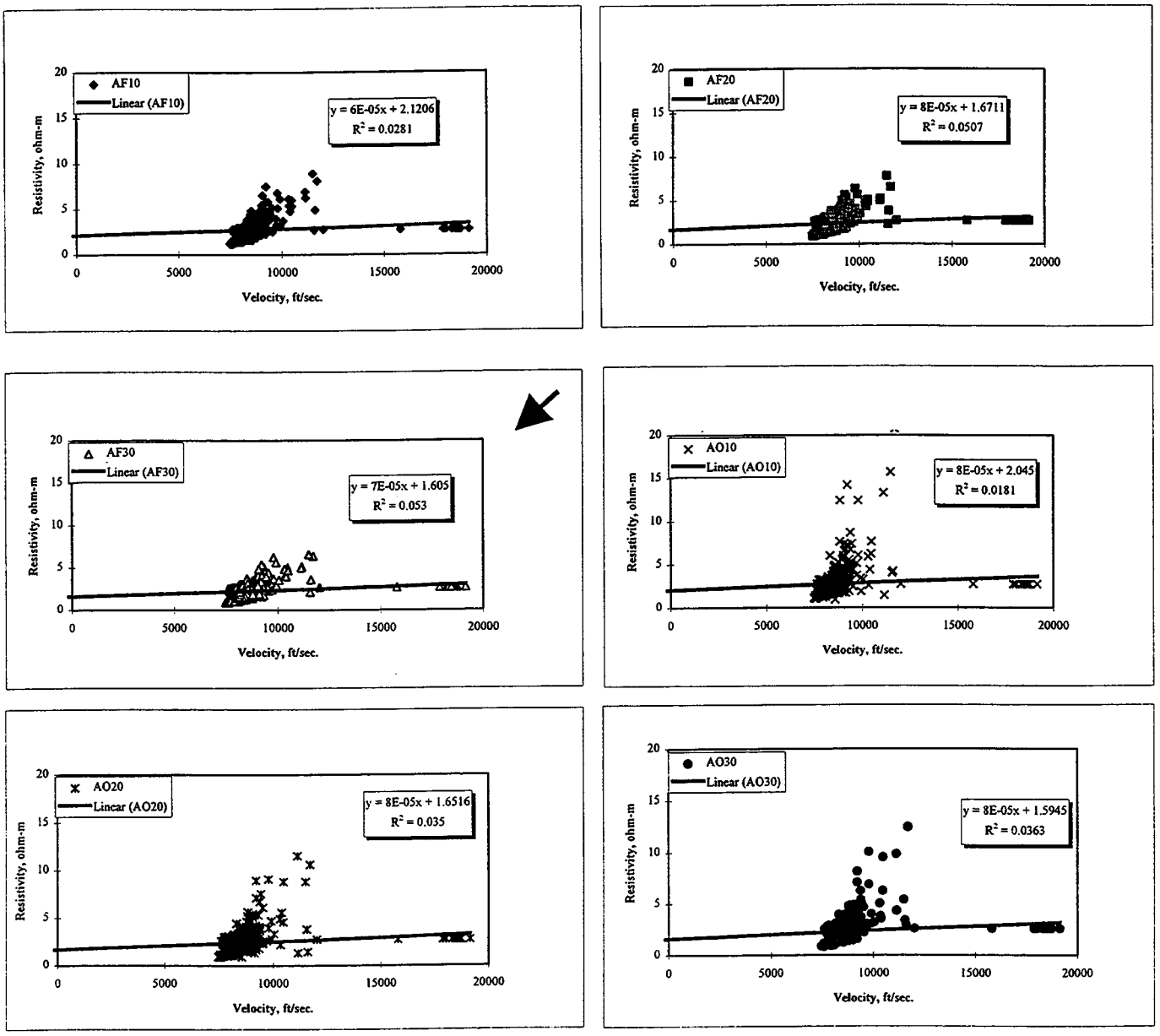

Figure XI-13. Selection of the best estimator of Rxo.

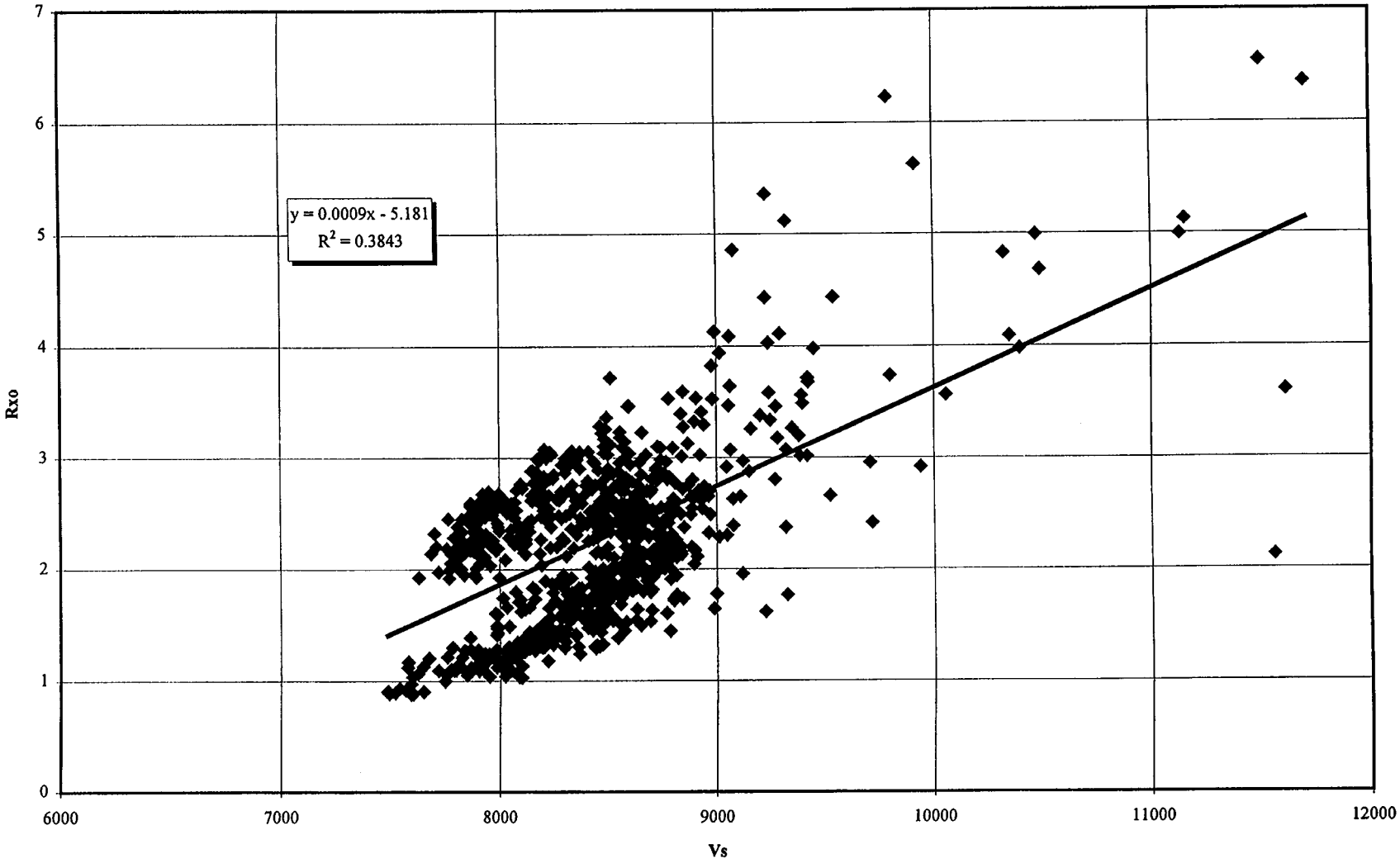

Figure X-14. Rxo vs sonic velocity after depth adjustment.

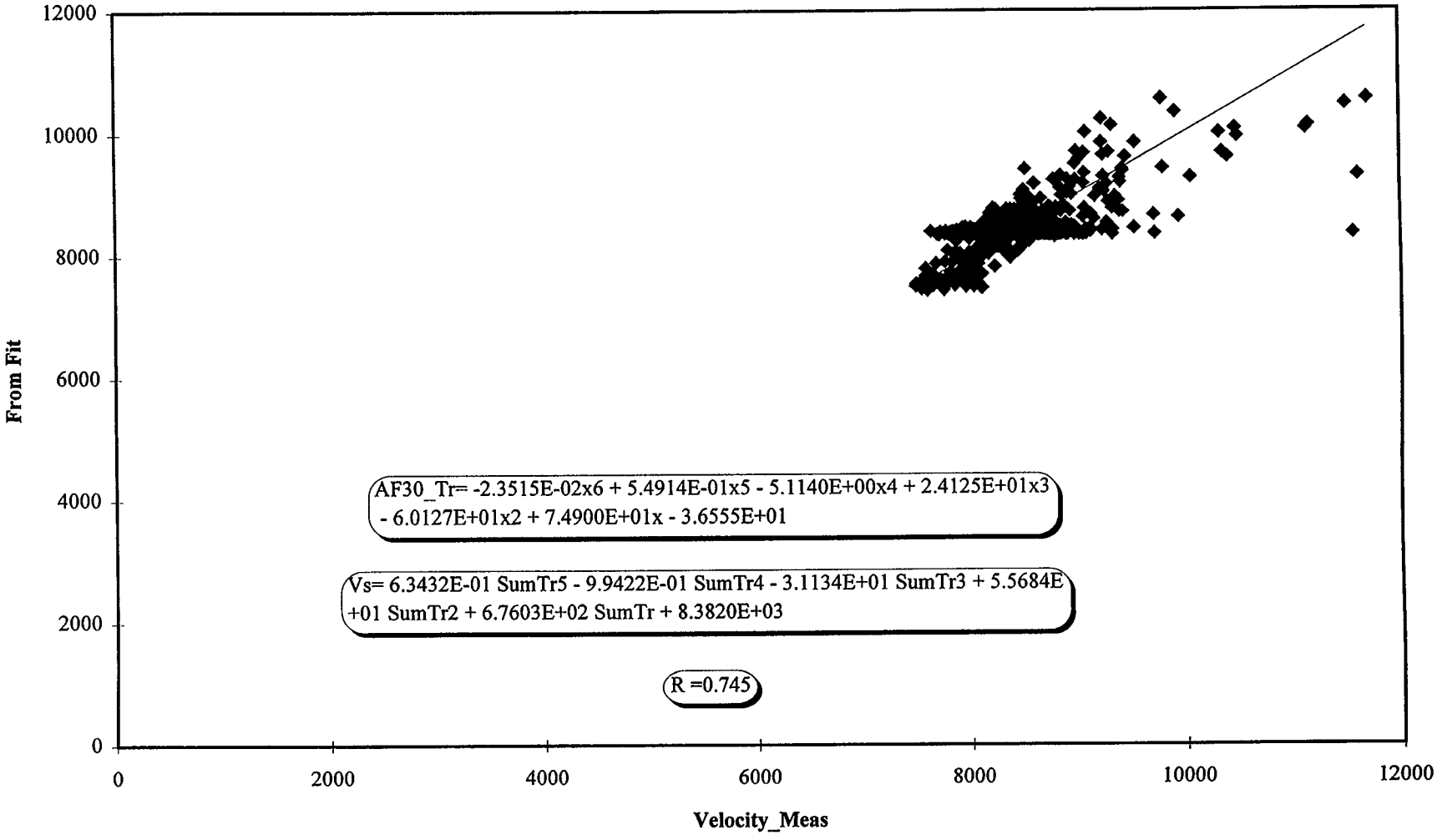

Figure X-15. Velocity measurement obtained by using GRACE.

E. Determination of the Resistivity Surface

Collocated cokriging is a reduced form of cokriging, which requires knowledge of only the hard data covariance model and the linear correlation coefficient between the hard and soft data. Although it is a kriging technique, a linear model of coregionalization is not required. This implies that a primary data variogram, a secondary variogram, and a cross variogram do not need to be jointly modeled, a highly problematic and time-consuming practice. In this case, the cross section between well 553 and well 653Z was analyzed. The hard data taken was *Rxo*, the soft data was the seismic velocity available (crosswell velocity or CWV), and the linear correlation coefficient was based on the previously derived correlation between sonic velocity and *Rxo*. The model used consists of 33 cells in the *X* direction and 100 cells in the *Y* direction. A sketch of the model is shown below:

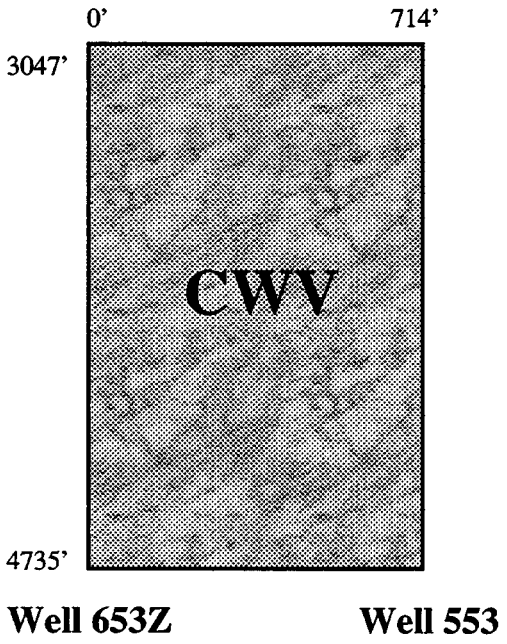

Figure XI-16 shows the CWV (secondary variable) surface, and the directional variogram is displayed in Figure XI-17. The parameters found for the directional variogram are summarized in Table 4.

Table 4

Model	Spherical
X-Range	571.43 ft
Y-Range	1600 ft
Alpha	47.5 °
Sill	0.89
Nugget	0.0

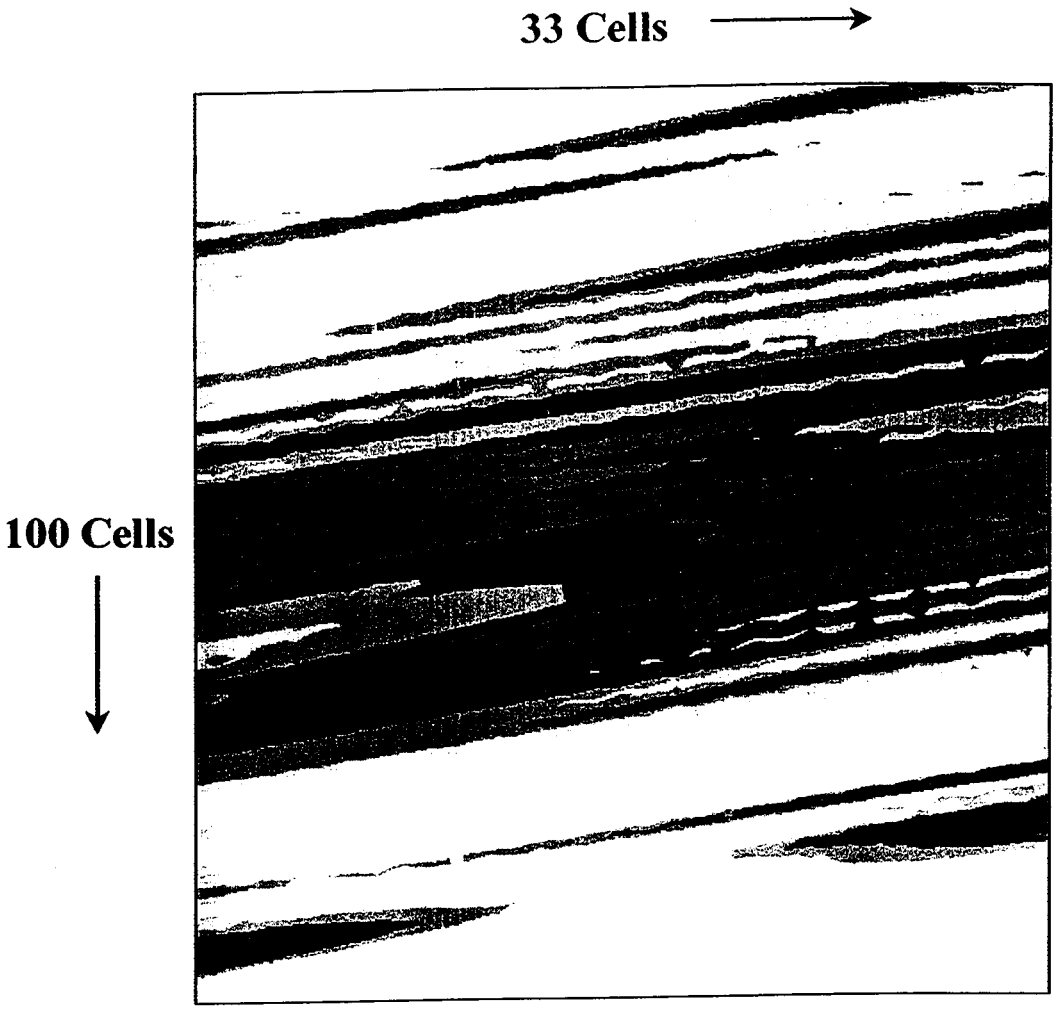

Figure XI-16. Crosswell Velocity surface between well 553 and well 653Z.

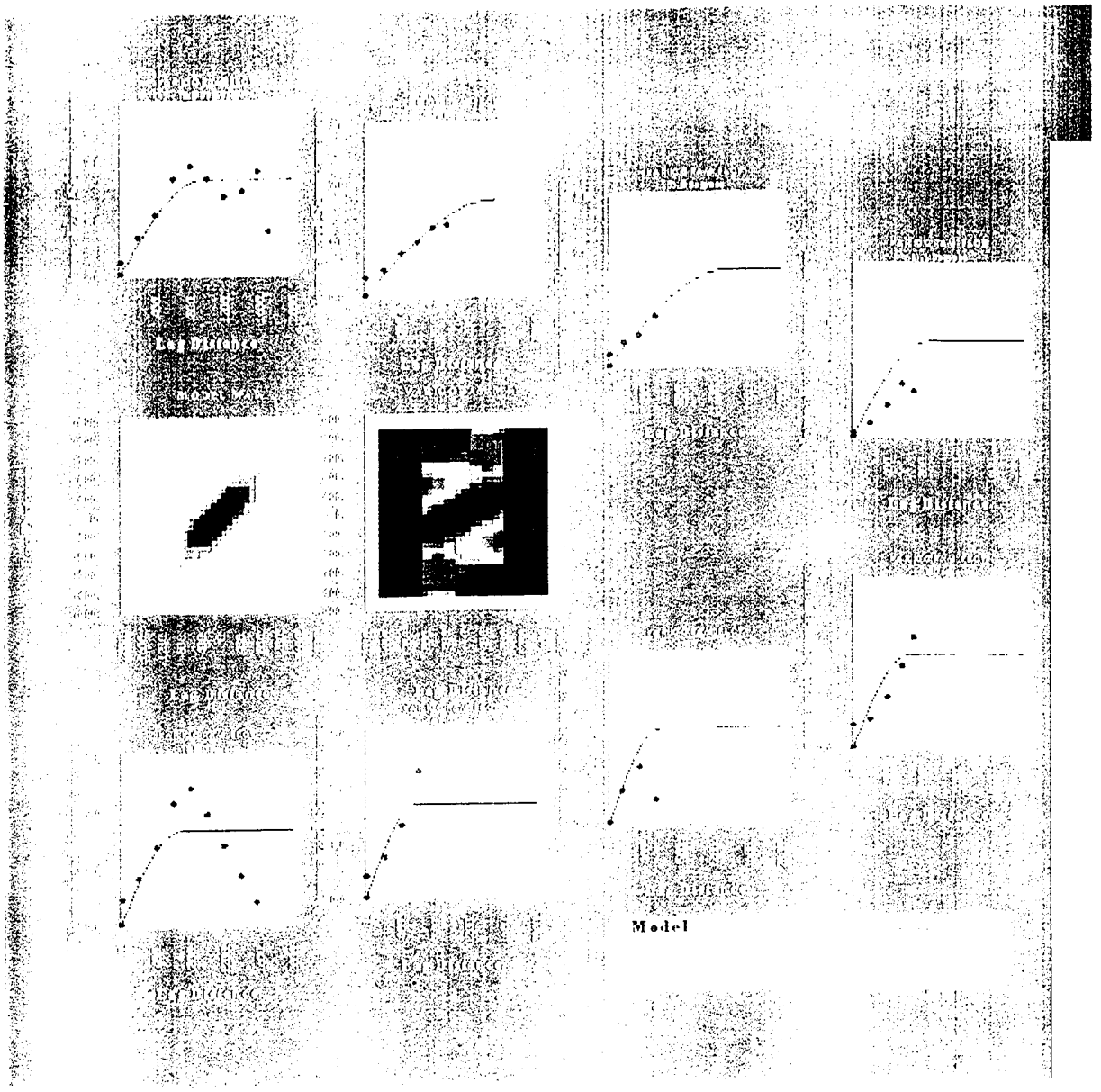

Figure XI-17. Directional variogram of the hard data.

As a result of collocated kriging, a surface map of *Rxo* was derived for the cross section of wells 553 and 653Z. This map is shown in Figure XI-18. Two extra scenarios are shown in Figures XI-19 and XI-20 for lower and higher correlation coefficients, 0.37 and 0.87 respectively, between *Rxo* and sonic velocity.

To calculate the water saturation map of the cross section, an attempt was made at finding a correlation between water saturation and resistivity based on the available well data. However, the correlation was found to be unsatisfactory. A possible reason of the unsatisfactory quality of the correlation obtained at well 653Z for porosity-velocity is the source of the porosity information. Porosity information is not measured data, but a result of mathematical manipulation that adds a certain degree of uncertainty. In this project, porosity curves were generated via a transform from the Spontaneous Potential (SP) log to Vshale and subsequently from Vshale to porosity and the correlation coefficient found in this process was 0.649.

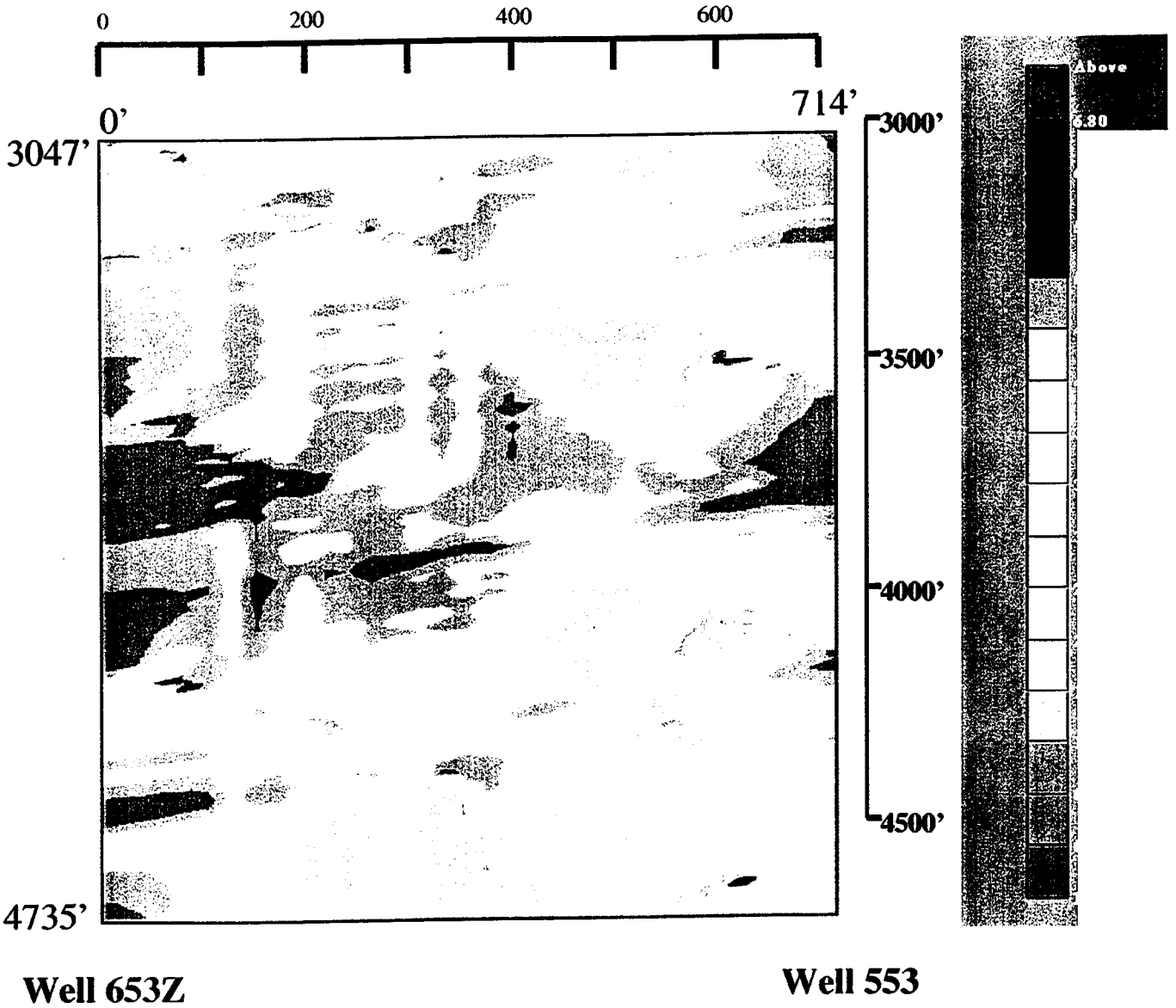

Figure XI-18. Rxo (resistivity) map using a correlation coefficient of R=0.62.

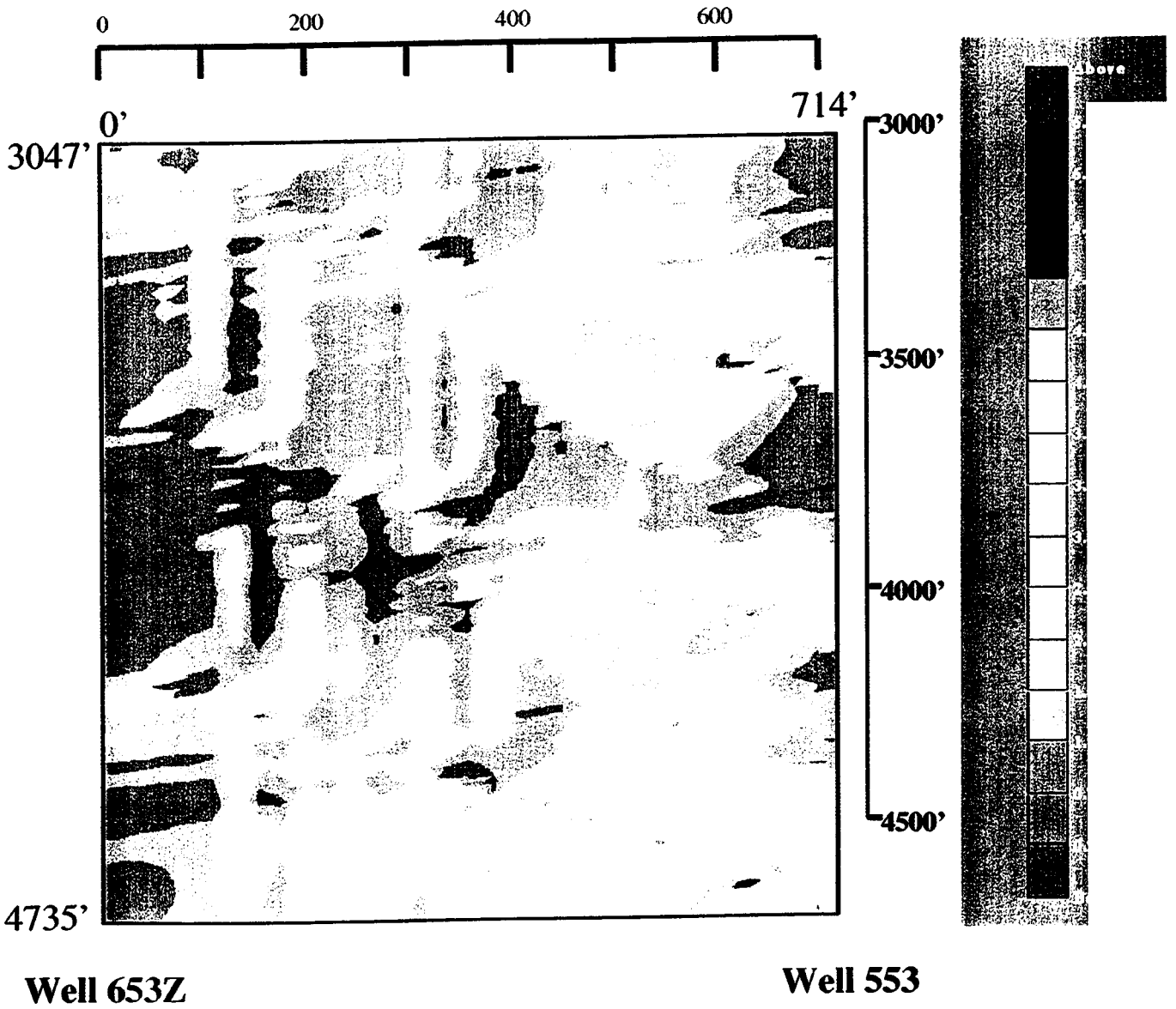

Figure XI-19. Rxo (resistivity) map using a correlation coefficient of R=0.37.

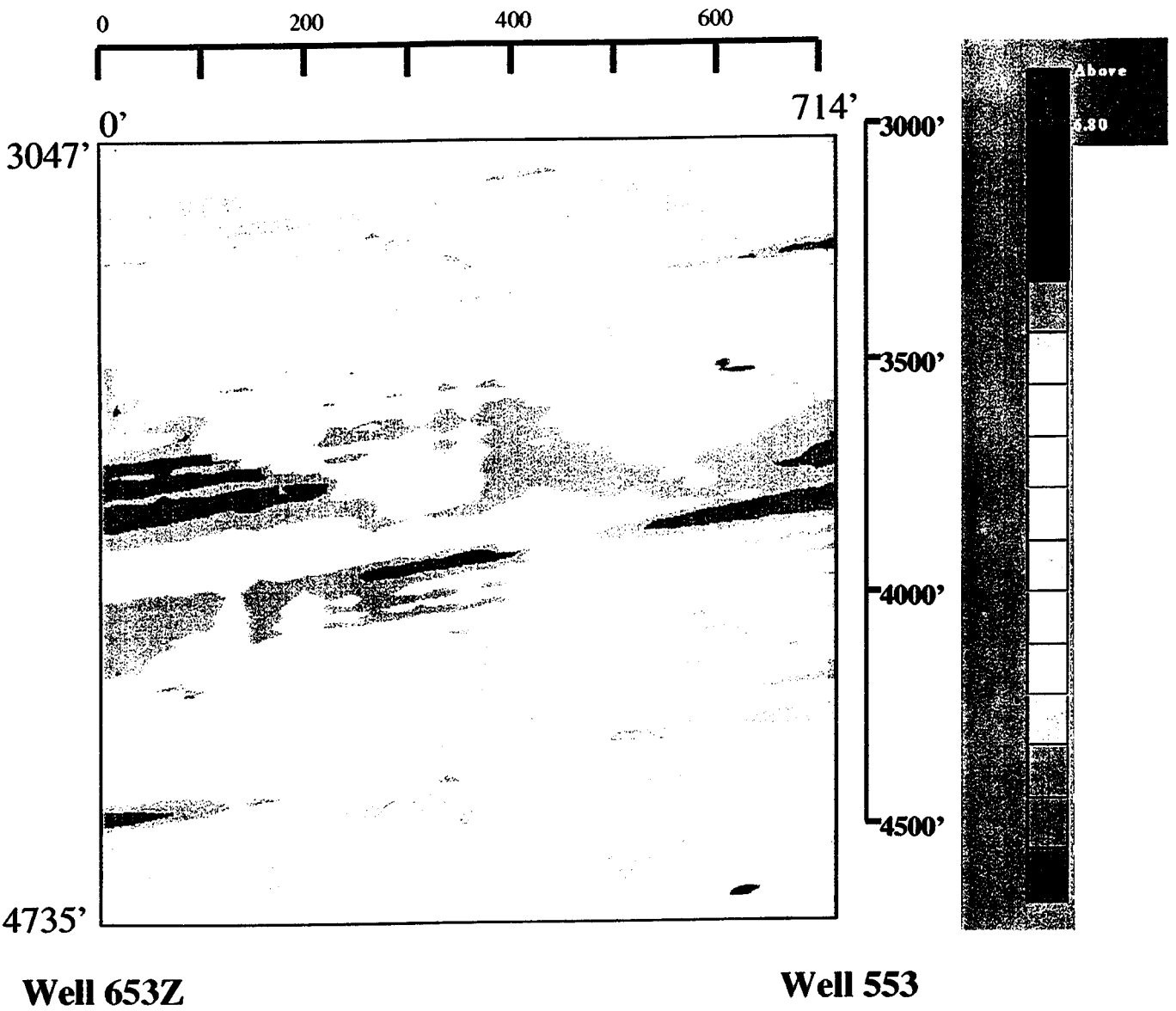

Figure XI-20. Rxo (resistivity) map using a correlation coefficient of R=0.87.

XII. CONCLUSIONS

The integration of petrophysics and geophysical data at the Buena Vista Hills fields confirms that numerous beds of sandstones and dolomites are correlatable over distances of the CO_2 pilot flood area. In particular, the tomographic images capture the stratigraphic sequences of the sandstone and dolomite formations as high velocity anomalies. Integration of the lithology and the images reveals the separation between these two geological units.

Resolution enhancement techniques were implemented and applied to Buena Vista Hills well log data. The results show the great potential of resolution matching techniques for providing high resolution information to characterize reservoirs at different scales. However, these techniques should be used with caution in reservoirs with a high degree of small variability. In particular, we have used resolution matching techniques using FMI and sonic data to provide elastic parameters at two scales to predict effective anisotropy and dispersion. On the basis of these results, we have developed a methodology that will lead to improved imaging of reservoir properties.

An analysis of the Buena Vista Hills data has shown the basic feasibility of this new method. To be successful, however, we must be able to obtain precise and accurate well log and anisotropy information from field measurements. We also expect this method to be better suited to reservoirs where the scale of the structure is more comparable to seismic wavelength.

In addition, modeling techniques based on the poroelastic wave equation with azimuthal anisotropy have been verified using crosswell data from the fractured Kankakee limestone reservoir in Illinois. The velocity dispersion data shows that fluid flow in the limestone is controlled by vertical fractures. Alternatively, the flow in a low-velocity zone within the Kankakee formation is controlled by porosity. We also modeled this velocity dispersion data using a solution based on acoustic waves propagating in media with randomly varying properties. The solution was verified using the velocity dispersion data. The modeling results showed that the strong dispersion in the low frequency range is caused by the scattering effects of reservoir heterogeneity, and the intrinsic effects (at higher frequencies) are caused by the viscoelastic properties of the reservoir. We expect that these two modeling techniques can be used to interpret dispersion and attenuation data from other type of heterogenous and fractured reservoirs.

We also related petrophysical properties and fracture distribution within the Twin Creek reservoir to seismic signatures. The petrographic and petrophysical analyses demonstrated that most fracturing occurs in dolomitic mudstone rocks and that an increase in dolomitization and a decrease in silt content correspond to an increase in fracturing. A high-velocity anomaly observed in the velocity inversion image correlates with a fracture zone intercepted by a horizontal well. As a result of this analysis, we conducted interwell seismic modeling for planning crosswell seismic measurements at the Lodgepole field. These measurements have the potential to delineate high velocity anomalies associated with small fractures zones.

XIII. REFERENCES

Aki, K., and Richards, P. G., 1980, *Quantitative Seismology: Theory and Methods*, Vol. I, W. H. Freeman and Co., New York, pp. 177-180.

Backus, G. E., 1962, "Long-wave elastic anisotropy produced by horizontal layering," *Journal of Geophysical Research*, Vol. 67, pp. 4427-4440.

Biot, M.A., 1955, "Theory of elasticity and consolidation for porous anisotropic solid," *Journal of Applied Physics,* Vol. 26, pp. 182-185.

Biot, M.A., 1962, "Generalized theory of acoustic propagation in porous dissipative media," *Journal of the Acoustical Society of America*, Vol. 34, pp. 1254-1264.

Bruce, C. L., 1988, "Jurassic Twin Creek Formation: a fractured limestone reservoir in the Overthrust Belt, Wyoming and Utah" *Rocky Mountain Association of Geologists*, pp. 105-120.

Carcione, J.M., Kosloff, D., and Behle, A., 1991, "Long-wave anisotropy in stratified media: a numerical test," *Geophysics,* Vol. 56, pp. 245-254.

Dvorkin, J. and Nur, A., 1993, "Dynamic poroelasticity: a verified model with the squirt and the Biot mechanisms," *Geophysics*, Vol. 58, pp. 523-533.

Esmersoy, C., Hsu, K., and Schoenberg, M., 1989, "Quantitative analysis of fine layering effects: medium averaging versus synthetic seismograms," Expanded Abstracts, 59th Annual Meeting of the Society of Exploration Geophysicists, Dallas, Texas.

Ganley, D. C., and Kanasewich, R. R., 1980, "Measurements of absorption and dispersion from check shot surveys," *Journal of Geophysical Research*, Vol. 85, pp. 5219-5226.

Harding, T.P., 1974, "Petroleum traps associated with wrench faults," *AAPG Bulletin*, Vol. 58, No. 7, pp. 1290-1304.

Helbig, K., 1984, "Anisotropy and dispersion in periodically layered media," *Geophysics*, Vol. 49, pp. 364-373.

Helbig, K., 1983, *Foundations of Anisotropy for Exploration Seismics, Vol. 22, Handbook of Geophysical Exploration, Section 1: Seismic Exploration*, Pergamon Press, Elsevier Science, Inc., Tarrytown, New York, 486 pages.

Hsu, K., Esmersoy, C., and Schoenberg, M., 1988, "Seismic velocities and anisotropy from high-resolution sonic logs," Expanded Abstracts, 59th Annual Meeting of the Society of Exploration Geophysicists, Dallas, Texas, pp. 114-116.

Hsu, K., Kurkjian, A., and Wiggins, R., 1988, "Tool deconvolution and borehole compensation of sonic measurements," Expanded Abstracts, 59th Annual Meeting of the Society of Exploration Geophysicists, Dallas, Texas, pp. 117-120.

Kalbfleisch, J. G., 1985, *Probability and Statistical Inference, Volume 1: Probability*, Springer-Verlag, New York.

Kerner, C., 1992, "Anisotropy in sedimentary rocks modeled as random media," *Geophysics*, Vol. 57, No. 4, pp. 564-576.

Kleyn, A.H., 1983, *Seismic Reflection Interpretation*, Applied Science Publishers, New York, 269 pages.

Landau, L. D., Lifshitz, E. M., and Pitaevskii, L. P., 1984, *Electrodynamics of Continuous Media*, Pergamon Press, New York, 2nd Edition, Vol. 43.

Leaney, W.S., 1994, "AVO and anisotropy from logs and walkaways," Exploration of Geophysicists.,Vol. 24, pp. 623-630.

Marion, D., Mukerji, T., and Mavko, G., 1994, "Scale effects on velocity dispersion: from ray to effective medium theories in stratified media," *Geophysics*, Vol. 59, pp. 1613-1619.

Melia, P.J., and Carlson, R.L., 1984, "An experimental test of P-wave anisotropy in stratified media," *Geophysics*, Vol. 49, pp. 374-378.

Morea, M.F., 1997a, "Advanced reservoir characterization in the Antelope Shale to establish the viability of CO_2 enhanced oil recovery in California's Monterey Formation siliceous shales," 1997 Second Quarter Report to DOE.

Morea, M.F., 1997b, "Advanced reservoir characterization in the Antelope Shale to establish the viability of CO_2 enhanced oil recovery in California's Monterey Formation siliceous shales," 1997 Third Quarter Report to DOE.

Morea, M.F., 1998, "Advanced reservoir characterization in the Antelope Shale to establish the viability of CO_2 enhanced oil recovery in California's Monterey Formation siliceous shales," 1997 Fourth Quarter Report to DOE.

Nelson, R. J., and Mitchell, W. K., 1991, "Improved vertical resolution of well logs by resolution matching," *The Log Analyst*, Vol. 32 No. 4, pp. 339-349.

O'Doherty, R.F., and Anstey, N.A., 1971, "Reflections on amplitudes," *Geophysical Prospecting*, Vol. 19, pp. 430-458.

Owen, T.E., and Parra, J.O., 1993, "Comparison of high-resolution wax embedded and pneumatically coupled borehole seismic detectors," *Geophysics*, Vol. 58, pp. 141-153.

Parra, J. O., 1995, "A feasibility study of high-resolution reverse VSP and interwell seismic methods for hydrocarbon reservoir characterization," *The Log Analyst*, May-June, pp. 164-181.

Parra, J.O., 1997, "The transversely isotropic poroelastic wave equation including the Biot and the squirt mechanisms: Theory and application," *Geophysics*, Vol. 62, No. 1, pp. 309-318.

Parra, J.O., 1998, "Dispersion and attenuation of acoustic waves in poroelastic media with azimuthal anisotropy," paper submitted to *Geophysics*.

Parra, J. O., 1998, "Dispersion of acoustic waves in poroelastic media with azimuthal anisotropy," Paper presented at the Biot Conference on Poromechanics, Universite Catholique de Louvain, Louvain-la-Neuve, Belgium, Sept. 14-16.

Parra, J. O., Ababou, A., Sablik, M. J., and Hackert, C. L., 1998a, "Elastic Wave Propagation in Random Geological Media: 1D Solution," submitted to *Journal of Applied Geophysics*.

Parra, J.O., Collier, H., Richards, T., 1997, "Seismic signatures of the fractured Twin Creek reservoir," 67th Ann. Internat. Mtg. Soc. Expl. Geophys., Expanded Abstracts, Dallas, Texas.

Parra, J. O., Hackert, C. L., Ababou, R., and Sablik, M. J., 1998b, "Seismic wave propagation in a randomly heterogeneous media: theory," submitted to *Journal of Applied Geophysics*.

Parra, J.O., Zook, B.J., and Collier, H.A., 1996, "Interwell seismic logging for formation continuity at the Gypsy Test Site, Oklahoma," *Journal of Applied Geophysics.*, Vol. 35, pp. 46-62.

Ryan-Grigor, S., 1997, "Empirical relationships between transverse isotropy parameters and Vp/Vs: Implications for AVO," *Geophysics*, Vol. 62, pp. 1-6.

Saito, H., 1991, "Anisotropic travel-time tomography at the Buckhorn Test Site, Illinois," Expanded Abstract, 61st Annual International Meeting of the Society of Exploration Geophysicists, pp.123-126.

Sams, M.S., 1995, "Attenuation and anisotropy: The effect of extra fine layering," *Geophysics,* Vol. 60, No. 6, pp. 1646-1655.

Sams, M.S., and Williamson, P.R., 1994, "Backus averaging, scattering and drift," *Geophysical Prospecting*, Vol. 42, pp. 541-564.

Schueller, G. I., and Shinozuka, M., 1987, *Stochastic Methods in Structural Dynamics*,

Martin Nijhoff Publishers, Boston.

Shapiro, S.A., and Zien, H., 1993, "The O'Doherty-Anstey formula and localization of seismic waves," *Geophysics*, Vol. 58, pp. 736-740.

Shapiro, S. A., Zien, H., and Hubral, P., 1994, "A generalized O'Doherty-Anstey formula for waves in finely layered media," *Geophysics*, Vol. 59, No. 11, pp. 1750-1762.

Svor, T.R. and Meehan, D.N., 1991a, "Quantifying horizontal well logs in naturally fractured reservoirs-I," SPE 22704, Annual Meeting of the Society of Petroleum Engineers, Dallas, Texas.

Svor, T.R. and Meehan, D.N., 1991b, "Quantifying horizontal well logs in naturally fractured reservoirs-II," SPE 22932, Annual Meeting of the Society of Petroleum Engineers, Dallas, Texas.

Thomsen, L., 1986, "Weak elastic anisotropy," *Geophysics*, Vol. 51, pp. 1954-1966.

Toronyi, R.M., 1997, "Advanced reservoir characterization in the Antelope Shale to establish the viability of CO_2 enhanced oil recovery in California's Monterey Formation siliceous shales," 1996 Annual Report to DOE.

Velzeboer, C. J., 1981, "The theoretical seismic reflection response of sedimentary sequences," *Geophysics*, Vol. 46, No. 6, pp. 843-853.

Vernik, L., and Nur, A., 1992, "Ultrasonic velocity and anisotropy of hydrocarbon source rocks," *Geophysics*, Vol. 57, pp. 727-735.

White, B., Sheng, P., and Nair, B., 1990, "Localization and backscattering spectrum of seismic waves in stratified lithology," *Geophysics*, Vol. 55, No. 9, pp. 1158-1165.

White, J.E., 1965, *Seismic Waves: Radiation, Transmission and Attenuation*, McGraw-Hill Book Co., New York, 302 pages.

White, J.E., 1983, *Underground Sound, Application of Seismic Waves*, Elsevier, New York, 253 pages.

Xue, G., Datta-Gupta, A., Valko, P., Blasingam, T., 1997, "Optimal transformation for multiple regression: application to permeability estimation from well logs," *SPE Formation Evaluation.*